

ABSTRACT

Title of Dissertation:

SATELLITE REMOTE SENSING OF
SMOKE PARTICLE OPTICAL
PROPERTIES, THEIR EVOLUTION
AND CONTROLLING FACTORS

Katherine Teresa Junghenn, Doctor of
Philosophy, 2021

Dissertation directed by:

Professor, Zhanqing Li, Department of
Atmospheric and Oceanic Science

The optical and chemical properties of biomass burning (BB) smoke particles greatly affect the impact wildfires have on climate and air quality. Previous work has demonstrated some links between smoke properties and factors such as fuel type and meteorology. However, the factors controlling BB particle speciation at emission are not adequately understood, nor are those driving particle aging during atmospheric transport. As such, modeling wildfire smoke impacts on climate and air quality remains challenging. The potential to provide robust, statistical characterizations of BB particles based on ecosystem and ambient conditions with remote sensing data is investigated here. Space-based Multi-angle Imaging Spectrometer (MISR) observations, combined with the MISR Research Aerosol (RA) algorithm and the MISR Interactive Explorer (MINX) tool, are used to retrieve smoke plume aerosol optical depth (AOD), and to provide constraints on plume vertical extent, smoke age,

and particle size, shape, light-absorption, and absorption spectral dependence. These capabilities are evaluated using near-coincident *in situ* data from two aircraft field campaigns. Results indicate that the satellite retrievals successfully map particle-type distributions, and that the observed trends in retrieved particle size and light-absorption can be reliably attributed to aging processes such as gravitational settling, oxidation, secondary particle formation, and condensational growth. The remote-sensing methods are then applied to numerous wildfire plumes in Canada and Alaska that are not constrained by field observations. For these plumes, satellite measurements of fire radiative power and land cover characteristics are also collected, as well as short-term meteorological data and drought index. We find statistically significant differences in the retrieved smoke properties based on land cover type, with fires in forests producing the tallest and thickest plumes containing the largest, brightest particles, and fires in savannas and grasslands exhibiting the opposite. Additionally, the inferred dominant aging mechanisms and the timescales over which they occur vary between land types. This work demonstrates the potential of remote sensing to constrain BB particle properties and the mechanisms governing their evolution, over entire ecosystems. It also begins to realize this potential, as a means of improving regional and global climate and air quality modeling in a rapidly changing world.

SATELLITE REMOTE SENSING OF SMOKE PARTICLE OPTICAL
PROPERTIES, THEIR EVOLUTION AND CONTROLLING FACTORS

by

Katherine Teresa Junghenn

Dissertation submitted to the Faculty of the Graduate School of the
University of Maryland, College Park, in partial fulfillment
of the requirements for the degree of
Doctor of Philosophy
2021

Advisory Committee:

Professor Zhanqing Li, Chair
Dr. Ralph A. Kahn, Co-Chair
Dr. William K. Lau
Professor Russell R. Dickerson
Professor Rachel T. Pinker

© Copyright by
Katherine Teresa Junghenn
2021

Dedication

Have you heard of tiny Melinda Mae,

Who ate a monstrous whale?

She thought she could,

She said she would,

So she started in right at the tail.

And everyone said, “You’re much too small,”

But that didn’t bother Melinda at all.

She took little bites and she chewed very slow,

Just like a good girl should...

... And in eighty-nine years she ate that whale

Because she said she would!

- Shell Silverstein

I dedicate this work to my parents Mary and Dieter, who taught me the importance of perseverance, patience, and *especially* laughter. Without these values, I would not have obtained my doctorate (at least, not in less than eighty-nine years). Thank you, Mom and Dad!

Acknowledgements

This research would not have been possible without the support and mentorship of my research advisors Drs. Zhanqing Li and Ralph Kahn, who have been excellent teachers, advocates, and colleagues over the years. Thank you both for taking me on as a student, and for always pushing me to reach my full potential while showing me nothing but patience and positive reinforcement. I have been extremely fortunate to work with the both of you, and I look forward to continuing to work together in the future as I begin my postdoctoral fellowship. I would also like to thank all those involved in the FIREX-AQ campaign, and to NASA for the support to participate. I also gratefully acknowledge the support of the Maryland Space Grant Consortium Scholarship, which helped fund this work.

Thank you to all the faculty and staff in the Atmospheric and Oceanic Science Department who have helped me along the way, especially Dr. Timothy Carty, Jeff Henrikson, and Tammy Hendershot. I would not have gotten very far in graduate school without their help and advice over the years. Furthermore, thank you to all the fellow graduate students I have met at UMD who have been my friends, study buddies, and partners in crime over the years. I am very thankful to have been a part of such a welcoming community, where students support each other and work together.

I would like to acknowledge my loving husband, Steven Noyes, for his unwavering support and for donating countless hours over the past six years to help me develop the coding skills that were so crucial to my research. I often jokingly tell

others, “I knew I married a software engineer for a reason!” Thank you, Steve, for your patience, guidance, and encouragement.

To all my friends and family, thank you for your encouragement along the way; and a special thank you to my father in particular, who’s passion for the pursuit of knowledge inspired my own. I did not originally intend to follow in his footsteps and obtain a doctorate, but I guess you win Dad!

Finally, thank you to my cats Luke and Finn, who always knew to sit on my keyboard when I needed to take a break (or even when I didn’t).

Table of Contents

Dedication.....	ii
Acknowledgements	iii
Table of Contents	v
List of Tables.....	vii
List of Figures.....	ix
List of Abbreviations.....	xiii
Chapter 1: Introduction.....	1
1.1. Background and Motivation	1
1.2. Research Objectives	6
Chapter 2: Experiment Design and Methods.....	9
2.1. Introduction	9
2.2. The MISR Instrument.....	9
2.3. Validating the MISR Retrievals	16
2.3.1. Experiment Design	16
2.3.1. Aircraft Data	17
2.4. Summary.....	30
Chapter 3: Validating Space-Based Observations of Wildfire Smoke Particle Properties: The Biomass Burning Observation Project.....	31
3.1. Introduction	31
3.2. Phase I Results and Discussion: Validation with Near-Coincident Flight Data	33
3.2.1. <i>In situ</i> Observations: A First Look	36
3.2.2. Satellite Observations: Validation and Providing a Broader Context	41
3.3. Phase II Results and Discussion: Using Non-Coincident RA and In Situ Observations.....	48
3.3.1. The Colockum Tarps Fire: Aircraft Observations Preceding Satellite Observations	49
3.3.2. The Douglas Complex Fire: Satellite Observations Preceding Aircraft Observations	50
3.4. Summary.....	51
Chapter 4: Validating Space-Based Observations of Wildfire Smoke Particle Properties: The FIREX-AQ Field Campaign	53
4.1. Introduction	53
4.2. Results and Discussion	56
4.2.1. Satellite Observations	62
4.2.2. <i>In situ</i> Observations and Comparison with MISR	66
4.2.3. Overview of Comparison.....	70
4.2.4. Connecting Downwind Plume Changes between MISR and FIREX.....	74
4.3. An Improved Understanding of MISR Capabilities.....	79
4.4. Summary.....	80
Chapter 5: Canadian and Alaskan Wildfire Smoke Particle Properties, Their Evolution, and Controlling Factors, Using Space-Based Observations	83
5.1. Introduction	83

5.2. Methodology.....	84
5.2.1. Experiment Setting and Case Selection.....	84
5.2.2. MODIS Fire Radiative Power and Land Cover Type	85
5.2.3. MERRA-2 Reanalysis	87
5.2.4. North American Drought Monitor.....	89
5.3. Results and Discussion	92
5.3.1. Overview of Smoke Plume Height Observations	96
5.3.2 Impact of Land Cover Type on Plume Heights	97
5.3.3. Overview of Smoke Particle Property Observations	101
5.3.4. Impact of Land Cover Type of Smoke Particle Properties.....	102
5.3.5 Downwind Particle Evolution and Differences Between Fire Types.....	105
5.3.6. Impact of Drought on Plume Heights and Particle Properties.....	107
5.4. Summary.....	111
Chapter 6: Concluding Remarks	113
6.1. Overview of Study.....	113
6.1.1. Conclusions from the Validation Experiments.....	114
6.1.2. Conclusions from the Canada-Alaska Regional Study.....	116
6.2. Plans for Future Work	118
Appendix A	120
Appendix B.....	145
Appendix C.....	168
Bibliography	171

List of Tables

Table 2.1. MISR components from Research Aerosol (RA) retrieval results, using the algorithm version summarized in this chapter, with a 774-mixture climatology. SSA—single scattering albedo.....	13
Table 2.2. Suite of field campaign instruments used for the two validation studies of the MISR RA. Note: Other aircraft instruments measuring the same quantity may have also been aboard the aircraft, but were not used here	20
Table 2.3. Size categories used to analyze the <i>in situ</i> observations in both BBOP and FIREX validation studies. PCASP—Passive Cavity Aerosol Spectrometer; CAS—Cloud and Aerosol Spectrometer; LAS—Laser Aerosol Spectrometer.....	26
Table 3.1. Flight dates, times, and locations compared with dates and times of the Multi-Angle Imaging Spectroradiometer (MISR) overpass of the same area. Positive time delays between satellite and aircraft observations indicate the satellite observed the fire after the aircraft, whereas negative numbers mean the satellite completed its overpass first. The last flight, on 21 August, is the focus of the validation portion of the study. UTC—Universal Coordinated Time.....	33
Table 3.2. Aircraft data: aerosol size, chemical, and physical properties for the Government Flats Complex Fire measured <i>in situ</i>	39
Table 3.3. MISR-observed particle properties for the Government Flats Complex Fire. AOD—aerosol optical depth; ANG—Ångström exponent; SSA—single scattering albedo; BlS—black smoke; BrS—brown smoke	42
Table 4.1. MISR-observed particle properties for the Williams Flats fire by region. AOD—aerosol optical depth; SSA—single scattering albedo (558 nm); ANG—extinction Ångström exponent (446–866 nm).	56
Table 4.2. Aircraft-measured particle properties, averaged by transect. Norm.-- CO-normalized.	68
Table 4.3. Aircraft data aggregated by plume region: aerosol size, chemical, and physical properties for the Williams Flats Fire measured <i>in situ</i> on 06 August 2019. Norm.-- CO-normalized.....	69
Table 5.1. Distributions of plume number, plume height, boundary layer height, location of burn, and dominant MODIS fuel type shown in three different ways: A) annually, B) monthly, and C) by fuel type. Note that an individual fire may burn in several biomes, so plumes in Table 1C are not in mutually exclusive categories. AGL— above ground level; PBL—planetary boundary layer. See footnotes for land type and region/territory abbreviations.	88

Table 5.2. Definitions of the land cover types detected in this study, from the MODIS International Geosphere-Biosphere Programme (IGBP) classification method	91
Table 5.3. Statistical summary of main smoke plume parameters for each fire category. FT—free troposphere; FRP —fire radiative power; AOD—aerosol optical depth; ANG—Ångström exponent; SSA—single scattering albedo; BlS—black smoke; BrS—brown smoke	94

List of Figures

- Figure 3.1.** The Government Flats Complex Fire as seen on 21 August 2013: (a) at MISR overpass time (19:07 UTC; Moderate Resolution Imaging Spectroradiometer (MODIS) Terra red–green–blue (RGB) context image), and (b) during the Department of Energy’s Biomass Burning Observation Project (BBOP) flight operations (20:49 UTC; MODIS Aqua RGB image; the aircraft flight began at 21:20 UTC). The red dots in Panel (a) indicate MODIS-identified hot spots, which are used to estimate source location. The dashed lines represent the plume outlines we use for analysis. At both observation times, the plume is divided into regions (I–IV) based on estimated plume age, to allow for easy, qualitative comparison of inter- and intra-plume properties. Panels (c) and (d) represent the aircraft *in situ* CO and total aerosol count measurements, respectively 35
- Figure 3.2.** BBOP aircraft observations of the Government Flats Complex fire on 21 August 2013: (a) 522-nm SSA (particle soot absorption photometer (PSAP)/neph); (b) aerosol oxidation (derived from the three-channel Oxides of Nitrogen Analyzer); (c) mass concentration of black carbon (BC) and size of BC-containing particles (single-particle soot photometer (SP2)); (d) concentration of particles that can act as cloud-condensation nuclei (CCN) at 0.15% supersaturation (CCN-200 instrument); (e) the CCN concentration divided by the CO concentration; (f) the total aerosol concentration divided by the CO concentration 36
- Figure 3.3.** Fractional contributions (from zero to one) to the total aerosol count for (a) very small, (b) small, (c) medium, and (d) large aerosols in the Government Flats Complex Fire, as measured by the PCASP and CAS *in situ* instruments on 21 August 2013. The gray lines represent the boundaries between regions defined in Figure 3.1. Note: approximate size ranges are given above each plot, and the scales differ between categories. 38
- Figure 3.4.** Plume properties for the Government Flats Complex Fire retrieved by MISR at 19:07 UTC (Orbit 72746, Path 45, Block 54) on 21 August 2013: (a) MISR Interactive Explorer (MINX) stereo height retrieval map; (b) MINX stereo height profile as a function of distance from the source, for both zero-wind (red) and wind-corrected (blue) analyses, with surface elevation indicated in green, (c) MINX-retrieved across-swath and along-swath wind vectors, and RA-derived (d) AOD at 558 nm, (e) extinction ANG, and (f) SSA at 558 nm. The transects for estimated plume ages corresponding to the regional boundaries in Figure 3.1 are indicated with thin gray lines in panels d–f. 43
- Figure 3.5.** The absolute and fractional AOD of various MISR components for the Government Flats Complex Fire on 21 August 2013, where (a–b) are the sum of all “flat,” i.e., BC-like components (BLS), (c–d) are the sum of all

“steep,” i.e., BrC-like components (BrS), (e–f) are the non-spherical dust-like components, and (g–h) are the sum of all non-light-absorbing components.....47

Figure 4.1. The Williams Flats Fire as seen on 06 August 2019: (a) at Multi-Angle Imaging Spectrometer (MISR) overpass time (19:06 UTC; MODIS Terra RGB image), and (b) during the Fire Influence on Regional to Global Environments Experiment-Air Quality (FIREX-AQ) flight operations (20:50 UTC; MODIS Aqua RGB image). The red dots indicate MODIS-identified hot spots, used to estimate source location. The dashed lines represent plume outlines we use for analysis. At both observation times, the plume is divided into distinct regions (I–III) based on estimated plume age, to allow for easy, qualitative comparison of inter- and intra-plume properties. At the time of MISR observation, there is an additional region (IV) that separates the southern-most plume from the other regions. The differential absorption CO measurements instrument (DACOM) CO mixing ratio and the laser aerosol spectrometer (LAS) total aerosol concentration observed by the aircraft (above 0.09 μm in diameter) are displayed in (c) and (d), respectively.....55

Figure 4.2. Height and wind properties for the Williams Flats Fire retrieved by MISR at 19:06 UTC (Orbit 104434, Path 45, Block 52) on 06 August 2019. The top panels (a–c) correspond to retrievals for the northern plume, whereas the bottom panels (d–f) correspond to the southern plume. Panels (a,d) are MISR-MINX stereo height retrieval map; (b,e) are MINX stereo height profiles as a function of distance from the source, for both zero-wind (red) and wind-corrected (blue) analyses, with surface elevation indicated in green; and (c,f) are the across-swath and along-swath wind vectors. The dashed grey lines in panels (b) and (c) represent the dividing lines between regions in the northern plume defined in Figure 4.1.....59

Figure 4.3. Basic plume properties for the Williams Flats Fire retrieved with the MISR RA at 19:06 UTC (Orbit 104434, Path 45, Block 52) on 06 August 2019, accompanied by a contemporaneous image of the fire (a) taken from the aircraft during sampling [credit: K. Junghenn Noyes]. MISR RA results are given in panels (b) AOD at 558 nm; (c) 446–866 nm extinction Ångström exponent (ANG); and (d) single scattering albedo (SSA) at 558 nm. The transects for estimated plume ages corresponding to the region boundaries in Figure 4.1 are indicated with thin grey lines.....60

Figure 4.4. The absolute and fractional AOD (558 nm) of various MISR RA aerosol components for the Williams Flats Fire on 06 August 2019, where (a,b) are the sum of all spectrally “flat” or BIS components, (c,d) are the sum of all spectrally “steep” or BrS components, (e,f) are the sum of all non-light-absorbing components, and (g,h) are the non-spherical, dust-like components. Fractional plots are given as a fraction of 1. Note: scales differ between panels.....60

Figure 4.5. The absolute and fractional AOD (558 nm) of various MISR RA aerosol size bins for the Williams Flats Fire on 06 August 2019, where (a,b) are

the sum of all “very small” components, (c,d) are the sum of all “small” components, (e,f) are the sum of all “medium” components, and (g,h) are the sum of all “large” components (which includes the non-spherical analog). Particles are assumed to be normally distributed around the effective radius (R_e) provided in the legend. Note that “large” aerosols include both the large spherical nonabsorbing component ($R_e = 1.28$) and the non-spherical component ($R_e = 1.21$). Fractional plots are given as a fraction of 1. Note: scales differ between panels.....61

Figure 4.7. FIREX aircraft observations of the Williams Flats Fire on 06 August 2019: (a) 530 nm SSA (PSAP/neph), (b) aerosol oxidation (derived from ozone-induced chemiluminescence), (c) Mass concentration of rBC (SP2), (d) rBC concentration normalized by CO (SP2, DACOM), (e) concentration of particles that can act as CCN at 0.34% supersaturation (CCN-100), and (f) CCN concentration normalized by CO (CCN-100, DACOM). The grey lines represent the boundaries between regions defined in Figure 4.1.73

Figure 4.8. Fractional contributions (from zero to one) to the total aerosol count for very small (a), small (b), medium (c), and large (d) aerosols in the Williams Flats Fire, as measured by the LAS *in situ* instrument on 06 August 2019. The grey lines represent the boundaries between regions defined in Figure 4.1. Note: Approximate size ranges are given in the corner each plot, and the scales differ between categories.....77

Figure 4.9. Mean particle number (a–c) and volume (d–f) concentrations and size distributions for each transect observed by the FIREX aircraft (from the LAS instrument), where (a) includes transect 1 and samples the downwind end of Region I, (b) includes transects 2 through 6, corresponding to Region II, and (c) contains transects 7 and 8 that observed Region III. The mode aerosol diameter for each transect is provided as well, where box and text color are matched with the corresponding transect color.78

Figure 5.2. Seasonal and inter-annual variability of plume number (a, c) and percent of these in the free troposphere (FT) (b, d). Each bar is divided up by color according to the relative contribution from each of the three fire types in the given month or year, with quantitative annotations. For example, 39 plumes were identified in May, 16 of which were W fires and 23 of which were F fires (panel c). Of the 39 fires that month, 42% were in the FT (17% that were classified at W fires, and 25% that were classified as F fires) (panel d). A plume is considered to be in the FT if its median height is 100 m greater than the PBL height as defined in the MERRA-2 dataset.92

Figure 5.3. Particle size distributions in terms of each RA component’s fractional contribution to the total AOD. All plume types are shown in (a), whereas panels (b-d) display color-coded results for individual plume types, denoted with the appropriate abbreviation in the right-hand corner. Points represent the mean values and whiskers show the standard deviations. Arrows

highlight the differences in the partitioning between small and medium particle fractions for the different plume types.....99

Figure 5.4. MISR mid-visible Ångström exponent (unfilled marker, dotted line) and single scattering albedo (filled marker, solid line) by smoke age for (a) Forest plumes, (b) Woody plumes, and (c) Grassy plumes. In (d), the MISR mid-visible AOD is plotted by age for Forest and Grassy plumes. The points represent the mean values, while the whiskers are standard deviations.....100

Figure 5.5. MISR particle-size component AOD fractions (in terms of contribution to the total AOD, from 0 to 1) by smoke age for (a) Forest plumes, (b) Woody plumes, and (c) Grassy plumes. In (d), the MISR mid-visible AOD is plotted by age for Forest and Grassy plumes, for reference. The points represent the mean values, while the whiskers are standard deviations. Arrows help highlight the point of important particle-size transitions.....103

Figure 5.6. MISR particle-type component AOD fractions (in terms of contribution to the total AOD, from 0 to 1) by smoke age for (a) Forest plumes, (b) Woody plumes, and (c) Grassy plumes. In (d), the MISR mid-visible AOD is plotted by age for Forest and Grassy plumes, for reference. The points represent the mean values, while the whiskers are standard deviations. Arrows help highlight the point of important particle-size transitions.....104

Figure 5.7. (a) The number of plumes observed in each drought category (see key), colored by plume type; and (b-g) the impact of drought level on maximum (top row) and median (bottom row) plume heights, for each plume type. The marker represents the mean value, and the whiskers are standard deviations.....108

Figure 5.9. MISR mid-visible single scattering albedo (top row) and the fraction of AOD from BIS vs. the sum of both BIS and BrS (bottom row) for different drought conditions. Decreasing values indicate lower amounts of BrS and higher amounts of BIS. Panels are color-coded by plume type and identified with the appropriate abbreviation in the top right corner. Points represent the mean, and whiskers are the standard deviations. Arrows help highlight the general trends with increasing drought index.....110

List of Abbreviations

ANG	Ångström exponent
AOD	Aerosol optical depth
BB	Biomass burning
BBOP	Biomass Burning Observation Project
BC	Black carbon
BIS	Black smoke
BrC	Brown carbon
BrS	Brown smoke
CAS	Cloud and Aerosol Spectrometer
CCN	Cloud condensation nuclei
CCN-100/200	Cloud Condensation Nuclei Counter-100/200
CO	Carbon monoxide
CO ₂	Carbon dioxide
DIAL-HSRL	Differential absorption lidar and high spectral resolution system
FIREX-AQ	Fire Influence on Regional to Global Environments Experiment- Air Quality
FT	Free troposphere
FRP	Fire radiative power
GSFC	Goddard Space Flight Center
LAS	Laser aerosol spectrometer
LIDAR	Light Detection and Ranging
LED	Light-emitting diode
MCE	Modified Combustion Efficiency
MERRA-2	Modern-Era Retrospective analysis for Research and Applications, Volume 2
MINX	MISR Interactive Explorer
MISR	Multi-angle Imaging Spectroradiometer
MODIS	Moderate Resolution Imaging Spectroradiometer
NASA	National Aeronautics and Space Administration
NEMR	Normalized Excess Mixing Ratio
Neph	Nephelometer
NIR	Near-infrared
NOAA	National Oceanic and Atmospheric Administration
OA	Organic Aerosol
PAS	Photoacoustic soot spectrometer
PBL	Planetary boundary layer
PCASP	Passive Cavity Aerosol Spectrometer
PSAP	Particle soot photometer
PTI	Photothermal interferometer
RA	Research aerosol algorithm
rBC	Refractory black carbon
REPA	Retrieved effective particle absorption
REPS	Retrieved effective particle size

SOA	Secondary organic aerosol
UTC	Universal Coordinated Time
UV	Ultra-violet
SP2	Single particle soot photometer
SSA	Single scattering albedo

Chapter 1: Introduction

1.1. Background and Motivation

Wildfire smoke emissions are a rich and complex mixture of gas and aerosol constituents, the impacts of which occur over wide temporal and spatial scales and can result in short-term regional air quality issues as well as climate forcing. Globally, wildfires are the most significant source of light-absorbing black carbon (BC) and brown carbon (BrC) airborne particles [Bond et al., 2013; Feng et al., 2013]; they can also be considerable sources of scattering aerosols and weakly absorbing soil or dust particles. The emission of all such particles can have broad consequences, many of which are interdependent and are not entirely understood at present. Smoke aerosols often contribute towards poor air quality regionally, as particulate matter is dangerous to respiratory health and large wildfire plumes can be transported to residential areas far downwind. Light-absorbing aerosols can affect the local radiative budget by warming the surrounding air layer and shading the surface. This in turn impacts atmospheric stability, potentially leading to changes in cloud distribution and the water cycle [Albrecht, 1989; Kaufman and Fraser, 1997; Koch and Del Genio, 2010]. If they escape the planetary boundary layer (PBL), smoke particles can stay aloft for several days or more and be transported long distances, extending their radiative impact in both time and space [Taubman et al., 2004; Vant-Hull et al., 2005; Colarco et al., 2004; Kahn et al., 2008]. As such, they may further impact cloud formation and lifetime, serving as cloud condensation nuclei (CCN) and

potentially increasing cloud albedo via the Twomey effect, or, conversely, contributing to droplet warming and evaporation via the semi-direct effect [Kaufman and Fraser, 1997; Koch and Del Genio, 2010; Warner and Twomey, 1967; Hobbs and Radke, 1969; Hansen et al., 1997]. The resulting changes in cloud reflectivity and lifetime may then generate significant climate forcing.

Emitted smoke composition varies widely among wildfires, and even over time for a single fire, with evidence suggesting there are systemic differences in particle size distribution, particle light-absorption, and the spectral dependence of absorption based on fuel type, fuel amount, burning characteristics, and meteorology [Dubovik et al., 2002; Chen et al., 2008; Eck et al., 2003; Shi et al., 2019; O'Neill et al., 2002]. For example, studies have suggested a connection between combustion efficiency (CE) and particle size at the point of emission, with smoldering fires (lower CE) generating larger particles than flaming fires (higher CE) under many conditions [Reid and Hobbs, 1998; Reid et al., 2005]. Fire regime has also been linked to smoke particle type—although BC is often the dominant absorbing aerosol in biomass burning (BB) smoke, smoldering fires tend to produce higher fractions of BrC than flaming ones [Chakrabarty et al., 2010, 2016; Petrenko et al., 2012]. Both smoldering and flaming regimes occur near-simultaneously in many fires; however smoldering conditions are more common and may even dominate where fuel is coarse and moist, such as in forests where the fire can penetrate the organic soil layer. In contrast, flaming conditions dominate over smoldering in regions of fine, grassy fuel that dry out quickly and can produce high-temperature combustion, such as savannas and grasslands [Ottmar, 2001; Urbanski, 2013;

Gonzalez-Alonso et al., 2019; van der Werf et al., 2010]. Compared to smoldering fires, flaming fires also emit less carbon monoxide (CO), volatile gases, and smoke per unit of fuel consumed [Urbanski, 2013]. We therefore might expect that geographic and meteorological conditions are important drivers in particle speciation and plume chemistry.

In addition to exhibiting distinct chemical properties, BC and BrC are also optically unique in that BC is highly absorbing across all visible wavelengths, whereas BrC is less absorbing overall and displays enhanced light-absorption at shorter wavelengths [Kirchstetter et al., 2004; Samset et al., 2018]. These and other observed differences in particle optical and physical properties indicate that the impacts of wildfires can vary over a wide range. However, the conditions that mediate these differences at the point of emission are not well understood. Furthermore, the microphysical properties and mixing state of BB particles can change dramatically even a short distance away from the source, as aerosols interact with water vapor, trace gases, and other particles through a variety of complex processes. For example, particles may increasingly undergo oxidation downwind as they interact with background air, trace gases and sunlight, leading to both chemical and structural changes. As smoke cools away from the flame front, semi-volatile gases (known as volatile organic compounds, or VOCs) can condense onto existing emitted particles, creating organic or inorganic coatings that result in increased particle size and alter particle scattering as well as CCN efficiency, especially in the case of BC (which is hydrophobic in its pure form) [Reid et al., 2005; Zhou et al., 2017; Yokelson et al., 2009; Akagi et al., 2012; Hennigan et al., 2012; Ahern et al.,

2019]. VOCs can also spontaneously condense into new, very small particles, a process known as secondary organic aerosol (SOA) formation, which increases the plume particle number concentration and shifts the overall plume particle size distribution to reflect smaller average diameters [Akagi et al., 2012; Wang et al., 2013]. (In the atmospheric chemistry community, SOA formation is considered to include both new particle formation and VOC condensation onto existing particles. Here, we consider them as distinct aging mechanisms; from a remote sensing perspective, condensation on existing particles is usually classified as particle growth rather than new particle formation, especially as we often cannot distinguish the condensation of volatile organic gases from hygroscopic growth.) Organic aerosol (OA) has also been known to evaporate, transitioning from the particle to the gas phase [May et al., 2013]. Further, particles can hydrate through the uptake of water vapor, leading to increases in size and light scattering. Lastly, size-selective dilution might move larger particles toward the bottom of the plume or even deposit them onto the surface, resulting in size distributions that are both narrower on average and reflect smaller sizes. These processes often occur in combinations that may change on relatively short temporal and spatial scales.

As wildfire frequency and severity are expected to increase with global warming, it is becoming increasingly important to improve our understanding of the factors controlling wildfire smoke particle properties. To date, most chemical transport and climate models do not discriminate between BC and BrC, despite their distinct optical and physical properties, which can therefore produce different environmental consequences [Feng et al., 2013; Samset et al., 2018]. Models are also

uncertain about the role wildfire smoke plays in the aerosol–cloud interaction. Better characterization of fire-generated particles is thus a pressing issue for many modeling efforts. Constraining particle properties and the dominant aging mechanisms in terms of fuel properties and meteorological conditions would greatly contribute towards this goal. Such insight would also have consequences for air quality modeling, as particle speciation and evolution are important factors in determining the atmospheric lifetime of harmful smoke particulates.

In recent years, significant efforts have been made to constrain BB particle properties both in the laboratory (e.g., Zhou et al. [2017]) and in aircraft-based field campaigns (e.g., Kleinman and Sedlacek [2013, 2016]; Toon et al. [2016]; Roberts et al. [2018]). These experiments are able to observe plume gas- and particle-phase chemistry in great detail, and in some cases, can directly measure different aerosol types within plumes [Forrister et al., 2015; Sedlacek et al., 2018; Adachi et al., 2019]. They also provide considerable detail about aerosol microphysical properties, such as SSA and size distribution, which, in the past, were comparatively less well represented in satellite retrieval algorithms and models. However, such experiments are unable to observe an entire plume in context, and they provide only a small set of BB cases, limiting their usefulness for robust statistical characterization of BB particle properties.

Satellite remote sensing data allows for snapshots of complete plumes and their surroundings, providing context for assessing plume evolution. In addition, satellites can provide much greater sampling compared to *in situ* techniques. However, satellite instruments are unable to capture the fine detail that can be

observed *in situ*, and in the past, have not provided ample constraints on key aerosol properties such as size and light-absorption [Wong and Li, 2001]. Early work was largely dedicated to retrieving the optical depth of ultraviolet (UV)-absorbing species, with substantial uncertainties due to the relatively coarse pixel resolution (~ 10 km or more) from most spacecraft UV instruments and the sensitivity of the results to the vertical distribution of the smoke and the contributions from other species [Jethva and Torres, 2011; Konovalov et al., 2017]. This work builds upon these studies using a unique set of satellite remote sensing tools that offer crucial improvements in interpreting optical retrievals from space.

1.2. Research Objectives

Recently developed techniques allow for better characterization of previously unconstrained wildfire plume heights and particle properties from space, with the potential to improve our understanding of BB particles globally by exploring the factors that control emitted and evolved BB particle properties (e.g., Kahn [2020]). These satellite products will achieve their greatest value when applied broadly, to numerous cases over entire ecosystems, yielding statistically robust patterns of smoke-plume behavior. However, the application of new satellite remote sensing techniques requires thorough validation against coincident *in situ* observations first.

The current work takes the first steps toward providing regional constraints on BB particle properties and their dependence on meteorology, vegetation, and burning conditions from space-based observations. Specifically, this study relies on measurements from the Multi-Angle Imaging Spectrometer (MISR) aboard the Earth Observing System's Terra satellite, in conjunction with the MISR Research Aerosol

(RA) algorithm, to assess BB particle properties and the MISR Interactive Explorer (MINX) tool to determine plume height and associated wind vectors. We first evaluate the strengths and limitations of these techniques with two extensive validation studies, using near-coincident *in situ* observations from the Biomass Burning Observation Project (BBOP) and the Fire Influence on Regional to Global Environments Experiment - Air Quality (FIREX-AQ) field campaigns. The validation experiments inform us how to interpret the optical MISR signatures in terms of the chemical and microphysical properties observed by the aircraft, and demonstrate the extent to which we can infer the specific aging mechanisms or burning conditions from the remote-sensing data alone. We then apply these techniques to a large ensemble of fire samples across Canada and Alaska, which are not constrained by field observations, in order to:

- 1) Characterize emitted and evolved smoke particle properties;
- 2) Identify patterns and establish relationships among biomass type, burning conditions, and ambient meteorology, and plume properties; and
- 3) Infer the relevant aging mechanisms from the observed patterns.

To this end, we compare the retrieved patterns associated with different ecosystems and environmental conditions with an array of other data, including fire radiative power (FRP) and land cover type from the MODerate resolution Imaging Spectroradiometer (MODIS), drought severity from the North American Drought Monitor (NADM), and MERRA-2 meteorological reanalysis. Statistical analysis of the relationships among these observations provides insight into the factors controlling BB particle type emissions and the associated aging processes, directly

addressing key elements missing from current climate and air quality modeling efforts.

Chapter 2 describes the tools and methods used during the validation portion of the study. Chapter 3 presents results and analysis of the BBOP validation cases, and Chapter 4 discusses the FIREX validation case. In Chapter 5, we present results for the regional-scale study in Canada and Alaska. Finally, conclusions and plans for future work are given in Chapter 6.

Chapter 2: Experiment Design and Methods

2.1. Introduction

Before the MISR RA can be applied to large, regional-scale studies of wildfires, it is necessary to properly validate the MISR-retrieved particle properties against *in situ* data so that future results can be interpreted at the appropriate level-of-detail. This chapter highlights the tools, data, and methods used to conduct the two validation experiments presented in this work. Section 2.2 provides an overview of the MISR instrument, and it describes the MINX software tool and the Research Aerosol (RA) algorithm. Section 2.3 explains the design of the field validation experiments and provides detailed overviews of each aircraft instrument used. Finally, a summary is given in Section 2.4.

2.2. The MISR Instrument

The MISR instrument is in a polar orbit aboard the NASA Earth Observing System's Terra satellite and has a swath width of ~380 km. As such, it samples locations at the equator approximately once every nine days, and every two days near the poles; over much of the planet, coverage occurs about once per week on average. MISR offers unique, multi-angle imagery through the use of nine cameras viewing in the forward, nadir, and rear directions along the satellite orbit track, and four spectral bands observed at each angle centered at approximately 446 nm, 558 nm, 672 nm, and 866 nm [Diner et al., 1998]. The use of multiple camera angles makes it possible

to retrieve height and motion vectors for clouds and aerosol plumes. This geometrical approach relies on the parallax of contrast features within the plume; therefore, plume features must exhibit sufficient optical thickness and contrast, relative to the surface, for plume height to be derived with this method. The MISR Interactive Explorer (MINX) software tool [Nelson et al., 2008, 2013] nicely accomplishes these retrievals and was used to derive stereo heights and associated wind vectors for plumes in this work. With MINX, the user manually defines the plume source, plume extent, and wind direction in the MINX imagery to retrieve heights and winds locally. MINX has been used in a number of studies, including but not limited to retrieving heights and winds for volcano, wildfire, and dust plumes [Junghenn Noyes et al., 2020a, 2020b; Val Martin et al., 2010, 2018; Scollo et al., 2012; Tosca et al., 2011; Kahn and Limbacher, 2012; Flower and Kahn, 2017a, 2017b, 2018, 2020a, 2020b; Yu et al., 2018; Vernon et al., 2018]. Under good retrieval conditions, MINX plume height estimates are accurate within ± 0.5 km or better. In this work, we use the retrieved wind vectors, along with the distance from the source measured in the images, to approximate smoke age at various points throughout smoke plumes, such that the comparison with the aircraft data can be focused on relating elements of similar age during validation (Chapters 3 and 4), and so that patterns in the evolution of downwind particle properties can be associated with general timescales in the Canadian and Alaskan wildfires (Chapter 5). The retrieved stereo heights are used to study how plume height and thickness may inform the evolution of particle size distribution (Chapters 3-5), to determine whether the smoke was injected above the planetary boundary layer (PBL) (Chapter 5), and to find potential relationships

between plume injection and burning intensity, as approximated by fire radiative power or FRP (Chapter 5). In addition, the MINX analysis provides some initial insight into the quality of the viewing conditions, as plumes lacking a clear source or easily identifiable wind direction in the satellite imagery can result in low-confidence height retrievals, and may need to be excluded from analysis. Lastly, if the MINX plume height is above about 2 km, the MISR images sometimes must be co-registered at the median plume height rather than at ground level to maximize aerosol-type retrieval performance when subsequently using the RA to derive particle properties.

Information relating to aerosol type was retrieved using the MISR research aerosol retrieval algorithm (RA) [Limbacher and Kahn, 2014, 2019], which compares the multi-angle, multi-spectral MISR observations with simulated top-of-atmosphere (TOA) reflectances to retrieve aerosol optical depth (AOD) and to constrain particle extinction Ångström exponent (ANG; calculated from measurements at 446 and 866 nm), particle single scattering albedo (SSA) and its spectral slope, and particle shape (spherical vs. non-spherical) for each ~1.1-km MISR pixel. The intended use of the RA (e.g., for pollution studies, or for wildfire, volcano, or dust plumes) determines the specific set of aerosol components, each having a different range of microphysical properties, to be included in the algorithm climatology. The particle property information content of MISR observations is qualitative, amounting to three to five size bins (e.g., “small,” “medium,” and “large”), two to four bins in SSA, and spherical vs. randomly oriented non-spherical particle shapes, under good but not necessarily ideal retrieval conditions [Kahn et al., 2010; Kahn and Gaitley, 2015]. For our studies, the RA includes one non-spherical component (a soil or dust grain optical

analogue, based on an optical model derived in Lee et al. [2017]) and 16 spherical components ranging in size and SSA values (Table 2.1). For light-absorbing aerosols, particle type is further classified based on the spectral variation in absorption across the visible and near-infrared spectrum, where “flat” aerosols display little to no wavelength dependence and are representative of typical urban pollution or BC-containing particles, whereas “steep” aerosols exhibit greater absorption at shorter wavelengths and are more similar to BrC from wildfire smoke [Chen et al., 2008; Samset et al., 2018; Limbacher and Kahn, 2014; Andreae and Gelencser, 2006]. In the atmospheric chemistry community, the term “BC” is used to refer specifically to the refractory black carbon component (mid-visible SSA \sim 0.4) that is usually internally mixed within aerosols, derived from *in situ* light-absorption measurements. In contrast, the remote sensing community often uses this term to describe the aerosol types (i.e., entire particles) that exhibit relatively strong (SSA $>\sim$ 0.7), spectrally flat light-absorption. To avoid confusion, we refer here to the MISR-derived smoke optical analogs as Black Smoke (BlS) and Brown Smoke (BrS), as these appropriately describe the spectral dependence of the retrieved SSA without directly connecting to specific chemical constituents. For each MISR pixel, the RA calculates AOD values for each particle component to create a best-guess mixture representing the aerosol plume composition, such that the simulated TOA reflectances best match those observed in the MISR multi-angle, multi-spectral measurements. This method has already been used for global aerosol typing [Kahn and Gaitley, 2015] and for characterizing particle type in volcanic and wildfire plumes [Toon et al., 2016; Kahn and Limbacher, 2012; Flower and Kahn, 2018, 2020a, 2020b].

Table 2.1. MISR components from Research Aerosol (RA) retrieval results, using the algorithm version summarized in this chapter, with a 774-mixture climatology. SSA—single scattering albedo.

Particle Size, Shape, Light-Absorption	r_e (μm) ^a	SSA (446) ^b	SSA (558) ^b	SSA (672) ^b	SSA (866) ^b	Code ^c
Very small, spherical, strongly absorbing (flat)	0.06	0.84	0.79	0.73	0.62	VSmSphSab(f)
Very small, spherical, strongly absorbing (steep)	0.06	0.76	0.80	0.83	0.76	VSmSphSab(s)
Very small, spherical, moderately absorbing (flat)	0.06	0.92	0.89	0.86	0.78	VSmSphMab(f)
Very small, spherical, moderately absorbing (steep)	0.06	0.88	0.90	0.90	0.87	VSmSphMab(s)
Small, spherical, strongly absorbing (flat)	0.12	0.81	0.79	0.78	0.74	SmSphSab(f)
Small, spherical, strongly absorbing (steep)	0.12	0.72	0.80	0.87	0.84	SmSphSab(s)
Small, spherical, moderately absorbing (flat)	0.12	0.90	0.89	0.88	0.85	SmSphMab(f)
Small, spherical, moderately absorbing (steep)	0.12	0.85	0.90	0.93	0.92	SmSphMab(s)
Medium, spherical, strongly absorbing (flat)	0.26	0.78	0.80	0.80	0.81	MeSphSab(f)
Medium, spherical, strongly absorbing (steep)	0.26	0.70	0.80	0.88	0.89	MeSphSab(s)
Medium, spherical, moderately absorbing (flat)	0.26	0.89	0.90	0.90	0.90	MeSphMab(f)
Medium, spherical, moderately absorbing (steep)	0.26	0.83	0.90	0.94	0.94	MeSphMab(s)
Very small, spherical, non-absorbing	0.06	1.0	1.0	1.0	1.0	VSmSphNab
Small, spherical, non-absorbing	0.12	1.0	1.0	1.0	1.0	SmSphNab
Medium, spherical, non-absorbing	0.26	1.0	1.0	1.0	1.0	MeSphNab
Large, spherical, non-absorbing	1.28	1.0	1.0	1.0	1.0	LaSphNab
Large, non-spherical, weakly absorbing	1.21	0.91	0.95	0.97	0.98	LaNsphWab

^a Each component has a designated effective radius (r_e).

^b Wavelengths are given in nm.

^c The code for each component includes four elements: size—very small (VSm), small (Sm), medium (Me), and large (La); shape—spherical (Sph) or non-spherical (Nsph); light-absorption—non-absorbing (Nab), weakly absorbing (Wab), moderately absorbing (Mab), and strongly absorbing (Sab); spectral light-absorption profile—equal in all spectral bands (flat), or varying between spectral bands (steep).

The particle property information derived from the MISR satellite data is based on column-effective, optical measurements rather than from direct sampling. In this work we therefore refer to the RA measurements of particle size and light-

absorption as the retrieved effective particle size (REPS; μm) and the retrieved effective particle absorption (REPA; dimensionless), respectively. These terms help reflect both the measured content and the limitations of the retrieved quantities. Particle property information is reduced when the mid-visible AOD is below about 0.15 or 0.2, but this is not a concern for well-defined smoke plumes. Along-plume changes in AOD, REPS, and REPA combined with available meteorological data, MINX stereo heights, and age estimates can help constrain the relevant aging mechanisms for a plume observed under good retrieval conditions. For example, decreasing AOD accompanied by decreasing REPS downwind may indicate size-selective gravitational settling, whereas uniform particle deposition would feature decreasing AOD accompanied by relatively constant REPS. Similarly, constant AOD accompanied by increasing REPS downwind might indicate particle aggregation, whereas constant or increasing AOD accompanied by decreasing REPS may suggest the formation of secondary aerosols. These and other patterns have been observed with MISR in volcanic and smoke plumes (e.g., Flower and Kahn [2020a, 2020b]; Junghenn Noyes et al [2020a, 2020b]).

The operation of the RA is described by Limbacher and Kahn [2014, 2019]. Recently, several advancements were made to the RA that increase particle property sensitivity, especially for over-land retrievals, and are leveraged in this work. Most importantly, the RA uses prescribed land-surface reflectances from the Moderate Resolution Imaging Spectroradiometer (MODIS) Multi-Angle Implementation of Atmospheric Correction (MAIAC) [Lyapustin and Wang, 2018]. In some RA versions, the surface reflectances are retrieved by the RA itself, which can be less

effective at separating the surface from atmospheric contributions, especially in the presence of optically thick, elevated plumes [Kahn et al., 2010]. Secondly, the TOA reflectances are also now co-registered at the plume height, allowing results to be keyed to various heights rather than assuming confinement to the near-surface boundary layer. Thirdly, in evaluating the retrieval cost function, the algorithm weights each channel (band and camera) based on the AOD retrieved when each aerosol mixture is considered. The weights are normalized such that the mean value is one. This allows for effective use of the MISR near-infrared (NIR) band, which improves retrieval sensitivity to large particles. Specifically, when the surface reflectance is high in the NIR, which is often the case over vegetated land, the aerosol retrieval in that channel is likely to be poor. However, the AOD required to match the observed reflectances will also be low due to the bright surface; thus, these channels are weighted less in such circumstances. Lastly, the number of iterations used to identify the best-fitting AOD was increased. For this work, we also introduced a revised particle climatology in the RA (Table 2.1) that is more focused on biomass burning plumes than in previous versions, such as the one used by Flower and Kahn [2017a, 2017b, 2018, 2020a, 2020b]. It offers a greater range of candidate spherical particle size and light-absorption combinations, and it is based on size and light-absorption ranges identified in a recent literature review of BB particle properties [Samset et al., 2018] and informed by particle properties retrieved *in situ* during recent aircraft field campaigns. Details of the 17-component optical and physical properties included are given in Table 2.1. In general, light-absorbing particles are classified as either strongly light-absorbing (mid-visible SSA~0.80), moderately

light-absorbing ($\text{SSA} \sim 0.90$), or weakly light-absorbing ($\text{SSA} \sim 0.95$). Particle size is classified as either “very small” (effective radius $r_e \sim 0.06 \mu\text{m}$), “small” ($r_e \sim 0.12 \mu\text{m}$), “medium” ($r_e \sim 0.26 \mu\text{m}$), or “large” ($r_e \geq 1.21 \mu\text{m}$), where particles are assumed to be log-normally distributed around the central point r_e .

2.3. Validating the MISR Retrievals

2.3.1. Experiment Design

Any comparison between satellite data and *in situ* observations is inherently challenging. The main obstacles are as follows: (1) satellite measurements probe large atmospheric volumes at comparatively low spatial resolution ($\sim 1 \text{ km}$), whereas *in situ* observations are collected at higher spatial resolution ($\sim 10\text{--}100 \text{ m}$), but cover only a fraction of the area seen from space, often lacking context and making large-scale averaging and interpretation difficult; (2) satellite remote-sensing observations of the atmosphere are affected by the presence of clouds, sun elevation effects, surface reflectance contributions, instrument degradation, and errors/assumptions made in the retrieval algorithms; (3) *in situ* instruments are subject to their own measurement uncertainties, such as sample inlet cut-off issues, typically requiring pre- or post-flight calibration; these measurements usually rely heavily on human operation, which reduces standardization; (4) passive remote sensing provides indirect measurements of column-integrated quantities that are not vertically resolved in most cases, whereas *in situ* suborbital data provide direct measurements, typically at specific points in three-dimensional (3D) space, making direct comparisons with satellite observations impossible for some variables.

For our studies, we face the additional challenge of time differences on the order of hours to a day between the satellite and *in situ* observations. The sampling differences and limitations of each dataset determine how the comparisons have to proceed. For example, the aircraft instruments may be capable of finding extreme values, even if they sample only a small portion of the plume, whereas MISR averages the signal over \sim 1.1 km or more horizontally, and vertically over the column. Likewise, MISR is capable of seeing more area and may find different signals in parts of the plume that were missed by the aircraft. We address these issues by (1) focusing the comparison between the satellite and aircraft data on the general trends in aerosol properties along the length of the plumes, rather than focusing on the absolute values of those properties at individual locations; and (2) considering the possibility that differences in spatial and temporal sampling between the data might contribute to some observed differences in reported aerosol properties. Because smoke plume particle properties often evolve rapidly only a short time after they are emitted, where possible, we compare locations sampled by the aircraft and satellite of similar estimated plume age.

2.3.1. Aircraft Data

Given the large suite of instruments with which the field campaign aircrafts were equipped, we leverage instrument data focused mostly on the aerosol size distribution and optical properties to which MISR is sensitive, but meteorological and atmospheric gas chemistry measurements are considered as well. Most *in situ* measurements are acquired at sufficiently high temporal resolution (0.2–10 s, depending on instrument) that at aircraft cruising velocity (\sim 100 m/s in the case of the

G-1 aircraft used during BBOP, and ~200 m/s for the DC-8 used during FIREX-AQ) they had to be aggregated for comparison with the 1.1 km MISR retrieval regions. Instrument noise smoothing was also required. We therefore parsed the aircraft data into ~1.1 km bins and obtained the median measurement values, acquisition times, and locations for further analysis. Table 2.2 summarizes the instruments used for each measured quantity that we analyzed in our validation studies from the BBOP and FIREX-AQ campaigns. As many of the instruments and methodologies used are similar between the two campaigns, we provide an overview in this chapter. Sections 2.3.1.1 and 2.3.1.2 discuss instrument measurements of aerosol optical and aerosol microphysical properties, respectively, for both field campaigns. Information relating to smoke age estimates during both studies is in Section 2.3.1.3. A discussion of the data leveraged only in the FIREX-AQ validation case is found in Section 2.3.1.4. Finally, we acknowledge the instrument teams in Section 2.3.1.5.

2.3.1.1. Aerosol Optical Properties

The degree of light-absorption by BB aerosols is a critical indicator of particle type and aging. We derive particle SSA from aerosol absorption, measured by the particle soot photometer (PSAP), and scattering from the nephelometer, both acquired at 1-s intervals [Chand and Schmid, 2015; FIREX-AQ Science Team: PSAP]. The nephelometer measures total as well as hemispheric aerosol scattering at 450, 550, and 700 nm by detecting the aerosol-scattered light and subtracting that scattered by the air. The nephelometer data provided were corrected using methods described by Anderson and Ogren [1998]. The PSAP measures absorption continuously at three visible wavelengths by monitoring changes in transmittance through a filter, using a

three-wavelength light-emitting diode (LED) (~ 470 ~ 532 , and ~ 660 nm). As the filter transmittance can also change from the deposition of scattering aerosols, correction methods using scattering measurements from the nephelometer were applied by the field scientists. During the BBOP campaign, correction methods were based on those described in Bond et al. [1999] and Ogren [2010], whereas during the FIREX-AQ campaign these methods were based on those in Virkkula [2010]. The uncertainty of the PSAP measurements is generally ill-defined [Springston, 2018], however in FIREX-AQ the uncertainty of both the PSAP and nephelometer measurements were estimated at $\sim 5\%$. At some points, in cleaner atmospheres where the nephelometer signal approached its detection limit, small negative scattering and absorption coefficients were reported. Therefore, SSA was only calculated in cases where scattering coefficients were $>-3 \text{ Mm}^{-1}$ and absorption coefficients were $>-5 \text{ Mm}^{-1}$.

To help identify BrC, which is more absorbing in the UV than the mid-visible range and can lead to enhanced light-absorption when acting as a BC coating, we analyzed aerosol absorption measurements at opposite ends of the visible spectrum. These were made by the photoacoustic soot spectrometer (PAS) in both campaigns [Arnott, 2013; FIREX-AQ Science Team: PAS], as well as a photothermal interferometer (PTI) in the BBOP campaign [Sedlacek, 2007]. During FIREX, the PAS was operated at 405 and 664 nm, whereas during BBOP it was operated at 355 nm. The PTI was operated at 532 nm. Both the PAS and PTI measure aerosol light-absorption directly by detecting acoustic waves generated by the absorption and subsequent heating of particles exposed to modulated laser light. The hallmark of this technique is that it is insensitive to aerosol light scattering; this is incredibly valuable,

as scattering is usually the chief aerosol light-extinction mechanism. Relative to traditional filter-based instruments used to measure light-absorption (e.g., the PSAP), these instruments exhibit a lower signal/noise ratio, but this problem is minimal for high smoke concentrations. The aerosol light scattering and absorption measurements in the PAS instruments have an estimated uncertainty of $\pm 15\%$ during the BBOP campaign, and $\pm 20\%$ in the case of FIREX. In previous studies, the uncertainty of the PTI technique was measured to be 10% (95% confidence interval) when using NO₂ as a calibration standard [Sedlacek, 2007].

Table 2.2. Suite of field campaign instruments used for the two validation studies of the MISR RA. Note: Other aircraft instruments measuring the same quantity may have also been aboard the aircraft, but were not used here

Measured Quantity	Aircraft Instrument Used	
	BBOP (Chapter 3)	FIREX (Chapter 4)
Mid-visible SSA	Particle Soot Photometer (PSAP) (532 nm); Nephelometer (550 nm)	Particle Soot Photometer (PSAP) (532 nm); Nephelometer (550 nm)
Spectral dependence of light-absorption (UV vs. Red)	Photoacoustic Soot Spectrometer (PAS) (355 nm); photothermal interferometer (PTI) (532 nm)	Photoacoustic Soot Spectrometer (PAS) (405/664 nm)
Particle size distribution & total aerosol concentration	Cloud and Aerosol Spectrometer (CAS); Passive Cavity Aerosol Spectrometer (PCASP)	Laser Aerosol Spectrometer (LAS)
BC mass concentration	Single Particle Soot Photometer (SP2)	Single Particle Soot Photometer (SP2)
CCN number concentration	Dual Column Cloud Condensation Nuclei Counter (CCN-200)	Single Column Cloud Condensation Nuclei Counter (CCN-100)
Aerosol Oxidation ($-\log_{10}[\text{NO}_x/\text{NO}_y]$)	Three-channel oxides of nitrogen analyzer	Three-channel oxides of nitrogen analyzer
CO mixing ratio	Integrated Cavity Output Spectroscopy Analyzer (ICOS)	Differential Absorption CO Measurement (DACOM)
CO ₂ mixing ratio	N/A	LI-COR 7000
Aerosol depolarization, lidar mixing ratio, color ratio, & aerosol backscatter	N/A	Differential Absorption Lidar-High Spectral Resolution Lidar system (DIAL-HSRL)

2.3.1.2. Aerosol Microphysical Properties

Biomass burning is a major global source of accumulation-mode aerosols (particle diameter $D_p < 1 \mu\text{m}$) in the atmosphere, and the vast majority of BB particulate emissions are within this size range [Reid and Hobbs, 1998; Reid et al., 2005]. However, wildfires can also inject soil or dust particles into the air near the source with $D_p > 1.0$, and even small changes in the size distribution for accumulation-mode particles can provide clues about particle type, age, and formation as well as atmospheric chemistry and burning conditions. For the FIREX validation, we utilize 1-s measurements of aerosol size and number concentration from the TSI-3340 laser aerosol spectrometer (LAS) [FIREX-AQ Science Team: LAS], which measures the light scattered by particles that pass through a He-Ne laser beam, to determine particle size. The instrument sizing was field-calibrated using size-classified ammonium sulfate aerosols (refractive index of $1.52 + 0i$). The LAS uses wide-angle optics to capture particle sizes across a large diameter spectrum (with an estimated uncertainty of $\sim 20\%$ in this case). During the BBOP campaign, the Cloud and Aerosol Spectrometer (CAS) and Passive Cavity Aerosol Spectrometer (PCASP) were used to derive aerosol concentration within discrete size bins at 1-s intervals by measuring the intensity of light scattered by aerosols. For the purpose of these studies, we only leverage data for particles within the approximate size range to which MISR is sensitive (~ 0.05 to $3.5 \mu\text{m}$ in diameter). In order to more directly compare aircraft size distributions with those observed by MISR, we summed the concentrations of multiple instrument size bins into larger size categories such that the mid-point effective radius (r_e) of the category approximates that defined by the

RA climatology (Table 2.1): “very small,” “small,” “medium,” and “large.” The range of accepted sizes and instruments used for each of the four size categories is shown in Table 2.3. Ranges do not match perfectly, as the RA is able to consider particle sizes at both extremes, whereas the aircraft instruments were limited to aerosols between 0.09 and 3.5 μm in diameter. Note that the comparisons made here are based on the qualitative size bins retrieved from MISR; thus, our analysis is not affected by small differences in the size bin definitions.

In our FIREX validation, we also illustrate size via the aircraft-transect-mean particle size distributions and estimate changes in the width of the distribution with approximations of $D_{(10\%)}$, $D_{(50\%)}$, and $D_{(90\%)}$, representing the sizes below which 10%, 50%, and 90%, respectively, of the total aerosol populations exist (within the range of observed sizes). $D_{(50\%)}$ is typically considered to represent the median aerosol size.

The hygroscopicity of BB aerosols might serve as a qualitative indicator of mixing state and age, particularly as it pertains to the evolution of BC. Although pure, freshly emitted BC is hydrophobic, these particles can become increasingly hydrophilic and may serve as CCN with increased age due to a combination of coagulation with more water-soluble species and condensation of volatile gases onto the particle surface [Reid et al., 2005; Dalirian et al., 2018]. To determine which aerosols could serve as CCN, we considered measurements at 1-s intervals from a DMT cloud condensation nuclei counter 200 (CCN-200) and 100 (CCN-200) for the BBOP and FIREX validation studies, respectively [FIREX-AQ Science Team: CCN]. The CCN-100/200 applies a thermal gradient across a continuous-flow diffusion chamber to create a supersaturated environment where water vapor can condense onto

particles. Particles that grow to at least $0.75\text{ }\mu\text{m}$ are considered activated and are then sized by the optical particle counter. The CCN-200 used in BBOP has two columns, one of which was kept at a supersaturation of 0.15% and the other at 0.25%. Both were maintained at approximately 600 mbar pressure throughout all the flights. The measurement uncertainty for the instrument is less than 30% [Uin, 2016; Mei, 2013]. When discussing CCN here, we refer to CCN that activate at 0.15% supersaturation as CCN_{15} and those that activate at 0.25% supersaturation as CCN_{25} , although we focus on CCN_{15} to avoid redundancy. For FIREX, the CCN-100 single chamber was maintained at 0.34% supersaturation (with 0.04% supersaturation uncertainty), meaning particles that are counted as CCN here are those that activate at 0.34% supersaturation or higher. The supersaturation was calibrated using ammonium sulfate aerosols following Rose et al. [2008] and Moore et al. [2010]. The concentrations given by the CCN-100 have a reported 10% uncertainty.

To account for plume dilution, in some parts of our analysis, we applied 1-s carbon monoxide (CO) measurements to the data. During BBOP, these were measured by a Los Gatos Integrated Cavity Output Spectroscopy (ICOS) Analyzer with $\pm 5\%$ uncertainty. During FIREX, these were measured by the differential absorption CO measurement (DACOM) instrument [Sachse et al., 1987, 1991], that operated with $\sim 2\%$ uncertainty at the time of observation [FIREX-AQ Science Team: DACOM]. Along with several other trace gases, CO is a frequently used tracer for plume dilution via the derived normalized excess mixing ratio (NEMR), defined as the ratio of the excess species of interest (ΔX) to the background-corrected CO (ΔCO). The NEMR has been used in previous studies to help identify secondary

formation of organic aerosol (OA) and inorganic aerosols in smoke plumes with measurements of particulate matter and OA mass [Yokelson et al., 2009].

The oxidation of aerosols occurs naturally as they interact with background air, altering the properties of organic aerosol components and usually increasing SSA and hygroscopicity. The degree of atmospheric processing of smoke was estimated using an independent proxy measurement for oxidation, defined here as $-\log_{10}(\text{NO}_x/\text{NO}_y)$, where NO_x is the steady-state mixture of NO and NO_2 , and NO_y is the sum of NO_x and the products formed when NO_x is oxidized (i.e., HNO_3 , peroxyacetyl nitrate (PAN), and organic nitrates). For this, we used nitrogen oxide measurements collected with an ozone-induced chemiluminescence technique from a three-channel Oxides of Nitrogen Analyzer reported at $+/- 10\%$ uncertainty during BBOP and $+/- 5\%$ uncertainty during FIREX [FIREX-AQ Science Team: Nitrogen oxides]. As NO_y is nearly conserved on timescales of less than one day, changes in the NO_x/NO_y ratio likely represent oxidative processes. Although not a quantitative measure of oxidation, this method has been shown to correlate well with O/C ratios, that are commonly used to measure photochemical oxidation and SOA formation [Kleinman et al., 2008; DeCarlo et al., 2008].

As BC is the most important climate influencer in smoke plumes, direct measurements of BC mass are very valuable. Refractory black carbon (rBC) mass measurements from the single-particle soot photometer (SP2) were analyzed to help characterize particle type and mixing state [FIREX-AQ Science Team: SP2]. The SP2 derives mass concentrations of rBC by measuring the amplitude of incandescence signals produced as rBC-containing particles traverse a continuous-wave laser beam,

[Sedlacek, 2012; Sedlacek et al., 2017] offering a ~25% and ~20% level of uncertainty in the BBOP and FIREX cases, respectively. During the BBOP campaign, the instrument also measured the size distribution ($dN/d\log D_p$) of the rBC-containing particles ranging from aerosols as small as $0.08 \mu\text{m}$ to as large as $0.65 \mu\text{m}$ in diameter. We approximate the size of rBC-containing particles at a given point using the size bin at which the $dN/d\log D_p$ curve peaks, put here in terms of effective radius and denoted as $r_{e(\text{BC})}$. It is important to remember that the particles are distributed around this value and, thus, actual sizes include particles that fall within an approximate range of $\pm 0.005 \mu\text{m}$. It should also be noted that, unlike most other data, we did not smooth the BBOP SP2 data into $\sim 1.1\text{-km}$ pixels, as its 10-s temporal resolution ($\sim 1.0\text{--}1.3\text{-km}$ spatial resolution) is already comparable to the spatial resolution of the MISR data. The size distribution of rBC particles was not readily available during the FIREX validation, but it should be noted the detection size range for rBC particles was $0.09\text{--}0.55 \mu\text{m}$ in diameter. For the remainder of this discussion, we refer to the rBC measured *in situ* using the more qualitative umbrella term “BC,” which describes the black carbon material in a way that is independent of the instrument technique.

2.3.1.3. Smoke Age

The progression of smoke aging is nonuniform within a plume due in part to variability in wind direction and speed, both of which also affect changes in plume geometry between non-coincident observations. Therefore, as with the satellite data, we estimate smoke age at various points throughout the plume based on wind speed and distance from the source. For the aircraft observations, this is based on wind

speeds measured by the on-board meteorological measurement system (MMS). In both campaigns, ages were calculated by one of the science team managers [Kleinman and Sedlacek, 2016; FIREX-AQ Science Team: Fire Flags]. During FIREX, this involved using a vertical profile of wind speed averaged from measurements on the DC-8 acquired within 2 degrees of the fire latitude/longitude. A single horizontal-transport time was estimated from the mid-point altitude, latitude, and longitude for each perpendicular transect of each smoke plume, assuming straight-line horizontal advection from the fire to this aircraft position.

Table 2.3. Size categories used to analyze the *in situ* observations in both BBOP and FIREX validation studies. PCASP—Passive Cavity Aerosol Spectrometer; CAS—Cloud and Aerosol Spectrometer; LAS—Laser Aerosol Spectrometer

Size Category	Size Range (R_e , μm)	Comparable RA Components	Instruments Used (BBOP; FIREX) ^a
Very Small	0.045–0.09	VSmSphSab(f), VSmSphSab(s), VSmSphMab(f), VSmSphMab(s), VSmSphNab	PCASP; LAS
Small	0.09–0.15	SmSphSab(f), SmSphSab(s), SmSphMab(f), SmSphMab(s), SmSphNab	PCASP; LAS
Medium	0.15–0.46	MeSphSab(f), MeSphSab(s), MeSphMab(f), MeSphMab(s), MeSphNab	PCASP; LAS
Large	0.46–1.725	LaSphNab, LaNsphWab	PCASP, CAS; LAS

^a PCASP data from the July flight in the BBOP study were used with caution as they were collected with the calibration curve for water (1.33) instead of aerosol (1.58), and then converted in post-processing.

2.3.1.4. FIREX-Only Datasets

As has been mentioned, smoke particle properties are largely dependent on fuel characteristics and burning regime, with smoldering conditions being more prevalent in fuels consisting of large woody debris such as branches and dead fallen trees, whereas flaming conditions are associated more strongly with fine fuels such as

grasses, shrubs, and small deadwood [Ottmar, 2001; Urbanski, 2013]. We use fuel type reports from the incident information system [Inciweb], land cover type from the MODIS satellite instrument (MCDQ1, Collection 6), and modeling from the fuel characteristic classification system (FCCS) [FIREX-AQ Science Team: Fuel2Fire] to link the observed particle properties from MISR with fire burning characteristics. We also attempt a more quantitative approach to determining burning conditions via the modified combustion efficiency (MCE; Equation 1), where ΔCO_2 and ΔCO represent the difference between the species' concentrations inside the plume vs. background levels outside the plume). As flaming combustion is more efficient than smoldering combustion and produces more CO_2 relative to CO [Ottmar, 2001], MCE values for flaming combustion are expected to be large, typically above 0.9, whereas MCE values for smoldering combustion are lower and vary over a range of ~0.65–0.85 [Akagi et al., 2012]. The changes in MCE between transects help shed light on the degree to which the observed changes in particle properties are a function of burning conditions at the source, as distinct from subsequent atmospheric processing; this was not possible with the data available for the BBOP study. We use transect-averaged MCE values calculated and provided by a FIREX Manager [FIREX-AQ Science Team: Fire Flags], where CO and CO_2 mixing ratios were those measured by the DACOM and LI-COR 7000 [FIREX-AQ Science Team: LI-COR] instruments, respectively. The LI-COR instrument measures CO_2 via non-dispersive infrared spectroscopy with a reported accuracy and precision of 0.25 and 0.1 ppm, respectively [Vay et al., 2003].

$$MCE = \frac{\Delta CO_2}{\Delta CO_2 + \Delta CO}. \quad (1)$$

Aircraft lidar measurements were obtained from the dual NASA Langley differential absorption lidar (DIAL) and high spectral resolution (HSRL) system (or DIAL-HSRL) [FIREX-AQ Science Team: DIAL-HSRL]. The DIAL-HSRL instrument uses five lasers to acquire ozone vertical profiles simultaneously with aerosol backscatter profiles in the visible (532 nm) and near-infrared (1064 nm). The DIAL-HSRL also measures aerosol extinction at 532 nm and depolarization at 532 nm and 1064 nm. The HSRL technique separates the aerosol and molecular signals, so aerosol extinction and backscatter are measured independently [Hair et al., 2008]. Retrieved intensive aerosol properties have been used to classify aerosol mixtures. Specifically, aerosol depolarization at each wavelength provides an indication of particle non-sphericity, the extinction/backscatter ratio (i.e., the lidar ratio) at 532 nm offers a loose constraint on particle composition, and the 1064 nm/532 nm color ratio is related to particle size [Burton et al., 2012, 2013 2014, 2015]. During the FIREX flight on 06 August 2019, the DC-8 performed three “remote sensing” longitudinal passes above the plume along its length, during which the DIAL-HSRL made soundings. In addition, lidar data were acquired for the eight across-plume transects within the plume, as the DC-8 *in situ* instruments also sampled the smoke plume. The first longitudinal overpass (referred to here as L1) occurred at approximately 19:00 UTC and is most nearly coincident with the 19:07 UTC MISR overpass; L2 took place ~20:30 UTC and L3 at ~21:50 UTC. The across-plume transects were flown between L2 and L3. For the locations of all the transects within the plume, see Figure B3 in Appendix B.

2.3.1.5. Instrument Team Acknowledgments

We would like to recognize the BBOP instrument PI's Fan Mei (CCN counter, Pacific Northwest National Laboratory), Duli Chand (PSAP and nephelometer, Pacific Northwest National Laboratory), William Arnott (PAS, University of Nevada Reno), Jason Tomlinson, (CAS and PCASP, Pacific Northwest National Laboratory), Arthur Sedlacek (SP2, Brookhaven National Laboratory), and Stephen Springston (trace gas instrument suite, Brookhaven National Laboratory).

We also thank the FIREX-AQ instrument PIs and their teams, listed as follows:

- DACOM: Glenn Diskin, Joshua DiGangi, John Nowak, Hannah Halliday, James Geiger, Johnny Mau, James Plant, Mario Rana, and Yoonghoon Choi (NASA LaRC)
- SP2: Joshua Schwarz, Laurel Watts, (NOAA ESRL), Joseph Katich (NASA LaRC), Anne Perring, and Brady Mediavilla, (Colgate University)
- PAS: Nick Wagner, Adam Ahern, Charles Brock (NOAA ESRL), and Ming Lyu (University of Alberta)
- Nitrogen Oxides: Je_ Peischl, Tom Ryerson, (NOAA ESRL) and Ilann Bourgeois (CIRES).
- AERONET: Brent Holben and the AERONET team participating from NASA GSFC and the University of Lille/LOA (PHOTONS)
- LAS,CCN-100, PSAP/neph: Richard Moore, Elizabeth Wiggins, Edward Winstead, Claire Robinson, Lee Thornhill, and Kevin Sanchez (LaRC)

2.4. Summary

In this chapter we describe the instruments, datasets, and methods used to validate the optical properties retrieved by MISR against the chemical and physical particle properties observed *in situ*. We include a wide range of data that allows us to evaluate MISR's ability to constrain particle light-absorption and its spectral slope (PSAP/neph, PAS, PTI), particle size (PCASP, CAS, LAS), and how changes in these properties downwind may reflect changes in particle hygroscopicity (CCN-100/200), particle composition (SP2, Nitrogen of Oxides Analyzer, DIAL-HSRL), plume dilution (ICOS, DACOM), or differences in emissions (MCE). In addition, we collect information on smoke age to determine the timelines over which potential changes in particle properties occur. In the following two chapters, we analyze the *in situ* measurements and compare them to the near-coincident MISR retrievals.

Chapter 3: Validating Space-Based Observations of Wildfire Smoke Particle Properties: The Biomass Burning Observation Project

3.1. Introduction

The goal of this study is to explore the degree to which MISR-based methods can qualitatively describe plume particle characteristics, setting the stage for future work at developing a global climatology of BB aerosol plume properties and processes. A partial validation of the RA is conducted here with the aim of placing on firmer ground MISR retrievals of smoke plumes that are less well constrained by field observations. This is done primarily with data obtained during the BBOP campaign, on the 21 August 2013 flight through the Government Flats Complex Fire in northern Oregon, for which there was a near-coincident MISR overpass (~2 h difference). Additional case studies presented here, having larger time differences between aircraft and satellite observations, bolster the comparison efforts and illustrate how the RA can help create a timeline of plume particle evolution, especially when combined with other coincident and noncoincident observations.

The BBOP campaign was conducted to enhance understanding of the atmospheric and environmental impacts of fire-generated particles, with particular focus on atmospheric chemistry [Kleinman and Sedlacek, 2013, 2016]. From July to September 2013, the Department of Energy Gulfstream-1 (G-1) research aircraft flew

through wildfire plumes in the Pacific Northwest, before moving to the lower Mississippi River Valley for the month of October to study agricultural burns. This field campaign was selected for the current study because it uniquely targeted the time evolution of smoke particles during the first few hours of atmospheric aging [Kleinman and Sedlacek 2016].

The second phase of this study uses the same type of data from other BBOP flights that took place approximately one day apart from MISR overpasses, the Colockum Tarps Fire and the Douglas Complex Fire (Table 3.1). Although these cases are less useful for validating the RA, they serve here as examples of the versatile and fluid nature of BB aerosol microphysical and optical properties. They also demonstrate the potential of the RA as a tool that both complements and enhances knowledge gained from *in situ* observations of wildfire smoke plumes.

Data sources and processing methods are described in Chapter 2, with specific instrument information neatly summarized in Table 2.2. Section 3.2 presents our analyses of the similarities and differences between the RA and aircraft observations for the Government Flats Complex Fire (Phase I), while Section 3.3 briefly summarizes results for two additional BBOP campaign fires for which the aircraft and MISR observations were ~24 h apart (Phase II). The aerosol property differences determined from remote sensing illustrate how unique data signatures can point to certain aerosol aging processes and plume evolution mechanisms. Finally, a summary is given in Section 3.4.

Table 3.1. Flight dates, times, and locations compared with dates and times of the Multi-Angle Imaging Spectroradiometer (MISR) overpass of the same area. Positive time delays between satellite and aircraft observations indicate the satellite observed the fire after the aircraft, whereas negative numbers mean the satellite completed its overpass first. The last flight, on 21 August, is the focus of the validation portion of the study. UTC—Universal Coordinated Time.

Fire Identifier	Aircraft Observations			MISR Observations			
	Date ^a	Start Time—End Time ^{a,b}	Location	Date ^a	Orbit; Block(s)	Time ^a	~Delay (h)
Colockum Tarp	7/26/13	20:00–22:20	Southern central WA	7/27/13	72382; 53–54	19:13	+23
Douglas Complex	8/6/13	19:30–21:00	Southern coastal OR	8/5/13	72513; 56	19:08	-23
Government Flats	8/21/13	21:20–22:30	Northern central OR	8/21/13	72746; 54	19:07	-2

^a Dates and times are in UTC

^b Indicates the approximate time range that the aircraft was actively observing the smoke plume(s) rather than the total flight time.

3.2. *Phase I Results and Discussion: Validation with Near-Coincident Flight Data*

The Government Flats Complex was a large system of three lightning-sparked fires: the Government Flats fire, the Blackburn fire, and the Wells Road fire. They burned near Mt. Hood in Wasco County, Oregon from 16 August to 26 August 2013. Cumulatively, these fires burned over 11,350 acres of land, although the Blackburn fire was responsible for 98% of this area. According to the US Forest Service, the fuel model in this area was summer hardwood litter [Oregon Department of Forestry]. The plume produced by this fire complex was observed by MISR on 21 August 2013, at ~19:07 Universal Coordinated Time (UTC), ~2 h before the BBOP G-1 aircraft began sampling the same area; the aircraft continued sampling this plume for an additional hour. At both observation times, the plume displays unique aerosol optical and physical property patterns that vary with downwind distance. We divide the MISR-observed plume into four regions based on these patterns: a near-source Region

(designated Region I), a near-downwind Region (II), a mid-downwind Region (III), and a far-downwind Region (IV) (Figure 3.1a). We calculate the approximate age of the smoke at regional boundaries using the ratio of the along-plume distance and mean wind vectors in the area derived from MINX (see Figure A1 in Appendix A). Based on plume age calculated by Kleinman and Sedlacek [2016], and similar trends in particle properties, the BBOP-observed plume was divided into regions of similar age (Figure 3.1b), although the aircraft did not sample the part of the plume corresponding to Region IV in the MISR imagery. In this section, we compare the particle properties retrieved from space with those obtained *in situ* from the aircraft measurements, paying particular attention to the differences between these regions. We then apply this information to current knowledge on how different aging processes affect particle properties in order to infer the active mechanisms at hand.

Only observations taken within the plume boundaries seen in Figure 3.1 are included in our analysis, except when comparing measurements to background values. For the MISR dataset, the boundary is a user-drawn plume outline created during the MINX retrieval. Some areas of optically very thin smoke can be seen in the imagery outside the boundary, but MISR had difficulty performing retrievals beyond a certain distance downwind (where the plume becomes thin), as can be seen by the lack of MINX plume results, and as indicated by some empty pixels in the RA retrievals shown subsequently. For the BBOP dataset, the RGB MODIS-Aqua image, acquired about 2 h after the MISR overpass, was used to draw the plume outline (Figure 3.1b). However, significant cloud contamination made it challenging to determine exact boundaries in the two most downwind regions; thus, carbon

monoxide and total aerosol count measurements from the aircraft were used to refine the shape (Figure 3.1c,d, respectively). This is also important, as plume geometry can change during the course of the flight itself; thus, the MODIS snapshot might not perfectly represent the plume as sampled by the aircraft, even without cloud contamination. Where applicable, all figures display the plume boundary as a dotted-line polygon and the dividing lines between regions as thin solid gray lines.

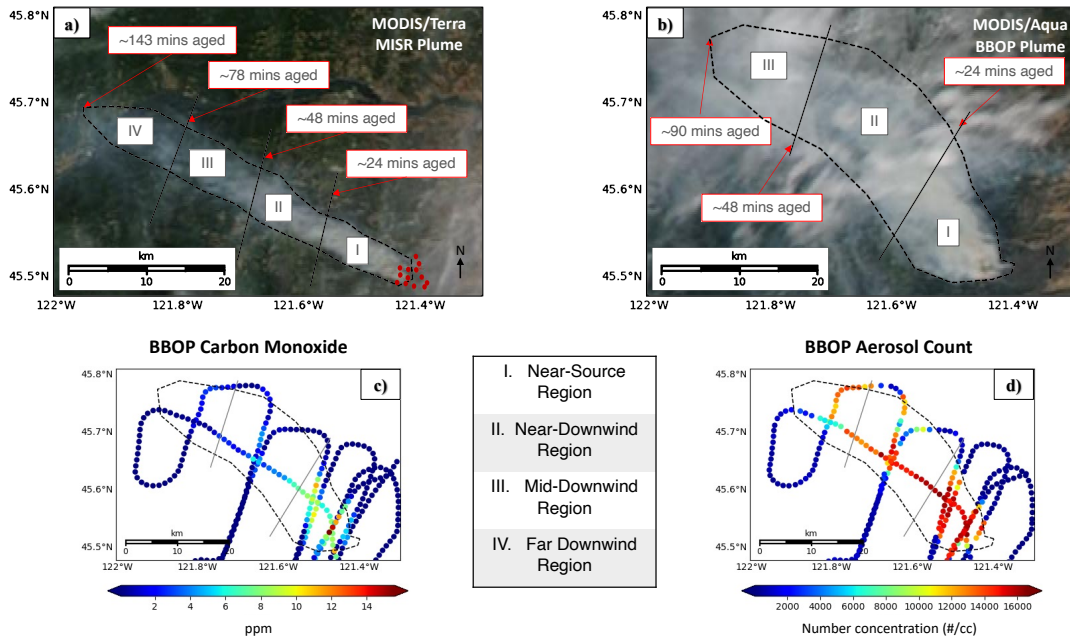


Figure 3.1. The Government Flats Complex Fire as seen on 21 August 2013: **(a)** at MISR overpass time (19:07 UTC; Moderate Resolution Imaging Spectroradiometer (MODIS) Terra red-green-blue (RGB) context image), and **(b)** during the Department of Energy's Biomass Burning Observation Project (BBOP) flight operations (20:49 UTC; MODIS Aqua RGB image; the aircraft flight began at 21:20 UTC). The red dots in Panel (a) indicate MODIS-identified hot spots, which are used to estimate source location. The dashed lines represent the plume outlines we use for analysis. At both observation times, the plume is divided into regions (I–IV) based on estimated plume age, to allow for easy, qualitative comparison of inter- and intra-plume properties. Panels **(c)** and **(d)** represent the aircraft *in situ* CO and total aerosol count measurements, respectively

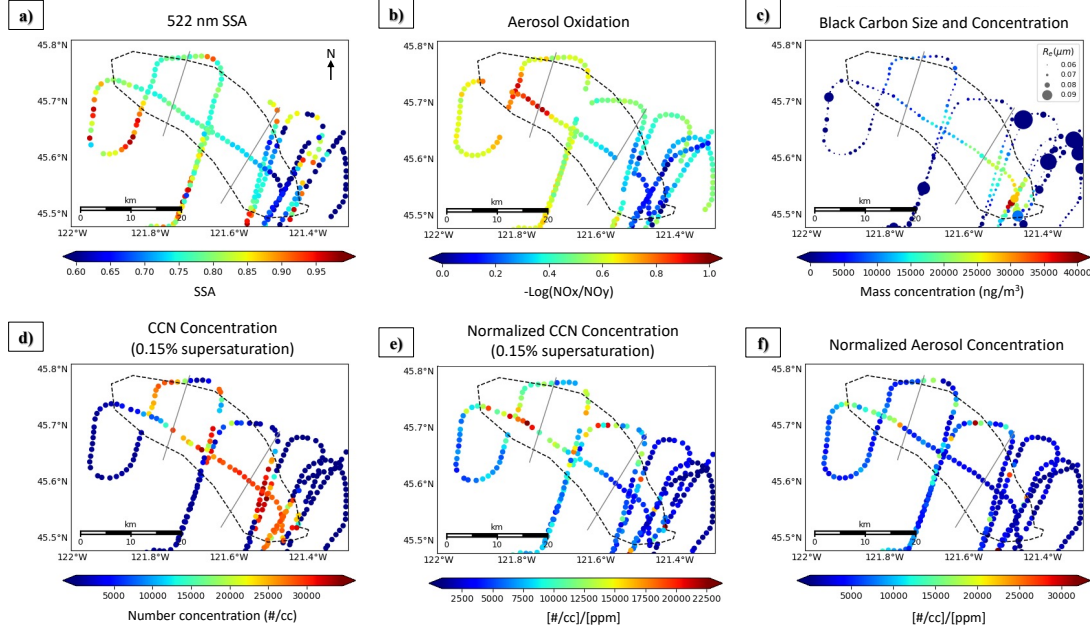


Figure 3.2. BBOP aircraft observations of the Government Flats Complex fire on 21 August 2013: (a) 522-nm SSA (particle soot absorption photometer (PSAP)/neph); (b) aerosol oxidation (derived from the three-channel Oxides of Nitrogen Analyzer); (c) mass concentration of black carbon (BC) and size of BC-containing particles (single-particle soot photometer (SP2)); (d) concentration of particles that can act as cloud-condensation nuclei (CCN) at 0.15% supersaturation (CCN-200 instrument); (e) the CCN concentration divided by the CO concentration; (f) the total aerosol concentration divided by the CO concentration.

3.2.1. *In situ* Observations: A First Look

We provide an overview of the aircraft observations first, with an emphasis on the differences in smoke properties between regions. Figures 3.2 and 3.3 illustrate, as latitude/longitude plots, the chemical, optical, and physical properties, measured using the methods described in Chapter 2. Each point represents the aggregated ~1.1-km median value of a given measurement (except for Figure 2c, which did not need to be aggregated because of a low temporal sampling frequency, as discussed in Chapter 2). Table 3.2 quantifies the mean, standard deviation (SD or σ), and median values of the measurements from Figures 3.2 and 3.3 for each region, and a comprehensive discussion of these statistics can be found in Appendix A.

In general, the plume contains fresh, highly absorbing smoke near the source that becomes both increasingly bright (SSA_{522}) and oxidized ($-\log[\text{NO}_x/\text{NO}_y]$) with downwind distance (Figure 3.2a,b, respectively). Both absolute and mean CO-normalized BC mass concentration decrease along the length of the plume (Figure 3.2c, Table 3.2); however, rates of BC dilution vary between the plume center (no increasing dilution with downwind distance) and the plume edges (increasing dilution with downwind distance). The disparities between the median and mean values in Table 3.2, as well as the differences in sampling seen in Figure 3.2, illustrate this pattern. CO-normalized CCN and aerosol concentration both increase along the length of the plume, particularly in the southern flank of Region III, where smoke is the most oxidized (Figure 3.2e–f). CAS and PCASP data indicate the plume is comprised almost entirely of particles with r_e of $0.46 \mu\text{m}$ or less (i.e., “very small,” “small,” and “medium” particles, similar to the aerosols of the same name identified within the MISR retrieval sensitivity limitations, discussed in Chapter 2). “Large” aerosols ($0.46 \mu\text{m} < r_e < 1.7 \mu\text{m}$) are essentially absent, never representing more than 0.35% of all particles, which is substantially below MISR retrieval sensitivity. Aerosol size decreases along the central plume transect, with the most dramatic decrease seen in the southern flank of Region III (Figure 3.3). PTI (532 nm) and PAS (355 nm) absorption measurements used to distinguish spectrally flat from spectrally steep aerosols show that BC-only light-absorption (which is approximately equal at both wavelengths) declines more dramatically downwind than BrC-only light-absorption (the residual of 355-nm absorption minus 532-nm absorption), and that CO-normalized BrC light-absorption and CO-normalized 355-nm scattering actually

increase dramatically in Region II (Table 3.2). In their final campaign report, Kleinman and Sedlacek [2016] also found that CO-normalized BrC light-absorption and scattering increased after ~30 min of plume aging. Although particle size is known to influence the spectral slope of SSA, the observed jump in 355-nm absorption and scattering does not correlate with significant changes in particle size, and thus it is likely that particle composition is the dominant factor driving the observed changes.

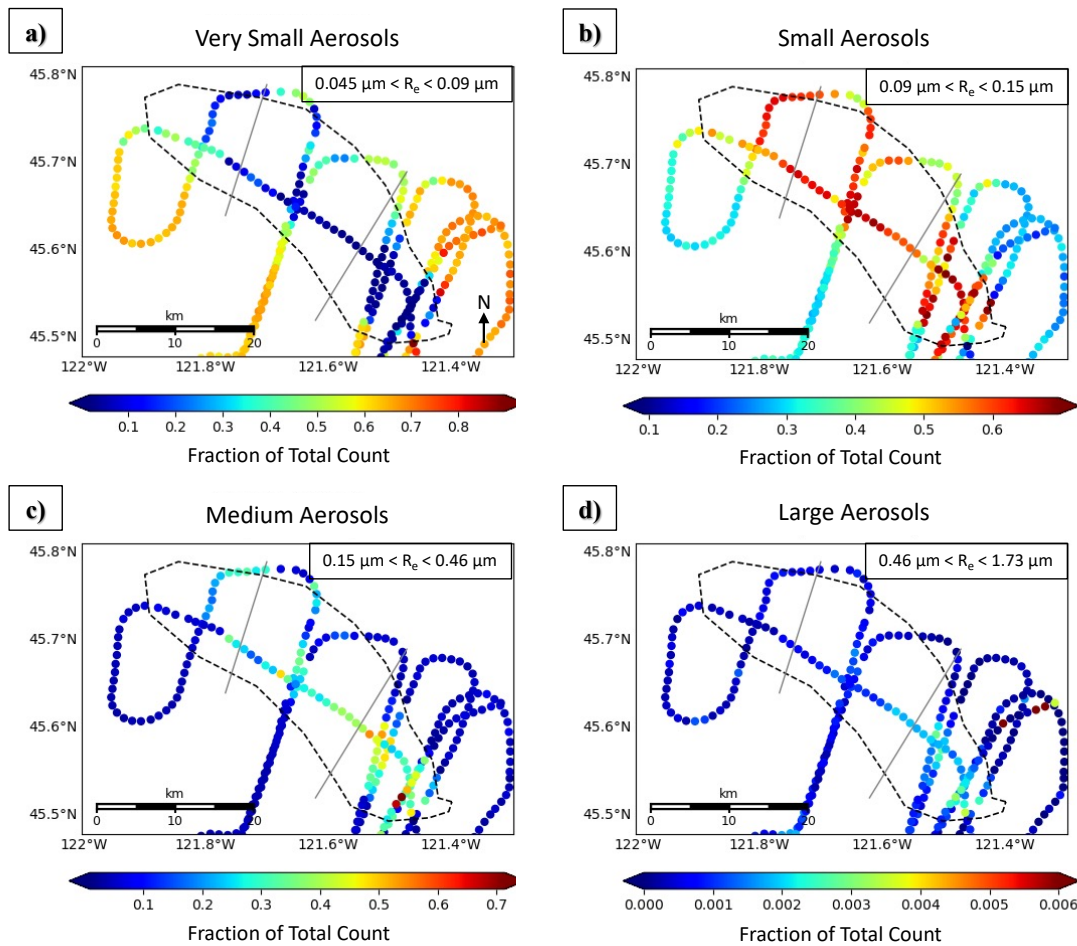


Figure 3.3. Fractional contributions (from zero to one) to the total aerosol count for (a) very small, (b) small, (c) medium, and (d) large aerosols in the Government Flats Complex Fire, as measured by the PCASP and CAS *in situ* instruments on 21 August 2013. The gray lines represent the boundaries between regions defined in Figure 3.1. Note: approximate size ranges are given above each plot, and the scales differ between categories.

Table 3.2. Aircraft data: aerosol size, chemical, and physical properties for the Government Flats Complex Fire measured *in situ*.

Plume Region:		Near-Source (Region I)	Near-Downwind (Region II)	Mid-Downwind (Region III)
Very small aerosols ^a	mean	0.1250	0.1904	0.2935
	$\pm\sigma$	±0.1712	±0.1626	±0.1573
	median	0.03893	0.1121	0.3473
Small aerosols ^a	mean	0.5662	0.5930	0.5609
	$\pm\sigma$	±0.1124	±0.07029	±0.1124
	median	0.5962	0.6096	0.5612
Medium aerosols ^a	mean	0.3072	0.2157	0.1452
	$\pm\sigma$	±0.1534	±0.1144	±0.09571
	median	0.3072	0.2383	0.09315
Large aerosols ^a	mean	0.001549	0.0008949	0.0004482
	$\pm\sigma$	±0.0007137	±0.0004193	±0.0002103
	median	0.001502	0.0008090	0.0004333
$\text{SSA}_{522}^{\text{b}}$	mean	0.7001	0.7679	0.7814
	$\pm\sigma$	±0.07297	±0.030083	±0.03647
	median	0.7029	0.7605	0.7748
Oxidation ^c	mean	0.2018	0.5307	0.7855
	$\pm\sigma$	±0.1447	±0.1400	±0.1115
	median	0.2037	0.5318	0.8026
rBC mass ^d	mean	16,383.15	8638.98	4805.65
	$\pm\sigma$	$\pm8,494.77$	$\pm5,765.73$	$\pm3,553.27$
	median	17,437.12	8,164.26	4,036.97
rBC mass normalized by CO ^e	mean	8,328.4	5,973.7	4,528.1
	$\pm\sigma$	$\pm15,678$	$\pm10,509$	±4298.5
	median	2,812.2	3,388.7	3,416.7
$R_{e(\text{BC})}^{\text{f}}$	mean	0.070	0.065	0.064
	$\pm\sigma$	±0.0064	±0.0049	±0.0060
	median	0.070	0.065	0.065
$\text{CCN}_{15}^{\text{g}}$	mean	24,273.13	19,976.24	15,497.54
	$\pm\sigma$	$\pm9,852.24$	$\pm11,071.74$	$\pm10,310.76$
	median	27,578.10	24,810.73	12,212.83
CCN_{15} normalized by CO ^h	mean	5,710.84	10,657.30	14,829.78
	$\pm\sigma$	$\pm3,566.64$	$\pm4,390.24$	$\pm4,112.40$
	median	4,716.05	9,408.83	13,340.70
Aerosol count normalized by CO ⁱ	mean	3,844.60	7,048.10	9,465.11
	$\pm\sigma$	$\pm4,960.87$	$\pm5,861.56$	$\pm5,191.19$
	median	2,328.85	5,015.14	7,451.74
BrC absorption normalized by CO ^j	mean	172.39	216.97	207.14
	median	163.66	210.10	217.69
355-nm scattering normalized by CO ^k	mean	1,771.90	2,447.76	2,515.30
	median	1,591.90	2,363.77	2,377.25

^a Fraction of total aerosol count, as measured by the PCASP and CAS instruments in accordance with Table 2.3

^b As measured by the PSAP/neph;

^c Defined as $-\text{Log}[\text{NO}_x/\text{NO}_y]$, using measurements provided by the three-channel Oxides of Nitrogen Analyzer, where 0 is fresh smoke and 1 is aged smoke;

^d As measured by the SP2, in ng/m^3 ;

^e The ratio of BC mass concentration (ng/m^3) and CO (ppm);

^f As measured by the SP2, in terms of effective radius R_e in μm ;

^g The concentration (#/cc) of CCN that activated at 0.15% supersaturation, as measured by the CCN-200;

^h The ratio of CCN_{15} measured by the CCN-200 instrument (#/cc) and CO concentration measured by the Los Gatos Integrated Cavity Output Spectroscopy (ICOS) Analyzer (ppm);

ⁱ The ratio of the total aerosol count from the PCASP/CAS instruments (#/cc) and the CO concentration measured by the Los Gatos ICOS Analyzer (ppm);

^j The residual of the ratio of 355-nm absorption (PAS; Mm^{-1}) and CO concentration (Los Gatos ICOS Analyzer; ppm) and the ratio of 522-nm absorption (PTI; Mm^{-1}) and CO concentration (Los Gatos ICOS Analyzer; ppm). Note that values only reflect data from the one along-plume transect. Standard deviations are not given as values were calculated by subtracting mean BC light-absorption from mean BrC light-absorption, rather than by the means of the residuals;

^k The ratio of 355-nm scattering (PAS; Mm^{-1}) and CO concentration (Los Gatos ICOS Analyzer; ppm). Note that values only reflect data from the one along-plume transect. Standard deviations are not given as values were calculated by subtracting mean BC light-absorption from mean BrC light-absorption, rather than by the means of the residuals

The *in situ* data alone do not provide enough information to fully explain these changes in aerosol properties. However, from available observations, we suggest several potential processes that could be affecting the plume particle properties: (1) gravitational settling and/or dilution that leads to the preferential decrease in medium-size particle concentration and BC particle concentration in Regions II and III compared to Region I; (2) oxidation and/or SOA production, leading to increased hygroscopicity and decreased light-absorption contributions in Regions II and III; (3) changes in burning conditions at the source, which alter the emitted smoke properties, reflected in particle-type differences between regions. Gravitational settling cannot be confirmed by the *in situ* data acquired at a single elevation. Particle oxidation state can be measured *in situ*, but can only be inferred from remote sensing, e.g., based on decreasing particle light-absorption, although

particle hydration is also possible, especially if particle size increases, hydrophilic particles (e.g., BrC) are present, and RH is high. If *in situ* measurements of particle size but not composition are available, the formation of secondary particles would have to be confirmed by total column measurements, as it is possible that decreases in particle size, as measured *in situ*, might instead be due to preferential gravitational settling of larger particles. However, the CO-normalized, absolute increase in small-particle concentration strongly supports the idea of particle formation in this case, as it indicates that dilution is minimal. Other particle evolution processes can occur, such as aggregation; however, based on the available *in situ* data, this does not seem likely here, unless it occurred very near source, where aerosol loading was extremely high. Changes in the burning conditions at the source cannot be confirmed or ruled out by remote sensing, and *in situ* measurements only allow us to infer the degree to which the fire may be changing. Several overlapping transects made by the BBOP aircraft at different times suggest measurements at a given distance from the source (i.e., similarly aged smoke at different times) are not dramatically different between these observations, indicating that changes in burning conditions may not be important here.

3.2.2. Satellite Observations: Validation and Providing a Broader Context

As demonstrated above, aircraft measurements provide highly detailed observations of the plume that allow us to identify general particle-type differences and to narrow down the list of potential aging mechanisms. However, the limited area sampled *in situ* across two hours, during which changes could have occurred, leaves us with an incomplete understanding of plume properties, and these data alone cannot

resolve key uncertainties regarding the atmospheric particle processes that operated. Here, we provide an overview of the satellite observations, with the same emphasis on differences between regions as in Section 3.2.1, and we compare them with the aircraft measurements to assess the fidelity of the RA. We also demonstrate how the RA places *in situ* observations into a broader context, providing information critical for understanding the processes responsible for plume evolution.

Table 3.3. MISR-observed particle properties for the Government Flats Complex Fire. AOD— aerosol optical depth; ANG—Ångström exponent; SSA—single scattering albedo; BIS—black smoke; BrS—brown smoke

Plume Region:		Near-Source (Region I)	Near-Downwind (Region II)	Mid-Downwind (Region III)	Far-Downwind (Region IV)
AOD	mean	2.222	1.556	0.9851	1.020
	$\pm\sigma$	± 0.7840	± 0.6195	± 0.2856	± 0.2164
	median	2.281	1.653	0.8913	1.007
ANG	mean	1.541	1.319	1.824	1.042
	$\pm\sigma$	± 0.3800	± 0.3234	± 0.3106	± 0.3272
	median	1.583	1.293	1.822	1.024
SSA	mean	0.8641	0.9251	0.9154	0.9688
	$\pm\sigma$	± 0.02926	± 0.03960	± 0.04117	± 0.03889
	median	0.8639	0.9217	0.9229	0.9802
BIS ^{a,b}	mean	0.5606	0.3649	0.2727	0.09674
	$\pm\sigma$	± 0.1681	± 0.2186	± 0.2546	± 0.1661
	median	0.5852	0.4156	0.2403	0
BrS ^{a,c}	mean	0.1260	0.08067	0.3024	0.02564
	$\pm\sigma$	± 0.1304	± 0.1106	± 0.2102	± 0.08594
	median	0.08545	0.03358	0.3049	0
Non-absorbing ^{a,d}	mean	0.1069	0.4434	0.3498	0.6914
	$\pm\sigma$	± 0.1726	± 0.2915	± 0.2547	± 0.2948
	median	0	0.4440	0.3835	0.7383
Non-spherical ^{a,e}	mean	0.2064	0.1110	0.07516	0.1863
	$\pm\sigma$	± 0.1307	± 0.1253	± 0.09498	± 0.1984
	median	0.2119	0.05470	0.0158	0.08771

^a In terms of fraction of total AOD (0 to 1);

^b The combined total all spectrally flat components, meant to represent black carbon analogs;

^c The combined total of all spectrally steep components, meant to represent brown carbon analogs;

^d The combined total of all non-absorbing components;

^e The only non-spherical component, meant to represent dust or soil.

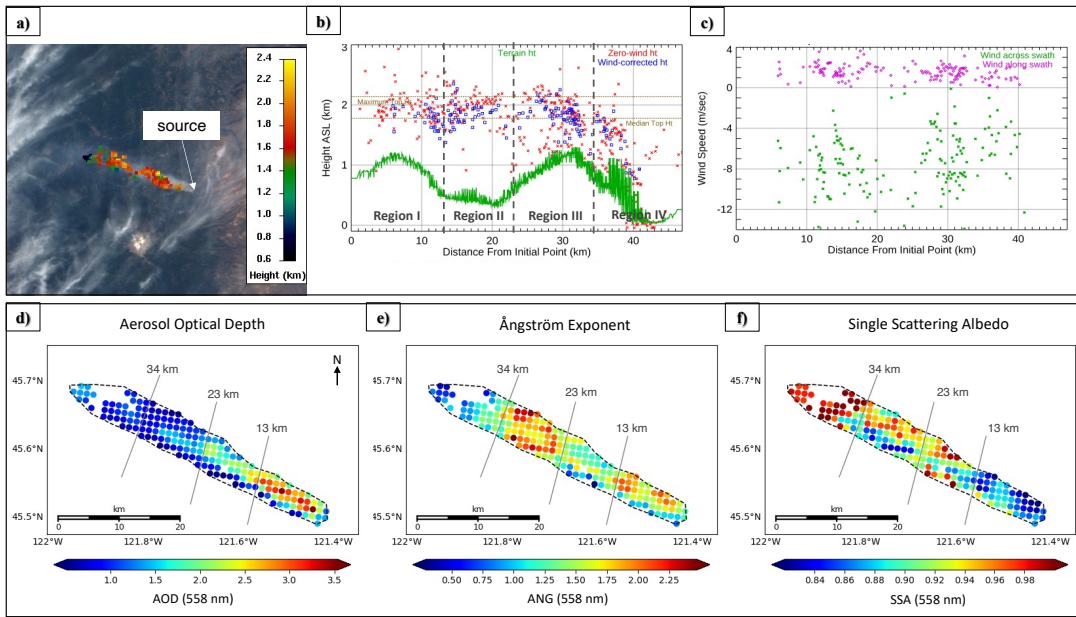


Figure 3.4. Plume properties for the Government Flats Complex Fire retrieved by MISR at 19:07 UTC (Orbit 72746, Path 45, Block 54) on 21 August 2013: (a) MISR Interactive Explorer (MINX) stereo height retrieval map; (b) MINX stereo height profile as a function of distance from the source, for both zero-wind (red) and wind-corrected (blue) analyses, with surface elevation indicated in green, (c) MINX-retrieved across-swath and along-swath wind vectors, and RA-derived (d) AOD at 558 nm, (e) extinction ANG, and (f) SSA at 558 nm. The transects for estimated plume ages corresponding to the regional boundaries in Figure 3.1 are indicated with thin gray lines in panels d–f.

Figure 3.4 contains standard MISR RA latitude/longitude plots of AOD, SSA, and ANG for the plume, with the MISR-MINX stereo heights included for reference. In addition to these, we map, in terms of both retrieved absolute AOD and AOD fractional component, the spectral dependence of aerosol light-absorption via the separate sums of (1) retrieved spectrally flat (BLS) and (2) spectrally steep (BrS) light-absorbing components (Figure 3.5a–d), (3) the retrieved aerosol shape, via the non-spherical component LaNsphWab (Figure 3.5e–f), and (4) further information on light-absorption via the sum of all non-absorbing components (Figure 3.5g–h). These particle properties are, for the most part, neatly distinctive between the four plume regions, as discussed subsequently. It is important to reiterate that, when considering

specific particle types (e.g., black carbon, brown carbon, dust, non-absorbing aerosols), the retrieved aerosol properties represent the optical equivalent of the aerosol present, i.e., the true aerosol is not necessarily a mixture of the specific components retrieved from among those in the RA climatology (e.g., Kahn and Limbacher [2012]). Table 3.3 quantifies the above-mentioned RA observations, giving the mean, standard deviation (SD or σ), and median for each region; a more in-depth analysis of these statistics can be found in Appendix A.

The MISR-MINX stereo heights indicate the plume is concentrated mostly within 2 km above sea level (ASL), with a median height of 1.78 km and a maximum height of 2.13 km (Figure 4a–b). The RA-retrieved particle properties indicate peak AOD of up to 3.5 near the source, decreasing with downwind distance to a minimum of ~ 0.5 in some pixels within the area we defined as the observable plume in the satellite imagery (Figure 3.4d). The plume REPA also decreases significantly with downwind distance, and SSA increases from < 0.84 near the source to nearly 1.0 in Region IV. Although most particles can be considered fine mode, having ANG > 1 , REPS increases slightly in Region II, dramatically decreases in Region III, and then dramatically increases again in Region IV (some pixels having ANG < 1), indicating significant changes in particle size throughout the length of the plume. Component analysis suggests that smoke near the source is largely a BIS-like mixture, but that subsequent regions transition to mixtures interpreted as mostly non-absorbing and BIS particles in Region II, then non-absorbing, BIS, and BrS particles in region III, and non-absorbing and dust- or soil-like optical analogues in Region IV (Figure 3.5). Bear in mind that these retrieved component AOD values and fractions represent an

interpretation of the MISR column-integrated reflectances in terms of the components included in the RA (Table 2.1), whereas the REPS and REPA are less dependent on algorithm assumptions. This is one reason why validation with the *in situ* data is so important.

The satellite and *in situ* measurements are substantially similar in their characterization of particle property evolution as a function of smoke age. In both cases, particle light-absorption systematically decreases downwind, accompanied by a transition from BlS to BrS particle-type analogues as the dominant light-absorbing aerosol. Significantly smaller particles appear in Region III and partway into Region IV, between 48 and 90 min of aging. However, the MISR-retrieved particle sizes for smoke between 24 and 48 min in age (Region II) are larger than those near the source (although still fine-mode), whereas the aircraft observes the opposite trend. Moreover, unlike the aircraft measurements, MISR indicates that particles in Region III are “small” in size, whereas the aircraft measures “very small” particles (Tables 3.2, 3.3). Lastly, MISR coverage continues past 90 min in age, observing Region IV, where the retrieval results indicate particles eventually appear somewhat coarser in size and significantly non-spherical. Despite these differences, both observation sets indicate that, overall, from the source until ~78 min of aging, most of the plume comprises a majority of small, very small, and medium particles, with monotonically decreasing light-absorption downwind.

Due to the comprehensive coverage, the MISR observations provide greater context for assessing the aerosol aging mechanisms that are suggested by the *in situ* data analysis. In Region II, the increased REPS is in contrast with the decrease in

particle size observed *in situ*. This may be explained by the difference in vertical sampling, as the aircraft measures at a single altitude, whereas the satellite observes the entire column. Column aerosol loading is dominated by the smoke plume in this case, but the plume is at least 0.75 km thick (Figure 3.4b); thus, measurements at a single elevation might not be representative. This would bolster the idea that gravitational settling is playing a role in this region. It is also possible that particle hydration, condensation of gaseous components onto existing particles, and/or particle aggregation are acting to increase particle size. The observed increase in relative humidity in this region (see Figure A2 in Appendix A) points toward hydration in particular, and the smaller sizes observed by the aircraft can be explained by differences in horizontal and possibly also vertical sampling. Aerosol oxidation is also acting in this region, as indicated by the increased oxidation values seen in Figure 3.2b and supported by the increased hygroscopicity seen in Figure 3.2e, as well as the decreased REPA in the MISR retrievals (Figure 3.4f).

In Region III, there is strong *in situ* evidence for high levels of aerosol oxidation, leading to the formation of BrS either from SOA production (via the nucleation of new particles) or from the deposition of organic material onto BIS particles, increasing hygroscopicity and decreasing light-absorption. The aircraft does not observe strong changes in particle light-absorption, as would be expected with these processes, although this could be due to limited sampling (Figure 3.2a). MISR does appear to see the expected increase in SSA (Figure 3.4f), at least along the northern part of the plume in this region. The main particle-type feature of Region III is the dramatic decrease in REPS, accompanied by a decrease in total-column AOD.

It is unclear from the limited *in situ* sampling (Figure 3.3c) whether medium particles are actually lost from the column here. However, Region III begins about 30 km downwind of the source, and the MISR stereo height profile indicates that the plume descends toward the surface at about this distance (Figure 3.4b), suggesting selective, large-particle deposition is possible. This is supported by a decrease in the total-column AOD for medium-sized particles between Regions II and III (Figure A3 in Appendix A). In addition, both absolute and fractional increases in small aerosol AOD are observed, strongly suggesting the formation of new particles. The dramatic increase in the CO-normalized aerosol concentrations in the aircraft data further supports this conclusion, as does the increase in both the absolute and the fractional BrS AOD observed by MISR. The formation of weakly absorbing organic aerosols (BrS) would also explain why SSA does not change more dramatically in this region.

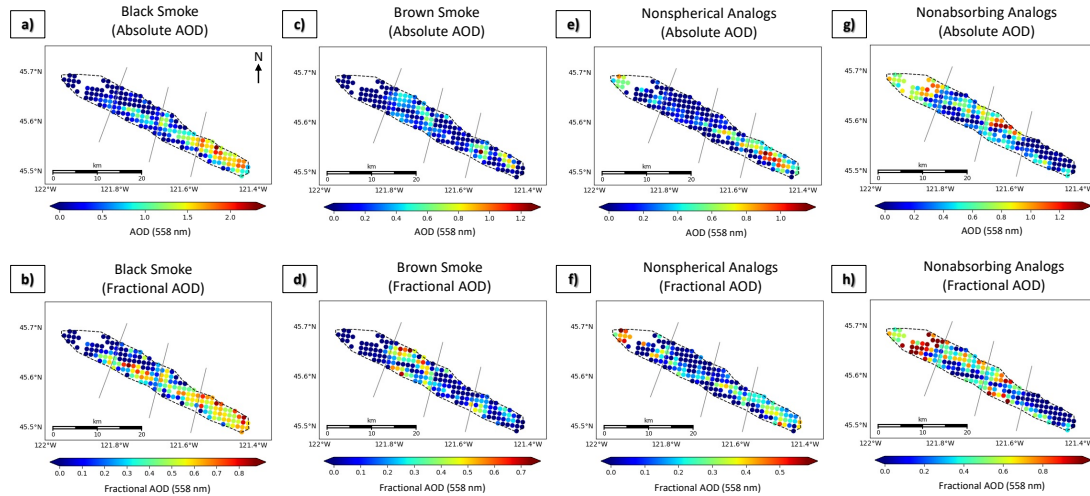


Figure 3.5. The absolute and fractional AOD of various MISR components for the Government Flats Complex Fire on 21 August 2013, where (a–b) are the sum of all “flat,” i.e., BC-like components (BlS), (c–d) are the sum of all “steep,” i.e., BrC-like components (BrS), (e–f) are the non-spherical dust-like components, and (g–h) are the sum of all non-light-absorbing components.

Although the aircraft did not observe Region IV, MISR points to potential aging mechanisms occurring here as well. Most notably, there is an increase in REPS, accompanied by decreasing MINX plume heights. Both the absolute and the fractional AOD of large and medium aerosols increase, suggesting that not only do small and very small particles disappear, but medium and large particles are being added (Figure A3 in Appendix A). At such a long downwind distance and with low overall AOD (Figure 3.4d), it is unlikely that particle aggregation is occurring in this region. Particle hydration might be involved, although the increase in non-spherical particles is not likely explained by this. Rather, these retrieval results might be due to a lack of larger, spherical, weakly absorbing particles in the aerosol climatology included in the MISR algorithm (Table 2.1), and, from a single satellite snapshot, we cannot rule out temporal changes at the smoke source.

3.3. *Phase II Results and Discussion: Using Non-Coincident RA and In Situ Observations*

In the previous section, we investigated the effectiveness of the MISR RA as a tool for retrieving BB smoke particle properties, using near-coincident *in situ* data for validation. We also demonstrated how the RA can go further in describing plume particle properties by providing critical context for the aircraft observations. Here, we briefly summarize the results obtained by comparing MISR retrievals with BBOP data from two flights ~1 day prior to and ~1 day after the satellite overpass. This builds upon the results shown in the previous sections and allows us to explore the utility of the RA for characterizing non-coincident observations (more complete results for these two cases are given in Appendix A). The observed differences

between the datasets illustrate the variable nature of BB plume dynamics and particle properties on time scales longer than a few hours, and they further highlight the value of combining satellite and *in situ* observations where possible to understand plume development more deeply. As such, combining multiple particle property observations, with different sensitivities and under different conditions, as well as with different spatial resolutions and coverage, creates a more complete picture of plume composition and evolution. Below are highlights from these comparisons, and we present detailed written and graphical analyses Appendix A (Figures A4–A10 for the Colockum Tarps Fire and Figures A11–A17 for the Douglas Complex Fire).

3.3.1. The Colockum Tarps Fire: Aircraft Observations Preceding Satellite Observations

The Colockum Tarps Fire, first ignited due to human causes, burned from 25 July 2013 through 15 August 2013 in southern central Washington [National Fire and Aviation Management]. The 26 July 2013 BBOP research flight and the subsequent 27 July MISR overpass observed the resulting smoke plume. Taken together, the satellite and *in situ* observations describe a plume with fine-mode, highly absorbing particles near the source that become brighter downwind, although the MISR RA observes slightly smaller particles overall than the CAS and PCASP data. From the available data, the main inferences we draw about particle evolution in the Colockum Tarps Fire plumes are that the near-source aerosols tend to be smaller and more light-absorbing than downwind. Plume dilution seems to be independent of particle size, as MISR-retrieved effective particle size (REPS) does not decrease systematically downwind, and the aircraft CO-normalized aerosol concentration does not change

significantly either. Aerosol oxidation is a factor in aging based on the *in situ* data and is likely also the explanation for a downwind increase in particle SSA observed by MISR the following day. Unlike the Government Flats fire plume, on both days, the Colockum Tarps plume retains areas of high BIS fraction over the entire plume extent. As particle properties vary non-uniformly with distance from the source on length scales under 10 km in this plume, it seems likely that the primary smoke emissions from this fire varied on time scales shorter than an hour.

3.3.2. The Douglas Complex Fire: Satellite Observations Preceding Aircraft Observations

The Douglas Complex fire was a large system originally comprised of dozens of lightning-sparked fires that ignited on 26 July 2013 and burned through 19 August 2013 in southern coastal Oregon [Oregon Department of Forestry]. The 5 August 2013 MISR overpass and the subsequent 6 August BBOP research flight observed the smoke plumes that were produced. The combined information from the satellite and aircraft data suggest small–medium particle sizes in the thickest parts of the plume and very small or small particles in the surrounding smoke, although the RA retrieves overall slightly larger particles than the aircraft data on the previous day, and also finds a significant AOD contribution from large particles in the plume core. Particles near the source are moderately light-absorbing as seen by MISR, but are brighter the next day during aircraft flight operations, when the fire appears to be a bit more active in the imagery. The horizontal structure of this plume suggests that the smoke observed here is stagnant, having piled up and just spread out locally due to low wind speeds, while undergoing atmospheric processing. This is supported by the presence

of larger particle sizes in the core on both days, as piled-up smoke could facilitate particle coagulation, condensation that leads to deposition of coatings on existing particles, and possibly particle hydration from fire-generated water vapor in a cooling plume. The increased CO-normalized CCN and aerosol concentrations outside the core area suggest possible SOA formation via the nucleation of new particles in the surroundings, where the fraction of very small particles is higher.

3.4. Summary

The primary focus of this chapter is a validation study of the MISR particle property retrievals using near-coincident BBOP data of the Government Flats fire. Overall, the satellite-retrieved particle properties are relatively well supported by the *in situ* observations, with minor disparities that can be explained by measurement uncertainty and sampling differences. Together, the data indicate that (1) there is a near-source region of high AOD with a mixture of dark, mostly spherical, small-medium particles, with light-absorption dominated by BIS, (2) there is an adjacent region downwind with reduced AOD comprising brighter, slightly larger particles that are less BIS-like, (3) there is a subsequent downwind region where AOD is reduced further, with significantly smaller particles that are brighter in nature and akin to BrS, and (4) there is a region at the nominal end of the plume with relatively low AOD, high SSA, and a significant fraction of larger, possibly non-spherical particles.

Our interpretation of the RA results parallels the atmospheric–aerosol interactions suggested by the *in situ* data. Through column-integrated particle-type retrievals and plume stereo heights, the preferential gravitational settling of larger

particles is supported in Regions II and III. Furthermore, decreased REPA throughout the length of the plume bolsters the idea of particle oxidation and/or hydration in Regions II and III. Lastly, a sharp decrease in REPS in Region III accompanied by a dramatic increase in BrS particle AOD strongly supports the idea of new-particle SOA formation here, although the RA results alone cannot rule out condensation of gaseous compounds onto existing particles.

This chapter also demonstrates that, despite some limitations, the use of the MISR RA in conjunction with non-coincident *in situ* measurements allows for a more comprehensive analysis of plume particle properties and presents a method for studying particle aging on larger spatial and longer temporal scales, where satellite coverage is acquired but aircraft data are lacking. For the two non-coincident cases analyzed here, the satellite and *in situ* data both captured the similarities and differences in plume structure, the relationships between denser, near-source smoke and more oxidized, less light-absorbing particles downwind, and the scales over which these transitions occurred. While the aircraft data captured the chemical and fine microphysical details of smoke along the sampled transects, the satellite snapshots provided extensive coverage, which makes it possible to infer particle evolution.

Chapter 4: Validating Space-Based Observations of Wildfire Smoke Particle Properties: The FIREX-AQ Field Campaign

4.1. Introduction

As has been discussed throughout this thesis, the application of new satellite remote sensing techniques requires thorough validation against coincident *in situ* observations. The study described in Chapter 3 represents the first part of this program. It compares the height and particle property results and interpretations from NASA Earth Observing System's Multi-Angle Imaging Spectrometer (MISR) instrument with detailed, near-coincident aircraft observations of three wildfire smoke plumes during the U.S. Department of Energy's 2013 Biomass Burning Observation Project (BBOP) field campaign [Kleinman and Sedlacek, 2013, 2016]. The current study is Part 2 of this validation effort, comparing the satellite data with coincident DC-8 aircraft measurements made during the 2019 NASA-NOAA Fire Influence on Regional to Global Environments Experiment-Air Quality (FIREX-AQ) field campaign. The FIREX-AQ campaign was conducted to investigate the impact of wildfire and biomass burning smoke on air quality and weather, with particular emphases on relating trace gas and aerosol emissions to fuel type and fire conditions at the point of emission, understanding downwind chemical transformation of smoke, and assessing the efficacy of satellite detections for estimating emissions [Roberts et al., 2018]. From 22 July to 19 August 2019, the NASA Douglas DC-8 research aircraft flew through wildfire plumes in the vicinity of Boise, Idaho, before moving to

Salina, Kansas for the remainder of August and the first week of September to study agricultural burns in the southeast U.S.

Aside from the BBOP plumes, the 06 August 2019 Williams Flats fire plume studied here is nearly the only other existing case for which we have near-coincident MISR and detailed *in situ* chemical observations. The validation study presented here aims to place the satellite-retrieved plume particle characteristics on firmer ground, expanding the validation sample size and augmenting the validation effort from Chapter 3. Although most of the aircraft instrument types used in FIREX-AQ are similar to those employed during BBOP, many of the instrument teams are different, and the FIREX-AQ campaign offered several additional validation resources, such as plume height, particle non-sphericity, and other lidar-retrieved measurements; the degree of flaming and smoldering measurements in the fire itself; and improved data on fuel type at the point of burning. These additions improve our previous understanding of MISR's ability to characterize wildfire plumes, compared to Chapter 3, and provide further insight into the relationships between measurements made by field scientists and the optical retrievals from satellites. The results from the combined validation studies set the stage for future work in developing a global climatology of BB aerosol plume properties and processes, which requires analyzing a broad, statistical sampling of MISR plume retrievals that are not also constrained by field observations (which we work towards realizing in Chapter 5). This study also highlights how a combined satellite–*in situ* approach is a superior method of observing wildfire smoke plumes during field campaigns.

Data sources and analysis methods are described in Chapter 2, with specific instrument information neatly summarized in Table 2.2. Section 4.2 presents our analyses of the similarities and differences between the MISR retrievals and the aircraft observations, as well as a set of proposed aerosol aging mechanisms that act to change the particle properties downwind. Section 4.3 highlights how the current work builds upon the previous validation study. A summary is given in Section 4.4.

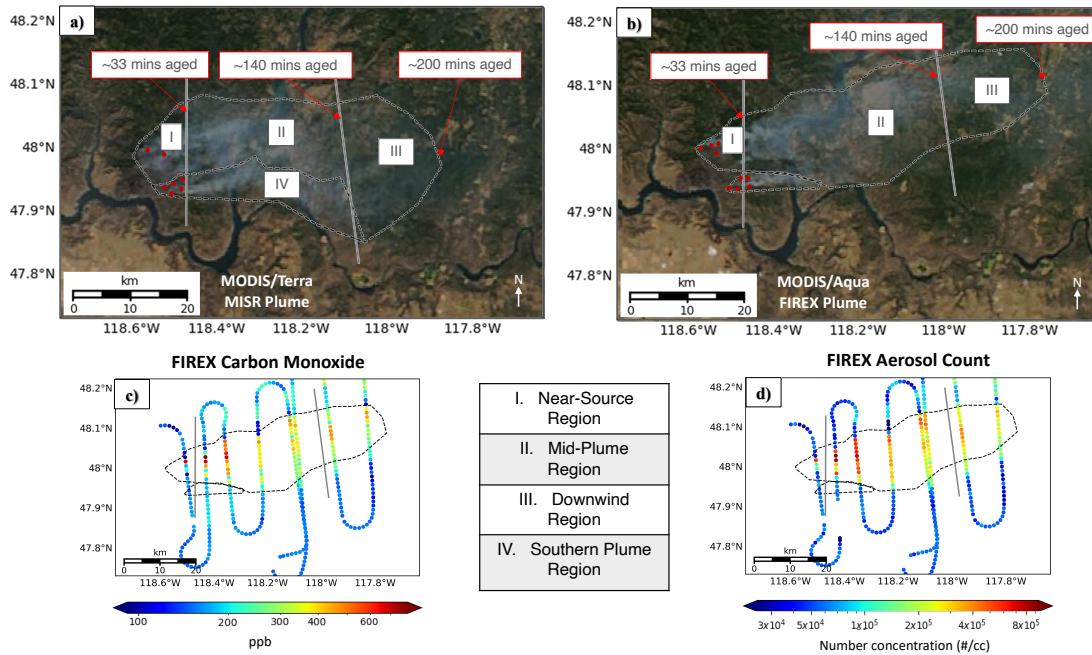


Figure 4.1. The Williams Flats Fire as seen on 06 August 2019: (a) at Multi-Angle Imaging Spectrometer (MISR) overpass time (19:06 UTC; MODIS Terra RGB image), and (b) during the Fire Influence on Regional to Global Environments Experiment-Air Quality (FIREX-AQ) flight operations (20:50 UTC; MODIS Aqua RGB image). The red dots indicate MODIS-identified hot spots, used to estimate source location. The dashed lines represent plume outlines we use for analysis. At both observation times, the plume is divided into distinct regions (I-III) based on estimated plume age, to allow for easy, qualitative comparison of inter- and intra-plume properties. At the time of MISR observation, there is an additional region (IV) that separates the southern-most plume from the other regions. The differential absorption CO measurements instrument (DACOM) CO mixing ratio and the laser aerosol spectrometer (LAS) total aerosol concentration observed by the aircraft (above $0.09 \mu\text{m}$ in diameter) are displayed in (c) and (d), respectively.

Table 4.1. MISR-observed particle properties for the Williams Flats fire by region. AOD— aerosol optical depth; SSA—single scattering albedo (558 nm); ANG—extinction Ångström exponent (446–866 nm).

Plume Region:		Near-Source (Region I)	Mid-Plume (Region II)	Downwind (Region III)	Southern (Region IV)
AOD	mean	0.8750	0.8653	0.5965	0.9196
	$\pm\sigma$	± 0.4550	± 0.2565	± 0.1123	± 0.2840
	median	0.8499	0.8747	0.6002	0.9500
SSA	mean	0.8773	0.9402	0.9549	0.9034
	$\pm\sigma$	± 0.06045	± 0.03135	± 0.03325	± 0.04425
	median	0.8659	0.9411	0.9574	0.8979
ANG	mean	1.568	1.325	1.5206	1.424
	$\pm\sigma$	± 0.3450	± 0.2831	± 0.1887	± 0.2857
	median	1.620	1.349	1.504	1.418
BIS ^{a,b}	mean	0.6026	0.2559	0.2170	0.5623
	$\pm\sigma$	± 0.3797	± 0.2349	± 0.2204	± 0.2993
	median	0.7459	0.1995	0.1591	0.6305
BrS ^{a,c}	mean	0.08076	0.1130	0.06004	0.06354
	$\pm\sigma$	± 0.1471	± 0.1825	± 0.1236	± 0.1337
	median	0	0.004544	0	0
Non-absorbing ^{a,d}	mean	0.2657	0.5022	0.6870	0.3610
	$\pm\sigma$	± 0.2787	± 0.2691	± 0.2559	± 0.2703
	median	0.1782	0.4733	0.7416	0.3020
Non-spherical ^{a,e}	mean	0.05080	0.1286	0.03584	0.01307
	$\pm\sigma$	± 0.1139	± 0.1745	± 0.08294	± 0.06604
	median	0	0.03690	0	0

^a In terms of fraction of total AOD (0 to 1);

^b The combined total of all spectrally flat components, meant to represent black carbon analogs;

^c The combined total of all spectrally steep components, meant to represent brown carbon analogs;

^d The combined total of all non-absorbing components;

^e The only non-spherical component, meant to represent dust or soil.

4.2. Results and Discussion

The Williams Flats Fire ignited on 02 August due to lightning from a band of early morning thunderstorms, burning primarily in the Confederated Tribes of the Colville Reservation and Washington Department of Natural Resources protected lands. The bulk of the fire activity was confined to 02 through 09 August, at which point a large precipitation event stifled burning so that the fire was effectively extinguished in subsequent days. However, re-invigoration and creeping activity

resulted in continued management efforts through 25 August, by which time over 44,000 acres had burned [Inciweb]. The fire was managed with both aviation and on-the-ground containment methods including helicopter water drops, air tanker retardant drops, building a direct line, and significant mop-up [Inciweb]. However, active fire suppression was not occurring during the FIREX-AQ operations on 06 August. The fuels involved were reportedly a mixture of timber, short grass, light slash from logging, and a coniferous overstory [Inciweb]; similarly, the MODIS Level 3 IGBP yearly land cover type shows the region is a mixture of grassland, savanna, and evergreen needleleaf forest, and fuel characteristic classification system (FCCS) modeling reveals primarily Douglas-fir-Pacific ponderosa pine was burning, followed by wheatgrass grassland [FIREX-AQ Science Team: Fuel2Fire].

The plume produced by this fire was observed by MISR on 06 August 2019, at ~19:07 Universal Coordinated Time (UTC), ~2 h before the FIREX DC-8 aircraft sampled the same area (for all but a first “remote sensing” overpass at ~19:00 UTC); the aircraft continued sampling this plume for an additional hour. During all observation times, it is clear the fire contained two main hotspots: a northern one that produced a large plume, and another to the south and east that produced a smaller plume burning slightly uphill (Figure 4.1). At the time of MISR observation, the distinction between these plumes is clear and the smoke displays unique patterns in optical and physical properties that can be linked to smoke age. We divide the MISR-observed plume into four regions based on these patterns: a near-source region (designated Region I), a mid-plume region (II), a downwind region (III), and a southern plume region (IV) (Figure 4.1a). It should be noted that despite the clear

distinction between the northern and southern plumes, there is still likely some degree of mixing, especially downwind. There is also optically thin smoke outside the plume boundaries both downwind to the east as well as to the north in the river valley. We exclude these from our analysis because very thin smoke layers cannot be retrieved reliably by MINX or the RA, so the focus of this study is on relatively thick smoke within the plume. We calculate the approximate age of the smoke at regional boundaries using the ratio of the along-plume distance and mean wind vectors in the area derived from MINX (Figure B1 in Appendix B). Estimated plume ages at the regional transition lines are given in Figure 1. It should be noted that these dividing lines only apply to the northern plume. The southern plume is treated as its own distinct region (Region IV) as its particle properties are fairly uniform at the level of detail we can retrieve from the satellite; and so its age is averaged across its entire length. The mean MINX-derived wind speeds in Region IV are greater than in the northern plume area (4.26 ± 1.66 vs. 3.88 ± 1.96 m/s; Figure B1 in the Appendix B) and the source is located further east, so smoke here is approximately 20 min younger than smoke at a similar downwind distance in the northern plume.

By the time the aircraft began its sampling two hours later, the northern and southern plumes had largely merged and only a small area of smoke near the south-east hotspot was clearly distinct from the rest (outline in Figure 4.1b). Due to altitude limitations, the aircraft did not sample this area in Transect 1, whereas subsequent transects sampled smoke from the merged northern and southern plumes where smoke had converged. We therefore do not define a Region IV for the FIREX plume, and, as shown subsequently, downwind particle properties from the aircraft do not

display the same north-south differences seen by MISR. Based on plume ages derived from the aircraft wind speeds, the rest of the plume was divided into regions of similar age as the MISR-observed northern plume (Figure 4.1b). However, because Region I contains only points sampled from the northern plume (Transect 1) and Region II experiences an influx of fresh smoke from the southeast source (Transects 2 and 3), the broad regional averages for many measurements are skewed and do not fully illustrate the along-plume changes in particle properties. We therefore focus the analysis of the *in situ* measurements on transect-by-transect changes, and return to regional analysis in later discussion.

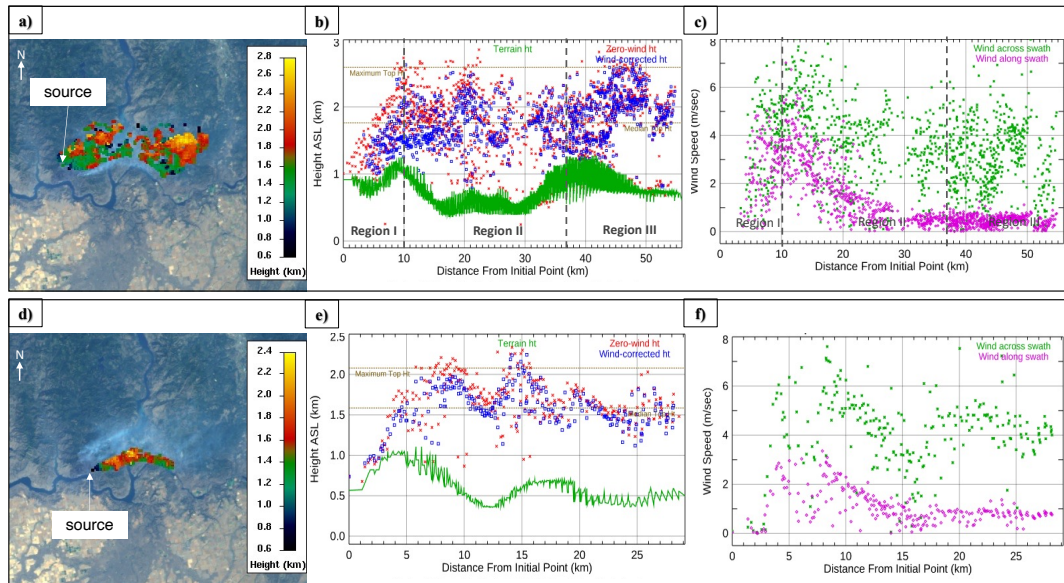


Figure 4.2. Height and wind properties for the Williams Flats Fire retrieved by MISR at 19:06 UTC (Orbit 104434, Path 45, Block 52) on 06 August 2019. The top panels (**a–c**) correspond to retrievals for the northern plume, whereas the bottom panels (**d–f**) correspond to the southern plume. Panels (**a,d**) are MISR-MINX stereo height retrieval map; (**b,e**) are MINX stereo height profiles as a function of distance from the source, for both zero-wind (red) and wind-corrected (blue) analyses, with surface elevation indicated in green; and (**c,f**) are the across-swath and along-swath wind vectors. The dashed grey lines in panels (**b**) and (**c**) represent the dividing lines between regions in the northern plume defined in Figure 4.1.

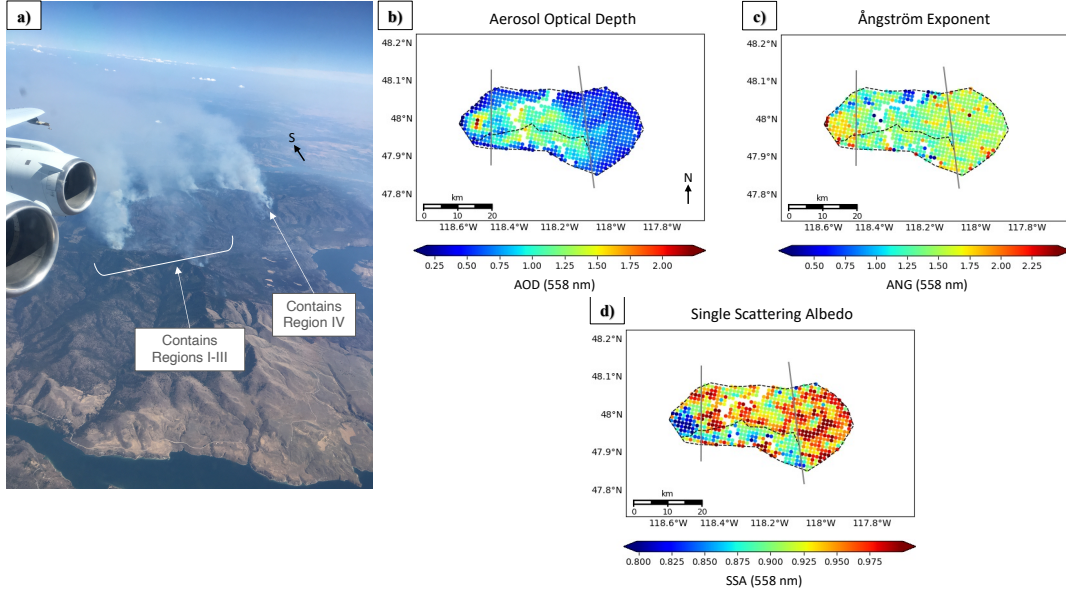


Figure 4.3. Basic plume properties for the Williams Flats Fire retrieved with the MISR RA at 19:06 UTC (Orbit 104434, Path 45, Block 52) on 06 August 2019, accompanied by a contemporaneous image of the fire (**a**) taken from the aircraft during sampling [credit: K. Junghehn Noyes]. MISR RA results are given in panels (**b**) AOD at 558 nm; (**c**) 446–866 nm extinction Ångström exponent (ANG); and (**d**) single scattering albedo (SSA) at 558 nm. The transects for estimated plume ages corresponding to the region boundaries in Figure 4.1 are indicated with thin grey lines.

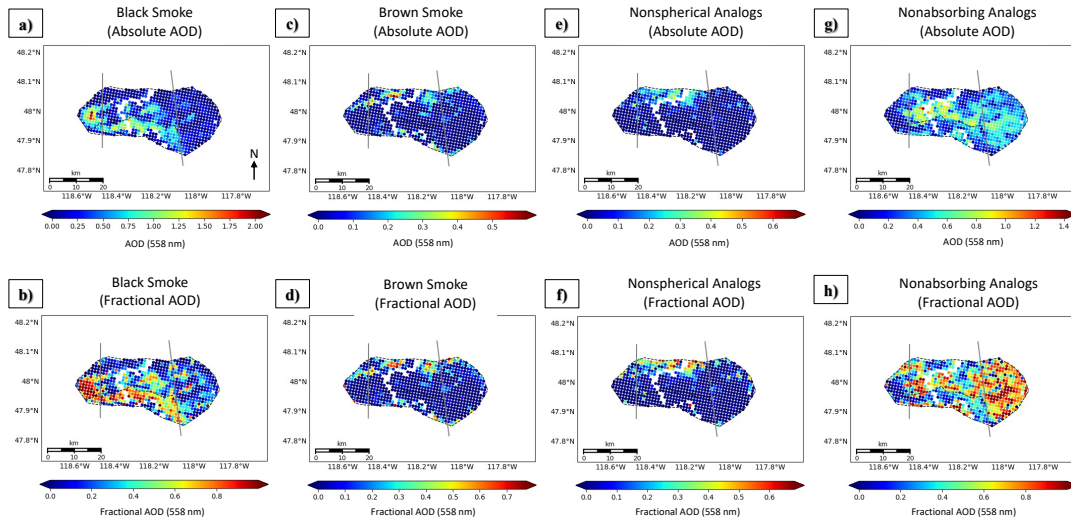


Figure 4.4. The absolute and fractional AOD (558 nm) of various MISR RA aerosol components for the Williams Flats Fire on 06 August 2019, where (**a,b**) are the sum of all spectrally “flat” or BIS components, (**c,d**) are the sum of all spectrally “steep” or BrS components, (**e,f**) are the sum of all non-light-absorbing components, and (**g,h**) are the non-spherical, dust-like components. Fractional plots are given as a fraction of 1. Note: scales differ between panels.

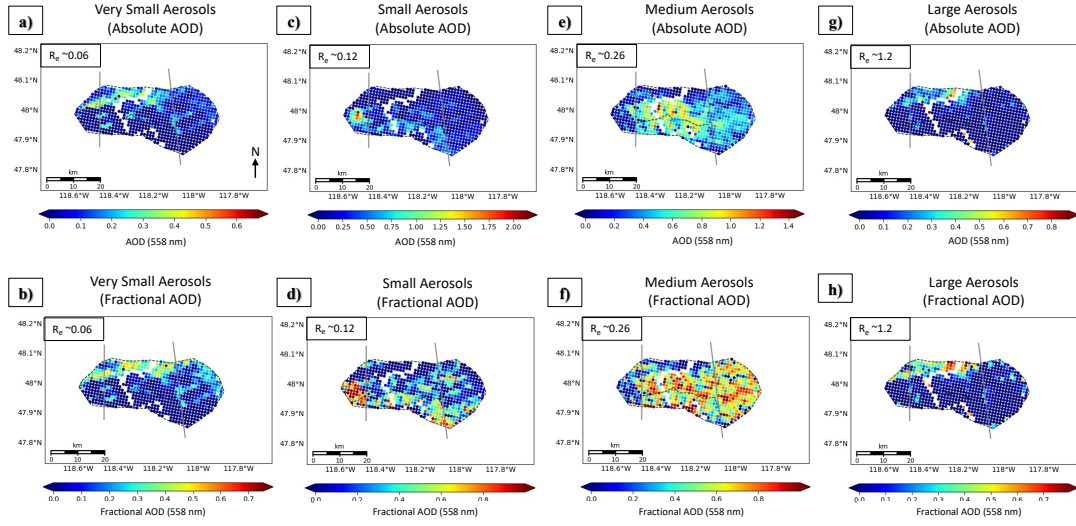


Figure 4.5. The absolute and fractional AOD (558 nm) of various MISR RA aerosol size bins for the Williams Flats Fire on 06 August 2019, where (a,b) are the sum of all “very small” components, (c,d) are the sum of all “small” components, (e,f) are the sum of all “medium” components, and (g,h) are the sum of all “large” components (which includes the non-spherical analog). Particles are assumed to be normally distributed around the effective radius (R_e) provided in the legend. Note that “large” aerosols include both the large spherical nonabsorbing component ($R_e = 1.28$) and the non-spherical component ($R_e = 1.21$). Fractional plots are given as a fraction of 1. Note: scales differ between panels.

In this section, we compare the particle properties retrieved by MISR with those obtained *in situ* from aircraft measurements, paying particular attention to changes with downwind distance. We then apply this information to current knowledge on how various aging mechanisms impact particle properties, in an effort to infer the active processes at hand. Only observations taken within the plume boundaries (Figure 1) are included in our analysis, except when comparing measurements to background values. For the MISR dataset, the boundary is a user-drawn plume outline created during the MINX retrieval (Figure 4.1a). For the FIREX dataset, the RGB MODIS-Aqua image, acquired minutes before FIREX sampling began, was used to draw the plume outline (Figure 1b), with slight adjustments based on aircraft-derived aerosol and CO concentrations that reflect potential changes in

plume geometry over the duration of the flight after the MODIS image was captured (Figure 4.1c,d). Where applicable, all figures display the plume boundary as a dotted-line polygon and the dividing lines between regions are shown as thin solid grey lines.

4.2.1. Satellite Observations

We first provide an overview of the satellite observations, with emphasis on the differences in smoke particle properties between regions. Figures 4.2 and 4.3 respectively contain the MISR-MINX stereo heights and wind vectors and the standard MISR RA latitude/longitude plots of AOD, SSA₅₅₈, and ANG₄₄₆₋₈₆₆. In addition to these, we map, in terms of both retrieved absolute AOD and AOD fractional component: the spectral dependence of aerosol light-absorption via the separate sums of retrieved (1) spectrally flat (BlS) and (2) spectrally steep (BrS) aerosol components (Figure 4.4a-d), (3) the retrieved aerosol shape via the non-spherical component (Figure 4.4e,f), (4) further information on light-absorption via the sum of all non-absorbing components (Figure 4.4g,h), and (5) further information on aerosol size via the separate sums of very small, small, medium, and large aerosols (Figure 4.5). Plots of absolute AOD map the AOD that can be attributed to the specific component(s) retrieved, whereas fractional AOD plots highlight the dominant characteristics of the plume over its extent. As discussed subsequently, these particle properties are, for the most part, neatly distinctive between the four plume regions. It is important to reiterate that, when considering specific particle types (e.g., black carbon, brown carbon, soil/dust, non-absorbing aerosols), the MISR-retrieved aerosol properties represent the optical equivalent of the true smoke particle mixture, which is

not necessarily a mixture of the specific components retrieved from among those prescribed by the RA climatology [Junghenn Noyes et al., 2020a, 2020b; Flower and Kahn, 2020a, 2020b; Kahn and Gaitley, 2015]. Note that the missing retrievals in the RA results are pixels located above the river, as the version of the RA used in this study is geared for land observations only (future versions will include an over-water component). Table 4.1 quantifies the above-mentioned RA observations, providing the mean, standard deviation, and median satellite-retrieved particle properties for each region. A more detailed discussion of these statistics can be found in Appendix B.

The MISR-MINX stereo heights indicate that both the northern and southern plumes are concentrated mostly within 2 km above sea level (ASL) at 19:07 UTC, with median and maximum heights of 1.76 and 2.59 km (northern) and 1.59 and 2.08 km (southern), respectively (Figure 4.2b,e). The RA-retrieved particle properties indicate peak mid-visible AOD of up to \sim 2.2 near the source, systematically decreasing with downwind distance to a minimum of <0.2 in some pixels of Region III, within the area we defined as the observable plume in the satellite imagery (Figure 4.3b). Both plumes are overall comprised of fine particles ($\text{ANG} > 1$), although there is a small area of larger particles in the northern plume along its northern edge, particularly in Region II. REPS is particularly low near the northwest source (Region I), increases in Region II, and subsequently decreases again in Region III (Figure 4.3c, Figure 4.5). Component analysis suggests the increased REPS in Region II is driven by both absolute and fractional increases in medium- and large-sized particles, accompanied by a decreased contribution from small-sized particles,

whereas the decreased REPS in Region III is driven by absolute and fractional decreases in large-sized particles alone (Figure 4.5). REPS in the southern plume is relatively constant throughout the plume length and is overall somewhere between the values seen in Regions I and II of the northern plume. As seen in Figure 4.5, particle size here is almost exclusively a mixture of small and medium particles, as compared to the combination of all four size categories seen in the northern plume (although small and medium categories still dominate in the northern plume).

The northern plume REPA spans the entire range of possible SSA values as defined in the MISR RA climatology, with significant light-absorption near the source in Region I ($\text{SSA} \sim 0.8$) that gradually decreases downwind to the point where the majority of pixels in Region III exhibit $\text{SSA} > 0.95$ (and some as high as 1.0) (Figure 4.3d, Table 4.1). REPA is somewhat variable throughout Region II, with distinct alternating patches of less absorbing aerosols ($\text{SSA} > 0.95$) and more absorbing aerosols ($0.90 < \text{SSA} < 0.95$). Conversely, the southern plume REPA is more consistent, with most SSA values below 0.90 throughout the length of the plume, in-between the average values seen in Regions I and II of the northern plume. Component analysis suggests that smoke from the northwest source (Region I) is largely a BIS-dominated mixture, but that subsequent regions of the northern plume increasingly transition to mixtures interpreted as mostly non-absorbing and BIS particles. However, a significant portion along the northern edge of Region II is retrieved almost entirely as a mixture of BrS and non-spherical analogs. This is the same area of the plume where sizes are retrieved as a combination of very small and large particles, suggesting that smoke here might contain a mixture of very fine

organic and large soil- or dust-like aerosols. In the southern plume, the mixture is almost entirely BIS and non-absorbing particles, with the former being dominant overall and decreasing only slightly with downwind distance (Figure 4.4, Table 4.1). Note that the MISR-retrieved component AOD values and fractions represent an interpretation of the MISR column-integrated reflectances in terms of the components included in the RA (Table 2.1 in Chapter 2), whereas the REPS and REPA are less dependent on algorithm assumptions. This is one reason why validation with the *in situ* data is so important.

Based on the satellite observations alone, we identify several processes that could be affecting plume particle properties. In particular, we infer that: (1) VOC condensation and/or coagulation of particles act to increase REPS in Region II compared to Region I; (2) gravitational settling leads to a preferential decrease in the fraction of large-sized particles in Region III compared to Region II; there is an increase in the oxidation state of particles progressively downwind throughout the plume, reflected in the increased AOD of non-absorbing analogs; and (4) there may be differences in the emissions between the northern and southern hotspots, leading to observed differences in particle size and light-absorption. Mechanism (1) is supported by the absolute increase in medium-particle AOD at the expense of the absolute small- and very small-particle AOD, suggesting particles in smaller categories are transitioning to the larger size categories. This cannot be validated directly with available *in situ* measurements, but changes in the particle number concentration and particle size distribution as well as changes in the oxidation state can offer supporting indications. Mechanism (2) is supported by MISR-MINX plume heights, where the

smoke column in the northwest plume approaches the surface approximately 40 km downwind at the beginning of Region III, so particles may be settling to the surface in this region (Figure 4.2b). As aircraft measurements sample a single elevation, this mechanism cannot be directly validated *in situ*. However, the differences between the satellite and aircraft size distributions can provide insight into how particles may be distributed within the atmospheric column (e.g., Flower and Kahn [2020b]). Mechanism (3) can be validated from the available *in situ* data via the changing oxidation state, BC mass, and SSA downwind. Mechanism (4) may be supported by *in situ* data as well. We test these hypotheses with the FIREX data in subsequent sections.

4.2.2. *In situ* Observations and Comparison with MISR

The satellite and *in situ* measurements are considerably similar in their characterization of particle property evolution as a function of smoke age, and most of the key differences in particle size and light-absorption can be attributed to differences in sampling and changes in the plume geometry between sampling times. Here, we assess the fidelity of the RA results by first presenting an overview of the aircraft observations and comparing them with the MISR-retrieved particle properties in the plume as a whole. We then provide detailed observations for along-plume changes in particle properties observed *in situ*, and assess how they connect to the MISR-observed properties. This step also allows us to demonstrate how the MISR-retrieved particle properties offer context for the aircraft data, providing critical information for understanding plume evolution and inferring particle aging mechanisms. These are summarized in Section 4.2.4.

As the distinction between the emitted smoke from the two main hotspots was no longer clear at the time of the FIREX aircraft observations, the *in situ* analysis focuses more on the differences in smoke properties between transects, rather than regions, although both are important to consider. We abbreviate across-plume transects using the letter T followed by the transect number (T1, T2, . . . , T8), and the longitudinal, nadir-viewing above-plume “remote sensing” transects with the letter L followed by the transect number (L1, L2, and L3). Figure 4.6 displays the lidar-retrieved aerosol backscatter (providing information on plume height and extent) and aerosol depolarization (providing information on particle non-sphericity) for L1-L3. Figures 4.7 and 4.8 illustrate, as latitude/longitude plots, the chemical, optical, and physical properties measured in the plume as described in Chapter 2. Each point represents the aggregated ~1.1 km median value of a given measurement. Figure 4.9 displays non-aggregated particle size distributions (in terms of both number and volume concentrations) by transect for points inside the plume outline, grouped into subplots based on the regions defined in Figure 4.1. Note that measurements for particles greater than 0.6 μm in diameter were not plotted, as their contributions to the measured aerosol abundance were negligible. Table 4.2 provides several non-aggregated, transect-averaged parameters from Figures 4.7-9 as well as transect age and MCE. This is supplemented by Table 4.3, which quantifies the regionally aggregated mean, standard deviation (SD or σ), and median values for many of the same measurements. As with the satellite observations, a comprehensive discussion of these statistics, plus the DIAL-HSRL measurements, can be found in Appendix B.

Table 4.2. Aircraft-measured particle properties, averaged by transect. Norm.-- CO-normalized.

Transect	Age ^a	MCE	Peak D _p ^b	D _(10%) ^c	D _(50%) ^d	D _(90%) ^e	Aerosol Count ^f	Norm. Aerosol Count ^g
1	32.67	0.874	0.148	<0.105	0.155	0.266	157122	682.192
2 ^p	45.59	0.896	0.122	<0.105	0.148	0.254	421668	1030.10
3	60.85	0.898	0.141	<0.105	0.155	0.254	466133	1024.62
4	84.89	0.931	0.141	<0.105	0.155	0.254	295146	907.454
5	112.8	0.887	0.134	<0.105	0.155	0.266	284720	844.080
6	115.6	0.892	0.155	<0.105	0.163	0.266	279631	853.498
7	142.9	0.899	0.155	0.11	0.163	0.28	286611	855.151
8	n/a	0.814	0.155	0.11	0.171	0.294	236239	734.102
Transect	BC ^h	Norm. BC ⁱ	CCN ^j	Norm. CCN ^k	Oxidation ^l	SSA ₅₃₀ ^m	Norm. BrC Absorption ⁿ	Norm. BC Absorption ^o
1	417.9	1.258	3619	11.98	0.3730	0.928	0.0565	0.0217
2	1413	2.899	7358	16.03	0.3236	0.927	0.0783	0.0371
3	1673	3.587	8712	18.86	0.3806	0.923	0.0850	0.0403
4	1151	3.469	5482	16.78	0.5498	0.928	0.0679	0.0358
5	1120	3.338	5377	15.78	0.6299	0.934	0.0632	0.0297
6	951.9	2.880	6567	19.89	0.6478	0.929	0.0718	0.0276
7	898.4	2.684	6252	18.17	0.7339	0.936	0.0702	0.0267
8	826.2	2.512	5110	15.68	0.6867	0.942	0.0662	0.02032

^a Estimated age of smoke measured in each transect in minutes, calculated based on aircraft-measured wind speed; ^b Bin size at which the transect-averaged particle size distribution peaks in μm (the mode aerosol size), as measured by the LAS instrument; ^c The diameter (μm) below which 10% of the total measured aerosol population exists, as measured by the LAS instrument; ^d The diameter (μm) below which 50% of the total measured aerosol population exists, as measured by the LAS instrument; ^e The diameter (μm) below which 90% of the total measured aerosol population exists, as measured by the LAS instrument; ^f The total concentration of aerosols (#/cc) as measured by the LAS instrument; ^g The ratio of the total aerosol count from the LAS instruments (#/cc) and the CO concentration measured by DACOM instrument (ppb); ^h Mass concentration of BC measured by the SP2 instrument, in ng/std*m³; ⁱ The ratio of BC mass concentration (ng/std*m³) from the SP2 and CO measured by DACOM instrument (ppb); ^j The concentration (#/cc) of CCN that activated at 0.34% supersaturation, as measured by the CCN-100 instrument; ^k The ratio of CCN measured by the CCN-100 instrument (#/cc) and CO measured by DACOM instrument (ppb); ^l Defined as $-\log[\text{NO}_x/\text{NO}_y]$, using measurements provided by the ozone-induced chemiluminescence technique, where 0 is interpreted as fresh smoke and 1 is aged smoke; ^m As measured by the PSAP/neph instruments; ⁿ The residual of the ratio of 405 nm absorption (PAS; Mm⁻¹) and CO concentration (DACOM; ppb) and the ratio of 664 nm absorption (PAS; Mm⁻¹) and CO concentration (DACOM; ppb); ^o The ratio of 664 nm absorption (PAS; Mm⁻¹) and CO concentration (DACOM; ppb); ^p The point at which the southern and northern plume merge in the aircraft data.

Table 4.3. Aircraft data aggregated by plume region: aerosol size, chemical, and physical properties for the Williams Flats Fire measured *in situ* on 06 August 2019. Norm.-- CO-normalized.

Plume Region:		Near-Source (Region I)	Mid-Plume (Region II)	Downwind (Region III)
Very small Aerosols ^a	mean	0.626	0.617	0.553
	$\pm\sigma$	±0.0218	±0.0298	±0.0173
	median	0.632	0.611	0.550
Small Aerosols ^a	mean	0.298	0.312	0.348
	$\pm\sigma$	±0.0166	±0.0211	±0.00883
	median	0.297	0.318	0.349
Medium Aerosols ^a	mean	0.0732	0.0678	0.0979
	$\pm\sigma$	±0.00912	±0.0101	±0.00970
	median	0.0718	0.0696	0.0968
Large Aerosols ^a	mean	0.0000458	0.0000567	0.000172
	$\pm\sigma$	±0.000102	±0.0001151	±0.000137
	median	0	0	0.000221
SSA_{530} ^b	mean	0.924	0.929	0.939
	$\pm\sigma$	±0.042	±0.0112	±0.00577
	median	0.937	0.932	0.939
Oxidation ^c	mean	0.354	0.526	0.711
	$\pm\sigma$	±0.0930	±0.158	±0.0540
	median	0.360	0.552	0.707
BC Mass Concentration ^d	mean	591.7	1187	855.0
	$\pm\sigma$	±936.8	±630.9	±247.5
	median	184.8	1058	788.0
Norm. BC Mass Concentration ^e	mean	1.30	3.10	2.56
	$\pm\sigma$	±0.729	±0.890	±0.233
	median	1.07	3.11	2.52
CCN ^f	mean	4081	6594	5728
	$\pm\sigma$	±5898	±3344	±1669
	median	1620	6364	5477
Norm. CCN Concentration ^g	mean	11.2	17.3	17.1
	$\pm\sigma$	±6.35	±4.34	±1.68
	median	9.78	17.2	16.8
Norm. Total Aerosol Count ^h	mean	547.1	903.1	800.0
	$\pm\sigma$	±227.1	±229.3	±102.9
	median	509.9	882.1	808.1

^a Fraction of total aerosol count, measured by the LAS instrument; ^b Measured by the PSAP/neph;

^c Defined as $-\text{Log}[\text{NO}_x/\text{NO}_y]$, using measurements from the ozone-induced chemiluminescence technique, where 0 is interpreted as fresh smoke and 1 is aged smoke; ^d Measured by the SP2, in $\text{ng}/\text{std}^*\text{m}^3$; ^e The ratio of BC mass concentration ($\text{ng}/\text{std}^*\text{m}^3$) from the SP2 and CO measured by the DACOM instrument (ppb); ^f The concentration (#/cc) of CCN that activated at 0.34% superstation, measured by the CCN-100; ^g The ratio of CCN measured by the CCN-100 instrument (#/cc) and CO measured by the DACOM instrument (ppb); ^h The ratio of the total aerosol count from the LAS instruments (#/cc) and the CO concentration measured by the DACOM instrument (ppb).

4.2.3. Overview of Comparison

The DIAL-HSRL aerosol backscatter at 532 nm illustrates the evolving vertical plume dynamics as the day progressed during FIREX sampling. The smoke layer was confined mostly below 2 km ASL during the first longitudinal overpass (L1) at ~19:00 UTC (Figure 4.6), consistent with the plume heights retrieved by MISR/MINX at approximately the same time. During L2, at ~20:30 UTC, the plume rose above 3 km, reaching as high as 4.0 km for L3 at ~21:50 UTC. This reflects typical diurnal fire behavior; burning often increases in intensity in the afternoon as temperatures rise and relative humidity decreases, amplifying smoke plume vertical and horizontal extent. Horizontal wind speeds measured by the DC-8 are relatively consistent with the MINX-retrieved wind speeds a few hours earlier. Furthermore, for the entire plume, there is a systematic decrease in the MISR AOD with downwind distance, which is confirmed by aircraft particle concentration measurements from FIREX. Lastly, inversions from the AERONET DRAGON [Holben et al., 2018] mobile photometers deployed during FIREX show particle mid-visible SSA of 0.94 and ANG of 1.74 measured in the plume vicinity. Though not within the plume as observed by MISR due to differences in the times of observation, these are consistent with the retrieved size and light-absorption measurements from both MISR and the DC-8 instruments.

In both the FIREX- and MISR-observed plume, particle light-absorption systematically decreases downwind, although the spread of SSA values is considerably smaller in the FIREX observations. There is also a clear favoring of BC/BIS from the southeast hotspot compared to the northwest hotspot in both

datasets; for FIREX, this is evident from the large injection of absolute and dilution-corrected BC mass concentrations at the point of convergence between the two plumes (Table 4.2), whereas for MISR this is evident from the consistently elevated BIS AOD throughout the length of the southern plume compared to the northern plume. Both sets of observations also indicate there is at least some presence of a spectrally steep light-absorbing component, with a varying level of contribution to the total light-absorption; for FIREX, this is evident from the differences in absorption at the long and short end of the visible spectrum as measured by PAS (Table 4.2), and for MISR this appears from the localized area of BrS particles along the northern edge of Region II.

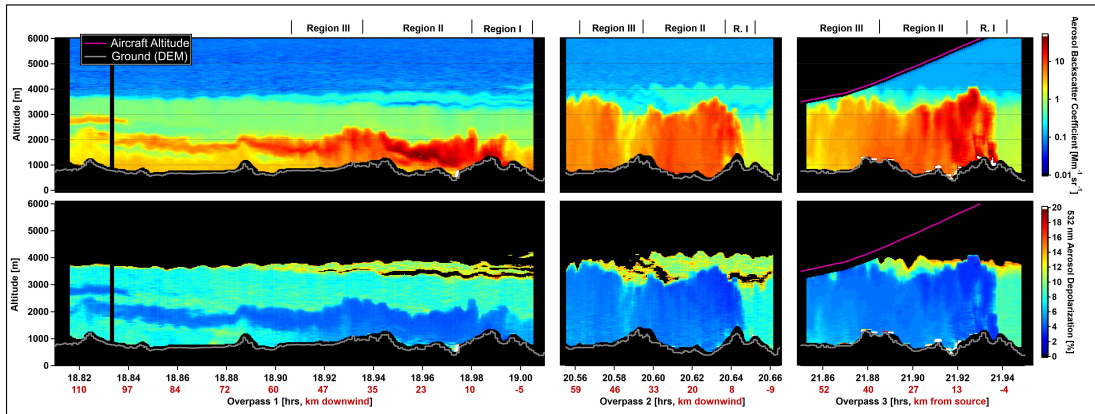


Figure 4.6. DIAL-HSRL nadir retrievals of 532 nm aerosol backscatter coefficient (**top row**) and depolarization ratio (**bottom row**) for the three longitudinal overpasses (L1-L3). During the MISR/MINX overpass (L1), the plume is less vertically developed and only reaches an altitude of approximately 2 km, consistent with the MISR/MINX retrievals shown in Figure 2. The anomalous high-scattering values very near the surface at ~[18.97, 20.66, and 21.88–21.92 hrs] are scattering contamination from the ground surface and should not be interpreted as aerosol signal. Note: Time is in UTC.

MISR indicates a significant presence of non-spherical aerosols along the northern plume boundary in Region II as well as in the surrounding background air. Although the *in situ* aerosol depolarization measurements are dominated by values reflective of less depolarizing biomass burning aerosols (between 3–6%) within the

plume, larger depolarization values just outside the plume reflect the presence of at least some background dust (bottom row of Figure 4.6, at ~20.65–20.66 and 21.94–21.95 h). It is also possible that MISR retrieves these non-spherical particles because they offer the best match in the RA climatology to the actual particle size, rather than due to matching particle shape (Table 2.1 in Chapter 2). Furthermore, the sporadic nature of aircraft sampling and the time difference between the satellite and aircraft observations may contribute to the apparent discrepancy.

Particles are overall fine at both times of observation, with slightly increasing size with age at least through Region II. However, MISR-retrieved REPS suggests decreasing particle size in Region III, whereas the aircraft shows continued increases in size (Table 4.2, Figure 4.8). Moreover, MISR indicates that particle size is increasingly dominated by “medium” aerosol fractions in Regions II and III, and although the aircraft measurements do exhibit increased fractions of aerosols in this size range (excluding in Transect 2, which brings down the regional average), overall aerosol size is comparatively more firmly rooted in the “small” and “very small” size categories (Figure 4.8, Table 4.3). However, both the *in situ* and MISR observations suggest smaller particles from the southeast hotspot; for FIREX, this is evident from the decreased particle size at the point of convergence between the two plumes, whereas for MISR this is evident from the consistently smaller particles throughout the length of the southern plume compared to the northern plume. The lidar 1064/532 nm color ratio is typical of values for BB plumes, but does not reflect the downwind increases in particle size observed by MISR and by the *in situ* LAS instrument, likely due to sensitivity limitations in the color ratio itself. (Although transect-by-transect

changes in the LAS are small, they are systemic and significant when taken over the whole plume). The apparent differences between MISR and the *in situ* size distributions in Regions II and III might be due to larger particles preferentially settling downward in the plume, as the aircraft samples at a single elevation whereas MISR REPS represents the entire vertical column (this is discussed further in Section 4.2.4).

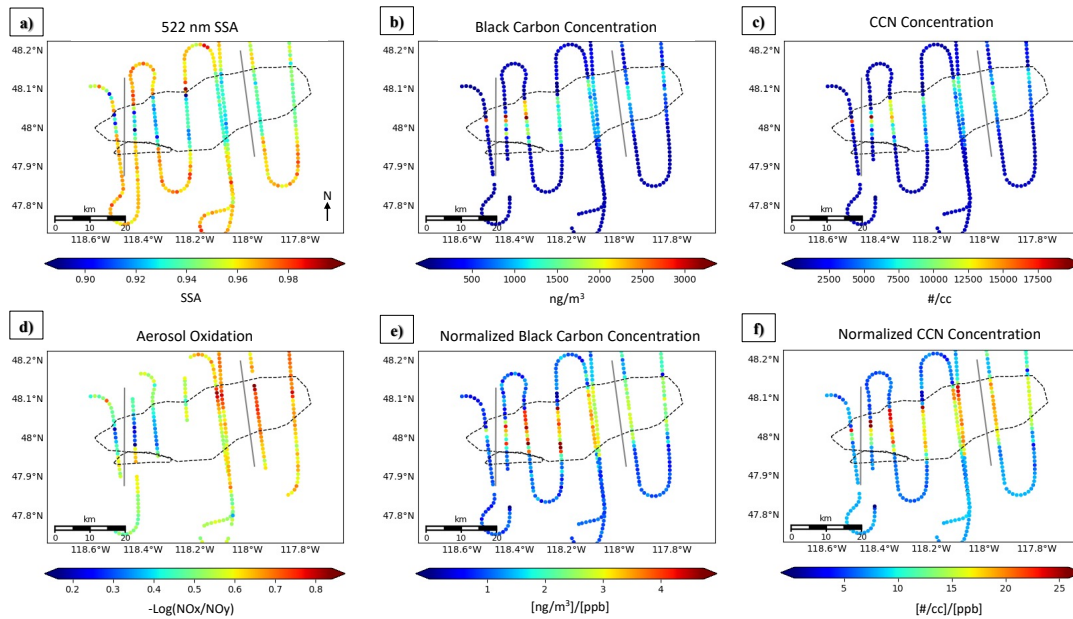


Figure 4.7. FIREX aircraft observations of the Williams Flats Fire on 06 August 2019: (a) 530 nm SSA (PSAP/neph), (b) aerosol oxidation (derived from ozone-induced chemiluminescence), (c) Mass concentration of rBC (SP2), (d) rBC concentration normalized by CO (SP2, DACOM), (e) concentration of particles that can act as CCN at 0.34% supersaturation (CCN-100), and (f) CCN concentration normalized by CO (CCN-100, DACOM). The grey lines represent the boundaries between regions defined in Figure 4.1.

The *in situ* observations provide some further constraints on particle properties that cannot be directly measured by satellite observations, such as oxidation state and particle hygroscopicity. The plume clearly becomes increasingly oxidized with downwind distance (Figure 4.7b); however, it does not exhibit significant increases in particle hygroscopicity except in Region II, where the aircraft

also observed enhanced BrC light-absorption (Figure 4.7f, Table 4.2). Furthermore, the lidar ratio, which typically provides information on particle composition, steadily increases downwind (Figures B8, B9, and B11 in Appendix B), consistent with values observed for fresh smoke [Burton et al., 2012]. (Interpretation of the lidar ratio is ambiguous in this case; see Appendix B for further discussion of the lidar measurements.

4.2.4. Connecting Downwind Plume Changes between MISR and FIREX

The aircraft data generally support the observed trends in MISR REPS and REPA as well as the general MISR particle type retrievals, as discussed above. In this section, we explore in further detail the relationships between the FIREX observations and the satellite-inferred aging mechanisms introduced in Section 4.2.1.

Because smoke from the southeast hotspot was not sampled during Transect 1 (T1), and smoke from both hotspots converged downwind, there are key differences in the aircraft-observed particle properties between the first two transects that may be attributed to differences in near-source emissions. As seen in Table 4.2, this is supported by: (1) lower average oxidation in Transect 2 (T2), as the sampling location is nearer the southeast hotspot, providing generally fresher smoke; (2) dramatically larger aerosol and CCN number concentrations in T2, indicating higher rates of particle production from the southeast hotspot; (3) dramatically larger absolute and dilution-corrected BC mass concentration in T2, indicating differential BC emissions relative to CO emissions between the two hotspots (this is further supported by larger CO-normalized BC-only light-absorption as well as larger MCE); and (4) a particle size distribution in T2 that is both narrower in range and skewed towards

comparatively smaller particles compared to T1, as fresh smoke is usually smaller in size. These aircraft-derived differences in particle properties are also seen directly in the MISR retrievals by comparing Region IV results with Regions I-III. As such, the *in situ* measurements support the inferred Mechanism (4) presented in Section 4.2.1. As mentioned in the discussion of the satellite results, the southern plume region is on average dominated by particles that are overall smaller and more BLS-like than those retrieved in the northern plume, indicating that the differences in the dominant emitted particle types between the two hotspots exist at both times of observation (~ 2 h apart). The emission differences may be due to differences in the vegetation burning in each hotspot: MODIS IGBP land cover suggests the northwest hotspot is burning in areas with relatively larger fractions of evergreen forest, whereas fuel in the southeast hotspot is mostly savanna and grassland. Finer grass-like fuels tend to produce larger fractions of BC particles than fuels with coarser materials such as wood found in forest. However, the difference in particle type may also be due to differences in elevation between the two hotspots, as fires burning uphill (in this case, the southern plume) tend to burn more quickly. Therefore, smoke in the southern plume may be fresher on average than smoke in the northern plume, resulting in higher fractions of BC. Lastly, wind speeds in the southern plume are somewhat faster, at least at the time of MISR observation (on average 4.26 ± 1.66 m/s vs. 3.88 ± 1.96 m/s; Figure B1 in Appendix B), further suggesting that the southeast plume smoke may be fresher. In the case of FIREX, there continues to be generally high BC mass for the first three transects, indicative of the increased level of mixing between

the northern and southern components. This mixing blurs the division between “near-source” and “mid-plume” regions as defined in the MISR plume.

In Region II, particle size steadily increases from T3 onward, supporting the observed trends in particle size observed by MISR. The increased oxidation levels in T3 and subsequent transects suggest that the increase in aerosol size may be due to the condensation of VOCs onto particle surfaces as plume aging progresses. Coagulation may also play a role, at least in T3, where the increase in particle size is accompanied by a decrease in the normalized aerosol concentration compared to T2. This could be attributed to ultrafine particles below the detection limit of the LAS and SP2 ($\sim 0.09 \mu\text{m}$) aggregating to form larger particles or coagulating onto existing ones, although this is not directly testable with available data. It is possible that a combination of coagulation and VOC condensation is occurring. The trends in particle size and oxidation here support inferred Mechanism (1) in Section 4.2.1.

The FIREX- and MISR-observed trends in particle size diverge in Region III, with *in situ* observations suggesting continued increases in size, whereas the satellite suggests particle size begins to decrease here. As mentioned above, this may be explained by the differences in vertical sampling, as the aircraft measures at a single altitude, whereas MISR observes the entire column. Column aerosol loading is dominated by the smoke plume in this case, but the plume is at least 0.75 km thick (Figure 4.2b); thus, aircraft measurements at a single elevation might not be representative if particles are size-sorted in the vertical. In Region II, the “large” aerosols observed by MISR may have preferentially settled below the altitude of aircraft sampling, and then proceeded to settle out of the column entirely in Region

III, deposited onto the surface at approximately 40 km downwind, where the plume extent reaches the surface (Figure 4.2b). This would explain both the differences in satellite and *in situ* size observations, as well as the along-plume changes in particle size observed by MISR. As such, we conclude that gravitational settling of larger particles may play a role downwind of the source, as suggested by Mechanism (2) in Section 4.2.1.

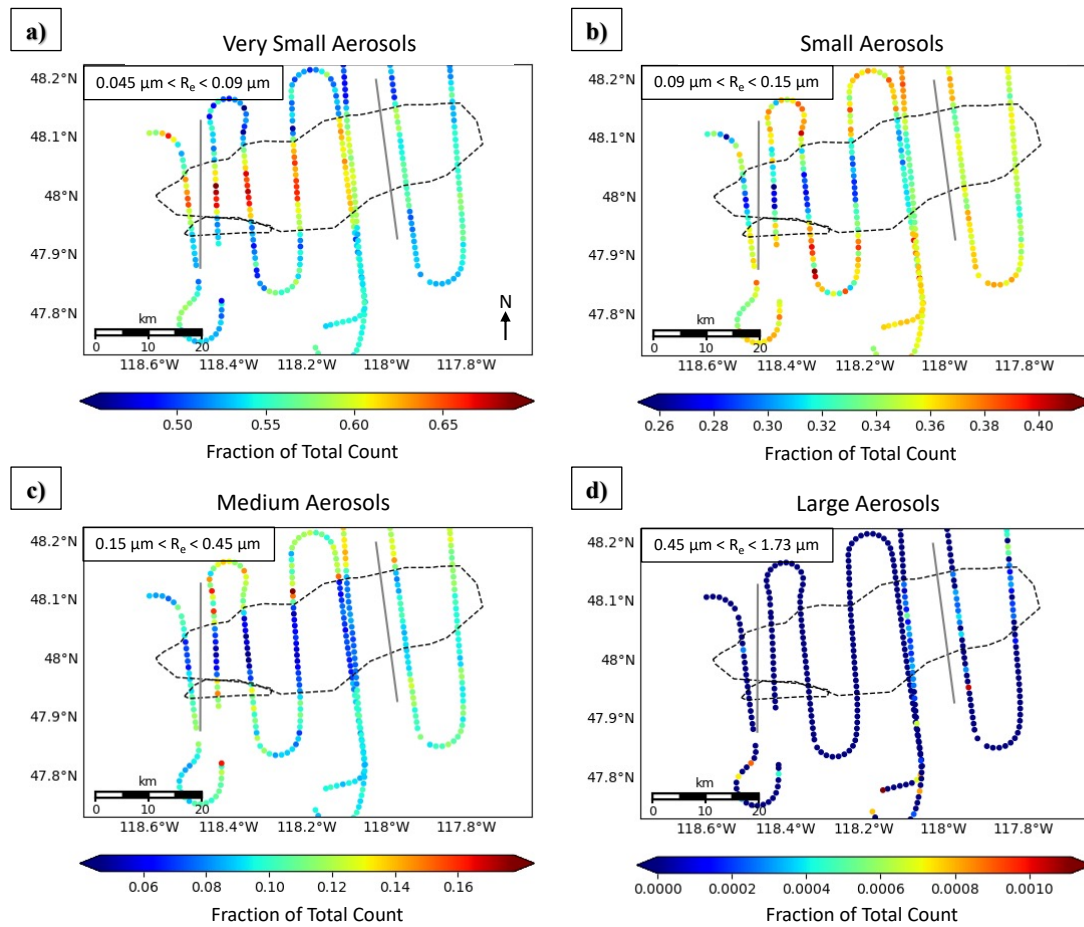


Figure 4.8. Fractional contributions (from zero to one) to the total aerosol count for very small (**a**), small (**b**), medium (**c**), and large (**d**) aerosols in the Williams Flats Fire, as measured by the LAS *in situ* instrument on 06 August 2019. The grey lines represent the boundaries between regions defined in Figure 4.1. Note: Approximate size ranges are given in the corner each plot, and the scales differ between categories.

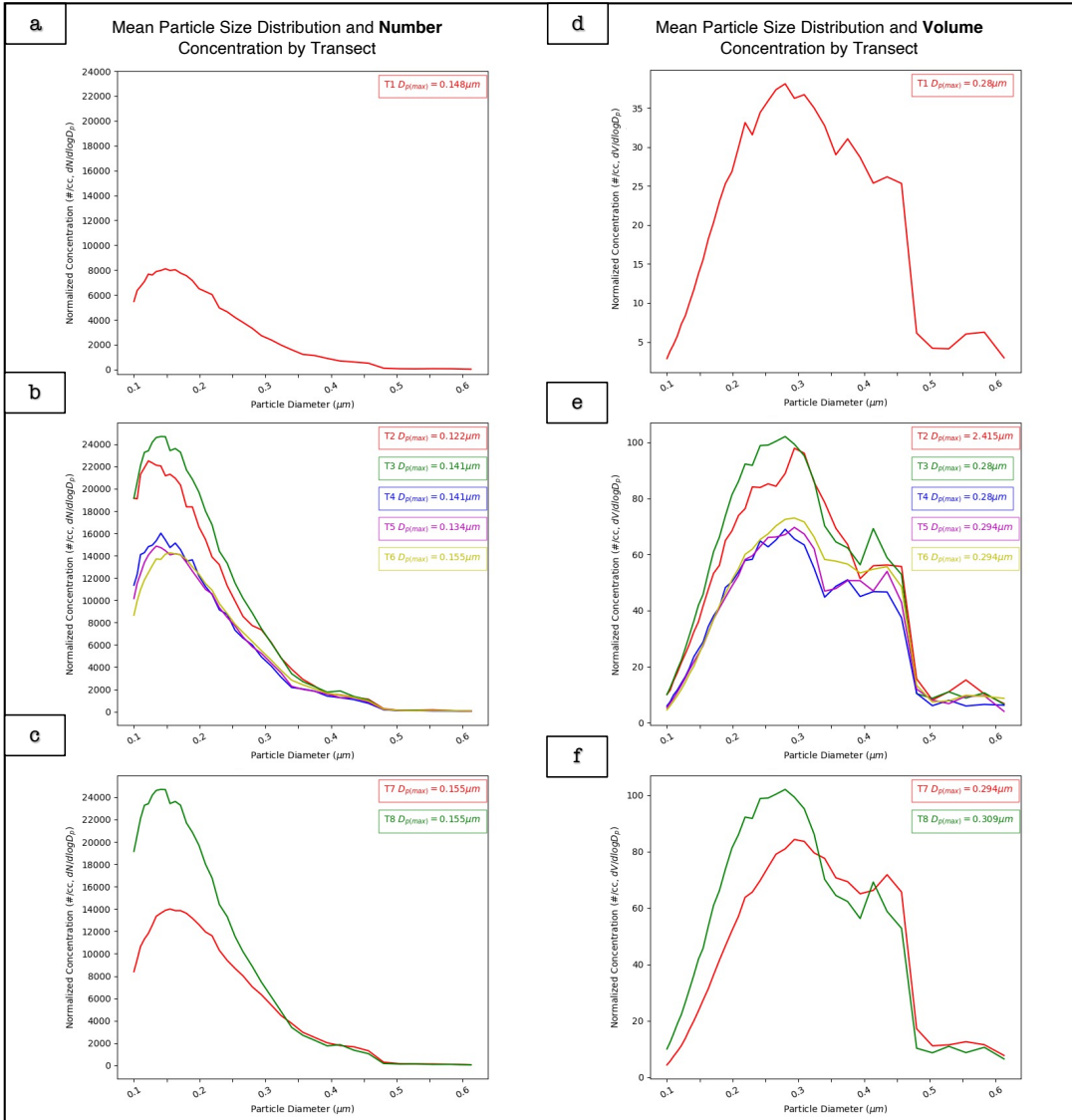


Figure 4.9. Mean particle number (**a–c**) and volume (**d–f**) concentrations and size distributions for each transect observed by the FIREX aircraft (from the LAS instrument), where (**a**) includes transect 1 and samples the downwind end of Region I, (**b**) includes transects 2 through 6, corresponding to Region II, and (**c**) contains transects 7 and 8 that observed Region III. The mode aerosol diameter for each transect is provided as well, where box and text color are matched with the corresponding transect color.

Both MISR and FIREX suggest decreasing particle light-absorption and a loss of BIS/BC particles with smoke age. The variations in SSA over the aircraft transects, on the order of ± 0.005 , are probably within the range of measurement uncertainty. However, SSA appears to systematically decrease by region on average, with the

exception of T2 and T3, which are more similar to T1 than the other Region II transects (possibly due to the injection of fresh BC particles at these points from the southeast hotspot). Furthermore, the spectral dependence of PAS measurements suggests that light-absorption due to BC (i.e., the absorption measured at 664 nm) systematically decreases throughout Regions II and III; the SP2-measured BC mass concentration similarly decreases. The steadily increasing level of oxidation observed *in situ* corresponds with these changes, supporting the inferred Mechanism (3) in Section 4.2.1.

4.3. An Improved Understanding of MISR Capabilities

Although an independent study, the investigation described here builds directly upon that described in Chapter 3. In both cases where near-coincident data were acquired, MISR particle properties reflect the systematic oxidation of particles with downwind distance, transitioning from highly light-absorbing particles near the source to non-absorbing particles downwind. In addition, in both studies, trends in retrieved particle size can be linked, to a significant degree, to the relative influences of condensational growth, particle coagulation, secondary particle formation, and size-selective gravitational settling. In the study in Chapter 3, decreasing particle size was correlated with the formation of new organic (brown carbon) aerosols as well as a possible loss of larger-size particles from the column, whereas increasing size was attributed to a combination of hydration, condensation, and aggregation. In the current study, decreasing particle size is similarly connected to the preferential settling of large particles, but significant new particle formation was not observed. Instead, the injection of fresh, very small particles from a different source (the

southern plume) drove decreasing particle size slightly downwind. The ability to distinguish particle properties between two adjacent sources and observe how the emissions interact downwind is a unique contribution demonstrated for the first time in the current study. Furthermore, linking these differences to observed variations in fuel characteristics and topography increases confidence in our interpretation of differences in MISR-retrieved smoke particle properties. In the same vein, the presence of non-spherical particles in the Williams Flats plume was at least somewhat confirmed by lidar data that was unavailable for the study in Chapter 3. Further, the lidar validated the plume heights retrieved by MISR, and documented the changes between the MISR overpass and subsequent aircraft sampling.

4.4. Summary

This chapter describes the second validation study of the MISR particle property retrievals, this time using near-coincident FIREX-AQ observations of the Williams Flats fire on 06 August 2013. MISR observes distinct differences in particle size and light-absorption properties in different regions of the plume produced by this fire. Overall, the satellite-retrieved particle properties indicate that it contained fine, highly absorbing, BIS-like aerosols near the source, whereas downwind, the plume tends to show a systematically increasing amount and fraction of weakly absorbing, less BIS-like aerosols. Furthermore, MISR suggests particles increase in size between ~30 and 140 min of aging, but decrease in size for smoke older than about 140 min. These observations are relatively well supported by the *in situ* observations, with minor disparities that fall within measurement uncertainty and/or sampling differences.

Due to the comprehensive coverage, the MISR observations provide greater context for the particle properties observed *in situ*; this additional information allows us to paint a more complete picture of plume mechanics and particle aging. Specifically, from MISR-retrieved plume height, REPS, REPA, and SSA spectral dependence, we infer (1) VOC condensation and possibly coagulation occur between ~30 and 140 min of aging (Region II of Figure 1), (2) gravitational settling and/or dilution alter vertically resolved particle size as the smoke ages beyond about 140 min (Region III), (3) particles on average become progressively more oxidized downwind along the entire plume, and (4) the southeast hotspot (Region IV) generates more smoke, a larger fraction of BIS, and generally smaller particles than the northwest hotspot. The FIREX-AQ *in situ* observations also largely support these inferences, as summarized above.

This study expands upon the validation work conducted in Chapter 3. As near-coincident MISR and field observations of smoke plumes are rare, taking advantage of all such opportunities is crucial to understanding the range of MISR's capabilities. To this end, we introduce a suite of new aircraft data and modeling, which further test our interpretation of the relationships between fire chemistry/dynamics and the particle properties observed from space. The results build upon the previous study, demonstrating reproducibility and bolstering our confidence in RA performance. As in Chapter 3, MISR tends to observe somewhat higher contributions from relatively larger size categories compared to the aircraft data, and in both validation studies, these larger particles appear to experience size-selective gravitational settling

downwind. Both studies also suggest that coagulation and condensation affect REPS, and oxidation plays a large role in particle REPA.

Chapter 5: Canadian and Alaskan Wildfire Smoke Particle Properties, Their Evolution, and Controlling Factors, Using Space-Based Observations

5.1. Introduction

In our previous studies, we demonstrated the efficacy of using MISR-based techniques to qualitatively describe plume particle characteristics, using near-coincident *in situ* data from aircraft-based field campaigns to validate the MISR retrievals [Junghenn Noyes et al., 2020a, 2020b]. These experiments demonstrated the strengths and limitations of MISR's ability to: 1) constrain particle size, shape, and light-absorption properties, and to do so at finer spatial scales and in greater detail than other currently orbiting satellite instruments, 2) map the entire plume, providing context for field observations that are usually only able to observe a disjointed, small percentage of the plume area, and 3) narrow down the likely suite of aging mechanisms acting upon the plume at various downwind distances, which were supported by near-coincident *in situ* data.

In the latest installment of the current research effort, we apply these MISR-based techniques to a wide statistical sampling of wildfire plumes over a region where the smoke plume characteristics are not well-constrained by field observations. Specifically, we compare the MISR plume height and particle property retrievals with land cover type and fire radiative power (FRP) from the MODIS satellite instrument,

the height of the planetary boundary layer (PBL) from MERRA-2 reanalysis modeling, and the drought index from the North American Drought Monitor. Trends in particle properties are also studied in the context of smoke age estimates derived from MINX wind vectors. We use the knowledge gained from Chapters 3 and 4 about the relationships between particle chemistry/microphysics and our interpretation of the top-of-atmosphere (TOA) optical signatures obtained by MISR to create a regional inventory of particle type (black smoke vs. brown smoke vs. soil/dust vs. non-light-absorbing particles), inferred trends in particle evolution (e.g., oxidation, size-selective dilution, hydration/condensation, etc.), and the modulating forces behind these, such as meteorology, land cover type, and fire intensity. The scope of this study covers wildfires in Canada and Alaska between 2016 and 2019, and represents the first regional study of an ongoing effort to characterize wildfire particles across the globe.

Data and analysis methods are described in Section 5.2. Section 5.3 presents analysis and discussion of our results . A summary is provided in Section 5.4.

5.2. Methodology

5.2.1. Experiment Setting and Case Selection

Suitable fires within the ~380 km MISR swath were identified from imagery and thermal anomalies in coincident MODIS/Terra data. The MODerate resolution Imaging Spectroradiometer (MODIS) instrument has a cross-track swath width of 2330 km that provides global coverage every 1 to 2 days. Well-defined plumes of sufficient optical thickness, having a clear source and minimal cloud contamination, were favored for analysis. A total of 663 plumes, burning between 01 May and 30

September, and spanning the four years of this study (2016-2019), were analyzed. Table 5.1 quantifies the relative distribution of the observed plumes across year, month, regional location, and land cover type (the latter is discussed more in Sect. 5.2.2). In a small number of cases, fires in the United States were included in the study if they were part of a larger complex that burned mostly within Canada, and are classified here as belonging to the nearest Canadian province.

As Terra crosses the equator at ~10:30 AM local time, the fires considered in this study are restricted to late-morning burns. Although burning usually peaks in the late afternoon, MISR observes a significant number of large, intense plumes, as has been shown in multiple studies previously (e.g., Val Martin et al. [2010]; Gonzalez-Alonso et al. [2019]) and with the success of the MISR Plume Height Project [Nelson et al.; <https://misr.jpl.nasa.gov/getData/accessData/MisrMinxPlumes2/>].

5.2.2. MODIS Fire Radiative Power and Land Cover Type

The MODIS/Terra Thermal Anomalies and Fire MOD14 product was used to identify fire pixel location and the 5-minute FRP values at the time of MISR observation [Giglio and Justice, 2015]. Each plume was assigned a mutually exclusive set of hotspots based first on which ones fell inside the user-defined MINX boundary, and secondly by proximity to the boundary based on MODIS/Terra RGB imagery from NASA Worldview. Pixels identified with 0% confidence in the FRP product were ignored, except in cases where a plume did not contain any fire pixels with higher confidence as these at least provide the locations of the burn and therefore land cover type (described below). In all but one plume, at least one fire pixel was detected. The MOD14 product has a spatial resolution of 1 km, and reports FRP

based on a detection algorithm that evaluates differences in the hotspot vs. background brightness temperature using the 4 μm and 11 μm channels [Giglio et al., 2003]. FRP is often used as a qualitative indicator of fire intensity; however, MODIS may underestimate FRP values under cloud or dense-smoke conditions, when the active fire only partly fills the MODIS pixel, as well as for plumes in the smoldering phase that can exhibit lower radiant emissivity and therefore lower FRP values [Kahn et al., 2007].

We systematically associated the fire pixels with annual 0.5-km land cover type data from the MCD12Q1 product [Friedl and Sulla-Menashe, 2019], which includes data from the MODIS instruments on both the Terra and Aqua satellites. We used this information to classify the type(s) of vegetation burning in each hotspot using: a) the International Geosphere-Biosphere Programme (IGBP) classification, which generally categorizes vegetation types based on canopy height, percent cover, woody vs. herbaceous, and evergreen vs. deciduous; and b) the FAO-Land Cover Classification System (LCCS) surface hydrology layer classification, which provides less specific information but contains several additional categories compared to IGBP. It is important to note that the MODIS land cover type products do not provide sufficient detail for determining the actual *fuel* type consumed by fires, which is a product of a variety of other factors (e.g. meteorology, pre-existing burned area, seasonality, etc.). However, land cover and fuel type are largely related and we can use the MODIS product to make educated inferences as to the types of fuels that are present. (Future work will involve the use of more detailed fuel type information, as will be discussed in Chapter 6).

Descriptions of the IGBP land cover types identified in this study are included in Table 5.2, and descriptions of all land cover types from both products can be found in Tables C1 and C2 in Appendix C. As the MCD12Q1 spatial resolution is finer than that of MOD14, some hotspots covered multiple land cover types, in which case we assigned land type as a split between the two that comprise the largest fractions of the fire pixel.

5.2.3. MERRA-2 Reanalysis

For each plume, we obtain the estimated height of the planetary boundary layer (PBLH) from the Modern Era Retrospective-analysis for Research and Applications (MERRA-2) reanalysis model [Bosilovich et al., 2016; Gelaro et al., 2017]. We use data provided at a 0.625° longitude by 0.5° latitude spatial resolution, and hourly temporal resolution, so we choose the data point closest to the time and location of each fire plume origin.

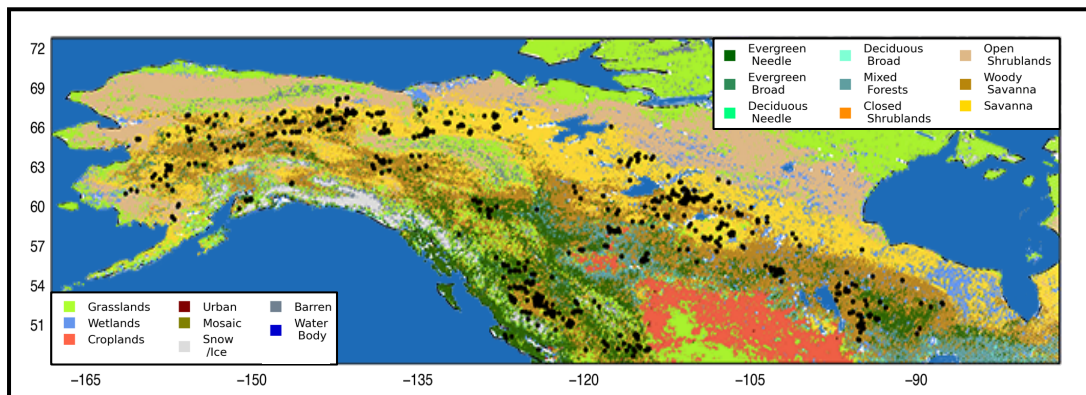


Figure 5.1. Map of all plumes used in this study (black dots) overlayed on the 2017 MODIS IGBP land cover types.

Table 5.1. Distributions of plume number, plume height, boundary layer height, location of burn, and dominant MODIS fuel type shown in three different ways: A) annually, B) monthly, and C) by fuel type. Note that an individual fire may burn in several biomes, so plumes in Table 1C are not in mutually exclusive categories. AGL— above ground level; PBL—planetary boundary layer. See footnotes for land type and region/territory abbreviations.

Table 5.1A. Plumes By Year					
	2016	2017	2018	2019	Total
No. Plumes	71	319	114	159	663
Median Plume Height (km) ¹	1.822	1.805	1.958	1.584	1.778
Max Plume Height (km) ²	2.648	2.581	2.766	2.635	2.627
No. / % > 2 km ³	28 / 39.44	121 / 37.93	51 / 44.74	37 / 23.27	237 / 35.75
No. / % Above PBL ⁴	24 / 33.80	68 / 21.32	17 / 14.91	34 / 21.38	143 / 21.57
Median PBL Height ⁵	2.082	2.096	2.431	1.936	2.079
Dominant Land Types Burned ⁶	W. Sav. Sav.	W. Sav. Sav.	W. Sav. Evergreen	W. Sav. Sav.	W. Sav. Sav.
Dominant Regions ⁷	Sask. (28%) AK (26%)	NWT (39%) BC (24%)	BC (70%) Yuk. (9%)	AK (47%) Alb. (25%)	BC (25%) NWT (21%)

Table 5.1B. Plumes By Month, Aggregated Over Four Years					
	May	June	July	August	Sept
No. Plumes	39	51	259	264	50
Median Plume Height (km) ¹	1.86	1.894	1.698	1.859	1.61
Max Plume Height (km) ²	2.746	3.028	2.519	2.601	2.906
No. / % > 2 km ³	12 / 30.77	22 / 43.14	79 / 30.50	110 / 41.67	14 / 28.00
No. / % Above PBL ⁴	17 / 43.59	18 / 35.29	51 / 19.69	51 / 19.32	6 / 12.00
Median PBL Height ⁵	1.908	2.045	2.018	2.305	1.795
Median Plume FRP (W/m ²) ⁸	54.13	49.09	46.39	49.38	37.97
Dominant Land Types Burned ⁶	W. Sav M.F.	W. Sav. Sav.	Sav. W. Sav.	W. Sav. Sav.	W. Sav. Evergreen
Dominant Regions ⁷	Alb. (54%) Ont. (21%)	AK (47%) Yuk. (14%)	AK (34%) NWT (22%)	BC (48%) NWT (31%)	Sask. (42%) BC (36%)

Table 5.1C. Plumes By Land Type, Aggregated Over Four Years

	<i>Evergreen</i>	<i>Mixed Forests</i>	<i>Deciduous</i>	<i>Woody Savanna</i>
No. Plumes	205	39	3	459
Median Plume Height (km) ¹	1.991	1.786	0.9376	1.841
Max Plume Height (km) ²	2.976	2.607	2.06	2.735
No. / % > 2 km ³	97 / 47.32	10 / 25.64	0 / 0	183 / 39.87
No. / % Above PBL ⁴	42 / 20.49	8 / 20.51	0 / 0	98 / 21.35
	<i>Savanna</i>	<i>Grassland</i>	<i>Shrubland</i>	<i>Wetlands</i>
No. Plumes	312	80	62	2
Median Plume Height (km) ¹	1.708	2.332	1.594	1.91
Max Plume Height (km) ²	2.572	3.416	2.478	2.452
No. / % > 2 km ³	99 / 31.73	52 / 65	17 / 27.42	1 / 50
No. / % Above PBL ⁴	82 / 26.28	20 / 25	13 / 20.97	1 / 50

¹ MINX-derived median plume heights AGL, averaged across the given category

² MINX-derived maximum plume heights AGL, averaged across the given category

³ Median plume height must be > 2.0 km AGL

⁴ Median plume height AGL must be > PBL height + 100 m

⁵ From MERRA-2 reanalysis data

⁶ M.F. = Mixed Forests; Sav. = Savannas, W. Sav. = Woody Savannas

⁷ AK = Alaska; Alb. = Alberta; BC = British Columbia; NWT = Northwest Territories; Ont. = Ontario; Sask. = Saskatchewan

⁸ The median plume MODIS fire radiative power, averaged across the given category

5.2.4. North American Drought Monitor

To evaluate the potential impacts of drought on smoke plume heights and particle properties, we leverage information on drought severity from the Canadian Drought Monitor (CDM) for plumes in Canada, and the United States Drought Monitor (USDM) for plumes in Alaska or just south of the US-Canada border. Both the CDM and USDM are part of the North American Drought Monitor (NADM) effort, a cooperative project between Canada, the United States, and Mexico that works to continually monitor drought extent and severity [Lawrimore et al., 2002] based on the methodology of the USDM [Svoboda et al., 2002]. This system uses a

blend of drought indicators such as the Normalized Vegetation Index (NDVI), streamflow values, the Palmer Drought Index, and others used by the agriculture, forest, and water management sectors [Agriculture and Agri-food Canada]. The synthesis of these reports is analyzed by federal, state, and local academic scientists until a consensus is reached on the best representation of current drought conditions. Assessing drought in this blended manner may be preferable to using just one indicator, as different drought indices measure drought in different ways and no single index works under all circumstances [Heim, 2002]. The NADM index is based on a convergence of evidence from a wide variety of objective inputs and subjective adjustments based on local impacts.

The NADM Drought classes range from D0 to D4, with D1 to D4 indicating moderate to exceptional drought and D0 representing abnormally dry conditions. The D0 class is not technically a drought classification, but might indicate if an area is vulnerable to or recovering from drought. Areas without an assigned drought class are considered to experience normal or wetter-than-normal conditions. The drought categories are based on the percent chance of those conditions occurring over a 100-year period, classified as follows:

- D0 (Abnormally Dry) – represents an event that occurs once every 3-5 years
- D1 (Moderate Drought) – represents an event that occurs every 5-10 years
- D2 (Severe Drought) – represents an event that occurs every 10-20 years
- D3 (Extreme Drought) – represents an event that occurs every 20-25 years

- D4 (Exceptional Drought) – represents an event that occurs every 50 years
[Agriculture and Agri-food Canada]

The USDM is a collaborative effort between the National Drought Mitigation Center (NDMC), the U.S. Department of Agriculture (USDA), and the National Oceanic and Atmospheric Administration (NOAA). It reports the state of drought on a weekly basis, and can be accessed at <https://droughtmonitor.unl.edu/>. The CDM is developed by the Department of Agriculture and Agri-food's (AAFC) National Agroclimate Information Service (NAIS) and reports on a monthly basis. The data can be accessed at <https://open.canada.ca/data/en/dataset/292646cd-619f-4200-afb1-8b2c52f984a2>.

Table 5.2. Definitions of the land cover types detected in this study, from the MODIS International Geosphere-Biosphere Programme (IGBP) classification method

Name	Description
Evergreen Needleleaf Forests	Dominated by evergreen conifer trees (canopy >2m). Tree cover >60%.
Evergreen Broadleaf Forests	Dominated by evergreen broadleaf and palmate trees (canopy >2m). Tree cover >60%.
Deciduous Needleleaf Forests	Dominated by deciduous needleleaf (larch) trees (canopy >2m). Tree cover >60%.
Deciduous Broadleaf Forests	Dominated by deciduous broadleaf trees (canopy >2m). Tree cover >60%.
Mixed Forests	Dominated by neither deciduous nor evergreen (40-60% of each) tree type (canopy >2m). Tree cover >60%.
Closed Shrublands	Dominated by woody perennials (1-2m height) >60% cover.
Open Shrublands	Dominated by woody perennials (1-2m height) 10-60% cover.
Woody Savannas	Tree cover 30-60% (canopy >2m).
Savannas	Tree cover 10-30% (canopy >2m).
Grasslands	Dominated by herbaceous annuals (<2m).
Permanent Wetlands	Permanently inundated lands with 30-60% water cover and >10% vegetated cover.

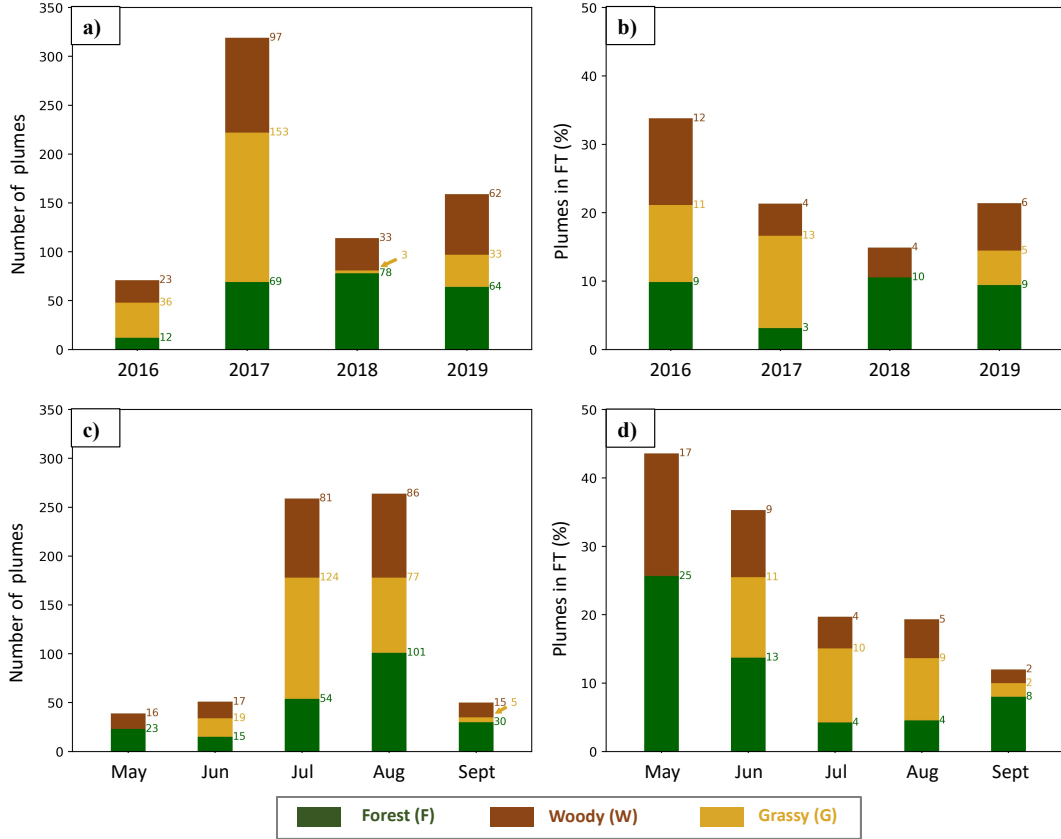


Figure 5.2. Seasonal and inter-annual variability of plume number (a, c) and percent of these in the free troposphere (FT) (b, d). Each bar is divided up by color according to the relative contribution from each of the three fire types in the given month or year, with quantitative annotations. For example, 39 plumes were identified in May, 16 of which were W fires and 23 of which were F fires (panel c). Of the 39 fires that month, 42% were in the FT (17% that were classified at W fires, and 25% that were classified as F fires) (panel d). A plume is considered to be in the FT if its median height is 100 m greater than the PBL height as defined in the MERRA-2 dataset.

5.3. *Results and Discussion*

Figure 5.1 maps the plumes used this study over Canada and Alaska, superposed on the 2017 MODIS IGBP land cover types. Table 5.1 shows how these plume observations are distributed by year, month, and land cover. The largest number of plumes in our study set was recorded in 2017 (48% of the total), whereas the smallest number was recorded in 2016 (11%). Plumes were observed mostly in British Columbia, the Northwest Territories, and Alaska, although a significant

number were located in other provinces and territories. (No plumes were included from Nunavut or east of Ontario.) Most plumes were observed in July and August (79%), at the peak burning season, and during abnormally dry or drought conditions (65%). Woody savanna (30-60% tree cover, canopy >2m) was the most common land cover type, followed closely by savanna (tree cover 10-30%, canopy >2m) and evergreen forest (tree cover >60%, canopy >2m, dominated by evergreen conifer, broadleaf, or palmate trees). A smaller, but still significant, number of plumes were from fires that at least partially burned in grassland (dominated by herbaceous annuals <2m tall), mixed forest (tree cover >60%, canopy >2m, comprised of 40-60% each of deciduous and evergreen trees), and open shrubland (10-60% cover, dominated by woody perennials 1-2m tall). Table 5.2 provides full definitions for all land types detected in this study.

We combine the MODIS land cover types into three broad categories to classify the observed fires: 1) “Forest” fires (denoted with an “F” where appropriate), which contain any number of MODIS hotspots located in evergreen, deciduous, or mixed forests; 2) “Woody” fires (W), which do not burn in forest but have at least 30% of their hotspots located in woody savanna and up to 70% located in savanna, grassland, or shrubland; and 3) “Grassy” fires (G), in which there are also no forest hotspots, but at least 70% are located in savannas, grasslands, or shrublands, and no more than 30% are located in woody savanna. This method of categorization roughly reflects the range of possible fuel sizes seen in most classification models (e.g., Ottmar et al. [2001]; Scott and Burgan [2005]). Forest plumes are the most likely to contain coarse, woody fuels that tend to maintain their moisture over longer periods

Table 5.3. Statistical summary of main smoke plume parameters for each fire category. FT—free troposphere; FRP —fire radiative power; AOD—aerosol optical depth; ANG—Ångström exponent; SSA—single scattering albedo; BlS—black smoke; BrS—brown smoke

	Forest Fires (F)	Woody Fires (W)	Grassy Fires (G)
Median Height (km)	mean: 1.9516 $\pm\sigma$: ± 0.7516	mean: 1.7539 $\pm\sigma$: ± 0.6604	mean: 1.6348 $\pm\sigma$: ± 0.5920
Max Height (km)	mean: 2.9272 $\pm\sigma$: ± 1.502	mean: 2.5756 $\pm\sigma$: ± 1.154	mean: 2.3962 $\pm\sigma$: ± 0.8877
Plumes in FT (%)	19.730	18.604	26.222
Median Plume MODIS FRP (W/m ²)	mean: 40.533 $\pm\sigma$: ± 33.939	mean: 55.190 $\pm\sigma$: ± 59.818	mean: 43.939 $\pm\sigma$: ± 43.384
	min: 6.0	min: 4.5	min: 0.0
	max: 229.6	max: 367.0	max: 306.5
Cumulative Plume MODIS FRP (W/m ²)	mean: 1575.5 $\pm\sigma$: ± 4115.4	mean: 829.86 $\pm\sigma$: ± 1805.1	mean: 682.67 $\pm\sigma$: ± 1295.1
	min: 6	min: 4.5	min: 0
	max: 40254.6	max: 20070.4	max: 11990.7
MISR AOD (558 nm)	mean: 1.5448 $\pm\sigma$: ± 1.0252	mean: 1.45077 $\pm\sigma$: ± 1.0393	mean: 1.1477 $\pm\sigma$: ± 0.78778
	min: 0.2012	min: 0.22397	min: 0.17805
	max: 6.449	max: 6.2703	max: 5.6979
MISR ANG (558 nm)	mean: 1.65 $\pm\sigma$: ± 0.278	mean: 1.70 $\pm\sigma$: ± 0.252	mean: 1.75 $\pm\sigma$: ± 0.243
	min: 0.912	min: 0.983	min: 0.746
	max: 2.40	max: 2.64	max: 2.20
MISR SSA (558 nm)	mean: 0.914 $\pm\sigma$: ± 0.0322	mean: 0.909 $\pm\sigma$: ± 0.0295	mean: 0.905 $\pm\sigma$: ± 0.0324
	min: 0.799	min: 0.812	min: 0.799
	max: 0.987	max: 0.984	max: 0.986
MISR BlS Fraction (% Total AOD)	mean: 44.4 $\pm\sigma$: ± 21.3	mean: 50.3 $\pm\sigma$: ± 20.6	mean: 53.7 $\pm\sigma$: ± 21.0
	min: 0.0	min: 0.0	min: 0.0
	max: 100	max: 96.2	max: 100
MISR BrS Fraction (% Total AOD)	mean: 7.05 $\pm\sigma$: ± 10.7	mean: 6.39 $\pm\sigma$: ± 12.3	mean: 4.71 $\pm\sigma$: ± 8.67
	min: 0	min: 0	min: 0
	max: 48.2	max: 73.9	max: 6.24
MISR BlS Ratio (%, BlS:BlS+BrS)	mean: 85.6 $\pm\sigma$: ± 21.1	mean: 88.1 $\pm\sigma$: ± 20.20	mean: 91.0 $\pm\sigma$: ± 16.3
	min: 0	min: 0	min: 0
	max: 100	max: 100	max: 100
MISR Nonabsorbing Fraction (% Total AOD)	mean: 34.6 $\pm\sigma$: ± 19.0	mean: 31.8 $\pm\sigma$: ± 17.2	mean: 29.2 $\pm\sigma$: ± 19.0
	min: 0.0	min: 0.0	min: 0.0
	max: 89.3	max: 80.9	max: 90.0
MISR Nonspherical Fraction (% Total AOD)	mean: 1.53 $\pm\sigma$: ± 4.86	mean: 0.949 $\pm\sigma$: ± 3.30	mean: 0.918 $\pm\sigma$: ± 3.38
	min: 0	min: 0	min: 0
	max: 40.0	max: 21.7	max: 9.4205
Number	223	215	225

of time and often tend to burn in the smoldering phase, whereas Grassy plumes are likely dominated by fine fuels that dry out quickly and burn mostly in the flaming phase [Ottmar, 2001; Urbanski, 2013]. The W plume category represent an intermediate step between these two.

There is important seasonal variability in the observed fire types, with G plumes comprising nearly half of all those observed in July, and almost none in the colder months of May and September (Figure 5.2c). In contrast, despite the overall lower plume numbers in these months, F plumes are highly dominant in May and September. This dichotomy can be traced to the latitudes of the burns – 87% of G plumes were observed in the Northwest Territories, Alaska, or the Yukon; all three are the northernmost areas of study and are dominated largely by grassy fuels (particularly savannas), whereas 64% of F plumes burned to the south in either British Columbia or Alberta, dominated by forests (Figure 5.1). The delay of peak fire season in the colder regions therefore prevents G plumes from contributing much to the plume count until later in the year.

Below we present our analysis of the significant trends in plume heights, particle properties, FRP, and atmospheric conditions, with a focus on the difference between the three fire types. Table 5.3 provides a statistical summary of some of the main smoke plume parameters for each fire type, which are explored in more detail in subsequent figures. Where appropriate, we perform independent t-tests to assess if differences in observations between fire types are statistically significant (p-value less than 0.05). We find that in most cases, the differences are significant at least between two out of three fire types. This suggests that, although some differences are distinct,

many patterns exist on a continuum and results are likely somewhat dependent on how we define our fire types. For example, plumes in the F category may actually contain only a small percentage of forest. Likewise, the IGBP categories have wide ranges of percent tree cover, and satellite data does not tell us the percent of woody/grass fuel actually consumed in the fire. This is why obtaining a large, statistical sampling is so important. Despite these caveats, many of the patterns we observe having to do with land type are consistent with current knowledge on fire properties, and the incorporation of additional datasets allow us to build upon this knowledge. The MISR-retrieved particle properties allow us to infer some of the driving forces behind particle emissions and particle evolution when put in the context of the land cover, FRP, drought level, and plume heights.

5.3.1. Overview of Smoke Plume Height Observations

Plume heights vary considerably across the dataset, ranging from less than 0.5 km to just above 4.0 km AGL. In general, however, median plume heights are centered ~1.7 km, and maximum heights ~2.6, with little seasonal variability except for a sharp drop in plume heights in September and somewhat lower heights in July. The lower heights in July are likely driven by changes in the relative distributions of F, W, and G, fires, which have statistically significant differences in their plume heights, on average (discussed more below), whereas the lower heights in September are likely partly driven at least in part by colder temperatures at this time of year, which are not as conducive to intense burning and vertical plume development. The relatively lower median plume FRP in September (38 W/m^2) supports interpretation (Table 5.1b).

There is a strong seasonal component to the percent of plumes injected into the free troposphere (FT); it steadily decreases from month to month as warming temperatures progressively increase PBL heights between May and August; this in turn contributes to making it increasingly less likely for plume heights to reach or exceed that of the bottom of the FT, although the strength of the temperature inversion at the top of the PBL may also play a role here. The median plume FRP is consistent across June, July, and August (Table 5.1b), which further suggests the progressive deepening of the PBL is the driving factor in this trend at least in the summer months. However, the higher FRP values in May suggest that the relatively high fraction of plumes injected above the PBL in this month may be driven by a combination of burning intensity and a low PBLH. Burning intensity may play an even larger role during the month of September which exhibits the lowest FRP values by far, and during which time the PBLH is at its lowest *and* we observe the smallest fraction of plumes enter the FT. Figure 5.2d illustrates the seasonal variability of plume count and FT injection for all three fire types.

5.3.2 Impact of Land Cover Type on Plume Heights

The highest-altitude plumes tend to be associated with the highest cumulative plume FRP values (i.e., the sum of all fire pixels in the plume, as opposed to the median value discussed in the previous section; Figure C1 in Appendix C), although there is considerable variability ($r^2=0.37$). This weak relationship is consistent with similar studies, including but not limited to Gonzalez-Alonso et al. [2019], and Val Martin et al. [2010, 2012]. Fires identified in forest (F) tend to have the highest median and max height retrievals compared to the other biomes, and have cumulative

plume FRP values that are essentially twice as high as other biomes ($p \leq 0.014$) (Table 5.3). (We observe $p \leq 0.047$ when comparing median heights between all types; differences in max heights between types were significant at $p \leq 0.006$ except when comparing W and G plumes to each other.) The fire pixel count for these plumes (i.e., estimated fire area) likely drives the latter, as the average number of hotspots in these fires also outnumbers those in the other biomes 2:1. In fact, *median* FRP for F fires is quite low – only 40 W/m² on average, whereas both W and G fires exhibit somewhat higher median FRP values (55 and 44 W/m² on average, respectively), with W fires showing the largest FRP values. The F fires we observed also never surpassed median FRP values of 230 40 W/m², whereas the W and G fires were observed to reach median FRP values of 367 and 307 40 W/m², respectively. This is also consistent with previous studies of forest fires, that show a key fuel component is at or below the surface, where roots systems allow fires to burn deeper into soil layers compared to biomes dominated by finer fuels, such as grass and savanna. The higher moisture content and lower oxygen availability in these layers are more conducive to the smoldering fire phase than the flaming one, which leads to higher smoke production (AOD) but lower radiant emissivity [Bertschi et al., 2003; Yokelson et al., 1997; Gonzalez-Alonso et al., 2019; van der Werf et al., 2010; Santoso et al., 2019]. Therefore, the comparatively lower average per-pixel FRP in F fires is consistent with a higher fraction of smoldering, and the higher FRP values in W and G fires are consistent with flaming conditions dominating. However, the differences in FRP between F and G fires were not found to be statistically significant with $p=0.35$, whereas the differences between W fires and F or G fires are significant

with $p \leq 0.025$. It is unclear why W fires may have the highest median FRP, as they should contain overall higher fractions of woody fuels compared to G plumes, and lower fractions compared to F plumes. This may be related to how the three fire types are defined, although it must be further investigated. Despite this, the idea that smoldering is favored in increasingly forested areas is supported by significantly higher MISR AOD in F plumes (~ 1.54) and W plumes (~ 1.45) compared G (~ 1.15) plumes ($p < 0.001$). (More on particle properties in Section 5.3.3.)

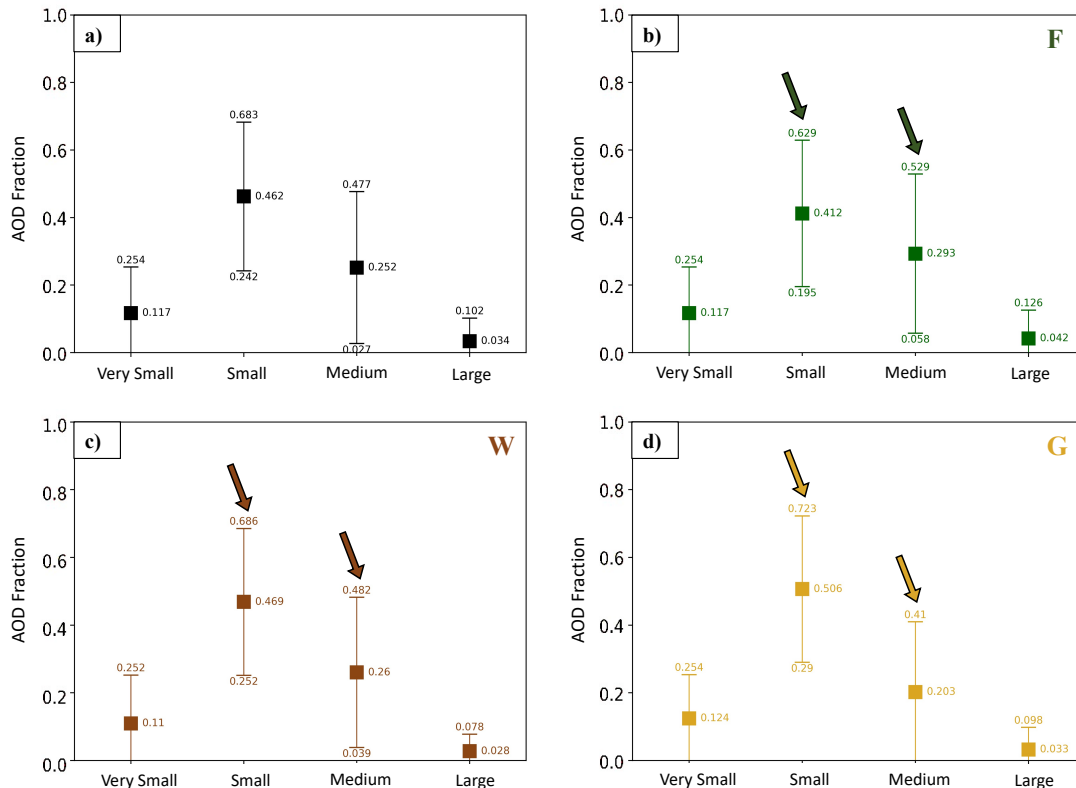


Figure 5.3. Particle size distributions in terms of each RA component's fractional contribution to the total AOD. All plume types are shown in (a), whereas panels (b-d) display color-coded results for individual plume types, denoted with the appropriate abbreviation in the right-hand corner. Points represent the mean values and whiskers show the standard deviations. Arrows highlight the differences in the partitioning between small and medium particle fractions for the different plume types.

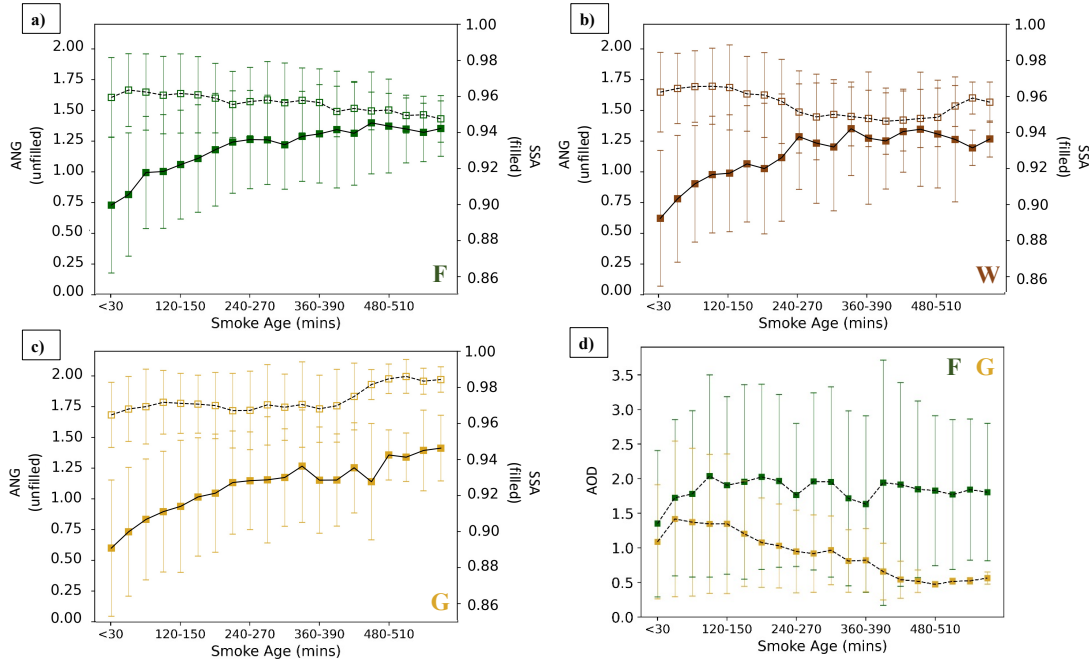


Figure 5.4. MISR mid-visible Ångström exponent (unfilled marker, dotted line) and single scattering albedo (filled marker, solid line) by smoke age for (a) Forest plumes, (b) Woody plumes, and (c) Grassy plumes. In (d), the MISR mid-visible AOD is plotted by age for Forest and Grassy plumes. The points represent the mean values, while the whiskers are standard deviations.

Despite having the lowest absolute heights AGL, G plumes are the most likely to be injected above the PBL, with 25% of these plumes having median heights greater than the PBLH + 100 meters (Table 5.3). (We add the 100-m margin of error to account for measurement uncertainty in the plume heights.) As stated previously, the vast majority of these plumes burned in relatively colder regions that tend to have lower PBL heights, and so fires in these areas that are large and intense enough for MISR detection are more likely to enter the free troposphere. However, the role of atmospheric stability at the top of the PBL in this regard should also be considered and warrants future investigation.

5.3.3. Overview of Smoke Particle Property Observations

The observed smoke plumes exhibit a wide range of MISR-retrieved light-absorption properties, with median plume mid-visible SSA ranging all the way from ~0.8 to 1.0, and fractional AOD of BlS and BrS ranging from 0 to 1 and 0 to ~0.75, respectively. Differences in plume REPA strongly drive the interpreted BlS content ($r^2 = -0.7$), whereas fractions of BrS are not correlated with retrieved light-absorption ($r^2 = -0.1$: Figure C2 in Appendix C). MISR-retrieved particle size is somewhat less variable than light-absorption, with all plumes but one exhibiting median ANG of at least 1.0 (fine-mode particles), and the highest plume ANG just below 2.7. Most plumes have retrieved ANG values of 1.5-2.0. To help interpret ANG, we analyze each of the four particle size bins defined in the RA climatology in terms of their fractional contribution to the total AOD. These are discussed in previous chapters and can be found in Table 2.1. However, to review, they are defined as follows:

- “Very small” particles: effective radius (r_e) $\sim 0.06 \mu\text{m}$
- “Small” particles: $r_e \sim 0.12 \mu\text{m}$
- “Medium” particles: $r_e \sim 0.26$
- “Large” particles: $r_e > 1.21 \mu\text{m}$

where large particles contain the non-spherical particle type as well as spherical types. The MISR REPS is a mixture of these size components, and so the retrieved ANG, which might be more representative of the actual particle size differences (i.e., relative, not absolute), might not strictly identify one of these specific sizes. The actual particle size distributions are constrained within bins by the retrievals, and so discussing size in terms of these bins is helpful. The algorithm climatology contains

these sizes because the sensitivity cluster analysis [Kahn et al., 2001] and subsequent validation studies showed that this is about the degree of size distinction possible under good but not necessarily ideal retrieval conditions. As expected, analysis of the size components in this study indicates small and medium particles are the dominant aerosol sizes in most smoke plumes regardless of fire type, on average constituting ~46% and ~25% of the median plume AOD, respectively. Very small particles make up ~11% of retrieved plume AOD, whereas large particles make up ~3% (Figure 5.3a). In most plumes, the fraction of non-spherical particles is low, constituting less than 5% of the total retrieved AOD in 93% of plumes.

5.3.4. Impact of Land Cover Type of Smoke Particle Properties

As stated in the plume height discussion, fires detected in forests (F) have the highest overall AOD values (1.54), whereas woody (W) and grassy (G) fires exhibit an average AOD of 1.45 and 1.15, respectively (Table 5.3). F plumes also have the highest fraction of non-spherical particles, with some plumes containing as much as 40% non-spherical particles, although on average these soil or dust analogs make up only ~1.5% of the total AOD and differences in this fraction between plume types were not found to be statistically significant. However, the higher relative contribution of non-spherical particles in F plumes would partially account for their overall lower ANG (1.65) compared to W (1.70) and G (1.75) plumes. These differences in REPS, although small, are significant with $p \leq 0.038$ in all three inter-biome comparisons. Figure 5.3 suggests the main driver of differences in particle size between plume types is the partitioning between small vs. medium particles, as the contribution from very small particles is nearly identical across fire type, and

differences in the fraction of large particles are only on the order of a few percent. In F plumes, the contribution from medium particles is highest (29%), although small particles still dominate (41%). In W plumes, these fractions transition to favor small particles significantly more (47%, $p < 0.05$). The greatest difference can be seen in G plumes, with nearly 51% of particles in the small category on average, and only a 20% contribution from medium particles. The extent to which these differences occur during emission vs. downwind aging are explored in Section 5.3.5.

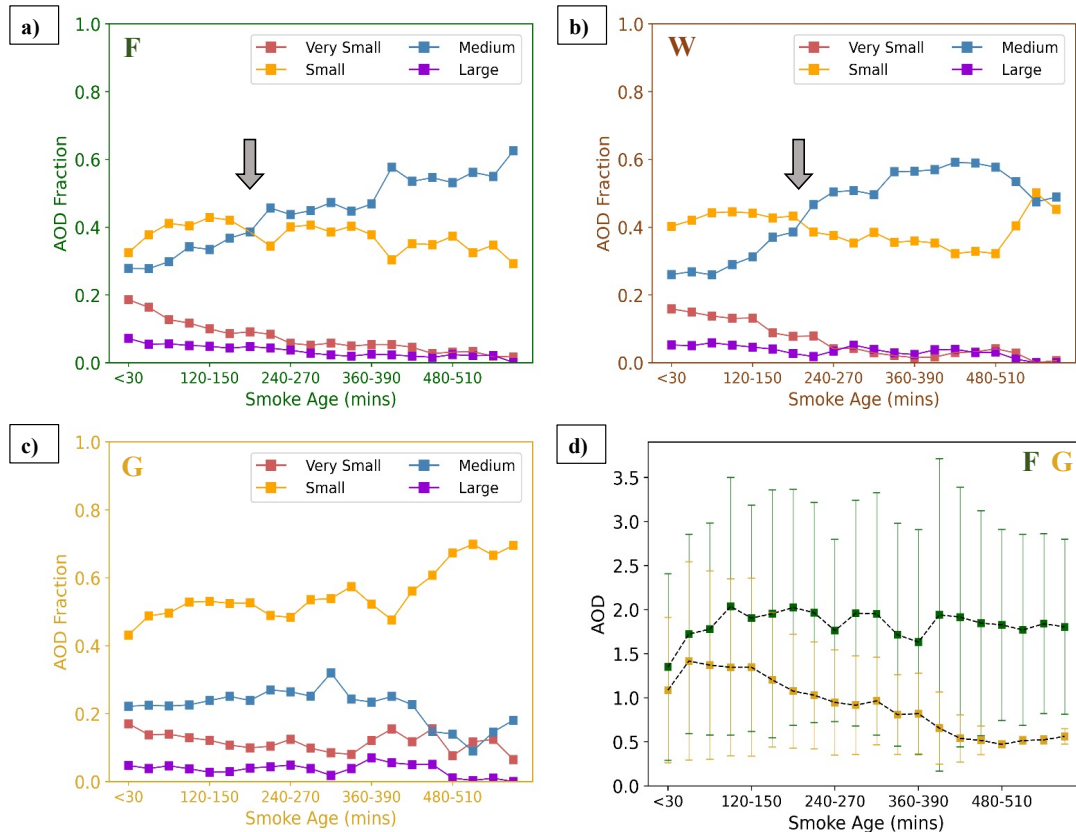


Figure 5.5. MISR particle-size component AOD fractions (in terms of contribution to the total AOD, from 0 to 1) by smoke age for (a) Forest plumes, (b) Woody plumes, and (c) Grassy plumes. In (d), the MISR mid-visible AOD is plotted by age for Forest and Grassy plumes, for reference. The points represent the mean values, while the whiskers are standard deviations. Arrows help highlight the point of important particle-size transitions.

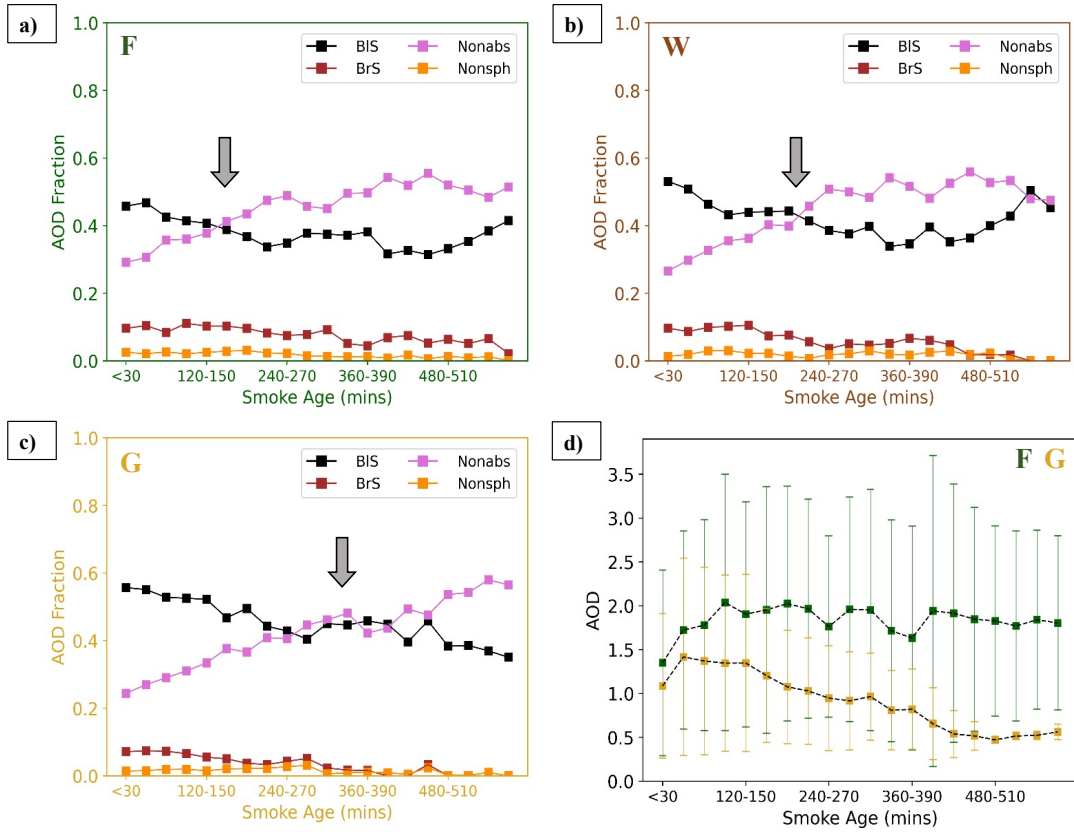


Figure 5.6. MISR particle-type component AOD fractions (in terms of contribution to the total AOD, from 0 to 1) by smoke age for (a) Forest plumes, (b) Woody plumes, and (c) Grassy plumes. In (d), the MISR mid-visible AOD is plotted by age for Forest and Grassy plumes, for reference. The points represent the mean values, while the whiskers are standard deviations. Arrows help highlight the point of important particle-size transitions.

Particles are significantly ($p=0.002$) less light absorbing in F fires (SSA ~ 0.914) compared to G fires (0.904), whereas W fires have SSA values between these two (0.909). All three fire types display a similar range of possible values (Table 5.3). Analysis of the individual contributions from moderately to strongly light-absorbing components (BIS and BrS), weakly absorbing components (non-spherical), and non-absorbing components suggests that differences in the plume-averaged REPA manifest in a combination of: 1) the *difference* in the fractional AOD of non-absorbing vs. moderately to strongly absorbing aerosols; 2) to a lesser degree, the *partitioning* of BIS vs. BrS; and 3) the *relative rate of change* in particle type with

plume age. To a certain degree, REPS also drives these factors, as particles having the same composition will have lower SSA with increased size. The first two factors can be seen in Table 5.3, with the sum of BlS and BrS higher in G fires compared to F fires, and especially high fractions of BlS in G fires and BrS in F fires ($p<0.001$ in both cases). W fires are not considered statistically different from F or G fires in this regard, and exhibit values in-between these two. These findings are consistent with other studies, as smoldering fires (which are more frequent in forests compared to grassland and savanna) tend to produce higher fractions of brown carbon particles compared to flaming fires, but fires in savannas and grasslands emit larger fractions of black carbon [Chakrabarty et al., 2010, 2016; Petrenko et al., 2012]. The third factor driven by inter-biome REPA differences is explored in Section 5.3.5, in our discussion of particle aging.

5.3.5 Downwind Particle Evolution and Differences Between Fire Types

To understand how particle properties change with smoke age both within and between plumes, we use MINX wind speeds and distance from the fire source to divide each plume into discrete age bins at approximately 30-minute intervals, where possible. In 6% of cases, poor retrieval quality and/or gaps in the retrieved plume area prevented us from calculating age in a plume.

Overall, REPS increases with age (lower ANG), whereas REPA decreases (higher SSA). This is generally consistent with literature on the typical aerosol aging processes in BB plumes, as particles oxidize and hydrate, and gaseous pre-cursors such as volatile organics condense onto their surface to increase particle size; these processes often lead to reduced light-absorption, especially in the case of BlS. As

coatings generally increase hygroscopicity, this can contribute to increased particle hydration, size and SSA, especially as the plume cools, which increases the effective RH. However, we find that plumes in the G category exhibit *decreased* REPS with age, unlike the trends seen in F and W plumes (Figure 5.4a-c). This is accompanied by a dramatic decrease in the downwind plume AOD not seen in F or W plumes (Figure 5.4d). In Figure 5.5., trends in REPS are further illustrated via the downwind evolution in the AOD fractions of the four particle-size components. In particular, the partitioning between small- and medium-particle AOD fractions is highlighted. We observe a transition from small-dominated to medium-dominated smoke at approximately the 3-hour mark in both F and W plumes, whereas G plumes never experience this transition and in fact tend to show the opposite. In the context of the total plume AOD decreasing, this may indicate that dilution with background air is more important in G plumes compared to F and W plumes, that instead probably experience downwind particle growth due to a dominance of condensation/hydration. Dilution in G plumes may also occur in the vertical, as the plume heights are generally lower, where larger particles might be deposited preferentially on the surface, reducing AOD. The decreased AOD and particle size may also indicate that G plumes experience a stronger shift in gas-particle partitioning downwind, as the mixing of cleaner background air into the plume shifts the equilibrium for semi-volatile compounds from the particle phase to the gas phase, resulting in stronger rates of evaporation at lower concentrations [Garafolo et al., 2019].

Although plume REPA decreases downwind in all three plume types, the timescales over which the particle-type components transition from absorbing-

dominated to non-absorbing-dominated are significantly different between G plumes and the other two plume types. Non-absorbing particles begin to dominate over the BIS components at approximately the 3-hour mark in F and W plumes, whereas the transition takes between ~4 and ~7 hours in G plumes. The longer retrieved lifetime for BIS in G plumes may indicate reduced levels of oxidation, which is consistent with the fact that flaming fires emit less VOCs, which are important in modulating gas-phase oxidation chemistry [Liu et al., 2017; Koppmann et al., 2005; Donahue et al., 2014]. This would also help account for smaller particle sizes in G plumes as VOC condensation is an important mechanism for particle growth.

5.3.6. Impact of Drought on Plume Heights and Particle Properties

Overall, maximum plume heights increase with drought level in both F and W fires, with the exception of the six fires observed in the most extreme drought class. (The small sample size must be taken into consideration when evaluating plumes in this class.) Median plume heights in F and W fires are slightly more variable, but also show an overall increase with increasing drought. In contrast, plumes from G fires show essentially no variation in height with drought conditions (Figure 5.7). These differences are consistent with other studies on fuel consumption across different biomes – areas with low tree-cover density experience lower tree mortality rates during drought stress compared to areas with high tree-cover density [van der Werf et al., 2010]. We therefore expect forested areas to experience larger swings in the amount of fuel available for burning based on drought, compared to low-biomass-density areas. The considerable increases in fuel availability translate to larger, more intense fires, and higher plume injection, in the F and W categories.

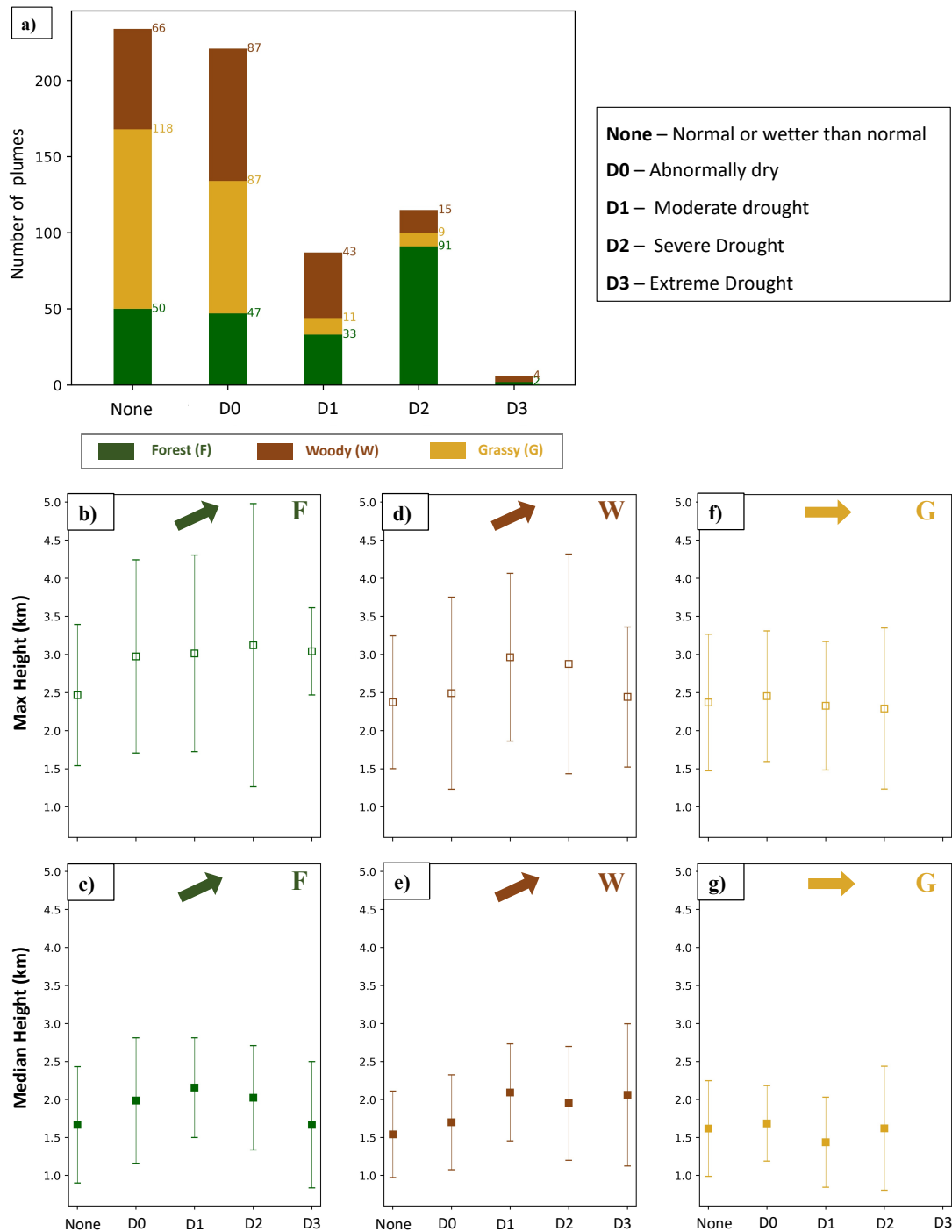


Figure 5.7. (a) The number of plumes observed in each drought category (see key), colored by plume type; and (b-g) the impact of drought level on maximum (top row) and median (bottom row) plume heights, for each plume type. The marker represents the mean value, and the whiskers are standard deviations.

A shift in the relative fraction of tree-dense areas contributing to the burn in F and W plumes is further supported by increasing AOD and decreasing median FRP with increasing drought severity (Figure 5.8), suggesting a change in the fraction of smoldering to flaming regimes. In addition, increased tree cover and higher smoke opacity may act to obscure the 4-micron radiance signatures detected by MODIS, contributing lower pixel FRP. The *cumulative* FRP over the burning area, however, increases with drought in F and W fires, corresponding to a larger number of fire detections per plume. As with plume heights, G plumes exhibit no significant changes in AOD and FRP with drought severity.

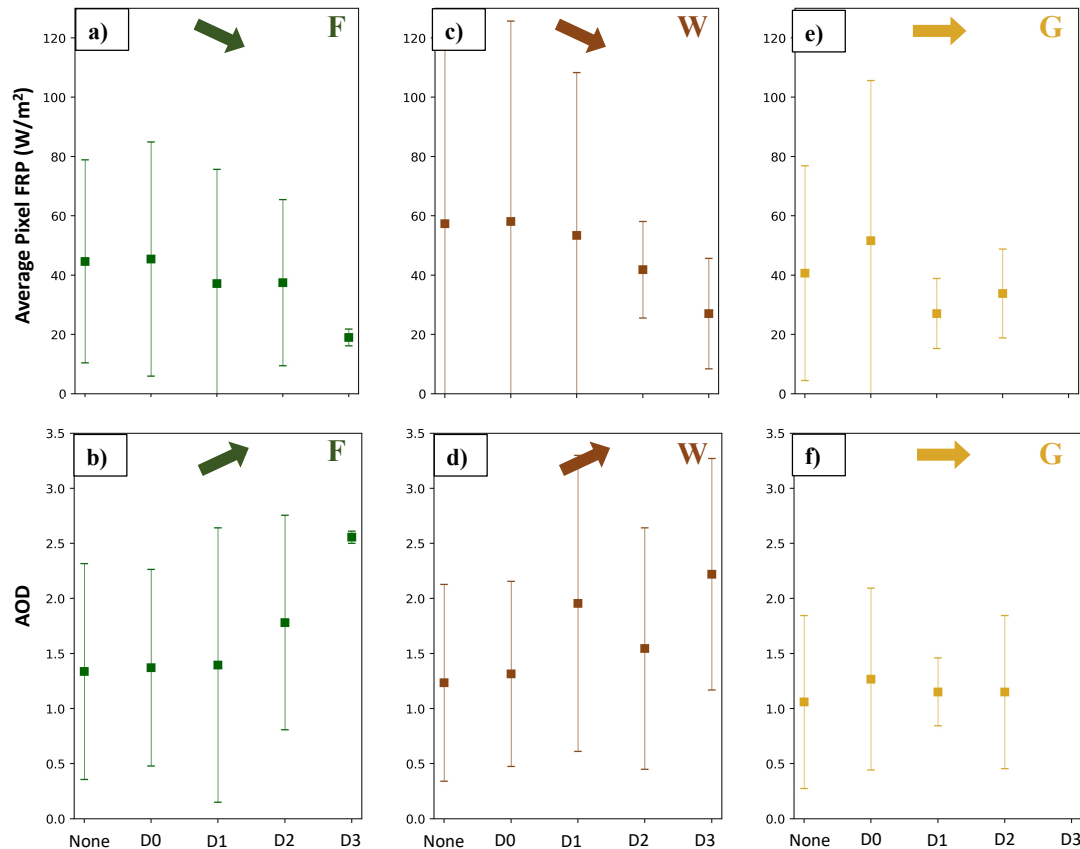


Figure 5.8. Median plume FRP (top row) according to plume type and drought level; Median plume AOD (bottom row) according to plume type and drought level. Panels are color-coded by plume type and identified with the appropriate abbreviation in the top right corner. Points represent the mean value, and whiskers are the standard deviations. Arrows highlight the general trends with increasing drought.

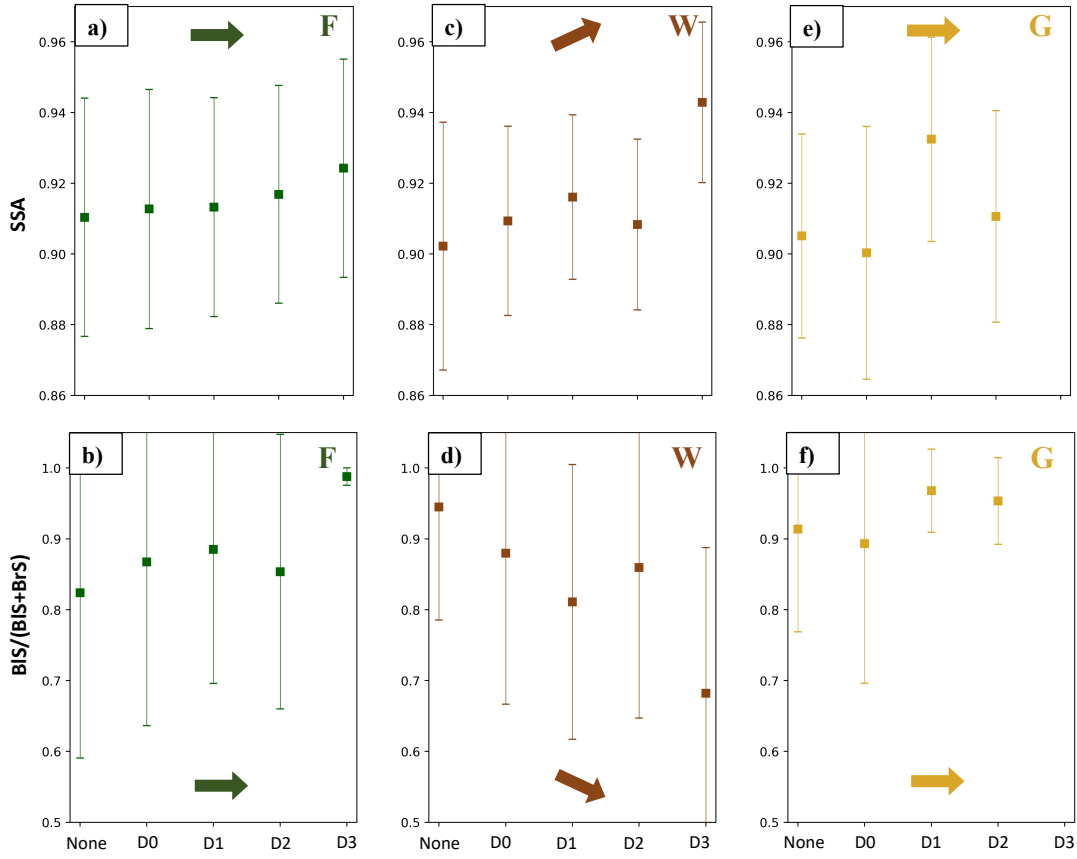


Figure 5.9. MISR mid-visible single scattering albedo (top row) and the fraction of AOD from BIS vs. the sum of both BIS and BrS (bottom row) for different drought conditions. Decreasing values indicate lower amounts of BrS and higher amounts of BIS. Panels are color-coded by plume type and identified with the appropriate abbreviation in the top right corner. Points represent the mean, and whiskers are the standard deviations. Arrows help highlight the general trends with increasing drought index.

We find that increasing drought index in W plumes is generally correlated with increasing particle light-absorption and BrS fractions, trends that are not present in F and G plumes (Figure 5.9). This may indicate that the aforementioned shifts in fuel type and burning regimes are more pronounced in W plumes. A possible explanation is that fires identified as W plumes experience some of the largest swings in the types of fuels available for burning, as they contain a more even mixture of grassy vs. woody vegetation based on our definitions. As drought persists, the relative increase in the amount of woody fuels available to burn in W fires outpaces that in F

fires, which consume more woody fuels to begin with, as per our fire type definitions. Similarly, the absence of coarse woody fuels in grassy biomes would prevent any significant shift in fuel types.

5.4. Summary

The MISR plume heights and particle properties exhibit patterns that match well with existing literature on the role on burning conditions and vegetation in wildfire smoke properties. Furthermore, the *combination* of MISR observations with other satellite and modeling datasets allow us to infer the dominant factors driving particle properties and their evolution under different conditions. This represents new territory in BB aerosol studies.

Specifically, we find distinct patterns in plume properties when the data are partitioned into three categories based on the relative fractions of forest (F), woody savanna (W), and grasslands/savannas/shrublands (G). The largest differences are typically found between F and G fires, as these represent the extremes in fuel type for fires in this region. The most statistically significant differences are observed in: 1) plume heights, with taller plumes in F fires; 2) MISR AOD, with thicker plumes in the F category; and 3) particle size and light-absorption, with F plumes exhibiting both larger and less absorbing particles than G plumes. These differences are likely driven at least partially by the relative fractions of flaming and smoldering fire in each category, as smoldering is more dominant in F fires.

There also appear to be distinct differences in how smoke particles age downwind with plume type, and the timescales over which these changes occur. In G plumes, particles do not experience increases in particle size, it takes comparatively

longer for the BIS AOD fraction to diminish, and total AOD drops significantly downwind. In F and W plumes, the near-source dominance of small particles transitions toward medium particles, non-absorbing particles begin to dominate over BIS particles much sooner, and total AOD is relatively consistent downwind. Based on these trends, we infer that G plumes and F/W plumes experience varying types and degrees of atmospheric aging. Namely, we infer that:

- 1) G plumes experience less oxidation and condensation compared to F and W plumes, evidenced by the higher overall absorbing aerosol fraction retrieved by MISR and the fact that flaming fires produce fewer VOC emissions
- 2) There is potentially a higher degree of large-particle deposition onto the surface in G plumes, supported by lower plume heights, decreasing particle sizes downwind, and reduced AOD downwind
- 3) Horizontal dilution may play a larger role in particle size for G plumes, evidenced by the same reduction in particle size in AOD as in #2.

We also find that drought plays a role in plume height and AOD in both F and W fires, but that only W fires appear to respond significantly to drought in terms of the smoke particle properties.

Chapter 6: Concluding Remarks

6.1. Overview of Study

As significant emitters of absorbing aerosols, wildfires are an increasingly important component in the consideration of air quality and global climate change. However, there are still many unresolved questions pertaining to the specific optical and physical properties of smoke particles, which vary widely both at emission and downwind as particles age, exerting different radiative and chemical impacts on the environment. Most climate and air quality models currently lack parameterizations of BB particles that sufficiently describe for these applications the range of light-absorption, light-absorption spectral dependence, and size that have been observed in field campaigns and laboratory experiments. With the proper tools, investigation of MISR's unique multi-angle, multi-spectral retrievals can provide insight into the climatologically probable range of smoke particle types under a variety of burning conditions. In this thesis we investigated the extent to which the MISR Research Aerosol (RA) algorithm and the MINX software tool can qualitatively describe wildfire particle properties and their evolution, as well as whether differences in the observed properties can be statistically linked to available data on burning conditions and meteorology. This first involved extensive and detailed validation of the MISR particle property retrievals using near-coincident *in situ* observations of smoke plumes from the BBOP and FIREX-AQ field campaigns. Next, we applied the same techniques in a regional study of smoke plumes across Canada and Alaska in search

of robust, statistical conclusions on particle type and evolution. For this investigation, we also analyzed land cover type and measurements of fire radiative power (FRP) from MODIS, the height of the planetary boundary layer (PBL) from MERRA-2, and the drought severity from the North American Drought Monitor (NADM).

6.1.1. Conclusions from the Validation Experiments

Two separate validation studies in this work leveraged near-coincident *in situ* aircraft data from the BBOP and FIREX-AQ field campaigns for comparison with MISR optical retrievals. The aircraft data allow us to explore the strengths and limitations of the satellite data for characterizing wildfire smoke plume extent and particle properties. Where near-coincident data were acquired, the MISR-retrieved particle properties and those measured *in situ* are similar, showing consistent spatial patterns, with measurement uncertainty and sampling differences easily accounting for the observed differences. With these caveats in mind, we conclude that the MISR retrievals accurately map the general ranges of particle size, light-absorption, and the spectral dependence of light-absorption in the smoke plumes.

The *in situ* data offer chemical and microphysical detail, such as the degree of particle oxidation and the specific distribution of particle sizes, as well as particle concentrations, which cannot be obtained from available satellite observations. However, the satellite snapshots offer maps of qualitative particle properties with extensive coverage, which can capture aspects of the plume missed by the aircraft transects. For example, differences in plume structure among the three cases analyzed in the BBOP study (Chapter 3) were captured most effectively by the whole-plume MISR observations: the systematic change in AOD and particle properties along the

length of the Government Flats plume, the patchy and more variable particle property distribution along the Colockum Tarps plume, and the seemingly stagnant pile-up of smoke particles for the Douglas Complex plume. As such, the satellite data provide the context needed to derive relationships among plume elements of different ages, making it possible to infer attributes of plume-particle evolution. In both the BBOP and FIREX studies, the aging mechanisms inferred from MISR data are supported by the near-coincident aircraft data. Specifically, we observed: 1) progressive oxidation throughout both plumes, reflected in decreasing plume REPA and BrS fraction and supported by direct aircraft measurements of BC mass concentration and oxidation products; 2) gravitational settling of larger particles and deposition onto the surface downwind in both plumes, reflected in MINX retrievals as well as decreasing plume REPS and AOD, and corroborated by differences in sampling between MISR and the aircrafts; 3) a combination of VOC condensation and particle hydration in both plumes, reflected in increasing plume REPS and decreasing plume REPA, and supported by aircraft measurements of SSA and particle size distributions; 4) new particle (SOA) formation downwind in the Government Flats plume (BBOP), reflected in a sudden decrease in particle REPS and increase in BrS fraction, and supported by aircraft measurements of light absorption across different wavelengths; and 5) differences in emissions between hotspots in the Williams Flats plume (FIREX), reflected in differences between particle REPS and REPA in separate plumes and supported by measurements of BC mass concentration and particle size distributions by the aircraft. These results demonstrate smoke-plume evolution generally consistent with previous modeling studies (e.g., Hodshire et al. [2019];

Konovalov et al. [2019]), but providing extensive observations of a number of key smoke-plume properties not previously obtained from remote sensing and demonstrating the possibility of obtaining statistical assessments of particle evolution timescales beyond previously available results. In the future, such data can help refine climate modeling of wildfire smoke-related processes.

6.1.2. Conclusions from the Canada-Alaska Regional Study

The validation results set the stage for applying the space-based, remote-sensing tools to a large, statistical sampling of wildfire plumes not constrained by *in situ* observations in Canada and Alaska. In this investigation we found distinct, statistically significant differences in plume heights, particle properties, and inferred aging mechanisms and timing, and we linked these systematically to differences in burned vegetation type, FRP, and drought conditions. Our results are not only consistent with previous studies, but they also provide brand new insight into the conditions surrounding specific smoke particle aging regimes.

We defined three plume classes based on dominant land cover type from the MODIS satellite instrument: (1) forest fires, which burn at least partially in forests; (2) woody fires, which burn in a mixture of the somewhat less tree-dense woody savanna biome and the tree-sparse savannas or grasslands; and (3) grassy fires, which burn in the same types of vegetation as woody fires but with larger fractions of grasslands and savannas. We find that most particle properties are strongly dependent on plume category, with forest fire smoke containing the largest, brightest particles and the highest AOD fraction of BrS and the lowest AOD fraction of BlS. forest smoke also typically have the highest AOD and plume heights. In contrast, grassy fire

smoke contains the smallest, darkest particles with the lowest BrS fraction and the highest BlS fraction. The sum of BlS and BrS is also at its highest in these plumes. Grassy smoke plumes generally have the lowest AOD and lowest plume heights. Woody smoke displays properties that are in-between those of forest and grassy plumes, and as such some differences in their particle properties are not found to be statistically significant (e.g., SSA and the partitioning of the different particle-absorption types). The observed differences between forest and grassy plumes are consistent with the existing literature on fuel type and wildfire emissions, and provide new insight into the driving mechanisms behind particle evolution (reviewed below).

We also observe differences in the response to drought based on plume type, with higher plume heights and AOD associated with higher drought severity in forest and woody plumes, and higher SSA and BrS fractions in woody plumes. Consistent with previous studies, grassy plumes display no statistically significant response to changing drought index.

Finally, we studied the evolution of particle properties based on smoke age estimated from MINX-derived wind vectors. Particles became both larger and brighter downwind in forest and woody plumes, with little change in plume AOD. Particles in grassy plumes also became brighter with age, but they experienced decreasing overall size and the plume AOD dramatically decreased downwind. In addition, the timescales over which particle-type and -size transitions occurred vary between plume types, with grassy plumes taking much longer to transition from BlS-dominated to non-light-absorbing-dominated, and never experiencing a transition from small-size-dominated to medium-size-dominated as observed in forest and

woody plumes. Based on these trends, we infer that condensation and hydration likely play a larger role in downwind size and light-absorption evolution in forest and woody plumes, whereas downwind dilution may dominate in grassy plumes. (Dilution is likely a combination of both horizontal entrainment of background air and gravitational settling of larger particles from the column.) These conclusions represent new territory, as to-date there have been no other large-scale regional studies relating particle properties to specific aging mechanisms and the timescales over which they occur.

6.2. *Plans for Future Work*

The last chapter of this thesis involved a pilot study in relating MISR-retrieved particle properties to the conditions surrounding wildfire activity. Analysis of additional satellite and modeling data that describe these conditions can provide us with a more complete picture of the factors driving emitted particle type and subsequent aging. For example, more detailed data on vegetation types could help us refine and expand our plume-type categorization. To this end, we will analyze the extensive fuel bed type maps produced by Canadian Wildlife Fire Information System (CWFIS) that define 16 fuel types at a higher level of detail than those from MODIS. We may find that the density and species of tree cover within forests affect smoke particle properties differently. Additionally, various fire weather indices (e.g., the Haines Index) provide information on live and dead fuel moisture amounts and atmospheric conditions that impact fire severity, and so we will investigate the extent to which we can leverage these with satellite or modeling data. Finally, future research will also include the analysis of atmospheric stability, particularly at the top

of the PBL, as this can provide us with an improved understanding of the modulating forces behind plume injection heights in our region of study.

As the MISR data record contains global coverage about once per week for over 20 years, there is a vast trove of smoke-plume observations available for further study. Future work will involve applying the MISR RA to plumes across a wide variety of other biomes and climate conditions. In particular, we have set goals to study the Western United States, Siberian Russia, Australia, and the Amazon Rainforest as part of a NASA post-doctoral fellowship. Based on current knowledge of the differences in fire properties between these regions, we expect to find significant differences in particle properties, plume heights, and other retrieved or modeled quantities, with implications for the underlying mechanisms and the timescales over which they operate. All these must be modeled correctly to make accurate forecasts and predictions of conditions in a changing climate. For example, given what MISR can offer and the results from this thesis, we expect to be able to distinguish differences in BIS vs. BrS ratios, the contribution from non-spherical soil or dust particles, and the broad particle size distribution patterns within plumes and between plumes from different fire types, as a function of smoke age and environmental conditions. This is new – we cannot predict how many of these relationships will manifest in each biome; we will learn this from our future work. Such observational constraints on BB particle-type distributions and aging regimes may greatly benefit regional and global climate and air quality modeling efforts.

Appendix A

In this appendix we provide supplementary information from Chapter 3.

Part I: We present in the first section of this supplement two figures that support the main text and are referenced in the discussion the Government Flats Complex Fire.

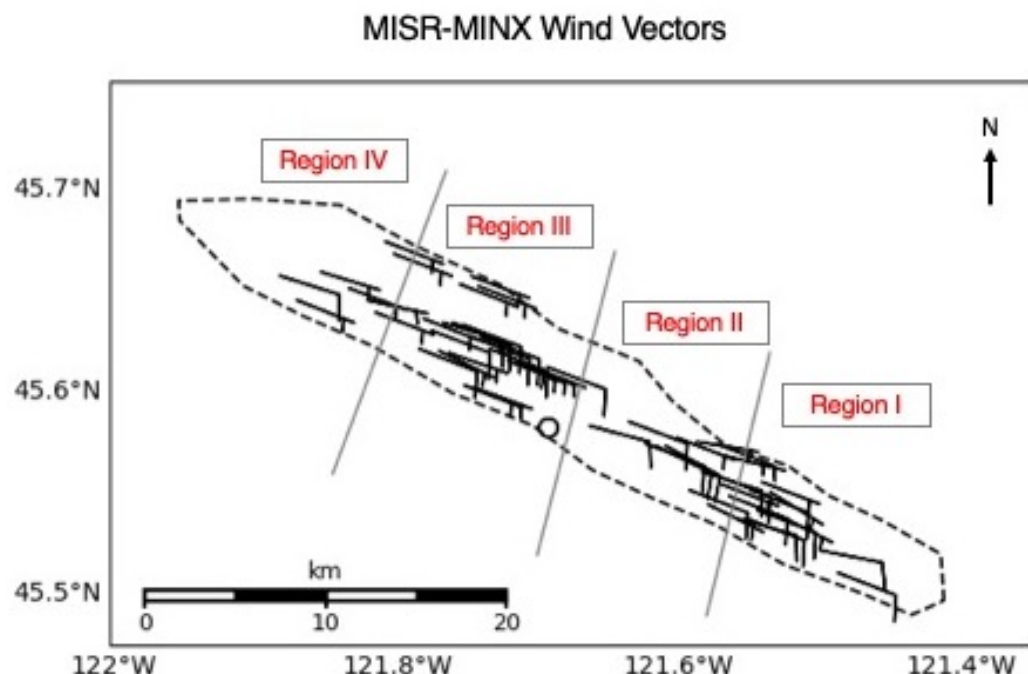


Figure A1. Wind trajectories retrieved from the MISR-MINX software tool (in units of knots) for the Government Flats Complex Fire. Half-bars indicate 5 knots, full bars are 10 knots. The grey lines represent the regional boundaries within the plume (See Fig. 1a). Empty circles are points where the retrieved wind speed was zero.

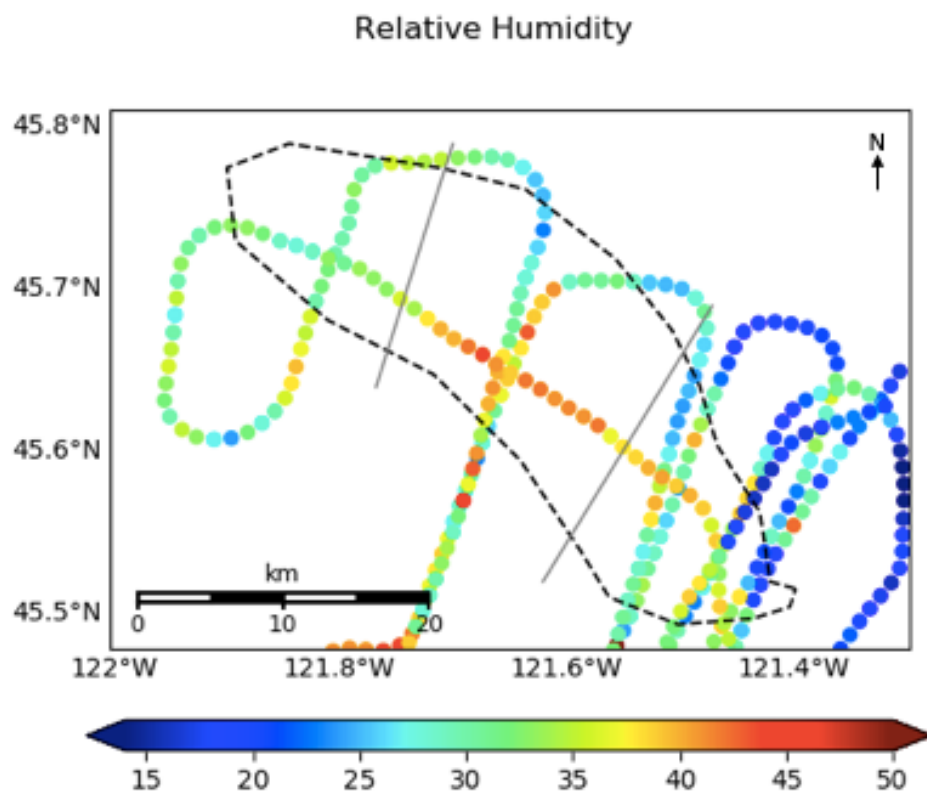


Figure A2. Percent relative humidity observed from the BBOP G-1 aircraft for the Government Flats Complex Fire.

Part II: We present in the second section of this supplement detailed descriptions of the *in situ* and spacecraft observations collected for the Government Flats Complex Fire, by region.

Aircraft *in situ* Observations of the Government Flats Complex Fire

As expected, the *in situ* observations indicate the highest CO and aerosol concentrations near the source, decreasing downwind. Virtually all points outside the plume boundaries contain fewer than 2,000 particles/cm³, as measured by the PCASP/CAS (Figure 3.1d), and less than 0.15 ppm of CO (Figure 3.1c). The sections below use the regional statistical data from Table 3.2 in conjunction with the lat/lon plots in Figures 3.2 and 3.3 to characterize in detail each plume region, with emphasis on the *differences* from one region to the next. This allows us to both quantify large-scale patterns as well as to visualize small-scale changes, and to account for any differences in sample size. Note that discussion of large aerosols has been omitted, as their fractions are negligible, although Figure 3.3 and Table 3.2 contain the available information on these particles. Also note that discussion of differences in $r_{e(BC)}$ are mostly omitted, as all are likely within the uncertainty of the SP2; however, we retain the regional mean values in Table 3.2.

Region I:

The near-source region contains, on average, the freshest ($-\log[NO_x/NO_y] \sim 0.2$) and darkest (SSA ~ 0.7) particles, as well as the highest mean BC mass and $r_{e(BC)}$

(over 16,000 #/cm³ and 0.070 μm , respectively) (Figure 3.2). Overall, the region is dominated by small and medium aerosols, with mean fractions of ~57% and ~31%, respectively (Table 3.2). Apart from the BC particles we know to be present from SP2 measurements, very small aerosols are almost absent throughout most of the region, except for two extreme outlier pixels that contain fractions higher than 60% and therefore inflate the mean to ~13% (the median is ~3.8%, a value that is more likely representative).

Region II:

Compared to upwind, the near-downwind region contains considerably more oxidized, brighter particles, with mean $-\log[\text{NO}_x/\text{NO}_y]$ and SSA of ~0.53 and ~0.77, respectively (Table 3.2 and Figure 3.2; as has been mentioned, filter-based SSA measurements tend to bias low under heavy aerosol burdens, so the actual SSA values may be somewhat higher). The mean absolute BC mass concentration decreases nearly two-fold to ~8,600 #/cm³, although it is higher within the central portion of this region compared to the plume edges (Figure 3.2c), where there is entrainment of fresh air. The mean CO-normalized BC mass concentration also decreases significantly, although the median increases. In the central, along-plume transect, there are dramatic increases in both the CO-normalized light-absorption attributed to BrC (over 25% on average) and the CO-normalized ultraviolet (UV) scattering (38% on average) (Table 3.2). The CO-normalized CCN₁₅ and aerosol concentrations both increase by more than 80% from Region I. Aerosol size decreases compared to upwind, with increasing fractions of small and very small particles along with a decreasing fraction of medium aerosols. However, this change is only seen along the

plume boundaries (Figure 3.3), where the fraction of very small particles is ~20-50% higher than the rest of the region, and similarly, medium aerosol fractions are 20-50% lower. Overall, the central, major portion of the plume appears to show no great differences in the partitioning of aerosol size categories compared to upwind, but SSA, aerosol oxidation, BrC light-absorption, UV scattering, and normalized CCN₁₅ concentration increase measurably, and BC mass concentration decreases.

Region III:

The mid-downwind region displays further oxidation and SSA enhancement (means of ~0.79 and ~0.78, respectively). Unsurprisingly, this is accompanied by a plume minimum in mean BC mass concentration. Mean CO-normalized BC mass concentration decreases again from Region II, while median concentration slightly increases. CO-normalized UV scattering slightly increases compared to Region II, whereas the mean and median CO-normalized BrC light-absorption slightly decrease and slightly increase, respectively (and the mean still remains much higher than that of Region I). Furthermore, both the normalized CCN₁₅ and normalized total aerosol count peak in this region (Figure 3.2). There is also a ~10% regional-mean increase in the fraction of very small aerosols, accompanied by a corresponding decrease in medium and small aerosol fractions (Table 3.2, Figure 3.3). These patterns are clearly driven by the southern flank of the region, where there is *particular* enhancement in the very small aerosol fraction, SSA, oxidation, and normalized aerosol and CCN₁₅ concentration compared to the northern flank. Particles in the southern flank are overwhelmingly very small and highly oxidized, and some reach SSA greater than

0.9. Note that the BBOP aircraft did not sample Region IV in the plume, as observed by MISR and MODIS (Figure 3.1).

Satellite Observations of the Government Flats Complex Fire

Table 3.3 quantifies the mean, standard deviation (SD or σ), and median values for the satellite observations for each region. The four subsequent sections provide qualitative analysis and context for these statistics, with an emphasis on *differences* between regions. It is important to reiterate that when discussing specific particle types (e.g., BIS, BrS, dust, non-absorbing aerosols), the retrieved aerosol properties represent the optical equivalent of the aerosol present; i.e., the true aerosol can be a blend of the size, shape, spectral slope, and absorption of the retrieved components, and is not necessarily a mixture of the specific, retrieved components themselves.

Region I:

The near-source region is strongly characterized by high REPA, with a mean SSA of 0.86 and a low SD indicating little variability (Figure 3.4). This can be attributed to: 1) a very large fraction of spectrally flat, BIS-like components throughout the region, with a mean contribution of 56% to the total mid-visible AOD (and upwards of 90% in some pixels); 2) an almost zero AOD fraction of non-absorbing aerosols (mean ~10%, median nearly 0%); and 3) a significant AOD fraction of non-spherical aerosols (mean ~20%), which are weakly absorbing and represent “dust” analog (possibly soil) particles. There are also some pixels with noteworthy fractions of spectrally steep BrS aerosols, but their contribution in Region I (mean~13%, median<1%) pales in comparison to BIS. Regional REPS is overall small, with a

mean extinction Ångström exponent (ANG) of 1.54. However, REPS is more variable than SSA due to several lower-ANG pixels along the region's southwest edge, so the mean may overestimate true particle size (median ANG=1.58; Figures 3.4-5, Table 3.3). Component analysis indicates the REPS is the result of a mixture of very small and large aerosols, the latter likely primarily nonspherical particles (Figure A3).

Region II:

The near-downwind region displays significantly lower REPA (mean SSA ~0.93), marked by a decrease in BlS, BrS, and dust-analog fractions and an increase in non-absorbing component fractions (means ~36%, 8%, 11%, and 44%, respectively). REPS is also higher here than in Region I, although overall still considered small (mean ANG ~1.32). Geographic variability within the region can explain the large SDs in Table 3.3 – the central area is darker and dominated by BlS and some dust-like particles similar to Region I, whereas the areas adjacent to the plume boundaries contain mostly non-absorbing particles, with essentially no non-spherical particles (Figures 3.4-5, Table 3.3). Furthermore, the southern portion of the region is retrieved as a mixture of large and very small aerosols, whereas the northern portion is dominated by medium and small aerosols (Figure A3).

Region III:

The mid-downwind region displays REPA similar to Region II, although slightly darker overall, with a mean SSA of 0.92. However, there is significant geographic variability in the particle brightness between the northern vs. southern halves when the region is split lengthwise along the plume central axis. The SSA is much higher in

the northeast than in the southwest. The entire region is distinct in that it is the only one to contain widespread, significant fractions of BrS components, based on the retrievals (regional mean ~30%, a 30-fold increase from upwind). This is accompanied by a corresponding overall regional decrease in the mean/median AOD fractions of the BIS, dust, and non-absorbing particle analogs. However, the southern half of the region contains a BIS fraction that appears at least equal to BrS. Furthermore, non-absorbing particles make a negligible contribution here, and there is a detectable fraction of the dust analog (~20-30%), all contributing to the low SSA overall. The northeast part of the region is dominated by both BrS and non-absorbing particles, whereas BIS and dust fractions are nearly zero, which raises the SSA here. Despite the geographic variability in light-absorption, ANG is consistent throughout the region, with a mean of 1.82, the highest of all four regions (Figures 3.4-5, Table 3.3), indicating a predominance of smaller particles. Component analysis indicates both absolute and fractional increases in small aerosols (Figure A3).

Region IV:

The far-downwind region contains both the brightest and largest particles in the plume, with a mean SSA of ~0.97 and a mean ANG of ~1.04, so the region is still fine-mode dominated. The coverage in this region is not as extensive as in the other three, but one can still see somewhat coarse particles of ANG<0.7 along the plume edge, and somewhat finer-mode particles further upwind. Based on the retrievals, the region is largely dominated by non-spherical and non-absorbing components, the former being particularly evident at the plume edge. Both BIS and BrS component fractions approach null (Figures 3.4-5, Table 3.3).

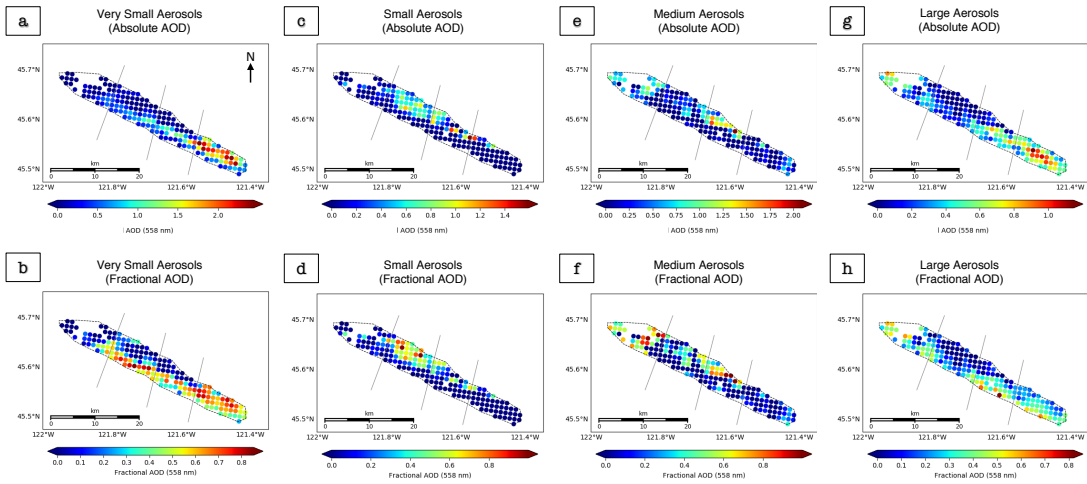


Figure A3. Absolute (top row) and fractional (bottom row) AOD of the four main particle size bins retrieved by the MISR RA for the Government Flats Complex Fire. Note: scales differ between categories.

Part III: We present in the third part of this supplement detailed descriptions of the *in situ* and spacecraft observations collected for the Colockum Tarps Fire and the Douglas Complex Fire. The aircraft and satellite observations of these fires were each separated by a day, which reduces their usefulness for formal validation of the satellite retrievals, but demonstrates the value in applying the satellite data in the vast number of situations where such data are available, but *in situ* data are lacking.

Colockum Tarps Fire: Aircraft Observations Preceding Satellite Observations

The Colockum Tarps Fire, first ignited due to human causes, burned from July 25th, 2013 through August 15th, 2013 in southern central Washington. The primary fuel was a mixture of grass, brush, and timber; over 80,000 acres burned in total. The July 26th, 2013 BBOP research flight and the subsequent July 27th MISR overpass observed the resulting smoke plume. Plume geometry changes significantly between observations; the plume extends toward the northeast from the fire source on July 26th, and toward the southeast on July 27th. The plume outline for the *in situ* observations was traced using the RGB MODIS Aqua image from ~20:10 UTC (Figure A4a; the aircraft flew in the area from ~20:00-22:20 UTC). There is a significant pocket of little-to-no smoke within the plume boundaries at this time, but as plume dynamics and smoke location may have changed during the course of the flight, we include this area within the boundary.

Measurements are considered “outside” the plume in areas where CO and aerosol concentrations were below thresholds of 0.11 ppm and 1000 #/cc, respectively, where

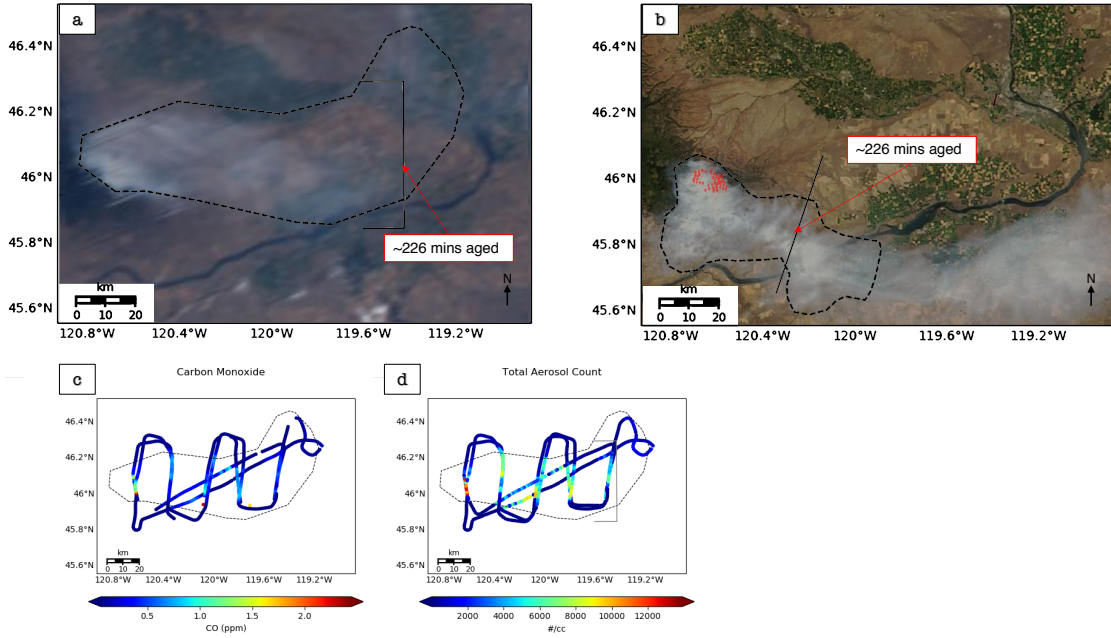


Figure A4. The Colockum Tarps fire in southern central WA as seen: **(a)** during BBOP flight operations, ~20:00-22:20 UTC on July 26th, (20:10 UTC, MODIS Aqua RGB image), and **(b)** at MISR overpass time on July 27th (19:13 UTC, MODIS Terra RGB image). The red dots indicate MODIS-identified hot spots and are used to estimate source location. The near-source plumes are outlined with thin dashed lines in these figures, and the location of smoke within the plume estimated as having aged ~3.8 hours is marked with a thin solid line. Panels **(c)** and **(d)** are maps of the aircraft *in situ* CO and total aerosol count measurements on July 26th, respectively.

measurements are particularly noisy, or where the plane was flying at an altitude thought to be above the smoke layer. These requirements usually all coincide (Figure A4c, d), and aircraft data obtained for points considered “outside” the plume, under very low particle concentration, are generally quite uncertain (e.g., the very low SSA values outside the plume boundaries in Figure A5a). Note also that the southern along-plume transect was flown at ~12:15 UTC, the very beginning of the ~2.5-h sampling period. As such, the seemingly anomalous along-plume data between cross-plume transects 3 and 4 in Figures A5a-c was probably outside the plume boundary at acquisition time, unlike the geographically nearby cross-plume transects obtained an

hour or more later. The following day, as shown in the broader-swath MODIS imagery (Figure A4b), MISR sees some, but not all, of the visible plume extent.

Aircraft Observations of the Colockum Tarps Fire

The flight observations depict a plume with particle properties that appear to change less systematically with downwind distance than the Government Flats Complex Fire, making it difficult to divide the plume neatly into characteristic regions as was done in Section 3 of the main text. From the measured wind speeds, we estimate the visible plume age to be ~ 226 minutes (~ 3.8 h) along the cross-plume transect indicated by the line in Figure A4a at the time of the flight.

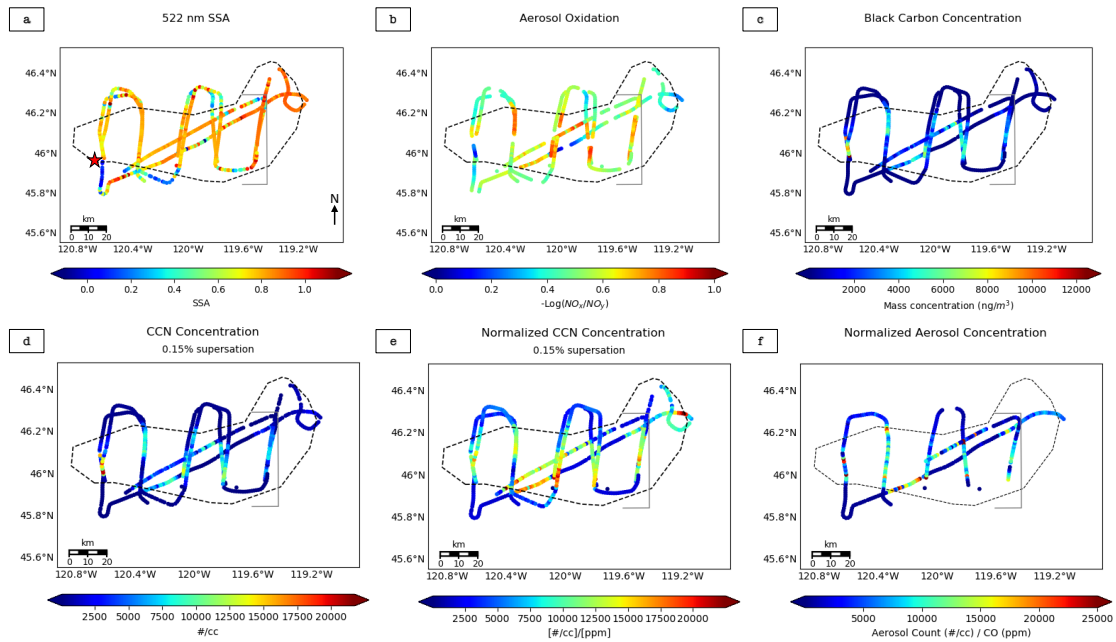


Figure A5. Aircraft observations from the Colockum Tarps fire in southern central WA of (a) 522-nm SSA (PSAP/neph), (b) aerosol oxidation (derived from 3-channel Oxides of Nitrogen Analyzer), (c) Mass concentration of BC and size of BC-containing particles (SP2), (d) the concentration of particles that can act as CCN at 0.15% supersaturation (CCN-200 instrument), (e) the CCN concentration divided by the CO concentration, and (f) the total aerosol concentration divided by the CO concentration. The star in (a) serves a reminder of the source location.

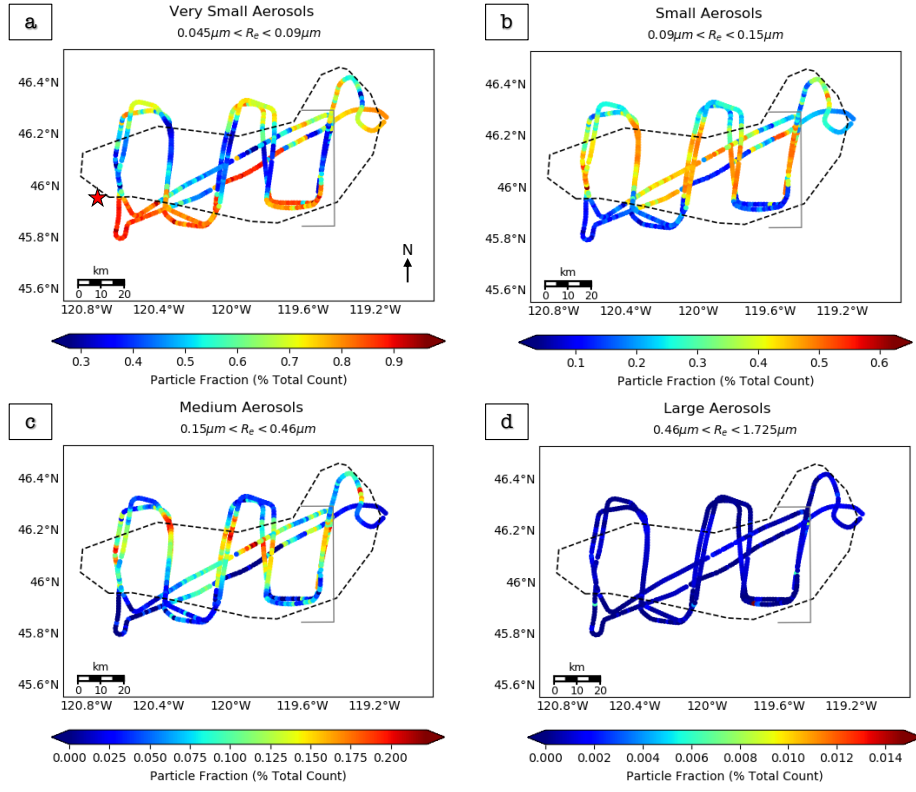


Figure A6. Fractional contributions to the total aerosol count for very small (a), small (b), medium (c), and large (d) aerosols in the Colockum Tarps fire in southern central WA, as measured by the PCASP and CAS *in situ* instruments. The star in (a) serves a reminder of the source location. Note: scales differ between categories.

Particle properties vary on short spatial scales (~ 1 km); however, some larger-scale patterns are also evident. There is an area of optically very thick smoke in the apparent source region(s), characterized by high total aerosol count, oxidation state, SSA, CCN concentration, and BC fraction and concentration, relative to background over most of the plume extent (Figures A4 and A5). However, very near the source, the particles are highly light-absorbing, with oxidation values near zero and SSA of 0.75 or lower – these SSA values are expected to be biased low due to measurement bias with the PSAP. In general, the plume is dominated by “small” particles, with “very small” particles contributing second-most, based on particle counts, and moderate contributions from medium aerosols in some areas (Figure A6). Large

particles are essentially absent, with fractional contributions well below 1%. When split lengthwise along the plume's central axis, the plume displays somewhat larger particle size toward the northern edge, where medium aerosols contribute up to 20% of the total aerosol count. The fraction of small aerosols is also somewhat higher here, whereas very small particles make up a noticeably smaller fraction. From plume source to nominal end, particle size overall appears to increase slightly along the plume central axis, to the extent this is sampled by the aircraft.

As mentioned above, particles sampled along the cross-plume aircraft transect closest to the source are highly absorbing and very fresh (Figures A5a and A5b). Both CCN number and BC mass concentrations also peak near the source, as might be expected. BC and CCN concentrations decrease considerably downwind within the near-source region, and oxidation state increases. There is also an increase in the CO-normalized aerosol concentration between the first two near-source, cross-plume aircraft transects (Figure A5f), indicating possible new particle formation shortly after emission, but there is no evidence in these data for additional particle production further downwind, and the increased concentration could arise from wind-driven convergence or changing emission at the source. Downwind of the first, near-source transect, SSA increases gradually over the length of the plume, BC and CCN concentrations remain relatively constant, whereas oxidation state and normalized CCN concentration are more variable. Toward the plume end (~226 minutes of aging), particles are only moderately absorbing (SSA ~0.9), are oxidized substantially ($-\log[\text{NO}_x/\text{NO}_y] > 0.6$) and contain considerably less BC mass contributing to the overall aerosol mass

loading. The gradual increase in SSA downwind, despite relatively constant BC fraction, could be due to particle hydration, as the small-particle fraction increases relative to the very small particle fraction. It could also be due to the condensation of VOC's onto existing aerosols, leading to increasing particle diameter of OA and increased coating thickness of BC-containing particles. Most BC-containing particles are less than 0.1 μm in radius, with smaller sizes of $\sim 0.06 \mu\text{m}$ closest to the source and larger particles, ranging from 0.07 up to 0.1 μm , downwind. Overall, $r_{e(\text{BC})}$ does not follow any systematic spatial pattern in the available data (Figure A7).

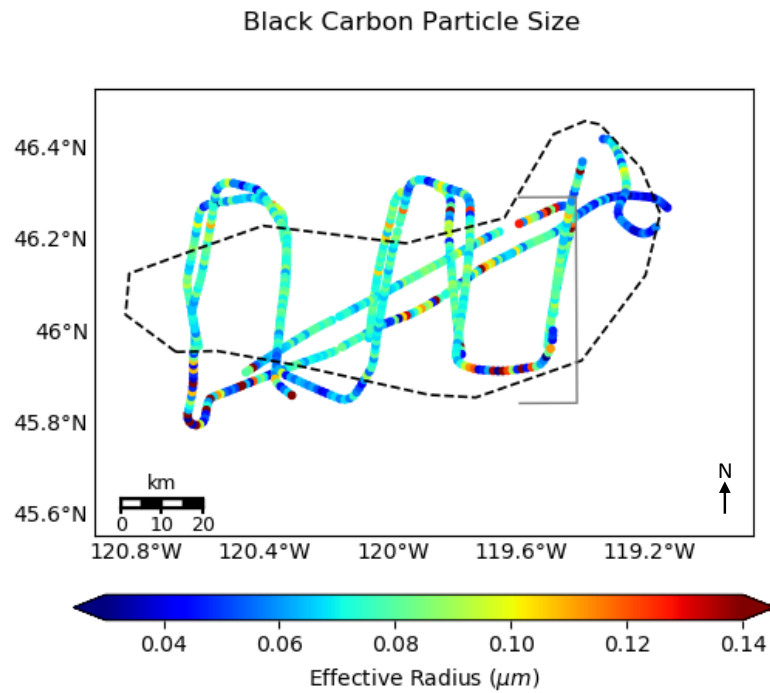


Figure A7. $r_{e(\text{BC})}$ for the Colockum Tarps fire observed by the SP2 aboard the BBOP G-1 aircraft.

MISR Observations and Discussion for the Colockum Tarps Fire

The next-day satellite observations show significant changes in plume geometry. The plume boundaries are better defined on this day (Figure A4b), and the satellite retrievals provide significant context beyond the aircraft transect observations. MISR-MINX stereo heights indicate the smoke stays mostly below 4 km and has a median height of \sim 2.9 km ASL (Figure A8a-b). Approximately 40 km downwind, the smoke becomes lofted about 1 km higher than the upwind area. At around this distance, the plume age is \sim 226 minutes (\sim 3.8 h), as estimated from wind speed roughly along the plume axis, at plume elevation (Figure A8c). The smoke is also optically very thick, with a nominal-retrieved mid-visible AOD near the source of 9, though the uncertainty in retrieved AOD becomes large once AOD exceeds a value of 4 or 5. The extinction Ångström exponent (ANG) suggests the plume at this time is dominated by small-to-very-small particles overall (median ANG \sim 1.74), particularly near the source (Figure A8e). Component analysis suggests heavy weighting of very small aerosols near the source, and a mixture of mostly small but also some medium particles downwind, with a near-complete lack of larger particles, as on the previous day (Figure A9).

As expected, the particles are darkest near the source. There is a patch of very small, dark particles extending from the source to about 20 km downwind along the northern boundary of the plume, with SSA \sim 0.83 or lower and ANG \sim 3.0 or higher. However, the particles brighten downwind and to the south, with SSA above 0.97 in some places (median plume SSA \sim 0.90) (Figure A8f). The SSA values and their observed increase with age is consistent with that reported by *Sedlacek et al, 2016*.

Further analysis of the RA components suggests that particles near the source are primarily a mixture of BIS- and BrS-like aerosols, with some nonabsorbing particles, but that BrS is confined near the source so that the downwind region is retrieved entirely as BIS and non-absorbing aerosols (Figures A9-10), yielding a net mid-visible SSA \sim 0.93. The apparent, abrupt particle-type transition might indicate changes in the burning conditions at the fire rather than particle evolution after emission.

Taken together, the satellite and *in situ* observations describe a plume with fine-mode, highly absorbing particles near the source that become brighter downwind. The MISR RA differs from the aircraft measurements in that it derives mostly very small particles near the source, with a significant increase in particle size a short distance downwind, whereas the aircraft CAS and PCASP observe particles *in situ* that are mostly in the same small size category throughout the plume (with pockets of enhanced medium particle fractions, similar to the pockets of lower ANG in the MISR RA). The difference in initial particle size could reflect changes in smoke properties between the two days or could be due to *in situ* measurement selective sampling, whereby plume properties would be more completely represented when the entire region is mapped with satellite observations.

The upper ranges of observed SSA values between the two days are very similar; in both cases, highly scattering aerosols, having SSA above 0.95, appear far from the source. As mentioned in the discussion of the Government Flats Complex Fire, the fact that the RA does not observe SSA as low as the aircraft could be due to the finer spatial resolution at which the aircraft samples, the limitations of filter-based

measurements, or to limitations in the RA particle climatology. Regardless, the same general light-absorption patterns apparently persist day to day for the Colockum Tarps Fire. A more noticeable difference is that BC mass concentration peaks near the source and decreases threefold after the first cross-plume transect, and then appears relatively constant further downwind during aircraft operations on July 26th (Figure A5c), whereas on July 27th, the MISR RA indicates that BIS AOD varies but preserves high values in patches over much of the plume downwind (Figure A10a-b). This difference could also be explained by limited aircraft sampling, though changing fire emissions cannot be ruled out.

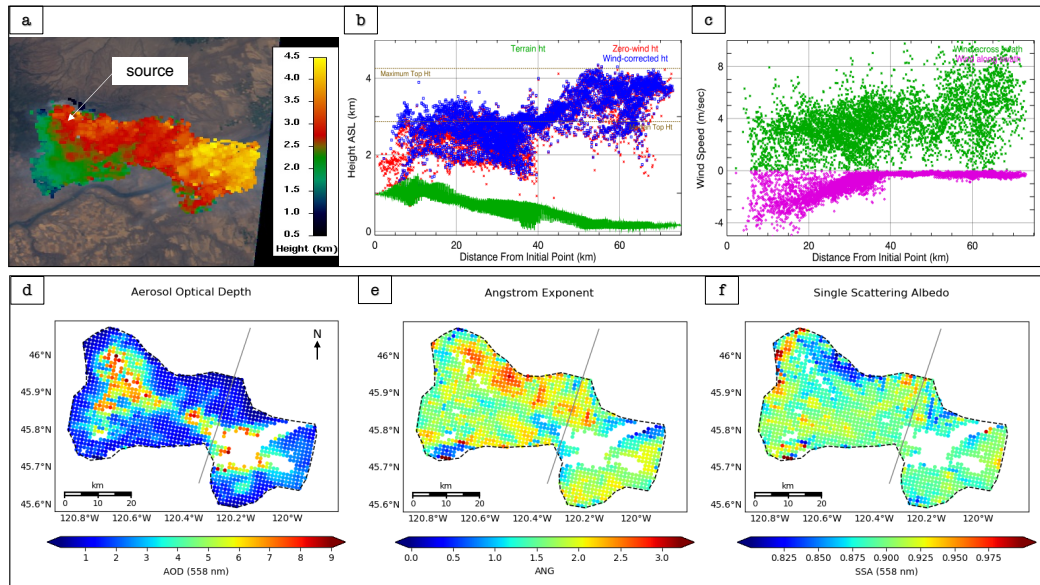


Figure A8. Plume properties for the Colockum Tarps fire in southern central WA retrieved by MISR at 19:13 UTC (Orbit 72382, Path 46, Blocks 53-54). **(a)** MISR-MINX stereo height retrieval map, **(b)** MINX stereo height profile as a function of distance from the source, for both zero-wind (red) and wind-corrected (blue) analyses, with surface elevation indicated in green, **(c)** the MINX-derived across-swath and along-swath wind vectors at plume level, **(d)** the RA-derived AOD at 558 nm, **(e)** ANG, and **(f)** the SSA at 558 nm. The transect for plume age estimated at ~226 minutes is indicated with a thin gray line in panels d-f.

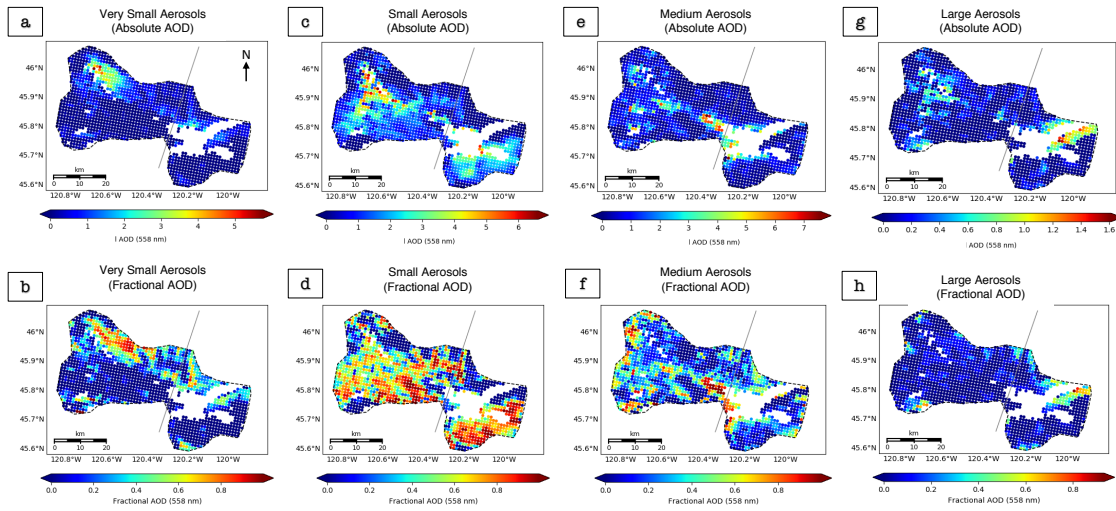


Figure A9. Absolute (top row) and fractional (bottom row) AOD of the four main particle size bins retrieved by the MISR RA for the Colockum Tarps fire. Note: scales differ between categories.

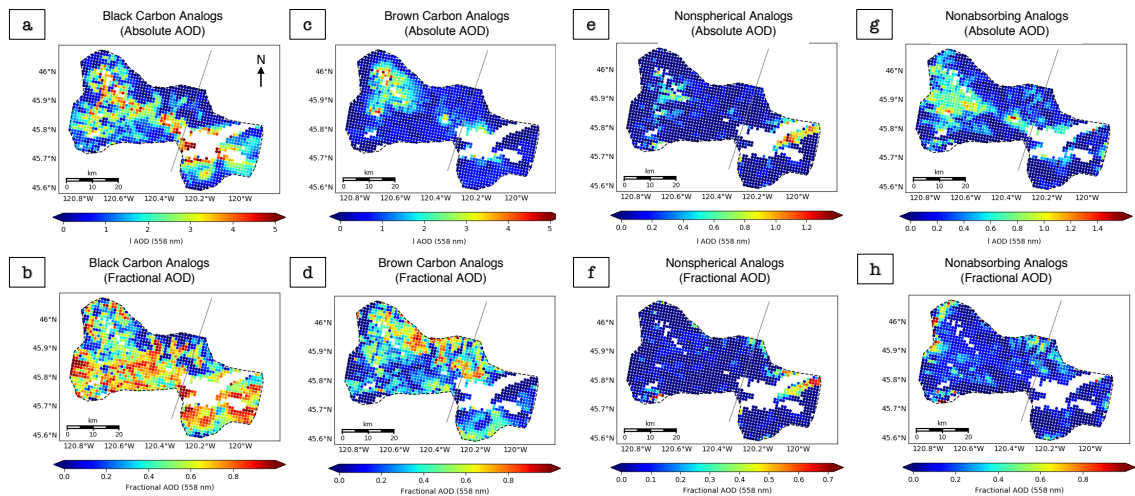


Figure A10. The absolute and fractional AOD of various MISR components, for the Colockum Tarps fire in southern central WA, where (a-b) are the sum of all “flat,” i.e., BIS components, (c-d) are the sum of all “flat,” i.e. BrS components, (e-f) are the non-spherical dust-like component, and (g-h) are the sum of all non-absorbing components.

Douglas Complex Fire: Satellite Observations Preceding Aircraft Observations

The Douglas Complex fire was a large system originally comprised of dozens of lightning-sparked fires that ignited on July 26th, 2013 and burned through August 19th, 2013 in southern coastal Oregon. The fuel was a mixture of old growth and second growth conifer. The August 5th, 2013 MISR overpass and the subsequent August 6th BBOP research flight observed the smoke plumes that were produced (Figure A11). The outline for the *in situ* observations was traced from the MODIS-Terra RGB image at 19:51 UTC (flight operations took place in the area from approximately 19:30-21:00 UTC). As one can see in Figure A11b, the plume outline selected does not fully capture all of the smoke in the scene; it is just meant to provide a reference for the apparent core region of the plume.

MISR Observations of the Douglas Complex Fire

On August 5th the plume had a well-defined plume core (Figure A11a), with AOD exceeding the nominal MISR RA AOD upper limit of 9 (Figure A12d), with a large uncertainty. The plume does not rise above 2.0 km ASL, and median smoke height is ~1.17 km ASL, which is not much above the terrain in this topographically complex region (Figure A12b). Wind speeds are low throughout the observed area (Figure A12c), which might explain the difficulty in locating the plume source, as the smoke tended to pile up over a small area. MISR-retrieved particle size and light-absorption data indicate the plume core is dominated by small-medium, moderately absorbing aerosols ($\text{ANG} \leq 1$, $\text{SSA} \sim 0.87\text{-}0.92$), whereas the surrounding, lower-AOD areas contain smaller, weakly or nonabsorbing particles ($\text{ANG} > 1$, $\text{SSA} \sim 0.92\text{-}1.0$) (Fig. A12e, S12f). Component analysis reflects the higher REPS and REPA in the plume

core than the surroundings (Figures A12-A14). Spectrally steep BrS and non-spherical dust optical analogs are also retrieved, concentrated in the core (Figure A14c-d and e-f, respectively). The retrieved non-spherical component suggests there may be externally mixed dust or soil particles ejected into the atmosphere during intense burning, or a lack of spherical particles of similar size distribution and SSA to the dust analog in the algorithm climatology (Table 2.1 in the main text).

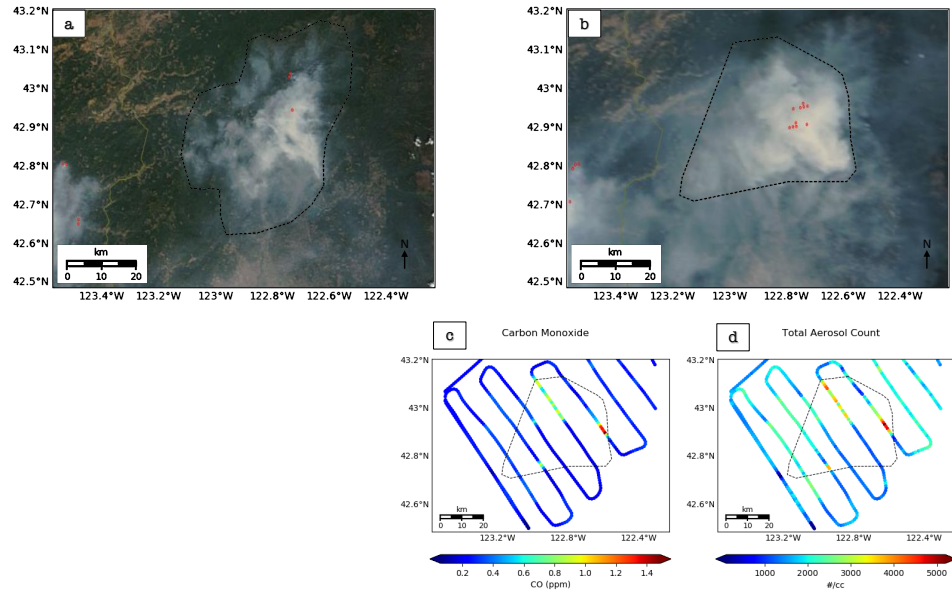


Figure A11. The Douglas Complex fire in southern coastal OR as seen: **(a)** at MISR overpass time on August 5th (19:08 UTC; MODIS Terra RGB image), and **(b)** during BBOP flight operations ~19:30-21:00 UTC on August 6th (19:51 UTC; MODIS Terra RGB image). The red dots indicate MODIS-identified hot spots, and are used to estimate source location. Panels **(c)** and **(d)** are maps of the aircraft CO and Total Aerosol Amount on August 5th, respectively.

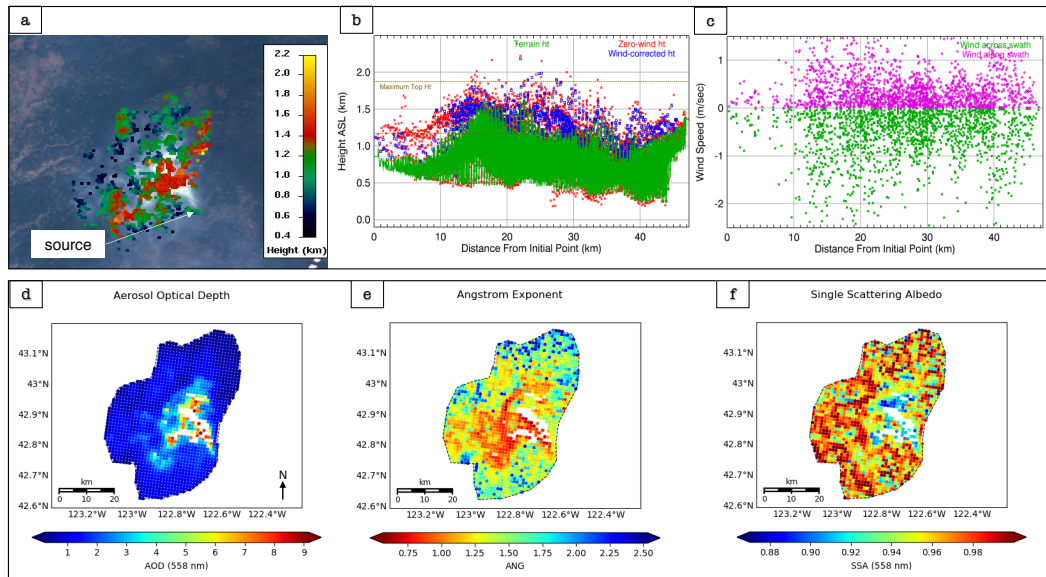


Figure A12. Plume properties for the Douglas Complex fire in southern coastal OR retrieved by MISR at 19:08 UTC (Orbit 72513, Path 45, Block 56). (a) MISR-MINX stereo height retrieval map, (b) MINX stereo height profile as a function of distance from the source, for both zero-wind (red) and wind-corrected (blue) analyses, (c) the across-swath and along-swath wind vectors, (d) the RA-derived AOD at 558 nm, (e) ANG, and (f) the SSA at 558 nm.

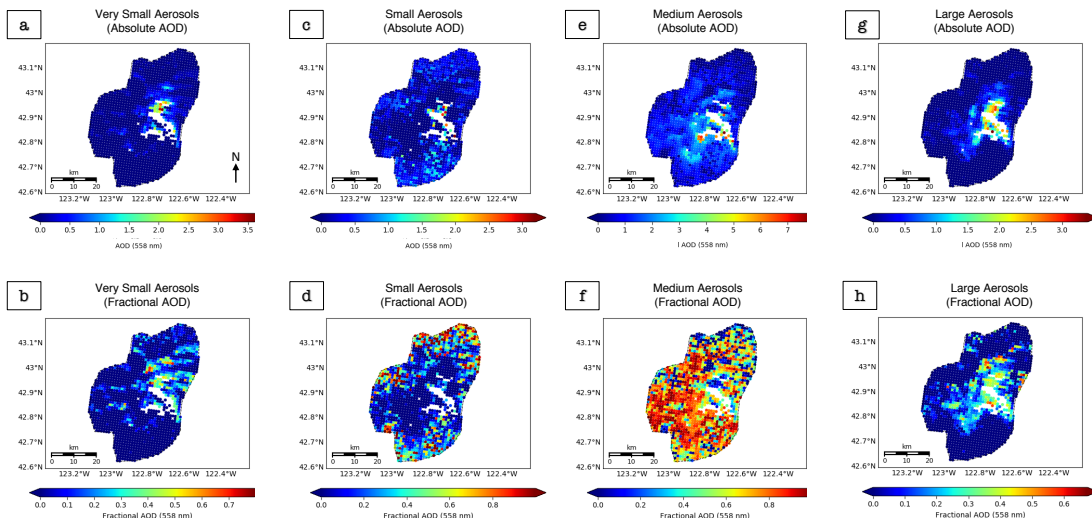


Figure A13. Absolute (top row) and fractional (bottom row) AOD of the four main particle size bins retrieved by MISR for the Douglas Complex fire. Note: scales differ between categories.

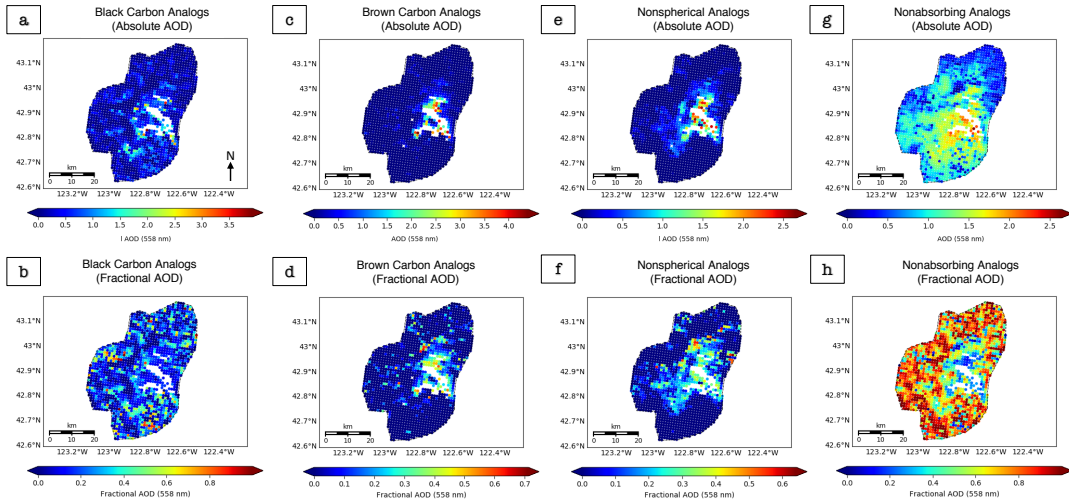


Figure A14. The absolute and fractional AOD of various MISR components for the Douglas Complex fire in southern coastal OR, where (a-b) are the sum of all “flat,” i.e. BC-like components (BIS), (c-d) are the sum of all “flat,” i.e. BrC-like components (BrS), (e-f) are the non-spherical dust-like component, and (g-h) are the sum of all non-absorbing components.

Aircraft Observations and Discussion for the Douglas Complex Fire

The BBOP *in situ* plume observations on the following day describe a scene with an expanded plume core area and considerable, diffuse smoke in the immediate surroundings (Figure A11b). The maximum CO and aerosol concentrations in the available measurements are located near the MODIS-identified hot spots (Figure A11c-d), but the aircraft did not fly directly over these spots, so the actual distribution is ambiguous. The sampled near-source areas also contained some of the brightest and the most highly oxidized particles in the available data record (Fig. A15a, b). However, they also contain the most BC mass of this plume (Figure A15c), though much less than the sampled regions of the Government Flats and July 26th Colockum Tarps fire plumes. (This could be a consequence of the elevation at which the aircraft sampled rather than the peak smoke concentrations of the Douglas Complex fire.) The particles in the plume core are primarily small and medium in size, whereas the

particles in the surroundings are mostly very small and small (Figure A16). BC effective particle size ($r_{e(BC)}$) shows no distinct pattern over the aircraft-sampled region (Fig. A17).

The combined information from the satellite and the aircraft data suggest larger particle sizes in the thickest parts of the plume compared to the surroundings. These particles fall within the small to medium size range; however, the RA retrieves overall slightly larger particles than the aircraft data on the previous day, including a significant contribution from large particles in the plume core. Particles near the source are moderately light-absorbing as seen by MISR (SSA ~ 0.92) but are brighter the next day during flight operations (SSA ~ 0.95), when the fire appears to be a bit more active in the imagery (Figure A11).

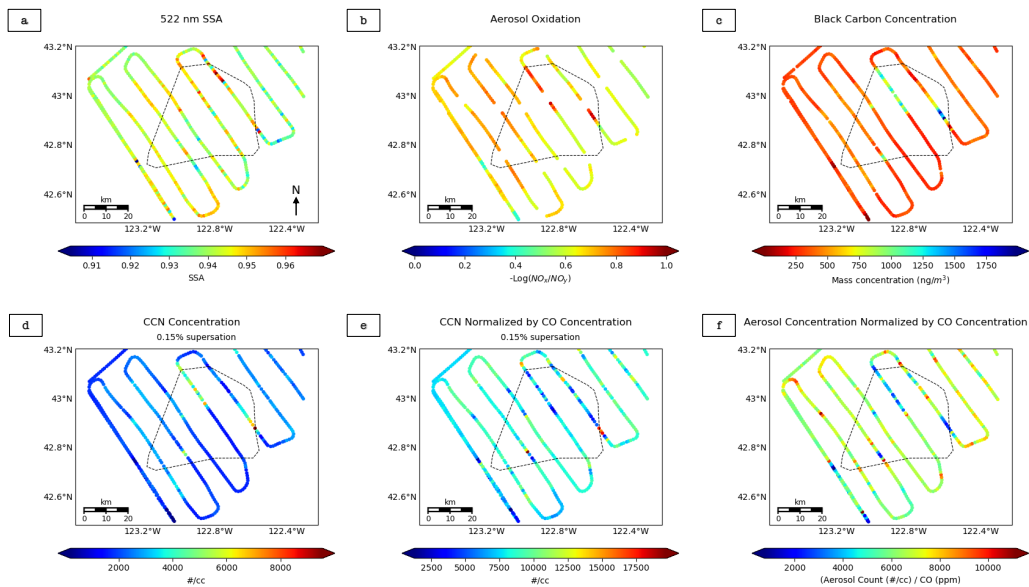


Figure A15. Aircraft observations from the Douglas Complex fire in southern coastal OR of (a) 522-nm SSA (PSAP/neph), (b) aerosol oxidation (derived from 3-channel Oxides of Nitrogen Analyzer), (c) Mass concentration of BC and size of BC-containing particles (SP2), (d) the concentration of particles that can act as CCN at 0.15% supersaturation (CCN-200 instrument), (e) the CCN concentration divided by the CO concentration, and (f) the total aerosol concentration divided by the CO concentration.

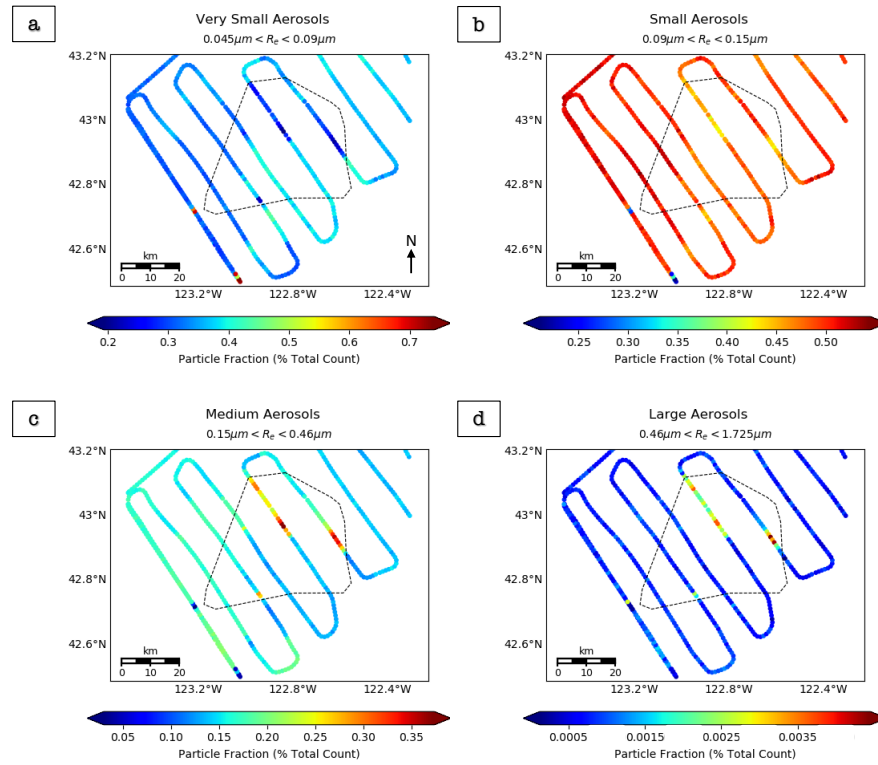


Figure S16. Fractional contributions (from zero to one) to the total aerosol count for very small (**a**), small (**b**), medium (**c**), and large (**d**) aerosols in the Douglas Complex fire in southern coastal OR, as measured by the PCASP and CAS *in situ* instruments. Note: scales differ between categories.

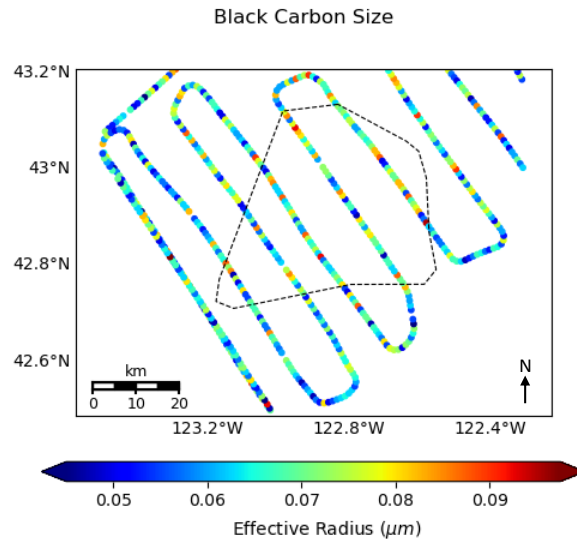


Figure S17. $r_{e(BC)}$ for the Douglas Complex fire, observed by the SP2 aboard the BBOP G-1 aircraft.

Appendix B

In this appendix we provide supplementary information from Chapter 4.

Part I: We present in the first section of this supplement two figures that support the main text and are referenced in the discussion the Williams Flats Fire. In addition, we provide a figure showing the locations of all transverse and longitudinal transects made by the DC-8.

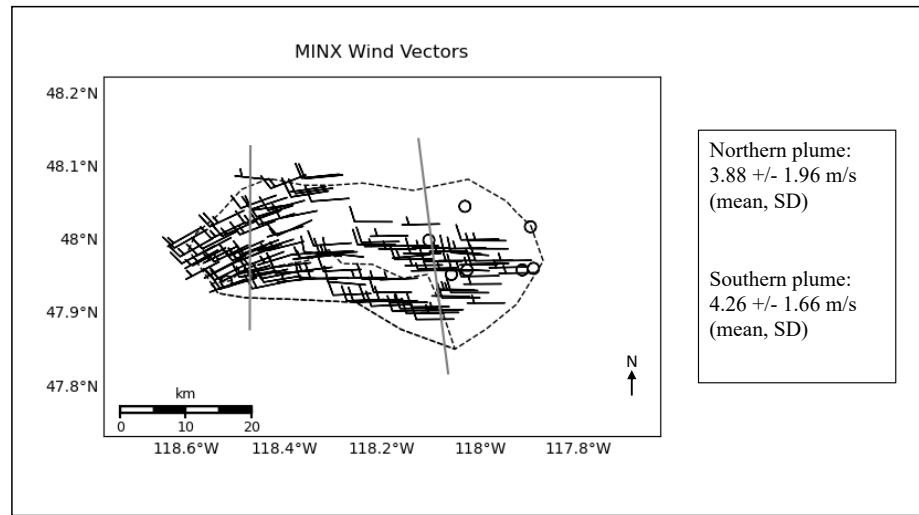


Figure B1. Wind trajectories retrieved from the MISR-MINX software tool (in units of knots) for the Williams Flats Fire. Half-barbs indicate 5 knots, full barbs are 10 knots. The grey lines represent the regional boundaries within the plume (See Fig. 1a). Empty circles are points where the retrieved wind speed was zero. Note: Only every tenth wind vector is plotted here to avoid over-crowding.

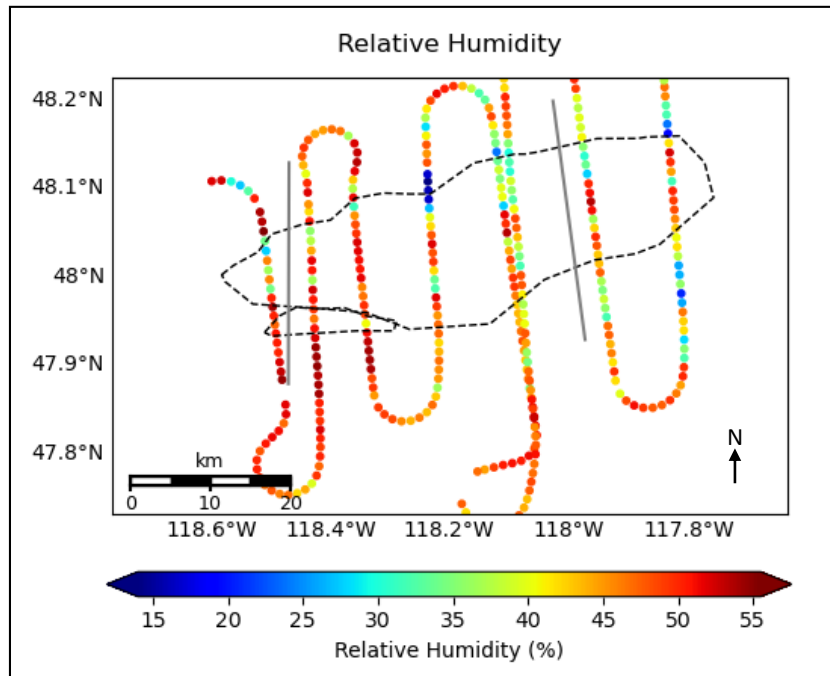


Figure B2. Percent relative humidity observed from the FIREX DC-8 aircraft for the Williams Flats Fire on 06 August 2019.

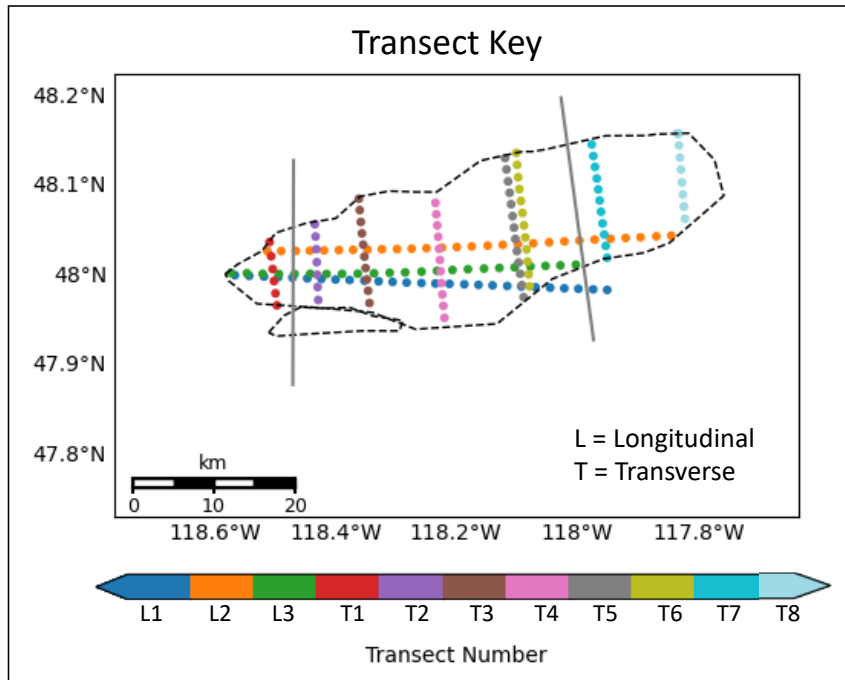


Figure B3. The location of sampling for the eight across-plume transects (T) and three along-plume transects (L).

Part II: We present in the second section of this supplement detailed descriptions of the *in situ* and spacecraft observations collected for the Williams Flats Fire, by transect. We also provide a separate, detailed discussion of the DIAL-HSRL measurements for both along- and across-plume transects, including line-graphs of the relevant measurements as a function of downwind distance from the fire source.

Satellite Observations of the Williams Flats Fire

The sections below use the regional statistical data from Table 4.1 in conjunction with the lat/lon plots in Figures 4.3-5 to characterize in detail each plume region, with emphasis on the *differences* from one to the next. This allows us to both quantify large-scale patterns as well as to visualize small-scale changes, and to account for any differences in sample size.

Region I:

The near-source region, within ~33 min of the source, is strongly characterized by moderate-to-high REPA, with a mean SSA of ~0.87 and a low SD indicating little variability (Figure 4.3, Table 4.1). This can be attributed to: 1) very high mean and median fractions of the spectrally flat, BlS-like component throughout the region (60% and 74% respective contributions to the mid-visible AOD); and 2) smaller AOD fractions of weakly-absorbing non-spherical aerosols (mean ~5%) and moderately absorbing, spectrally steep BrS-like aerosols (mean ~8%), both of which are significant contributors to total AOD along the northern plume edge. Regional REPS is overall small, with a mean extinction Ångström exponent (ANG) of ~1.57;

however, there is some across-plume variability, with slightly larger aerosols retrieved in northern half of the region. Component analysis indicates REPS is the result of a mixture of mostly “small” aerosols, but with significant fractions of “very small” and “large” particles to the north, as per the MISR size categories defined in Table 2.1 in the main text (Figure 4.5).

Region II:

The mid-plume region, with smoke aged \sim 33 to 140 min, displays significantly lower REPA (mean SSA \sim 0.94), characterized by a sharp decrease in the BIS AOD fraction (mean \sim 25%), and a near-doubling of the non-absorbing aerosol fraction (mean \sim 50%). The northern regional edge exhibits significant contributions by both BrS and dust-analog particles, leading to slightly increased regional mean fractions, although their contributions are negligible elsewhere within the region. REPS is also higher than in Region I, with mean ANG reduced to 1.3, but particles are still fine overall except in pixels that contain high fractions of the non-spherical and BrS components. This geographic variability is reflected in component analysis of the four size categories, with the northern edge of the region retrieved as a mixture of large and very small aerosols, whereas the rest of the region is dominated by medium and small particles (Figure 4.5). In general, the regional increase in REPS appears to be driven mostly by increased fractional contributions from medium particles (and to a lesser extent, large particles) accompanied by a decreased fractional contribution from small aerosols. Furthermore, these changes are also reflected in increased *absolute* AOD of the medium particles, and possibly also for the small size category

Region III:

The downwind region, where smoke is estimated to be between about 140 and 200 min from the source, displays a small reduction in REPA (mean SSA ~0.95), reflected in small decreases in each of the absorbing components accompanied by a large increase in the non-absorbing aerosol fraction (mean ~69%). Of the remaining absorbing aerosols, BIS is still by far the dominant contributor, with a mean fraction of over 20%. The absolute AOD of all four aerosol types appears to decrease (Figure 4.4), which suggests that new particle formation is not significant and if it occurs, is outweighed by aerosol removal processes. Regional REPS decreases significantly relative to Region II, with a mean ANG of ~1.52, so aerosols in this region are still larger than those in Region I. The smoke here is retrieved as a mixture of mostly medium-sized particles throughout the region, with lesser contributions from small and very small aerosols (the latter being mostly confined to the northern half of the region) (Figure 4.5). Compared to Region II, there is a significant loss of the large particle fraction and an increase in the small particle fraction, which we interpret as the driver behind the general decrease in effective particle size.

Region IV:

The southern plume region exhibits REPS and REPA that are in-between those seen in Regions I and II of the northern plume, with mean SSA ~0.90 and mean ANG ~1.42. Particles are retrieved as a mixture of primarily BIS-like particles throughout the length of the region, although the BIS particle fraction decreases slightly with downwind distance. Unlike in the northern plume, there is little to no contribution from BrS except for a handful of pixels along the southern border, and

there is a negligible non-spherical aerosol fraction. On average, non-absorbing aerosols comprise at least a third of the AOD fraction, although near the source their contribution is little to none. Particle size is retrieved as nearly exclusively a mixture of small and medium aerosols (Figure 4.5).

Aircraft *in situ* Observations of the Williams Flats Fire

The sections below use the transect statistical data from Table 4.2 and the regional data from Table 4.3 in conjunction with the lat/lon plots in Figures 4.7-8 and particle size distributions from Figure 4.9 to characterize in detail each plume region and transect, with emphasis on the *differences* from one to the next. This allows us to both quantify large-scale patterns as well as to visualize small-scale changes, and to account for any differences in sample size. Occasionally, we abbreviate transects using the letter T followed by the number of the transect (T1, T2, etc.) For the “remote sensing” longitudinal transects, we use the letter L (L1, L2, and L3). Taking the difference in observation timing into account, T1 is near the downwind end of MISR Region I in terms of smoke age, T2-T6 traverse MISR Region 2, and T7 and T8 fall within MISR Region 3 (Figures 4.1, B3). L1 observed the plume within minutes of MISR, whereas L2 and L3 sampled the plume later (refer to Figure B3 for the locations of sampling for all transects). Where possible, we emphasize comparisons between transect-to-transect particle property differences and trends observed by MISR.

Transect 1:

The first aircraft transect only sampled smoke emitted from the northwest source, with an estimated smoke age on the order of 30 minutes. The estimated MCE

of 0.87 suggests burning is a mixture of flaming and smoldering. The mode particle size is firmly within the “very small” size category with peak $D_p=0.148 \mu\text{m}$; however, there is a broad distribution of aerosol size overall (Figure 4.9), and “small” aerosols comprise nearly 30% of the total aerosol fraction on average (Table 4.3, Figure 4.8b). The smoke sampled here is overall relatively fresh ($-\log[\text{NO}_x/\text{NO}_y] \sim 0.37$) and moderately absorbing ($\text{SSA}_{540} \sim 0.928$). Note that the MISR-retrieved mid-visible SSA at the downwind end of Region I is ~ 0.92 or higher, comparable to the T1 values, and greater than the MISR values nearer the source (Figure 4.3d). Furthermore, MISR also suggests that the region is primarily a mixture of small and very small particles (Figure 4.5a-d).

Transect 2:

The second transect sampled smoke with an estimated age of ~ 45 minutes, corresponding to the upwind part of MISR Region II terms of smoke age, although fresher smoke from the southeast hotspot begins to converge with the rest of the plume at this point and so actual smoke age may vary north to south. The influx of new smoke is reflected in a reduction in transect-averaged oxidation and no significant increase in SSA values (~ 0.323 and 0.927 respectively) compared to T1. There are sharp increases in both absolute and dilution-corrected BC, CCN, and total aerosol concentrations relative to T1 (Table 4.2), which are well outside the range of measurement uncertainties. The CO-normalized estimates of BrC-only and BC-only light-absorption also dramatically increase compared to T1, with a particularly strong increase in BC-only light-absorption. The increase in the normalized BC mass and light-absorption are likely due to differential BC emissions relative to CO between

the northwest and southeast hotspots, with the southeast hotspot producing comparably more BC-like smoke particles that are injected into the main plume here. Particle size is also overall smaller and narrower in range at T2, with decreased mean and mode particle size as well as decreased $D_{(90\%)}$ (i.e., the size below which 90% of the particle are found) (Table 4.2). This is also likely due to the influx of fresher smoke, which tends to contain smaller particles. Estimated transect-averaged MCE is slightly higher (~0.89), indicating flaming conditions may have been somewhat more favored for smoke in this transect compared to T1. This would follow from the idea that there are higher BC emissions in this transect as flaming conditions tend to emit higher fractions of BC. Note that, similarly, MISR observes higher fractions of BIS AOD and overall slightly smaller particle size in the southern plume compared to the northern plume (Figure 4.4b, 4.5). Furthermore, the MISR-observed mid-visible SSA in the southern plume is mostly ~0.92 or lower in the approximate sampling location of T2, which may explain why the merged northern and southern smoke in T2 does not exhibit strong changes in SSA despite the decreased REPA in the northern plume component (Figure 4.3d). Lastly, as the northern and southern components are distinct at the time of MISR observation, we do not observe an increased AOD for smoke of similar age, which one might expect from increased CO mixing ratios and aerosol concentrations measured *in situ*.

Transect 3:

Estimates place smoke age in T3 at approximately one hour, about a quarter of the way into MISR Region II in terms of smoke age, and MCE is nearly identical to that in T2. Smoke from the southeast hotspot continues to be mixed into this sample

as it was at T2; this can be seen in the increased CO mixing ratio in Figure 4.1c and further increases in absolute and normalized measurements of BC mass and CCN number concentrations, although the change in BC is just within the range of the SP2 uncertainty. These changes are accompanied by: increases in the mean and median aerosol size ($D_p=0.141$, $D_{(50\%)}=0.155$), increased oxidation state (~0.38), and a relatively static normalized total aerosol count compared to T2. The differences in trends from T2 to T3 compared to trends from T1 to T2 are important: between T1 and T2 we see that increased CO mixing ratio, BC mass, and CCN concentrations are correlated with *smaller* particles of *higher* number concentrations displaying *decreased* levels of aging (oxidation), whereas between T2 and T3 the CO, BC, and CCN trends are correlated with *larger* particles of roughly the *same* number concentration displaying *increased* levels of aging. This *may* suggest that the increase in BC and CCN concentrations reaching T3 is not as driven by the injection of fresher particles as it is by particle growth via coagulative processes, where previously ultrafine BC particles below the size detection limit of the SP2 and LAS (~0.09 μm) have aggregated to form larger aerosols or coalesced onto existing ones. This method of particle growth is known to be important in areas of dense smoke where aerosol concentrations are high, as is the case here, yet the smoke here is considerably downwind from both sources. However, this process would also account for the fact that the normalized aerosol count does not increase with the BC mass, as these particles would just be growing larger rather than more numerous. Additionally, larger and/or more aged particles tend to be more efficient CCN, which would account for the increased CCN number concentration. However, particle growth here

is also likely due to condensational growth. Contrary to expectations, the increased oxidation is not accompanied by an increase in SSA (actually a slight decrease to ~0.924, although, as with the SSA change in T2, this may be within the range of uncertainty of the PSAP/neph measurements). Lastly, this transect exhibits slight enhancements of both BC-only and BrC-only light-absorption of similar magnitude. Note that the increasing aerosol size in T3 corresponds with an increase in REPS from MISR for smoke of similar age in the northern plume. However, as mentioned in the discussion of T2, the MISR plume does not exhibit increased AOD for smoke of similar age since the northern and southern components had not yet merged at the time of MISR observation.

Transect 4:

Burning conditions for smoke observed in T4 are firmly in the flaming category, with MCE ~0.93 (the highest of all transects), and the smoke is estimated at about 85 minutes old at the time of observation, about the middle of MISR Region II in terms of smoke age. The smoke is significantly more oxidized here compared to T3, with $-\log[\text{NO}_x/\text{NO}_y] \sim 0.55$, although again the change in SSA is very small (an increase to 0.928, within the range of instrument uncertainty). Both BC- and BrC-only light-absorption decrease, as do the absolute and normalized measurements of CCN, BC, and total aerosol count, the latter of which is within the range of uncertainty (for the normalized measurement) and so might not be a reliable indicator of true particle dilution or loss. The particle size distribution is essentially identical to that in T3 despite the reduced number concentration, suggesting that if there is particle loss between these transects then it is not size-selective.

Transect 5:

The transect-averaged MCE at T5 slightly decreases to ~0.88 and smoke is estimated at 112 minutes old, roughly three-quarters of the way downwind within MISR Region II in terms of smoke age. Despite a decrease in the mode aerosol size (Peak $D_p=0.134 \mu\text{m}$), at least some particles increase in diameter, as seen by an increased $D_{(90\%)}$; this is accompanied by decreases in the CO-normalized aerosol count and the absolute and normalized CCN number and BC mass concentrations; however, all these differences are within the instruments' uncertainty ranges. Oxidation continues to increase with $-\log[\text{NO}_x/\text{NO}_y] \sim 0.63$, which is accompanied by decreased mid-visible light-absorption (SSA~0.934) and decreases in BrC and BC light-absorption specifically. Note that MISR observes a relatively significant fractional increase in large aerosols for smoke of similar age along the northern edge here, with a corresponding decrease in ANG. The total MISR AOD also decreases in this same area.

Transect 6:

The average MCE in T6 is ~0.89, and smoke age is estimated at 115 minutes old, essentially the same as T5, so differences might better indicate internal plume variability or measurement uncertainty rather than trends in particle evolution. Particle size in T6 is overall slightly larger (Peak $D_p=0.155 \mu\text{m}$ vs. $0.134 \mu\text{m}$ for T5) and with a narrower distribution width compared to T5. Oxidation values differ only slightly (~0.647 compared to ~0.63 for T5). There is a large decrease in both the absolute and normalized BC mass concentration (951 vs. 1120 ng/m^3 and 2.88 vs. $3.33 \text{ ng/ppm}^*\text{m}^3$, respectively), despite a small decrease in SSA (~0.929). The SSA

change is likely driven by an increase in BrC-only light-absorption, which increases for the first time since T3. Particles are also more hygroscopic in T6, with both absolute and normalized CCN concentrations increasing (6567 vs. 5377 #/cc and 19.89 vs. 15.78 #/cc*ppb, respectively). The differences between T5 and T6 illustrate the extent to which measured particle properties can differ for smoke of nearly the same age, placing in context the observed differences between MISR and the DC-8.

Transect 7:

Smoke in T7 is approximately 140 minutes old, emitted with an estimated MCE of 0.89, near the boundary between MISR Regions II and III. Particle oxidation values increase to ~0.734, reflecting a significant change in the degree of aerosol aging at this point. Particle size is slightly larger than what was observed in T6 with increased $D_{(90\%)}$ and $D_{(10\%)}$; however, the normalized total aerosol count is essentially unchanged from that in T6. There is a decrease in both absolute and normalized concentrations of BC mass and CCN number, the former of which is mirrored in decreased BrC and BC light-absorption (leading to an increased SSA of 0.936, the largest single transect-to-transect change). These changes correspond with a similar area of transition for smoke of the same age as seen by MISR, where BIS AOD decreases and SSA increases along the boundary of Regions II and III (Figures 4.3-4.4). Interestingly, there is an increase in the absolute total aerosol count compared to T6, which is most likely due to different sampling, as AOD is apparently not uniformly distributed in this area of the plume according to MISR (Figure 4.3b). Furthermore, smoke in this area approximately corresponds with the points at which MISR observes a decrease in particle size, reflected by a loss of large-size particles.

This diverges from the *in situ* observations, but as explained the main text is likely due to differences in vertical sampling and gravitational settling of larger particles.

Transect 8:

Estimates of smoke age are unavailable for T8 from the aircraft, but it is toward the downwind end of MISR Region III, perhaps close to 200 min from the source. Interestingly, oxidation values indicate the smoke is not as well oxidized as in T7 (~0.687, vs. ~0.734 for T7). Particles are also less hygroscopic and less absorbing (SSA ~0.94), and there is a large increase in particle size, reflected in increased $D_{(50\%)}$ and $D_{(90\%)}$. Furthermore, the width of the distribution is comparatively larger than in T7. This could reflect the influence of background aerosols, as MISR retrievals suggest the background particle size distribution is influenced by all four size categories to some degree, while smoke of similar age to T8 is mainly influenced by medium and small aerosols.

DIAL-HSRL Measurements

Large values of the DIAL-HSRL depolarization ratio are typically driven by ice or dust particles (30-40%) and differ significantly from the less depolarizing particles such as urban pollution or smoke. With few exceptions, the aerosol depolarization ratios (vertical median values) at both 532 and 1064 nm are consistently between 3-6% within the Williams Flats plume (Figures B4-B7), typical of fresh biomass burning smoke [Burton et al., 2013]. There are only small changes in depolarization at both wavelengths along the length of the plume and these are within the variability of the measurement. Furthermore, there is little vertical variation in

the depolarization ratios across the plume, suggesting that any non-spherical component is not stratified within the smoke layer. Within the plume, the less polarizing smoke particles dominate the depolarization values. However, the larger depolarization values seen just outside and above the smoke plume (Figure 4.6 in the main text) suggest that background dust is present in the air layer, which is seen by MISR along the plume's northern edge.

The 1064/532 nm color ratio is typically between 0.5-0.7 inside the plume, with a notable exception in L3, where values as high as 0.9 were observed near the boundary of MISR Regions I and II (Figures B8-B11). Otherwise, only small, unsystematic changes (typically <<0.1) are seen along the length of the plume and between times of observation, which are well within the measurement variability. Burton et al. (2013) indicate ranges of color ratio from fresh smoke to be 0.40-0.48 (note: author uses color ratio as 532/1064 nm). Larger color ratios can indicate larger aerosols; however, there is no clear numerical separation between large and small particles. Although data from the LAS suggest particles increasing in size as the plume evolved, these changes are small enough that they are not reflected in the color ratio observations.

The lidar ratio, for the most part, ranges from \sim 35-45 sr^{-1} throughout the plume, although there are several points where its value exceeds or dips below this range. The values are in line with those previously observed for fresh smoke (Burton et al., 2012, 2013). In all three longitudinal overpasses as well as the across-plume transects, the lidar ratio systematically increases with downwind distance from the source within the first few hours (Figures B8-B11). Existing literature also shows

lower lidar ratios for fresh smoke than aged smoke (e.g, Burton et al., 2012); however “aged” smoke in these studies is sampled at time scales much longer than those observed in the Williams Flats Fire (on the order of 1-2 days rather than several hours old). The reason for the increase in lidar ratio with age requires further investigation, especially over these shorter time scales. In this case, it is generally correlated with decreasing light-absorption, increased particle size, increased oxidation, and variable hygroscopicity observed in Table 4.2. (Note that although the transect-by-transect changes in these properties are often small, they are systematic and significant when taken across the whole plume.) One of these particle property changes might also be acting to decrease the backscatter relative to the extinction (which is the sum of absorption and scattering); this topic requires further study.

On the following pages, Figure B4-B11 illustrate the depolarization, color ratios, and lidar ratios from the DIAL-HSRL instrument for each transect, and Figures B12-B19 illustrate their standard deviation. (We show this variability separately so as to avoid crowding on individual graphs.)

References:

Burton, S. P.; Ferrare, R. A.; Hostetler, C. A.; Hair, J. W.; Rogers, R. R.; Obland, M. D.; Butler, C. F.; Cook, A. L.; Harper, D. B.; Froyd, K. D. Aerosol classification using airborne High Spectral Resolution Lidar measurements – methodology and examples. *Atmos. Meas. Tech.* **2012**, *5*, 73–98, doi:10.5194/amt-5-73-2012.

Burton, S. P.; Ferrare, R. A.; Vaughan, M. A.; Omar, A. H.; Rogers, R. R.; Hostetler, C. A.; Hair, J. W. Aerosol classification from airborne HSRL and comparisons with CALIPSO vertical feature mask. *Atmos. Meas. Tech.*, **2013**, *6*, 1397–1412, doi:10.5194/amt-6-1397-2013.

Dash = total
Solid = aerosol

Depolarization Ratios by Longitudinal Transect – Overpass 1 (19:00 UTC)

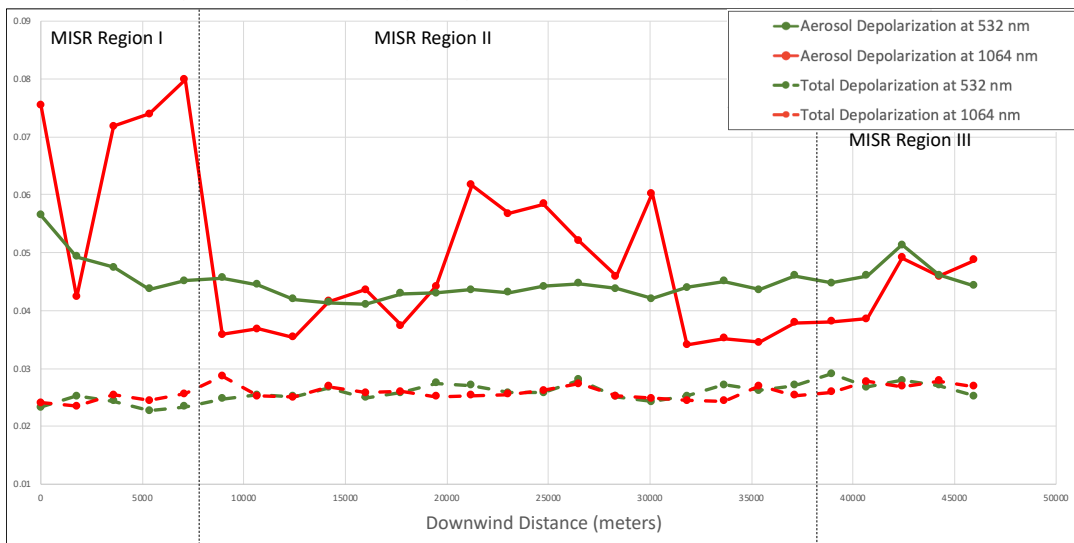


Figure B4. Median total volume and aerosol depolarization values retrieved by the DIAL-HSRL instrument during the first longitudinal overpass at ~19:00 UTC (L1). Indications of the dividing lines between the MISR Regions I-III are provided as dotted lines.

Dash = total
Solid = aerosol

Depolarization Ratios by Longitudinal Transect – Overpass 2 (20:38 UTC)

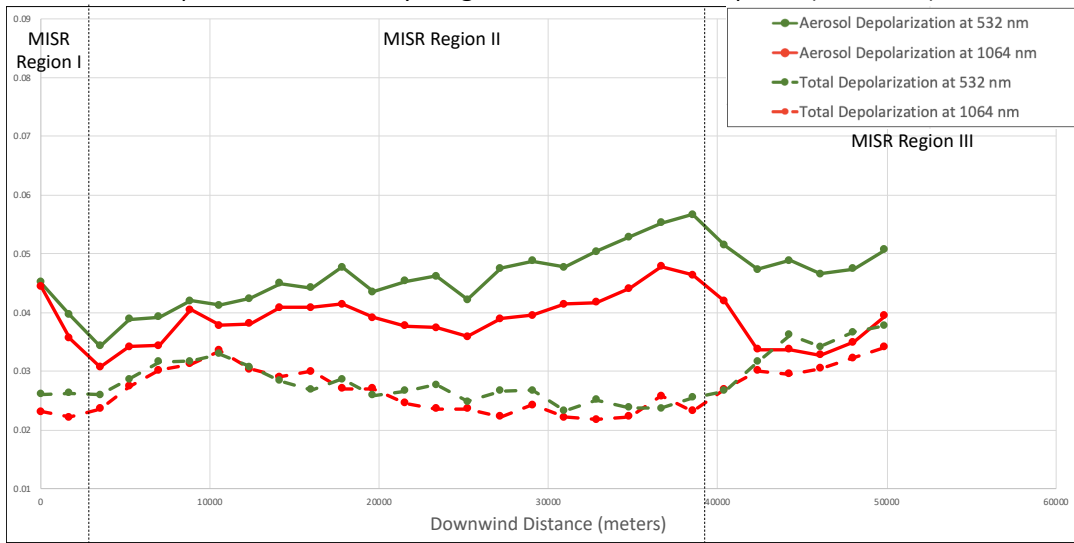


Figure B5. Median total volume and aerosol depolarization values retrieved by the DIAL-HSRL instrument during the second longitudinal overpass at ~20:38 UTC (L2). Indications of the dividing lines between the MISR Regions I-III are provided as dotted lines.

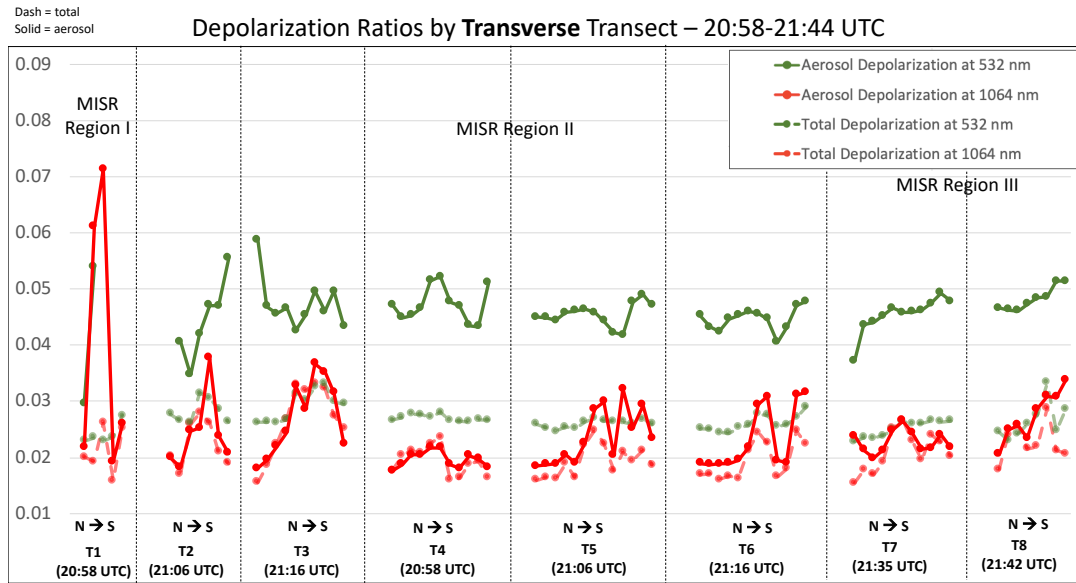


Figure B6. Median total volume and aerosol depolarization values retrieved by the DIAL-HSRL instrument during the eight along-plume transects (T1-T8). The dotted lines separate the transects from one another, the data from which are ordered north to south. Approximate locations of the MISR Regions I-III are labeled.

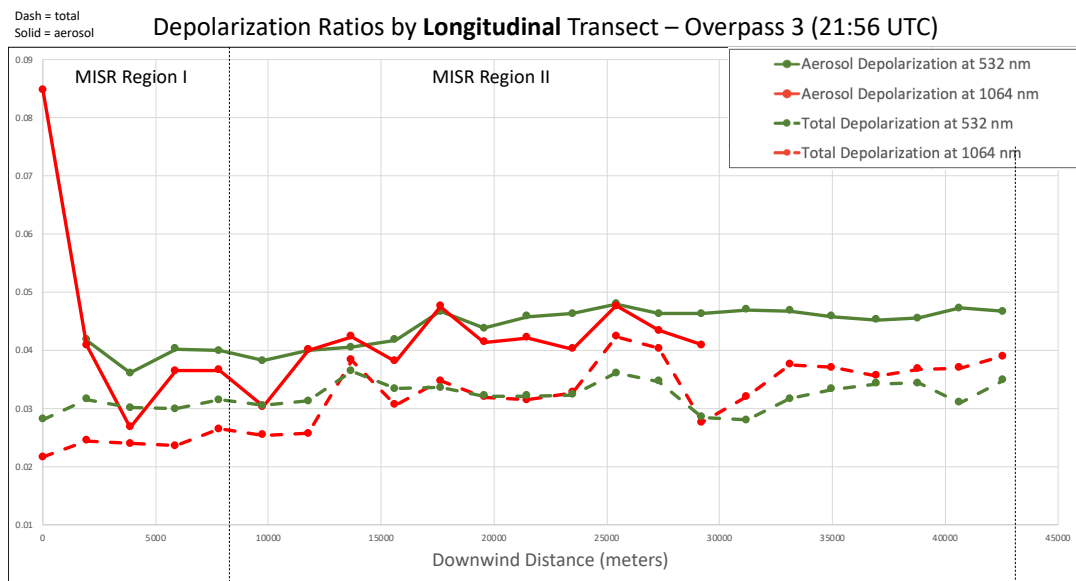


Figure B7. Median total volume and aerosol depolarization values retrieved by the DIAL-HSRL instrument during the third longitudinal overpass at ~21:56 UTC (L3). Indications of the dividing lines between the MISR Regions I-III are provided as dotted lines.

Lidar and Color Ratios by Longitudinal Transect – Overpass 1 (19:00 UTC)

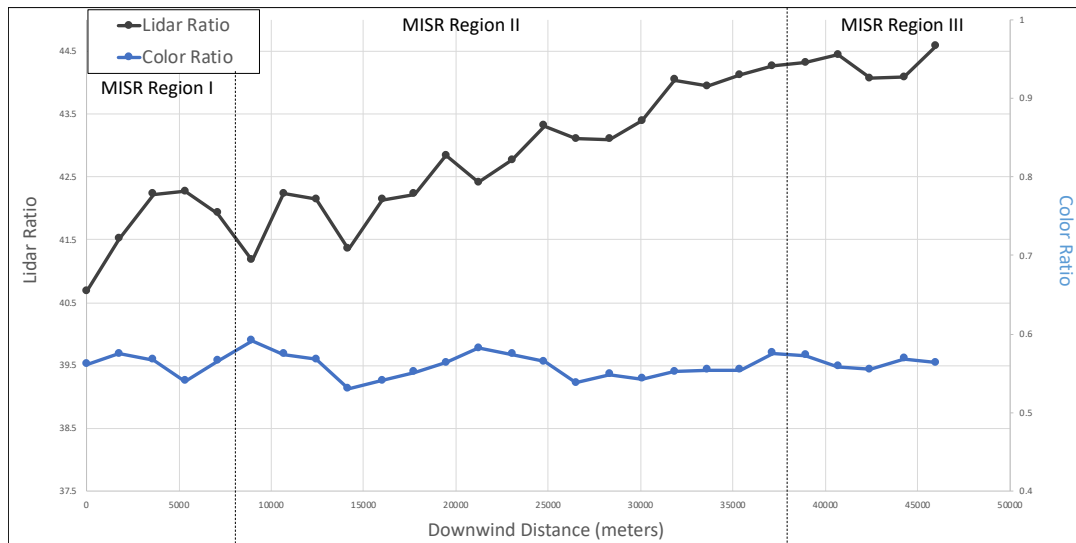


Figure B8. The lidar ratio and color ratio values retrieved by the DIAL-HSRL instrument during the first longitudinal overpass at ~19:00 UTC (L1). Indications of the dividing lines between the MISR Regions I-III are provided as dotted lines.

Lidar and Color Ratios by Longitudinal Transect – Overpass 2 (20:38 UTC)

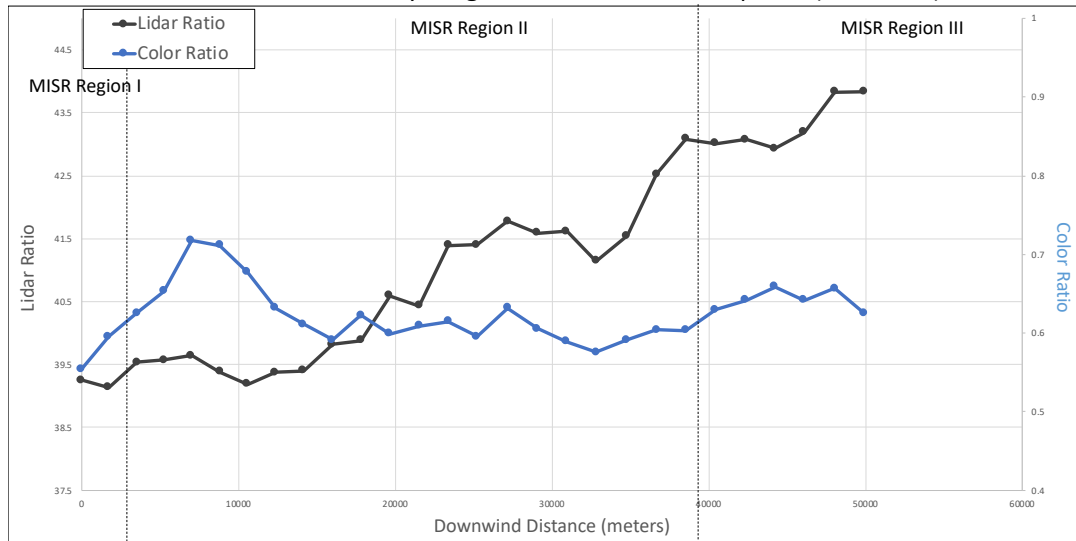


Figure B9. The lidar ratio and color ratio values retrieved by the DIAL-HSRL instrument during the second longitudinal overpass at ~20:38 UTC (L2). Indications of the dividing lines between the MISR Regions I-III are provided as dotted lines.

Lidar and Color Ratios by Transverse Transect – 20:58-21:44 UTC

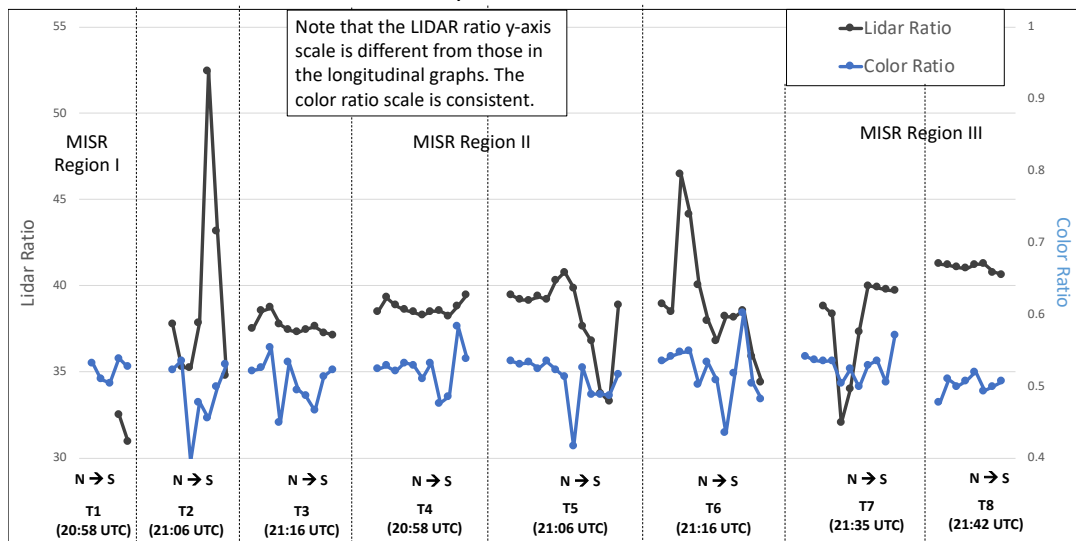


Figure B10. The lidar ratio and color ratio values retrieved by the DIAL-HSRL instrument during the eight along-plume transects (T1-T8). The dotted lines separate the transects from one another, the data from which are ordered north to south. Approximate locations of the MISR Regions I-III are labeled.

Lidar and Color Ratios by Longitudinal Transect – Overpass 3 (21:56 UTC)

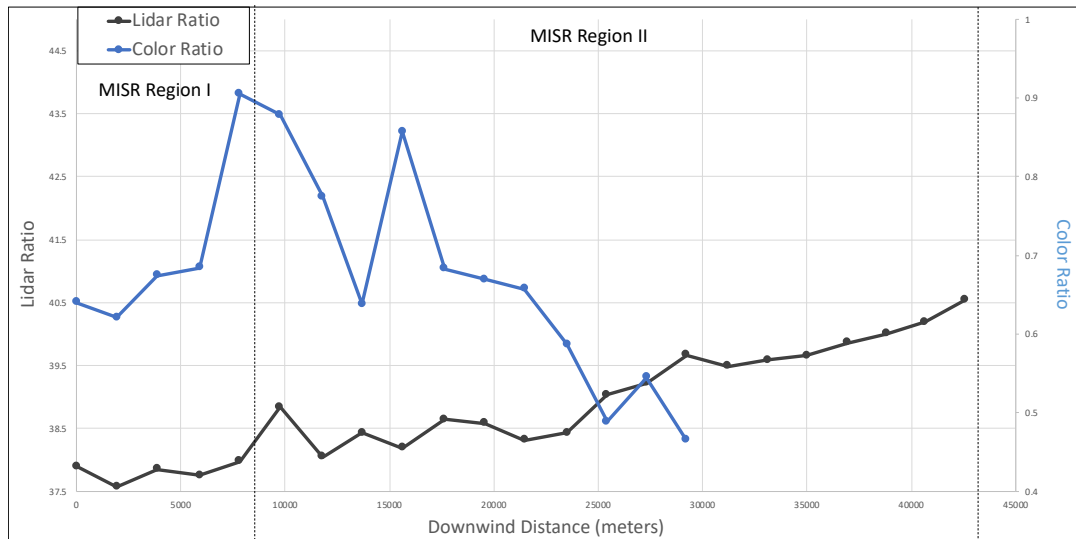


Figure B11. The lidar ratio and color ratio values retrieved by the DIAL-HSRL instrument during the third longitudinal overpass at ~21:56 UTC (L3). Indications of the dividing lines between the MISR Regions I-III are provided as dotted lines.

Dash = total
Solid = aerosol

Depolarization Variability – Overpass 1 (19:00 UTC)

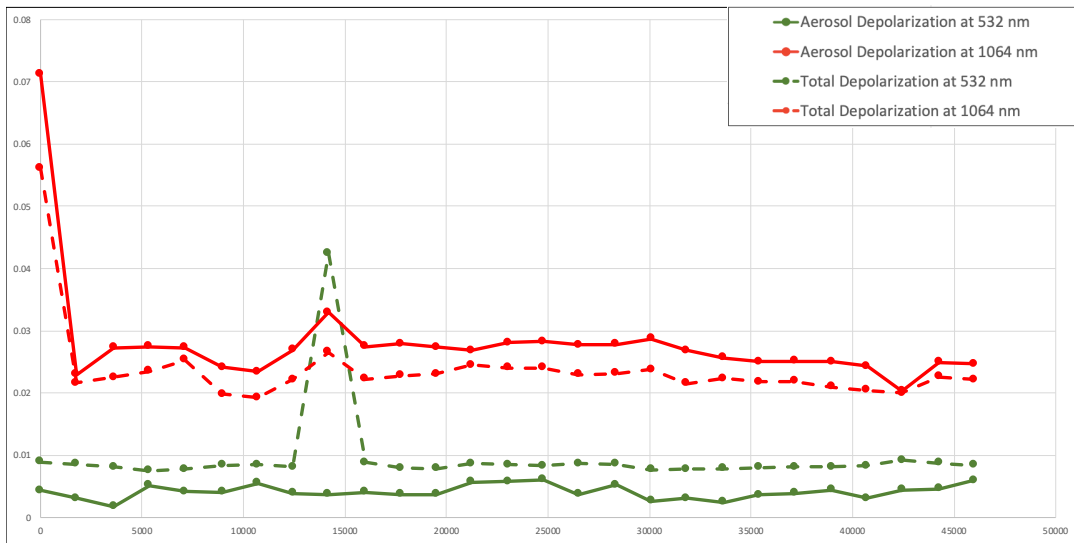


Figure B12. Standard deviation in the total volume and aerosol depolarization values retrieved by the DIAL-HSRL instrument during the first longitudinal overpass at ~19:00 UTC (L1) – Corresponds with B4.

Dash = total
Solid = aerosol

Depolarization Variability– Overpass 2 (20:38 UTC)

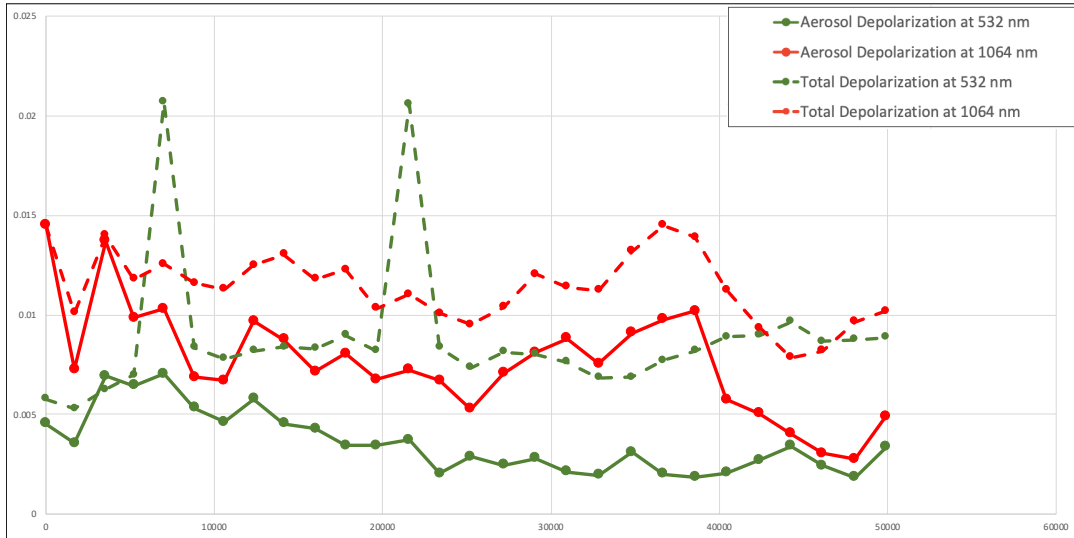


Figure B13. Standard deviation for the total volume and aerosol depolarization values retrieved by the DIAL-HSRL instrument during the second longitudinal overpass at ~20:38 UTC (L2) – Corresponds with B5.

Dash = total
Solid = aerosol

Depolarization Variability – 20:58-21:44 UTC

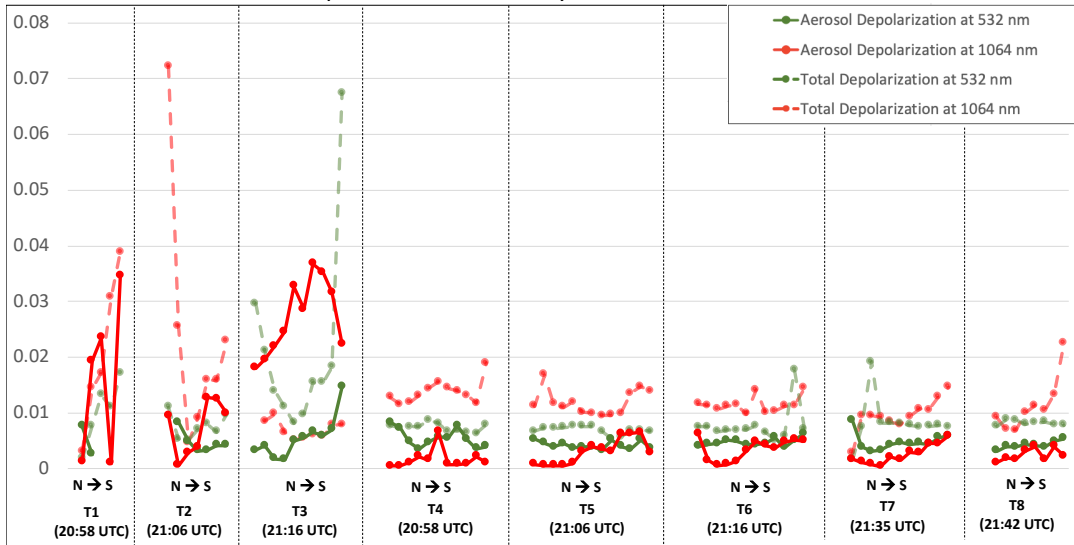


Figure B14. Standard deviation for the total volume and aerosol depolarization values retrieved by the DIAL-HSRL instrument during the eight along-plume transects (T1-T8). The dotted lines separate the transects from one another, the data from which are ordered north to south – *Corresponds with B6*.

Dash = total
Solid = aerosol

Depolarization Variability – Overpass 3 (21:56 UTC)

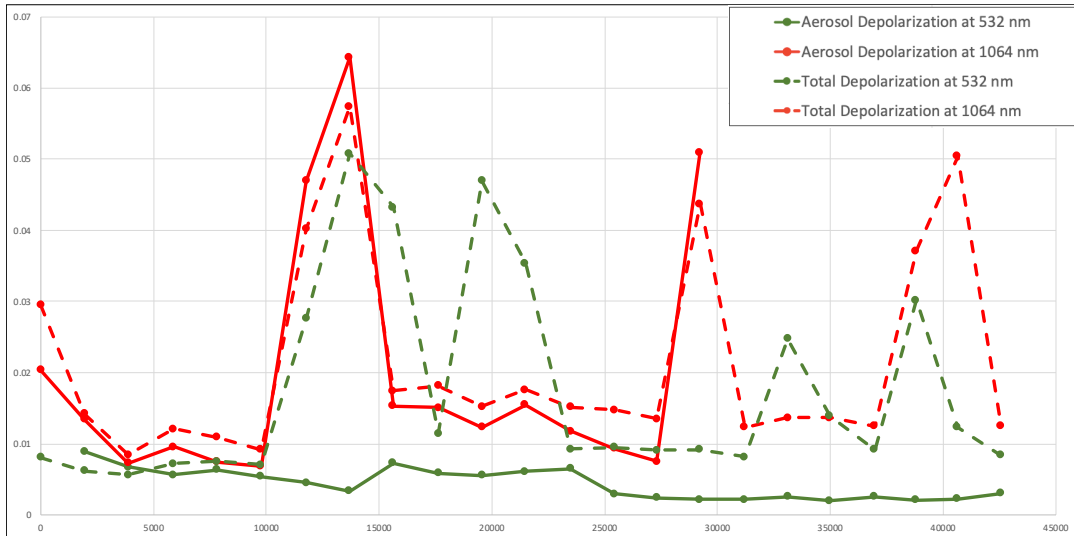


Figure B15. Standard deviation for the total volume and aerosol depolarization values retrieved by the DIAL-HSRL instrument during the third longitudinal overpass at ~21:56 UTC (L3) – *Corresponds with B7*.

Lidar and Color Ratio Variability – Overpass 1 (19:00 UTC)

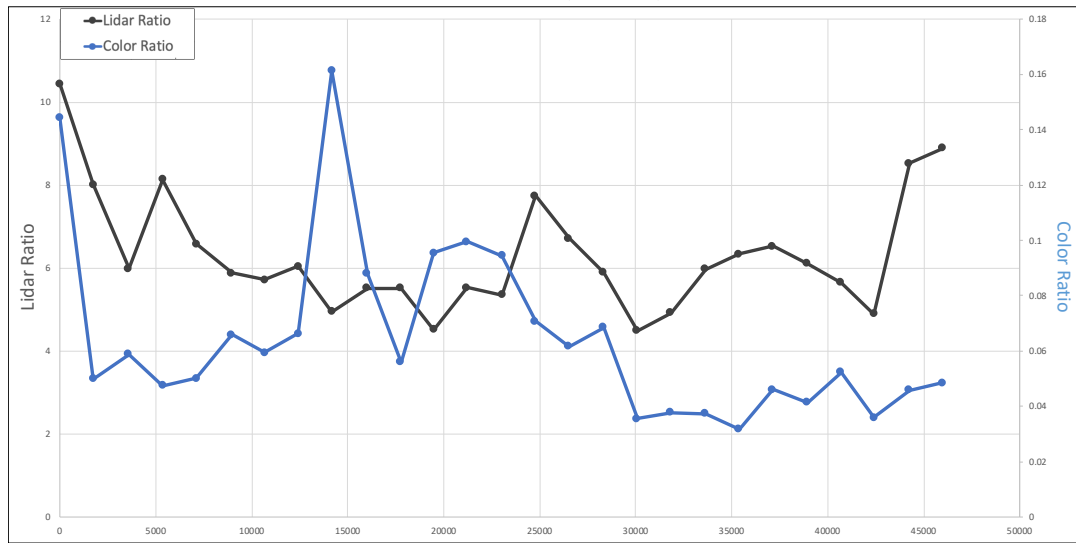


Figure B16. Standard deviation for the lidar ratio and color ratio values retrieved by the DIAL-HSRL instrument during the first longitudinal overpass at ~19:00 UTC (L1) – Corresponds with B8 .

Lidar and Color Ratio Variability – Overpass 2 (20:38 UTC)

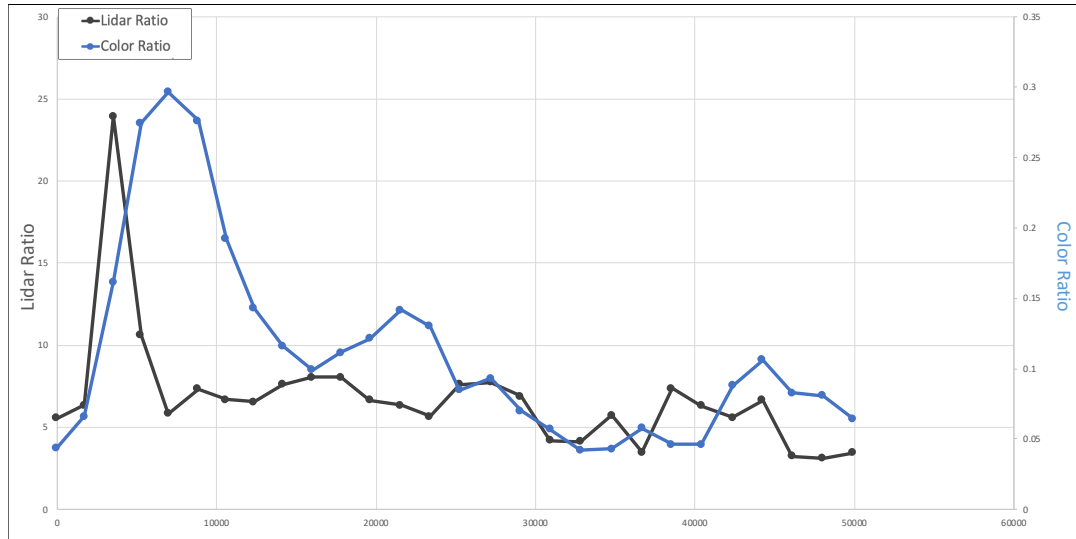


Figure B17. Standard deviation for the lidar ratio and color ratio values retrieved by the DIAL-HSRL instrument during the second longitudinal overpass at ~20:38 UTC (L2) – Corresponds with B9.

Lidar and Color Ratio Variability – 20:58-21:44 UTC

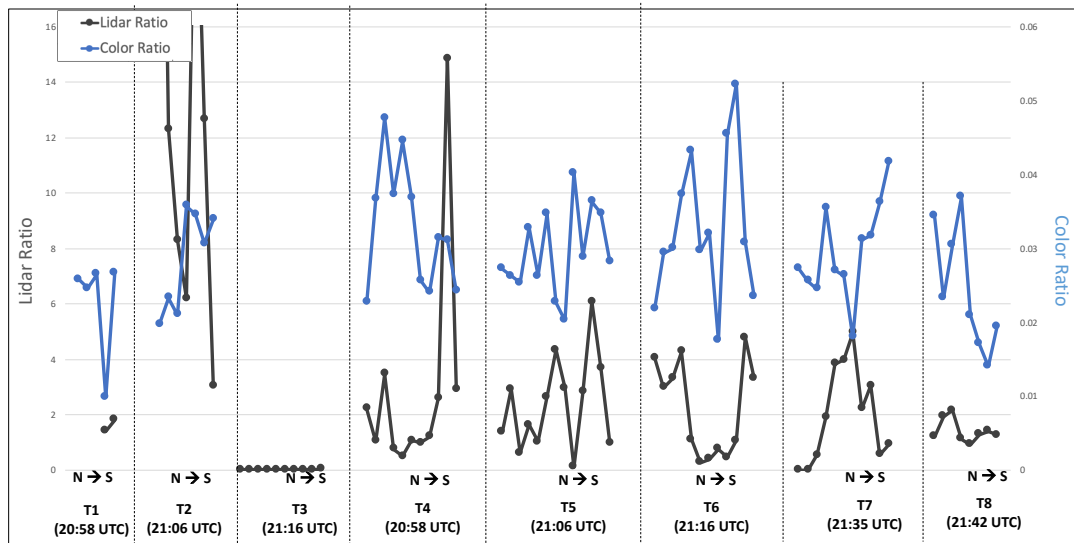


Figure B18. Standard deviation for the lidar ratio and color ratio values retrieved by the DIAL-HSRL instrument during the eight along-plume transects (T1-T8). The dotted lines separate the transects from one another, the data from which are ordered north to south – Corresponds with B10.

Lidar and Color Ratio Variability – Overpass 3 (21:56 UTC)

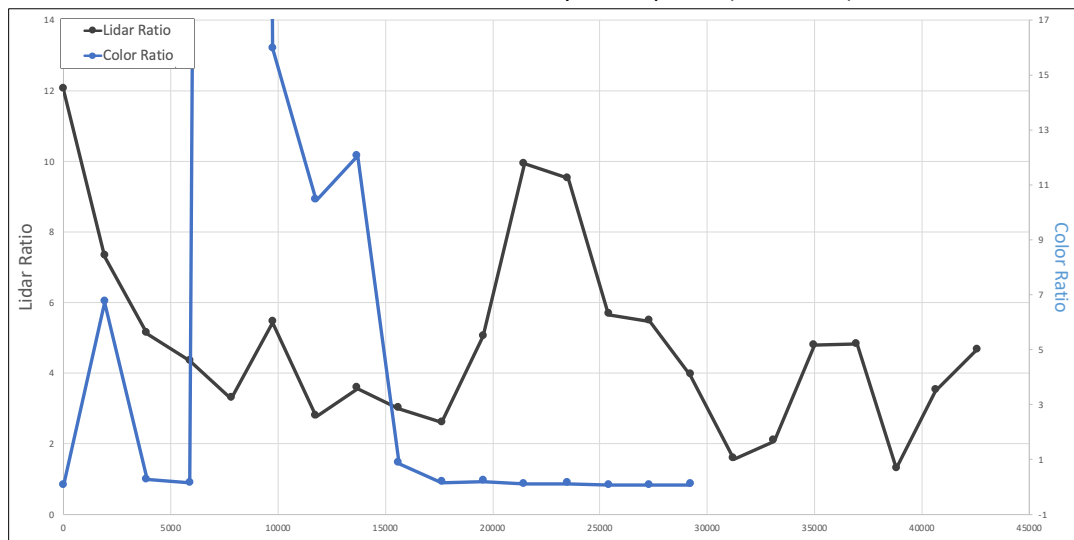


Figure B19. The lidar ratio and color ratio values retrieved by the DIAL-HSRL instrument during the third longitudinal overpass at ~21:56 UTC (L3) – Corresponds with B11.

Appendix C

In this appendix we provide supplementary information from Chapter 5.

Table C1. Land cover type legend for the MODIS International Geosphere-Biosphere Programme (IGBP) classification method (* = observed in this study).

Name	Description
Evergreen Needleleaf Forests *	Dominated by evergreen conifer trees (canopy >2m). Tree cover >60%.
Evergreen Broadleaf Forests *	Dominated by evergreen broadleaf and palmate trees (canopy >2m). Tree cover >60%.
Deciduous Needleleaf Forests *	Dominated by deciduous needleleaf (larch) trees (canopy >2m). Tree cover >60%.
Deciduous Broadleaf Forests *	Dominated by deciduous broadleaf trees (canopy >2m). Tree cover >60%.
Mixed Forests *	Dominated by neither deciduous nor evergreen (40-60% of each) tree type (canopy >2m). Tree cover >60%.
Closed Shrublands	Dominated by woody perennials (1-2m height) >60% cover.
Open Shrublands *	Dominated by woody perennials (1-2m height) 10-60% cover.
Woody Savannas *	Tree cover 30-60% (canopy >2m).
Savannas *	Tree cover 10-30% (canopy >2m).
Grasslands *	Dominated by herbaceous annuals (<2m).
Permanent Wetlands	Permanently inundated lands with 30-60% water cover and >10% vegetated cover.
Croplands	At least 60% of area is cultivated cropland.
Urban and Built-up Lands	At least 30% impervious surface area including building materials, asphalt, and vehicles.
Cropland/Natural Vegetation Mosaics	Mosaics of small-scale cultivation 40-60% with natural tree, shrub, or herbaceous vegetation.
Permanent Snow and Ice	At least 60% of area is covered by snow and ice for at least 10 months of the year.
Barren	At least 60% of area is non-vegetated barren (sand, rock, soil) areas with less than 10% vegetation.
Water Bodies	At least 60% of area is covered by permanent water bodies

Table C2. Land cover type legend for the FAO-Land Cover Classification System (LCCS) surface hydrology classification method.

Name	Description
Dense Forests	Tree cover >60% (canopy >2m).
Open Forests	Tree cover 10-60% (canopy >2m).
Shrublands	Shrub cover >60% (1-2m).
Grasslands	Dominated by herbaceous annuals (<2m) >10% cover.
Woody Wetlands	Shrub and tree cover (>1m) >10% cover. Permanently or seasonally inundated.
Herbaceous Wetlands	Dominated by herbaceous annuals (<2m) >10% cover. Permanently or seasonally inundated.
Tundra	Tree cover <10%. Snow-covered for at least 8 months of the year.
Permanent Snow and Ice	At least 60% of area is covered by snow and ice for at least 10 months of the year.
Barren	At least 60% of area is non-vegetated barren (sand, rock, soil) or permanent snow/ice with less than 10% vegetation.
Water Bodies	At least 60% of area is covered by permanent water bodies.

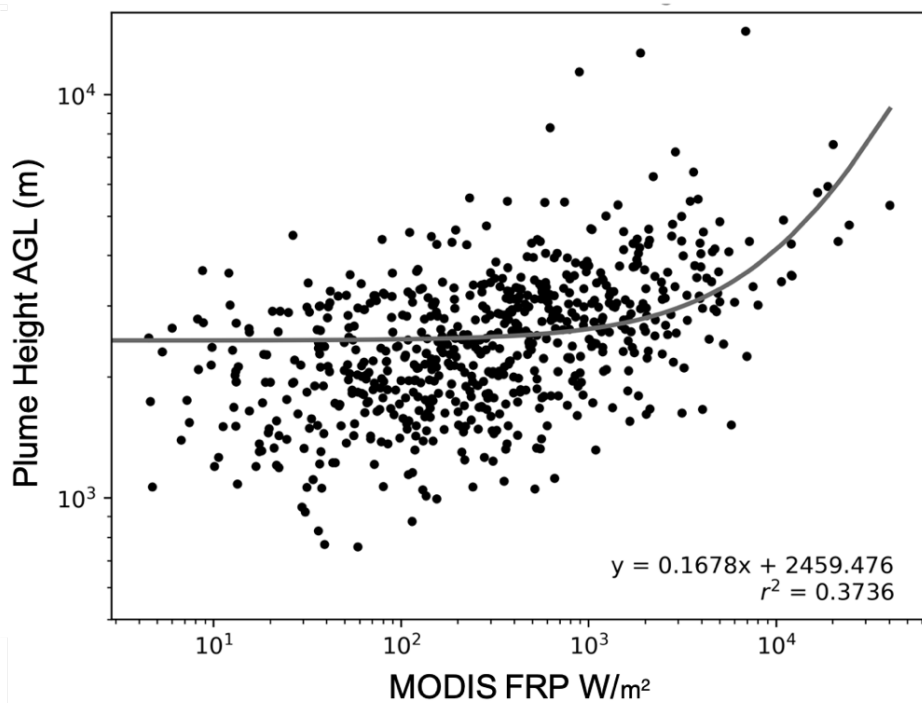


Figure C1. MISR-MINX maximum plume stereo heights vs. total plume FRP from MODIS.

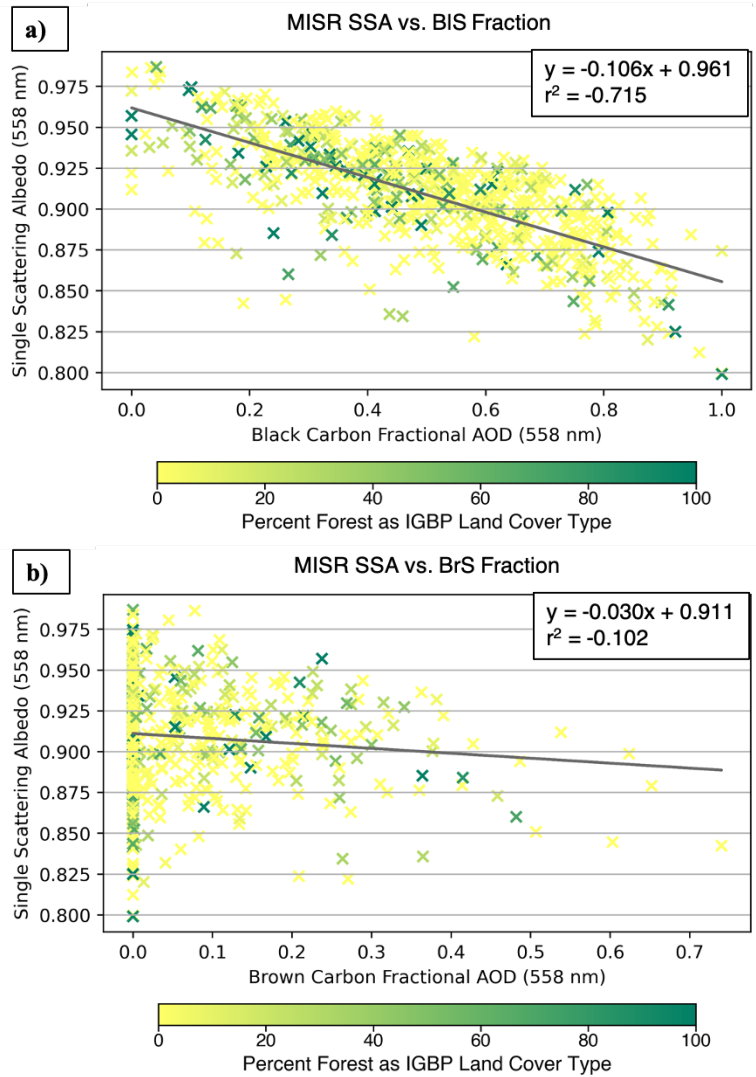


Figure C2. Relationship between MISR SSA and the interpreted amount of **(a)** BIS and **(b)** BrS

Bibliography

Adachi, K.; Sedlacek, A.J.; Kleinman, L.; Springston, S.R.; Wang, J.; Chand, D.; Hubbe, J.M.; Shilling, J.E.; Onasch, T.B.; Kinase, T.; et al. Spherical Tarball Particles Form through Rapid Chemical and Physical Changes of Organic Matter in Biomass-Burning Smoke. *Proc. Natl. Acad. Sci. USA*. **2019**, *116*, 19336–19341. DOI: [10.1073/pnas.1900129116](https://doi.org/10.1073/pnas.1900129116).

Agriculture and Agri-food Canada. ISO 19131 Canadian Drought Monitor – Data Product Specifications. Available Online: https://www.agr.gc.ca/atlas/supportdocument_documentdesupport/canadianDroughtMonitor/en/ISO_19131_Canadian_Drought_Monitor_Data_Product_Specification.pdf.

Ahern, A.T.; Robinson, E.S.; Tkacik, D.S.; Saleh, R.; Hatch, L.E.; Barsanti, K.C.; Stockwell, C.E.; Yokelson, R.J.; Presto, A.A.; Robinson, A.L.; et al. Production of secondary organic aerosol during aging of biomass burning smoke from fresh fuels and its relationship to VOC precursors. *J. Geophys. Res. Atmos.* **2019**, *124*, 3583–3606. DOI: [10.1029/2018JD029068](https://doi.org/10.1029/2018JD029068).

Akagi, S.K.; Craven, J.S.; Taylor, J.W.; McMeeking, G.R.; Yokelson, R.J.; Burling, I.R.; Urbanski, S.P.; Wold, C.E.; Seinfeld, J.H.; Coe, H.; et al. Evolution of Trace Gases and Particles Emitted by a Chaparral Fire in California. *Atmos. Chem. Phys.* **2012**, *12*, 1397–1421. DOI: [10.5194/acp-12-1397-2012](https://doi.org/10.5194/acp-12-1397-2012).

Albrecht, B.A. Aerosols, Cloud Microphysics, and Fractional Cloudiness. *Science* **1989**, *245*, 1227–1230. DOI: [10.1126/science.245.4923.1227](https://doi.org/10.1126/science.245.4923.1227).

Anderson, T.L.; Ogren, J.A. Determining Aerosol Radiative Properties Using the TSI 3563 Integrating Nephelometer. *Aerosol Sci. Technol.* **1998**, *29*, 57–69. DOI: [10.1080/02786829808965551](https://doi.org/10.1080/02786829808965551).

Andreae, M.O.; Gelencser, A. Black Carbon or Brown Carbon? The Nature of Light-Absorbing Carbonaceous Aerosols. *Atmos. Chem. Phys.* **2006**, *18*, 3419–3463. DOI: [10.5194/acp-6-3131-2006](https://doi.org/10.5194/acp-6-3131-2006).

Arnott, W.P. PAS, BBOP. Atmospheric Radiation Measurement Climate Research Facility. **2013**. Available online: <https://adc.arm.gov/discovery/#v/results/s/s::bbop>. (Accessed on 20 December 2019).

Bertschi, I.; Yokelson, R.J.; Ward, D.E.; Babbitt, R.E.; Susott, R.A.; Goode, J. G.; Hao, W.M. Trace gas and particle emissions from fires in large diameter and belowground biomass fuels. *J. Geophys. Res.* **2003**, *108*, 8472. DOI: [10.1029/2002JD002100](https://doi.org/10.1029/2002JD002100).

Bond, T.C.; Anderson, T.L.; Campbell, D. Calibration and Intercomparison of Filter-Based Measurements of Visible Light Absorption by Aerosols. *Aerosol Sci. Technol.* **1999**, *30*, 582–600. DOI: [10.1080/027868299304435](https://doi.org/10.1080/027868299304435).

Bond, T.C.; Doherty, S.J.; Fahey, D.W.; Forster, P.M.; Berntsen, T.; DeAngelo, B.J.; Flanner, M.G.; Ghan, S.; Kärcher, B.; Koch, D.; et al. Bounding the role of black carbon in the climate system: A scientific assessment. *J. Geophys. Res. Atmos.* **2013**, *118*, 5380–5552. DOI: [10.1002/jgrd.50171](https://doi.org/10.1002/jgrd.50171).

Bosilovich, M.; Lucchesi, R.; Suarez, M. MERRA-2: File specification. **2016**. Available online: <https://gmao.gsfc.nasa.gov/pubs/docs/Bosilovich785.pdf>. (Accessed on 20 March 2021).

Burton, S.P.; Ferrare, R.A.; Hostetler, C.A.; Hair, J.W.; Rogers, R.R.; Oblad, M.D.; Butler, C.F.; Cook, A.L.; Harper, D.B.; Froyd, K.D. Aerosol classification using airborne High Spectral Resolution Lidar measurements—Methodology and examples. *Atmos. Meas. Tech.* **2012**, *5*, 73–98. DOI: [10.5194/amt-5-73-2012](https://doi.org/10.5194/amt-5-73-2012).

Burton, S.P.; Ferrare, R.A.; Vaughan, M.A.; Omar, A.H.; Rogers, R.R.; Hostetler, C.A.; Hair, J.W. Aerosol classification from airborne HSRL and comparisons with CALIPSO vertical feature mask. *Atmos. Meas. Tech.* **2013**, *6*, 1397–1412. DOI: [10.5194/amt-6-1397-2013](https://doi.org/10.5194/amt-6-1397-2013).

Burton, S.P.; Hair, J.W.; Kahnert, M.; Ferrare, R.A.; Hostetler, C.A.; Cook, A.L.; Harper, D.B.; Berkoff, T.A.; Seaman, S.T.; Collins, J.E.; et al. Observations of the spectral dependence of linear particle depolarization ratio of aerosols using NASA Langley airborne High Spectral Resolution Lidar. *Atmos. Chem. Phys.* **2015**, *15*, 13453–13473. DOI: [10.5194/acp-15-13453-2015](https://doi.org/10.5194/acp-15-13453-2015).

Burton, S.P.; Vaughan, M.A.; Ferrare, R.A.; Hostetler, C.A. Separating mixtures of aerosol types in airborne High Spectral Resolution Lidar data. *Atmos. Meas. Tech.* **2014**, *7*, 419–436. DOI: [10.5194/amt-7-419-2014](https://doi.org/10.5194/amt-7-419-2014).

Chakrabarty, R.K.; Gyawali, M.; Yatavelli, R.L.N.; Pandey, A.; Watts, A.C.; Knue, J.; Chen, L.-W.A.; Pattison, R.R.; Tsibart, A.; Samburova, V.; et al. Brown Carbon Aerosols from Burning of Boreal Peatlands: Microphysical Properties, Emission Factors, and Implications for Direct Radiative Forcing. *Atmos. Chem. Phys.* **2016**, *16*, 3033–3040. DOI: [10.5194/acp-16-3033-2016](https://doi.org/10.5194/acp-16-3033-2016).

Chakrabarty, R.K.; Moosmüller, H.; Chen, L.-W.A.; Lewis, K.; Arnott, W.P.; Mazzoleni, C.; Dubey, M.K.; Wold, C.E.; Hao, W.M.; Kreidenweis, S.M. Brown Carbon in Tar Balls from Smoldering Biomass Combustion. *Atmos. Chem. Phys.* **2010**, *10*, 6363–6370. DOI: [10.5194/acp-10-6363-2010](https://doi.org/10.5194/acp-10-6363-2010).

Chand, D.; Schmid, B. Nephelometer PSAP, BBOP. Atmospheric Radiation Measurement Climate Research Facility. **2015**. Available online: <https://www.osti.gov/biblio/1461871-nephelometer-psap-bbop>. (Accessed on 30 January 2020).

Chen, W.-T.; Kahn, R.A.; Nelson, D.; Yau, K.; Seinfeld, J.H. Sensitivity of Multiangle Imaging to the Optical and Microphysical Properties of Biomass Burning Aerosols. *J. Geophys. Res.* **2008**, *113*, D10203. DOI: [10.1029/2007JD009414](https://doi.org/10.1029/2007JD009414).

Colarco, P.R.; Schoeberl, M.R.; Doddridge, B.G.; Marufu, L.T.; Torres, O.; Welton, E.J. Transport of Smoke from Canadian Forest Fires to the Surface near Washington, D.C.: Injection Height, Entrainment, and Optical Properties. *J. Geophys. Res.* **2004**, *109*. DOI: [10.1029/2003JD004248](https://doi.org/10.1029/2003JD004248).

Dalirian, M.; Ylisirniö, A.; Buchholz, A.; Schlesinger, D.; Ström, J.; Virtanen, A.; Riipinen, I. Cloud droplet activation of black carbon particles coated with organic compounds of varying solubility. *Atmos. Chem. Phys.* **2018**, *18*, 12477–12489. DOI: [10.5194/acp-18-12477-2018](https://doi.org/10.5194/acp-18-12477-2018).

DeCarlo, P.F.; Dunlea, E.J.; Kimmel, J.R.; Aiken, A.C.; Sueper, D.; Crounse, J.; Wennberg, P.O.; Emmons, L.; Shinozuka, Y.; Clarke, A.; et al. Fast Airborne Aerosol Size and Chemistry Measurements above Mexico City and Central Mexico during the MILAGRO Campaign. *Atmos. Chem. Phys.* **2008**, *8*, 4027–4048. DOI: [10.5194/acp-8-4027-2008](https://doi.org/10.5194/acp-8-4027-2008).

Diner, D.J.; Beckert, J.C.; Reilly, T.H.; Bruegge, C.J.; Conel, J.E.; Kahn, R.A.; Martonchik, J.V.; Ackerman, T.P.; Davies, R.; Gerstl, S.A.W.; et al. Multi-Angle Imaging SpectroRadiometer (MISR) Instrument Description and Experiment Overview. *IEEE Trans.* **1998**, *36*, 1072–1087. DOI: [10.1109/36.700992](https://doi.org/10.1109/36.700992).

Donahue, N.M.; Robinson, A.L.; Trump, E.R.; Riipinen, I.; Kroll, J.H. Volatility and aging of atmospheric organic aerosol. *Top Curr Chem.* **2014**, *339*, 97–143. DOI: [10.1007/128_2012_355](https://doi.org/10.1007/128_2012_355).

Dubovik, O.; Holben, B.; Eck, T.F.; Smirnov, A.; Kaufman, Y.J.; King, M.D.; Tanre, D.; Slutsker, I. Variability of Absorption and Optical Properties of Key Aerosol Types Observed in Worldwide Locations. *J. Atmos. Sci.* **2002**, *59*, 19. DOI: [10.1175/1520-0469\(2002\)059<0590:VOAAOP>2.0.CO;2](https://doi.org/10.1175/1520-0469(2002)059<0590:VOAAOP>2.0.CO;2).

Eck, T.F.; Holben, B.N.; Reid, J.S.; O'Neill, N.T.; Schafer, J.S.; Dubovik, O.; Smirnov, A.; Yamasoe, M.A.; Artaxo, P. High Aerosol Optical Depth Biomass Burning Events: A Comparison of Optical Properties for Different Source Regions. *Geophys. Res. Lett.* **2003**, *30*. DOI: [10.1029/2003GL017861](https://doi.org/10.1029/2003GL017861).

Feng, Y.; Ramanathan, V.; Kotamarthi, V.R. Brown Carbon: A Significant Atmospheric Absorber of Solar Radiation? *Atmos. Chem. Phys.* **2013**, *13*, 8607–8621. DOI: [10.5194/acp-13-8607-2013](https://doi.org/10.5194/acp-13-8607-2013).

FIREX-AQ Science Team. Fire Influence on Regional to Global Environments and Air Quality Campaign [Data set]. NASA Langley Atmospheric Science Data Center DAAC: Hampton, VA, USA, **2019**. DOI: [10.5067/SUBORBITAL/FIREXAQ2019/DATA001](https://doi.org/10.5067/SUBORBITAL/FIREXAQ2019/DATA001).

Flower, V.J.B.; Kahn, R.A. Assessing the Altitude and Dispersion of Volcanic Plumes Using MISR Multi-Angle Imaging from Space: Sixteen Years of Volcanic Activity in the Kamchatka Peninsula, Russia. *J. Volcanol. Geoth. Res.* **2017a**, *337*, 1–15. DOI: [10.1016/j.volgeores.2017.03.010](https://doi.org/10.1016/j.volgeores.2017.03.010).

Flower, V.J.B.; Kahn, R.A. Distinguishing Remobilized Ash From Erupted Volcanic Plumes Using Space-Borne Multiangle Imaging: Remobilized Ash Plumes. *Geophys. Res. Lett.* **2017b**, *44*, 10772–10779. DOI: [10.1002/2017GL074740](https://doi.org/10.1002/2017GL074740).

Flower, V.J.B.; Kahn, R.A. Karymsky Volcano Eruptive Plume Properties Based on MISR Multi-Angle Imagery and the Volcanological Implications. *Atmos. Chem. Phys.* **2018**, *18*, 3903–3918. DOI: [10.5194/acp-18-3903-2018](https://doi.org/10.5194/acp-18-3903-2018).

Flower, V.J.B.; Kahn, R.A. Interpreting the Volcanological Processes of Kamchatka, Based on Multi-Sensor Satellite Observations. *Remote Sens. Environ.* **2020a**, *237*, 111585. DOI: [10.1016/j.rse.2019.111585](https://doi.org/10.1016/j.rse.2019.111585).

Flower, V.J.B.; Kahn, R.A. The evolution of Icelandic volcano emissions, as observed from space in the era of NASA's Earth Observing System (EOS). *J. Geophys. Res. Atmos.* **2020b**, *125*, e2019JD031625. DOI: [10.1029/2019JD031625](https://doi.org/10.1029/2019JD031625).

Forrister, H.; Liu, J.; Scheuer, E.; Dibb, J.; Ziembra, L.; Thornhill, K.L.; Anderson, B.; Diskin, G.; Perring, A.E.; Schwarz, J.P.; et al. Evolution of Brown Carbon in Wildfire Plumes. *Geophys. Res. Lett.* **2015**, *42*, 4623–4630. DOI: [10.1002/2015GL063897](https://doi.org/10.1002/2015GL063897).

Friedl, M.; Sulla-Menashe, D. MCD12Q1 MODIS/Terra+Aqua Land Cover Type Yearly L3 Global 500m SIN Grid V006 [Data set]. NASA EOSDIS Land Processes DAAC. 2019. DOI: [10.5067/MODIS/MCD12Q1.006](https://doi.org/10.5067/MODIS/MCD12Q1.006).

Garofalo, L.A.; Pothier, M.A.; Levin, E.J.T.; Campos, T.; Kreidenweis, S.M.; Farne, D.K. Emission and Evolution of Submicron Organic Aerosol in Smoke from Wildfires in the Western United States. *ACS Earth Space Chem.* **2019**, *3*(7), 1237–1247. DOI: [10.1021/acsearthspacechem.9b00125](https://doi.org/10.1021/acsearthspacechem.9b00125).

Gelaro, R.; McCarty, W.; Suárez, M. J.; Todling, R.; Molod, A.; Takacs, L.; Randles, C. A.; Darmenov, A.; Bosilovich, M.G.; Reichle, R.; Wargan, K.; Coy, L.; Cullather, R.; et al. The Modern-Era Retrospective Analysis for Research and Applications, Version 2 (MERRA-2). *J. of Climate* **2017**, *30*(14), 5419–5454. DOI: [10.1175/JCLI-D-16-0758.1](https://doi.org/10.1175/JCLI-D-16-0758.1).

Giglio, L.; Descloitres, J.; Justice, C. O.; Kaufman, Y. J. An enhanced contextual fire detection algorithm for MODIS. *Remote Sens. Environ.* **2003**, *87*, 273–282. DOI: [10.1016/S0034-4257\(03\)00184-6](https://doi.org/10.1016/S0034-4257(03)00184-6).

Giglio, L.; Justice, C. MOD14 MODIS/Terra Thermal Anomalies/Fire 5-Min L2 Swath 1km V006 [Data set]. NASA EOSDIS Land Processes DAAC. **2015**. DOI: [10.5067/MODIS/MOD14.006](https://doi.org/10.5067/MODIS/MOD14.006).

Gonzalez-Alonso, L.; Val Martin, M.; Kahn, R.A. Biomass burning smoke heights over the Amazon observed from the space. *Atmos. Chem. Phys.* **2019**, *19*, 1685–1702. DOI: [10.5194/acp-19-1685-2019](https://doi.org/10.5194/acp-19-1685-2019).

Hair, J.W.; Hostetler, C.A.; Cook, A.L.; Harper, D.B.; Ferrare, R.A.; Mack, T.L.; Welch, W.; Izquierdo, L.R.; Hovis, F.E. Airborne High Spectral Resolution Lidar for profiling aerosol optical properties. *Appl. Opt.* **2008**, *47*, 6734–6752. DOI: [10.1364/AO.47.006734](https://doi.org/10.1364/AO.47.006734).

Hansen, J.; Sato, M.; Ruedy, R. Radiative forcing and climate response. *J. Geophys. Res.* **1997**, *102*. DOI: [10.1029/96JD03436](https://doi.org/10.1029/96JD03436).

Heim, R.R., Jr. A Review of Twentieth-Century Drought Indices Used in the United States. *Bulletin of the American Meteorological Society* **2002**, *83*(8), 1149–1166. DOI: [10.1175/1520-0477-83.8.1149](https://doi.org/10.1175/1520-0477-83.8.1149).

Hennigan, C.J.; Westervelt, D.M.; Riipinen, I.; Engelhart, G.J.; Lee, T.; Collett, J.L.; Pandis, S.N.; Adams, P.J.; Robinson, A.L. New particle formation and growth in biomass burning plumes: An important source of cloud condensation nuclei. *Geophys. Res. Lett.* **2012**, *39*, L09805. DOI: [10.1029/2012GL050930](https://doi.org/10.1029/2012GL050930).

Hobbs, P.V.; Radke, L.F. Cloud Condensation Nuclei from a Simulated Forest Fire. *Science* **1969**, *163*, 279–280. DOI: [10.1126/science.163.3864.279](https://doi.org/10.1126/science.163.3864.279).

Hodshire, A.L.; Bian, Q.; Ramnarine, E.; Lonsdale, C.R.; Alvarado, M.J.; Kreidenweis, S.M.; Jathar, S.H.; Pierce, J.R. More than emissions and chemistry: Fire size, dilution, and background aerosol also greatly influence near-field biomass burning aerosol aging. *J. Geophys. Res. Atmos.* **2019**, *124*, 5589–5611. DOI: [10.1029/2018JD029674](https://doi.org/10.1029/2018JD029674).

Holben, B.N.; Kim, J.; Sano, I.; Mukai, S.; Eck, T.F.; Giles, D.M.; Schafer, J.S.; Sinyuk, A.; Slutsker, I.; Smirnov, A.; et al. An overview of mesoscale aerosol processes, comparisons, and validation studies from DRAGON networks. *Atmos. Chem. Phys.* **2018**, *18*, 655–671. DOI: [10.5194/acp-18-655-2018](https://doi.org/10.5194/acp-18-655-2018).

InciWeb. Available online: <https://inciweb.nwcg.gov/incident/6493/>. (Accessed on 12 August 2020).

Jethva, H.; Torres, O. Satellite-Based Evidence of Wavelength-Dependent Aerosol Absorption in Biomass Burning Smoke Inferred from Ozone Monitoring Instrument. *Atmos. Chem. Phys.* **2011**, *11*, 10541–10551. DOI: [10.5194/acp-11-10541-2011](https://doi.org/10.5194/acp-11-10541-2011).

Junghenn Noyes, K.; Kahn, R.; Sedlacek, A.; Kleinman, L.; Limbacher, J.; Li, Z. Wildfire Smoke Particle Properties and Evolution, from Space-Based Multi-Angle Imaging. *Remote Sens.* **2020a**, *12*, 769. DOI: [10.3390/rs12050769](https://doi.org/10.3390/rs12050769).

Junghenn Noyes, K.; Kahn, R.A.; Limbacher, J.A.; Li, Z.; Fenn, M.A.; Giles, D.M.; Hair, J.W.; Katich, J.M.; Moore, R.H.; Robinson, C.E.; Sanchez, K.J.; Shingler, T.J.; Thornhill, K.L.; Wiggins, E.B.; Winstead, E.L. Wildfire Smoke Particle Properties and Evolution, From Space-Based Multi-Angle Imaging II: The Williams Flats Fire during the FIREX-AQ Campaign. *Remote Sens.* **2020b**, *12*, 3823. DOI: [10.3390/rs12223823](https://doi.org/10.3390/rs12223823).

Kahn, R.A. A global perspective on wildfires. *EOS Am. Geophys. Union* **2020**, *101*. DOI: [10.1029/2020EO138260](https://doi.org/10.1029/2020EO138260).

Kahn, R.A.; Banerjee, P.; McDonald, D. Sensitivity of multiangle imaging to natural mixtures of aerosols over ocean. *J. Geophys. Res.* **2001**, *106*(D16), 18219–18238. DOI: [10.1029/2000JD900497](https://doi.org/10.1029/2000JD900497).

Kahn, R.A.; Chen, Y.; Nelson, D.L.; Leung, F.-Y.; Li, Q.; Diner, D.J.; Logan, J.A. Wildfire Smoke Injection Heights: Two Perspectives from Space. *Geophys. Res. Lett.* **2008**, *35*, L04809. DOI: [10.1029/2007GL032165](https://doi.org/10.1029/2007GL032165).

Kahn, R.A.; Gaitley, B.J. An Analysis of Global Aerosol Type as Retrieved by MISR: MISR Aerosol Type. *J. Geophys. Res. Atmos.* **2015**, *120*, 4248–4281. DOI: [10.1002/2015JD023322](https://doi.org/10.1002/2015JD023322).

Kahn, R.A.; Gaitley, B.J.; Garay, M.J.; Diner, D.J.; Eck, T.; Smirnov, A.; Holben, B.N. Multiangle Imaging SpectroRadiometer global aerosol product assessment by comparison with the Aerosol Robotic Network. *J. Geophys. Res.* **2010**, *115*, D23209. DOI: [10.1029/2010JD014601](https://doi.org/10.1029/2010JD014601).

Kahn, R. A.; Li, W.-H.; Moroney, C.; Diner, D. J.; Martonchik, J. V.; Fishbein, E. Aerosol source plume physical characteristics from space-based multiangle imaging. *J. Geophys. Res.* **2007**, *112*, D11205. DOI: [10.1029/2006JD007647](https://doi.org/10.1029/2006JD007647).

Kahn, R.A.; Limbacher, J. Eyjafjallajökull Volcano Plume Particle-Type Characterization from Space-Based Multi-Angle Imaging. *Atmos. Chem. Phys.* **2012**, *12*, 9459–9477. DOI: [10.5194/acp-12-9459-2012](https://doi.org/10.5194/acp-12-9459-2012).

Kaufman, Y.J.; Fraser, R.S. The Effect of Smoke Particles on Clouds and Climate Forcing. *Science* **1997**, *277*, 1636–1639. DOI: <http://doi.org/10.1126/science.277.5332.1636>.

Kirchstetter, T.W.; Novakov, T.; Hobbs, P.V. Evidence that the spectral dependence of light absorption by aerosols is affected by organic carbon. *J. Geophys. Res. Atmos.* **2004**, *109*, D21208. DOI: [10.1029/2004JD004999](https://doi.org/10.1029/2004JD004999).

Kleinman, L.I.; Sedlacek, A.J. Biomass Burning Observation Project Science Plan; DOE/SC-ARM; Brookhaven National Laboratory (BNL): Upton, NY, USA, **2013**. Available online: <https://www.arm.gov/publications/programdocs/doe-sc-arm-13-014.pdf?id=4>. (Accessed on 10 August 2019).

Kleinman, L.I.; Sedlacek, A.J. Biomass Burning Observation Project (BBOP): Final Campaign Report; DOE ARM Climate Research Facility: Washington, DC, USA, **2016**. DOI: [10.2172/1236490](https://doi.org/10.2172/1236490)

Kleinman, L.I.; Springston, S.R.; Daum, P.H.; Weinstein-Lloyd, J.; Alexander, M.L.; Hubbe, J.; Ortega, J.; Canagaratna, M.R.; Jayne, J. The Time Evolution of Aerosol Composition over the Mexico City Plateau. *Atmos. Chem. Phys.* **2008**, *17*, 14461–14509. DOI: [10.5194/acp-8-1559-2008](https://doi.org/10.5194/acp-8-1559-2008).

Koch, D.; Del Genio, A.D. Black carbon semi-direct effects on cloud cover: Review and synthesis. *Atmos. Chem. Phys.* **2010**, *10*, 7685–7696. DOI: [10.5194/acp-10-7685-2010](https://doi.org/10.5194/acp-10-7685-2010).

Konovalov, I.B.; Beekmann, M.; Berezin, E.V.; Formenti, P.; Andreae, M.O. Probing into the Aging Dynamics of Biomass Burning Aerosol by Using Satellite Measurements of Aerosol Optical Depth and Carbon Monoxide. *Atmos. Chem. Phys.* **2017**, *17*, 4513–4537. DOI: [10.5194/acp-17-4513-2017](https://doi.org/10.5194/acp-17-4513-2017).

Konovalov, I.B.; Beekmann, M.; Golovushkin, N.A.; Andreae, M.O. Nonlinear behavior of organic aerosol in biomass burning plumes: A microphysical model analysis. *Atmos. Chem. Phys.* **2019**, *19*, 12091–12119. DOI: [10.5194/acp-19-12091-2019](https://doi.org/10.5194/acp-19-12091-2019).

Koppmann, R.; von Czapiewski, K.; Reid, J.S. A review of biomass burning emissions, part I: gaseous emissions of carbon monoxide, methane, volatile organic compounds, and nitrogen containing compounds. *Atmos. Chem. Phys. Discuss.* **2005**, *5* (5), 10455–10516. DOI: [10.5194/acpd-5-10455-2005](https://doi.org/10.5194/acpd-5-10455-2005).

Lee, J.; Hsu, N.C.; Sayer, A.M.; Bettenhausen, C.; Yang, P. AERONET-Based Nonspherical Dust Optical Models and Effects on the VIIRS Deep Blue/SOAR Over Water Aerosol Product. *J. Geophys. Res. Atmos.* **2017**, *122*, 10384–10401. DOI: [10.1002/2017JD027258](https://doi.org/10.1002/2017JD027258).

Lawrimore, J.; Heim Jr., R.R.; Svoboda, M.; Swail, V.; Englehart, P.J. Beginning a new era of drought monitoring across North America. *Bulletin of the American Meteorological Society* **2002**, *83*, 1191–1192. DOI: [10.1175/1520-0477-83.8.1191](https://doi.org/10.1175/1520-0477-83.8.1191).

Limbacher, J.A.; Kahn, R.A. MISR Research-Aerosol-Algorithm Refinements for Dark Water Retrievals. *Atmos. Meas. Technol.* **2014**, *7*, 3989–4007. DOI: [10.5194/amt-7-3989-2014](https://doi.org/10.5194/amt-7-3989-2014).

Limbacher, J.A.; Kahn, R.A. Updated MISR Over-Water Research Aerosol Retrieval Algorithm—Part 2: A Multi-Angle Aerosol Retrieval Algorithm for Shallow, Turbid, Oligotrophic, and Eutrophic Waters. *Atmos. Meas. Technol.* **2019**, *12*, 675–689. DOI: [10.5194/amt-12-675-2019](https://doi.org/10.5194/amt-12-675-2019).

Liu, X.; Huey, G.; Yokelson, R.J.; Selimovic, V.; Simpson, I.J.; Müller, M.; Jimenez, J.L.; et al. Airborne measurements of western U.S. wildfire emissions: Comparison with prescribed burning and air quality implications. *J. Geophys. Res. Atmos.* **2017**, *122*, 6108–6129, DOI: [10.1002/2016JD026315](https://doi.org/10.1002/2016JD026315).

Lyapustin, A.; Wang, Y. MODIS Multi-Angle Implementation of Atmospheric Correction (MAIAC) Data User's Guide. NASA: Greenbelt, MD, USA, **2018**. Available online: https://modis-land.gsfc.nasa.gov/pdf/MCD19_UserGuide_final_Feb-6-2018.pdf. (Accessed 20 June 2019).

May, A.A.; Levin, E.J.T.; Hennigan, C.J.; Riipinen, I.; Lee, T.; Collett, J.L.; Jimenez, J.L.; Kreidenweis, S.M.; Robinson, A.L. Gas-particle partitioning of primary organic aerosol emissions: 3. Biomass burning. *J. Geophys. Res. Atmos.* **2013**, *118*, 11327–11338. DOI: [10.1002/jgrd.50828](https://doi.org/10.1002/jgrd.50828).

Mei, F. AAC-CCN, BBOP. Atmospheric Radiation Measurement Climate Research Facility. **2013**. Available online: <https://adc.arm.gov/discovery/#v/results/s/s::bbop>. (Accessed on 20 September 2019).

Moore, R.H.; Nenes, A.; Medina, J. Scanning Mobility CCN Analysis—A Method for Fast Measurements of Size-Resolved CCN Distributions and Activation Kinetics. *Aerosol Sci. Tech.* **2010**, *44*, 861–871. DOI: [10.1080/02786826.2010.498715](https://doi.org/10.1080/02786826.2010.498715).

National Fire and Aviation Management. Incident Status Summary. Available online: https://fam.nwrg.gov/fam-web/hist_209/hist_r_print_209_head_2013?v_number=WA-SES-349&v_report_date=08/18/2013&v_hour=1200&v_gaid=NW. (Accessed on 28 December 2019).

Nelson, D.L.; Chen, Y.; Kahn, R.A.; Diner, D.J.; Mazzoni, D. Example Applications of the MISR INteractive EXplorer (MINX) Software Tool to Wildfire Smoke Plume Analyses. *Remote Sens. Fire Sci. Appl.* **2008**, *708909*. DOI: [10.1111/12.795087](https://doi.org/10.1111/12.795087).

Nelson, D.; Garay, M.; Kahn, R.; Dunst, B. Stereoscopic Height and Wind Retrievals for Aerosol Plumes with the MISR INteractive EXplorer (MINX). *Remote Sens.* **2013**, *5*, 4593–4628. DOI: [10.3390/rs5094593](https://doi.org/10.3390/rs5094593).

Ogren, J.A. Comment on “Calibration and Intercomparison of Filter-Based Measurements of Visible Light Absorption by Aerosols”. *Aerosol Sci. Technol.* **2010**, *44*, 589–591. DOI: [10.1080/02786826.2010.482111](https://doi.org/10.1080/02786826.2010.482111).

O'Neill, N.T.; Eck, T.F.; Holben, B.N.; Smirnov, A.; Royer, A.; Li, Z. Optical properties of boreal forest fire smoke derived from Sun photometry. *J. Geophys. Res. Atmos.* **2002**, *107*. DOI: [10.1029/2001JD000877](https://doi.org/10.1029/2001JD000877).

Ottmar, R.O. Smoke Management Guide for Prescribed and Wildland Fire. National Interagency Fire Center: Boise, ID, USA **2001**. Available online: <https://www.nwrg.gov/sites/default/files/publications/pms420-2.pdf>. (Accessed on 22 June 2020).

Ottmar, R.O.; Sandberg, D.V.; Riccardi, C.L.; Prichard, S.J. An overview of the Fuel Characteristic Classification System – quantifying, classifying, and creating fuelbeds for resource planning. USDA Forest Service **2001**. Available online: https://www.fs.fed.us/pnw/fera/fccs/manuscripts/ottmar_et_al_overview_final.pdf. (Accessed on 20 June 2020).

Oregon Department of Forestry: Fires List. Available online: https://apps.odf.oregon.gov/DIVISIONS/protection/fire_protection/fires/FIREList.asp. (Accessed on 28 December 2019).

Petrenko, M.; Kahn, R.; Chin, M.; Soja, A.; Kucsera, T.; Harshvardhan. The Use of Satellite-Measured Aerosol Optical Depth to Constrain Biomass Burning Emissions Source Strength in the Global Model GOCART. *J. Geophys. Res.* **2012**, *117*. DOI: [10.1029/2012JD017870](https://doi.org/10.1029/2012JD017870).

Reid, J.S.; Hobbs, P.V. Physical and optical properties of young smoke from individual biomass fires in Brazil. *J. Geophys. Res.* **1998**, *103*. DOI: [10.1029/98JD00159](https://doi.org/10.1029/98JD00159).

Reid, J.S.; Koppmann, R.; Eck, T.F.; Eleuterio, D.P. A Review of Biomass Burning Emissions Part II: Intensive Physical Properties of Biomass Burning Particles. *Atmos. Chem. Phys.* **2005**, *28*, 799–825. DOI: [10.5194/acp-5-799-2005](https://doi.org/10.5194/acp-5-799-2005).

Roberts, J.; Trainer, M.; Murphy, D.; Brown, S.; Brewer, A.; Gao, R.-S.; Fahy, D. Fire Influence on Regional to Global Environments and Air Quality (FIREX-AQ): A NOAA/NASA Interagency Intensive Study of North American Fires, **2018**. Available online: <https://www.esrl.noaa.gov/csl/projects/firex-aq/whitepaper.pdf>. (Accessed on 12 August 2020).

Rose, D.; Gunthe, S.S.; Mikhailov, E.; Frank, G.P.; Dusek, U.; Andreae, M.O.; Pöschl, U. Calibration and measurement uncertainties of a continuous-flow cloud condensation nuclei counter (DMT-CCNC): CCN activation of ammonium sulfate and sodium chloride aerosol particles in theory and experiment. *Atmos. Chem. Phys.* **2008**, *8*, 1153–1179. DOI: [10.5194/acp-8-1153-2008](https://doi.org/10.5194/acp-8-1153-2008).

Sachse, G.W.; Collins, J.E., Jr.; Hill, G.F.; Wade, L.O.; Burney, L.G.; Ritter, J.A. Airborne tunable diode laser sensor for high-precision concentration and flux measurements of carbon monoxide and methane. *Proc. SPIE 1433, Measurements of Atmospheric Gases* **1991**. DOI: [10.1117/12.46162](https://doi.org/10.1117/12.46162).

Sachse, G.W.; Hill, G.F.; Wade, L.O.; Perry, M.G. Fast-response, high-precision carbon monoxide sensor using a tunable diode laser absorption technique. *J. Geophys. Res.* **1987**, *92*, 2071–2081. DOI: [10.1029/JD092iD02p02071](https://doi.org/10.1029/JD092iD02p02071).

Samset, B.H.; Stjern, C.W.; Andrews, E.; Kahn, R.A.; Myhre, G.; Schulz, M.; Schuster, G.L. Aerosol Absorption: Progress Towards Global and Regional Constraints. *Curr. Clim. Chang. Rep.* **2018**, *4*, 65–83. DOI: [10.1007/s40641-018-0091-4](https://doi.org/10.1007/s40641-018-0091-4).

Santoso, M.A.; Christensen, E.G.; Yang, J.; Rein, G. Review of the Transition From Smouldering to Flaming Combustion in Wildfires. *Front. Mech. Eng.* **2019**, *5*. DOI: [10.3389/fmech.2019.00049](https://doi.org/10.3389/fmech.2019.00049).

Scollo, S.; Kahn, R.A.; Nelson, D.L.; Coltellini, M.; Diner, D.J.; Garay, M.J.; Realmuto, V.J. MISR Observations of Etna Volcanic Plumes. *J. Geophys. Res.* **2012**, *117*. DOI: [10.1029/2011JD016625](https://doi.org/10.1029/2011JD016625)

Scott, J.H.; Burgan, R.E. Standard Fire Behavior Fuel Models: A Comprehensive Set for Use with Rothermel's Surface Fire Spread Model. Gen. Tech. Rep. RMRS-GTR-153. Fort Collins, CO: U.S. Department of Agriculture, Forest Service, Rocky Mountain Research Station, **2005**. Available Online: <https://www.fs.fed.us/rm/pubs/rmrsgtr153.pdf>. (Accessed on 17 February 2021).

Sedlacek, A.J. Single Particle Soot Photometers (SP2) Instrument Handbook; DOE ARM Climate Research Facility: Washington, DC, USA, **2017**. DOI: [10.2172/1344179](https://doi.org/10.2172/1344179).

Sedlacek, A.J., III; Buseck, P.R.; Adachi, K.; Onasch, T.B.; Springston, S.R.; Kleinman, L. Formation and Evolution of Tar Balls from Northwestern US Wildfires. *Atmos. Chem. Phys.* **2018**, *18*, 11289–11301. DOI: [10.5194/acp-18-11289-2018](https://doi.org/10.5194/acp-18-11289-2018).

Sedlacek, A.; Lee, J. Photothermal Interferometric Aerosol Absorption Spectrometry. *Aerosol Sci. Technol.* **2007**, *41*, 1089–1101. DOI: [10.1080/02786820701697812](https://doi.org/10.1080/02786820701697812).

Sedlacek, A.J.; Lewis, E.R.; Kleinman, L.; Xu, J.; Zhang, Q. Determination of and Evidence for Non-Core-Shell Structure of Particles Containing Black Carbon Using the Single-Particle Soot Photometer (SP2). *Geophys. Res. Lett.* **2012**, *39*. DOI: [10.1029/2012GL050905](https://doi.org/10.1029/2012GL050905).

Shi, S.; Cheng, T.; Gu, X.; Guo, H.; Wu, Y.; Wang, Y. Biomass Burning Aerosol Characteristics for Different Vegetation Types in Different Aging Periods. *Environ. Int.* **2019**, *126*, 504–511. DOI: [10.1016/j.envint.2019.02.073](https://doi.org/10.1016/j.envint.2019.02.073).

Springston, S.R. Particle Soot Absorption Photometer (PSAP) Instrument Handbook. DOE ARM Climate Research Facility: Washington, DC, USA, **2018**. DOI: [10.2172/1246162](https://doi.org/10.2172/1246162).

Svoboda, M.; LeComte, D.; Hayes, M.; Heim, R.; Gleason, K.; Angel, J.; Rippey, B.; Tinker, R.; Palecki, M.; Stooksbury, D.; Miskus, D.; Stephens, S. The Drought Monitor. *Bulletin of the American Meteorological Society* **2002**, *83*(8), 1181–1190. DOI: [10.1175/1520-0477-83.8.1181](https://doi.org/10.1175/1520-0477-83.8.1181).

Taubman, B. F.; Marufu, L. T.; Vant-Hull, B. L.; Piety, C. A.; Dodridge, B. G.; Dickerson, R. R.; Li, Z. Smoke over haze: Aircraft observations of chemical and optical properties and the effects on heating rates and stability. *J. Geophys. Res.* **2004**, *109*, D02206. DOI: [10.1029/2003JD003898](https://doi.org/10.1029/2003JD003898).

Toon, O.B.; Maring, H.; Dibb, J.; Ferrare, R.; Jacob, D.J.; Jensen, E.J.; Luo, Z.J.; Mace, G.G.; Pan, L.L.; Pfister, L.; et al. Planning, Implementation, and Scientific Goals of the Studies of Emissions and Atmospheric Composition, Clouds and Climate Coupling by Regional Surveys (SEAC4RS) Field Mission. *J. Geophys. Res. Atmos.* **2016**, *121*, 4967–5009. DOI: [10.1002/2015JD024297](https://doi.org/10.1002/2015JD024297).

Tosca, M.G.; Randerson, J.T.; Zender, C.S.; Nelson, D.L.; Diner, D.J.; Logan, J.A. Dynamics of Fire Plumes and Smoke Clouds Associated with Peat and Deforestation Fires in Indonesia. *J. Geophys. Res.* **2011**, *116*, D08207. DOI: [10.1029/2010JD015148](https://doi.org/10.1029/2010JD015148)

Uin, J. Cloud Condensation Nuclei Particle Counter Instrument Handbook. DOE ARM Climate Research Facility: Washington, DC, USA, **2016**. (Available Online: https://www.arm.gov/publications/tech_reports/handbooks/ccn_handbook.pdf).

Urbanski, S.P. Combustion efficiency and emission factors for wildfire-season fires in mixed conifer forests of the northern Rocky Mountains, US. *Atmos. Chem. Phys.* **2013**, *13*, 7241–7262. DOI: [10.5194/acp-13-7241-2013](https://doi.org/10.5194/acp-13-7241-2013)

Val Martin, M.; Kahn, R.; Tosca, M. A Global Analysis of Wildfire Smoke Injection Heights Derived from Space-Based Multi-Angle Imaging. *Remote Sens.* **2018**, *10*, 1609. DOI: [10.3390/rs10101609](https://doi.org/10.3390/rs10101609)

Val Martin, M.; Logan, J.A.; Kahn, R.A. Smoke Injection Heights from Fires in North America: Analysis of 5 Years of Satellite Observations. *Atmos. Chem. Phys.* **2010**, *10*, 1491–1510. DOI: [10.5194/acp-10-1491-2010](https://doi.org/10.5194/acp-10-1491-2010).

van der Werf, G. R.; Randerson, J. T.; Giglio, L.; Collatz, G. J.; Mu, M.; Kasibhatla, P. S.; Morton, D. C.; DeFries, R. S.; Jin, Y.; van Leeuwen, T. T. Global fire emissions and the contribution of deforestation, savanna, forest, agricultural, and peat fires (1997–2009). *Atmos. Chem. Phys.* **2010**, *10*, 11707–11735. DOI: [10.5194/acp-10-11707-2010](https://doi.org/10.5194/acp-10-11707-2010).

Vant-Hull, B.; Li, Z.; Taubman, B. F.; Levy, R.; Marufu, L.; Chang, F.-L.; Doddrige, B. G.; Dickerson, R. R. Smoke over haze: Comparative analysis of satellite, surface radiometer, and airborne in situ measurements of aerosol optical properties and radiative forcing over the eastern United States. *J. Geophys. Res.* **2005**, *110*, D10S21, DOI: [10.1029/2004JD004518](https://doi.org/10.1029/2004JD004518).

Vay, S.A.; Woo, J.-H.; Anderson, B.E.; Thornhill, K.L.; Blake, D.R.; Westberg, D.J.; Kiley, C.M.; Avery, M.A.; Sachse, G.W.; Streets, D.G.; et al. Influence of regional-scale anthropogenic emissions on CO₂ distributions over the western North Pacific. *J. Geophys. Res.* **2003**, *108*, 8801. DOI: [10.1029/2002JD003094](https://doi.org/10.1029/2002JD003094).

Vernon, C.J.; Bolt, R.; Canty, T.; Kahn, R.A. The Impact of MISR-Derived Injection Height Initialization on Wildfire and Volcanic Plume Dispersion in the HYSPLIT Model. *Atmos. Meas. Technol.* **2018**, *11*, 6289–6307. DOI: [10.5194/amt-11-6289-2018](https://doi.org/10.5194/amt-11-6289-2018).

Virkkula, A. Correction of the Calibration of the 3-wavelength Particle Soot Absorption Photometer (3λ PSAP). *Aerosol Sci. Technol.* **2010**, *44*, 706–712. DOI: [10.1080/02786826.2010.482110](https://doi.org/10.1080/02786826.2010.482110).

Wang, Z.B.; Hu, M.; Yue, D.L.; He, L.Y.; Huang, X.F.; Yang, Q.; Zheng, J.; Zhang, R.Y.; Zhang, Y.H. New particle formation in the presence of a strong biomass burning episode at a downwind rural site in PRD, China. *Tellus B* **2013**, *65:1*, 19965. DOI: [10.3402/tellusb.v65i0.19965](https://doi.org/10.3402/tellusb.v65i0.19965).

Warner, J.; Twomey, S. The Production of Cloud Nuclei by Cane Fires and the Effect on Cloud Droplet Concentration. *J. Atmos. Sci.* **1967**, *24*, 704–706. DOI: [10.1175/1520-0469\(1967\)024<0704:TPOCNB>2.0.CO;2](https://doi.org/10.1175/1520-0469(1967)024<0704:TPOCNB>2.0.CO;2).

Wong, J.; Li, Z. Retrieval of optical depth for heavy smoke aerosol plumes: uncertainties and sensitivities to the optical properties. *J. Atmos. Sci.* **2002**, *59*, 250–261. DOI: [10.1175/1520-0469\(2002\)059<0250:ROODFH>2.0.CO;2](https://doi.org/10.1175/1520-0469(2002)059<0250:ROODFH>2.0.CO;2).

Yokelson, R.J.; Crounse, J.D.; DeCarlo, P.F.; Karl, T.; Urbanski, S.; Atlas, E.; Campos, T.; Shinozuka, Y.; Kapustin, V.; Clarke, A.D.; et al. Emissions from Biomass Burning in the Yucatan. *Atmos. Chem. Phys.* **2009**, *28*, 5785. DOI: [10.5194/acp-9-5785-2009](https://doi.org/10.5194/acp-9-5785-2009).

Yokelson, R. J.; Susott, R.; Ward, D. E.; Reardon, J.; Griffith, D. W. T. Emissions from smoldering combustion of biomass measured by open-path Fourier transform infrared spectroscopy. *J. Geophys. Res.* **1997**, *102(D15)*, 18865–18877. DOI: [10.1029/97JD00852](https://doi.org/10.1029/97JD00852).

Yu, Y.; Kalashnikova, O.V.; Garay, M.J.; Lee, H.; Notaro, M. Identification and Characterization of Dust Source Regions Across North Africa and the Middle East Using MISR Satellite Observations. *Geophys. Res. Lett.* **2018**, *45*, 6690–6701. DOI: [10.1029/2018GL078324](https://doi.org/10.1029/2018GL078324).

Zhou, S.; Collier, S.; Jaffe, D.A.; Briggs, N.L.; Hee, J.; Sedlacek, A.J., III; Kleinman, L.; Onasch, T.B.; Zhang, Q. Regional Influence of Wildfires on Aerosol Chemistry in the Western US and Insights into Atmospheric Aging of Biomass Burning Organic Aerosol. *Atmos. Chem. Phys.* **2017**, *17*, 2477–2493. DOI: [10.5194/acp-17-2477-2017](https://doi.org/10.5194/acp-17-2477-2017).